Faculteit Wetenschappen
Departement Fysica

Confined quantum systems in topological insulator heterostructures

---

Ingeperkte kwantumsystemen in topologische-isolatorheterostructuren

Proefschrift voorgelegd tot het behalen van de graad van
DOCTOR IN DE WETENSCHAPPEN: FYSICA
aan de Universiteit Antwerpen te verdedigen door

Christophe De Beule

Promotoren:
Prof. dr. Bart Partoens (Universiteit Antwerpen)
Prof. dr. Björn Trauzettel (Universität Würzburg)

Antwerpen, 2017

Doctoral jury

Chairman:	Prof. Dr. Michiel Wouters (Universiteit Antwerpen)
Supervisors:	Prof. Dr. Bart Partoens (Universiteit Antwerpen) Prof. Dr. Björn Trauzettel (Universität Würzburg)
Other members:	Prof. Dr. Bart Sorée (Universiteit Antwerpen and IMEC) Prof. Dr. Johan Verbeeck (Universiteit Antwerpen) Prof. Dr. Thomas Schmidt (Université du Luxembourg) Dr. Stijn De Baerdemacker (Universiteit Gent)

Contact

christophe.debeule@gmail.com

Contents

Acknowledgements

First, I would like to thank my supervisor Prof. Bart Partoens for his guidance, interesting physics discussions, and teaching opportunities during my PhD at the CMT group in the University of Antwerp. During my time at the CMT group, my research was supported by the Research Foundation Flanders (FWO) with an aspirant grant. I am also grateful to Dr. O. Leenaerts, Dr. M. Zarenia, Dr. F. Crépin, and Dr. N. T. Ziani for sharing their knowledge of physics. Next, I would like to thank my good friends at the University of Antwerp for the great moments we shared together. Thank you Ben, Matthias, Mario, Nikolas, Pieter, Roeland, Ruben, and Sam! I would also like to thank Prof. Björn Trauzettel for letting me visit his group at the University of Würzburg and sharing his passion for physics. I thank his whole group for their hospitality and the wonderful time I had during my visit in Germany. A special thanks goes out to my office buddies, Daniel and Florian, for being great friends, solving riddles, and helping me with the practical aspects of life in Germany. Finally, I would like to thank my parents for their unconditional support throughout the years and the opportunity to pursuit a higher education, my grandmother for being my biggest fan, and my girlfriend 簡梅潔 (Jiǎn MéiJié) for her love and support. 我非常感謝你!

Christophe De Beule
Antwerpen, November 2017

1 Introduction

1.1 What is a topological insulator?

Topological insulators (TIs) are exotic materials that are electrically insulating in their interior, but conduct on their surface regardless of surface orientation, purity of the material, or any other details as long as the interior remains insulating and the system preserves time-reversal symmetry. In mathematics, the study of properties that are unchanged despite continuous changes in parameters is called *topology*, hence the name *topological insulator* [1]. To illustrate how topology applies to TIs, we draw an analogy between the surface conduction of TIs and the number of holes in closed two-dimensional (2D) surfaces such as a sphere (zero holes) or a donut (one hole). Consider, for example, a sphere made from modeling clay that is deformed to an egg shape without creating any holes. Similarly, a donut can be deformed to a mug, where the donut hole becomes the mug handle. Hence, a sphere (donut) and an egg (mug) are said to be topologically equivalent, because they can be transformed into each other without changing the number of holes: spheres and eggs or donuts and mugs belong to the same topological class, labeled by the number of holes. The same ideas can be applied to TIs: as long as the interior remains insulating, changing the material parameters does not change the topological class which is characterized by the presence (or absence) of robust surface conduction. While the number of holes in closed 2D surfaces can be any positive integer, there are only two topologically distinct types of time-reversal-invariant insulators: *topological insulators* (surface conduction) and *trivial insulators* (no surface conduction). Just as we can only deform a sphere to a donut if a hole is created, we can only transition between trivial and topological insulator if the interior of the materials stops being an insulator. Because the surface of a topological insulator is a boundary with air, which is a trivial insulator, the material has to become conducting at the interface in order to transition between two topologically different regions. This is why the surface of a topological insulator conducts electricity, regardless of details.

1.2 Motivation

Topological insulators (TIs) have attracted great attention due to their topologically protected surface states [2–6] and possible applications in low-power electronics, spintronics [7, 8], and the switching of magnetic memory [9] to name a few. Hence, it is of great interest to tailor the properties of the topological surface state, for example by interfacing the surface with other materials, to suit specific needs. Furthermore, exotic phenomena such as the quantum anomalous Hall effect [10, 11], the topological magnetoelectric effect [12], and the appearance of Majorana bound states [13], were proposed and explored for TIs interfaced with other types of materials. It is therefore interesting to investigate such interfaces and explore how they can be used to construct confined quantum systems with exotic properties.

In this doctoral thesis, we have theoretically investigated topological states in junctions made from different types of TIs and confined quantum systems in heterostructures made from TIs interfaced with other materials such as magnetic and superconducting films and graphene, that are deposited on the surface of a topological insulator. To this end, we employ continuum models based on effective low-energy Hamiltonians since they capture the essential physics of these systems, which would be unfeasible with *ab initio* methods.

We proceed by giving a brief historical overview of the paradigm shift represented by topological phases, the discovery of topological insulators, and a more detailed look at the basic physical properties of these exotic materials.

1.3 The discovery of topological insulators

All matter is made of atoms but it can appear in different forms such as crystalline solids, which in turn can be magnetic or superconducting, for example. Different phases of matter emerge from the different types and organizations of the constituent atoms and their electrons. Condensed matter physics is concerned with the classification and understanding of the physical properties of these phases of matter. Most states of matter can be classified by the principle of *spontaneous symmetry breaking* [14]. A symmetry is spontaneously broken when the ground state breaks the symmetry of the underlying physical laws. For example, liquids like water have complete rotational and translational symmetry on average: a microscopic movie of water looks the same no matter where the container is placed or oriented. However, when water is sufficiently cooled, it forms an ice crystal in which the water molecules are arranged periodically and which is only invariant under specific rotations and translations. Hence, we can distinguish between a symmetrical or disordered phase at high temperature (liquid) and an ordered phase at low temperature (crystal). Similarly, in a piece of iron above the Curie temperature, the magnetic spins are randomly aligned and the material has rotational symmetry with respect to these spins (paramagnet). Below the Curie temperature, neighboring spins

align and the material attains a local magnetization that points in a certain direction, which breaks this rotational symmetry (ferromagnet). In this case, the symmetry is often not broken uniformly, but the ground state still corresponds to the state where all magnetic domains line up. As a final example of spontaneous symmetry breaking, we consider the transition towards a superconducting state of an ordinary metal (e.g. lead) when it is cooled below a critical temperature. In an ordinary metal, the quantum mechanical phases of the electrons near the Fermi level are randomly distributed so that the system is invariant under a global $U(1)$ phase rotation. However, in the superconducting state, these electrons form a condensate of Cooper pairs with a coherent macroscopic phase which is only invariant under rotations by 0 and π (because the Cooper pairs have charge $2e$). Hence, the $U(1)$ symmetry is broken down to $\mathbb{Z}_2$ which corresponds to the breaking of charge conservation down to charge parity since the Cooper pair condensate acts as a reservoir of pairs of electrons.

However, this paradigm was challenged in 1980 with the discovery of the integer quantum Hall (IQH) effect [15]. The IQH state is realized when a two-dimensional electron gas (2DEG) is subjected to low temperatures and strong magnetic fields. The different IQH states have the same symmetry and therefore they cannot be classified with spontaneous symmetry breaking. Instead, it was the first example of a topological phase where certain properties, such as the quantized value of the Hall conductance, are insensitive to adiabatic (sufficiently slow) changes in the material parameters. Topological phases are gapped phases characterized by a topological invariant, which, in case of the IQH state, is an integer corresponding to plateaus in the Hall conductance. The topological invariant can only change if the energy gap vanishes and the system goes trough a quantum phase transition. Hence, there should exist low-energy excitations in the bulk gap that are localized at the boundaries of a topological phase. This is called *bulk-boundary correspondence* [16]. In case of the IQH state, these excitations correspond to the semiclassical skipping orbits of electrons at the edges. This is illustrated in Fig. 1.1 (a). The vanishing of the energy gap is accompanied with a peak in the longitudinal conductance as the Fermi level moves through a Landau level, which is shown together with Hall conductance plateaus in Fig. 1.1 (b).

Later, Haldane showed that the IQH state can also be realized without an external magnetic field as long as time-reversal (TR) symmetry is broken [17]. With the experimental discovery of graphene in 2004, researchers were presented with simple models for real 2D systems [18]. This culminated in 2005, when a new topological phase, called the quantum spin Hall (QSH) insulator, was proposed in graphene with spin-orbit coupling included [19, 20]. In its simplest form, it consists of two versions of the Haldane model, one for each spin, where the spin-orbit interaction now plays the role of a magnetic field that is opposite for each spin so that TR symmetry is not broken on the whole. Moreover, the QSH phase persists even when the spins are mixed by TR-invariant perturbations such as the Rashba effect due to an electric field, as long as the bulk energy gap does not close. Since the QSH phase preserves TR symmetry, the Hall conductance is zero so that it is not characterized with an integer topological invariant ($n \in \mathbb{Z}$) like

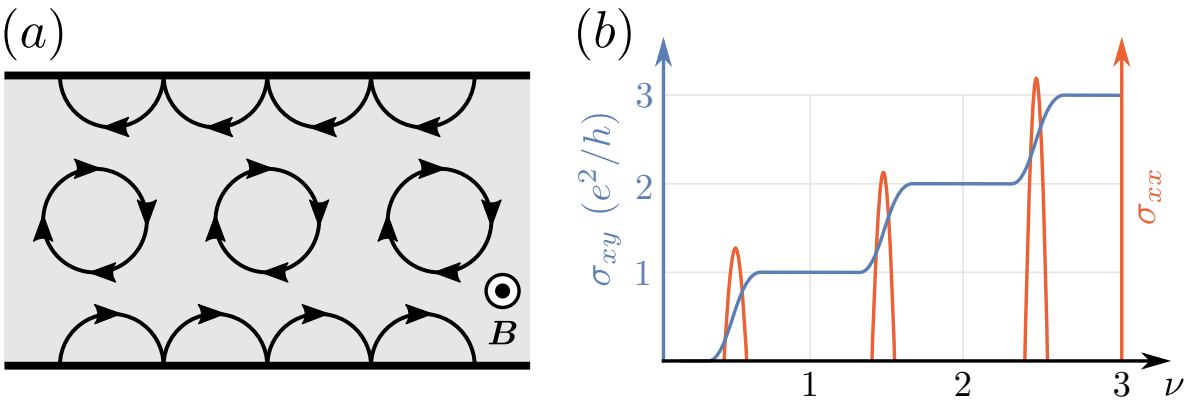

Figure 1.1: (*a*) Top view of a 2DEG in a strip geometry in the IQH state where the uniform magnetic field normal to the sample is denoted by $\boldsymbol{B}$. We show the semiclassical electron cyclotron orbits which are closed in the bulk and skipping at the edges, giving rise to chiral edge states. (*b*) Illustration of the Hall conductance σ_{xy} (blue) and longitudinal conductance σ_{xx} (red) as a function of the filling factor $\nu = N/N_\phi \propto |\boldsymbol{B}|^{-1}$ where N is the number of electrons and N_ϕ is the number of flux quanta through the sample.

the IQH. Instead, it is characterized by a $\mathbb{Z}_2 = \{0, 1\}$ topological invariant. Under this classification, there are only two topologically distinct 2D TR-invariant bulk insulators: the trivial insulator and the QSH insulator. The hallmark of the QSH phase is the existence of a pair of *gapless helical edge states*: gapless since they correspond to two conducting channels at each edge even though the bulk is insulating, and helical since their spin polarization is correlated with their direction of motion. This is illustrated in Fig. 1.2 (*a*). These helical edge modes are protected by TR symmetry against elastic backscattering from nonmagnetic disorder and weak interactions as long as the bulk gap remains finite [21]. Unfortunately, the spin-orbit coupling, which drives the QSH state, is very weak for carbon atoms so that the induced topological gap in graphene is too small to be observed. To find feasible candidates for the QSH state, researchers had to consider materials consisting of heavier atoms which have stronger spin-orbit coupling.

In 2007, the QSH state was experimentally discovered in (Hg,Cd)Te quantum wells at the University of Würzburg [22, 23]. Amongst others, transport measurements confirmed theoretical predictions that the quantum well undergoes a topological phase transition at a critical thickness of HgTe [24]. For example, for a two-terminal setup, illustrated in Fig. 1.2 (*b*), measurements show a conductance plateau at $2e^2/h$ (one conductance quantum for each edge) when the Fermi level was in the energy gap, independent of the dimensions of the sample as long as the sample was shorter than the inelastic scattering length. On the other hand, when the Fermi level was outside of the gap, the measurements scaled with the dimensions of the sample. Moreover, in samples below the critical thickness of the well, the measured conductance was close to zero when the

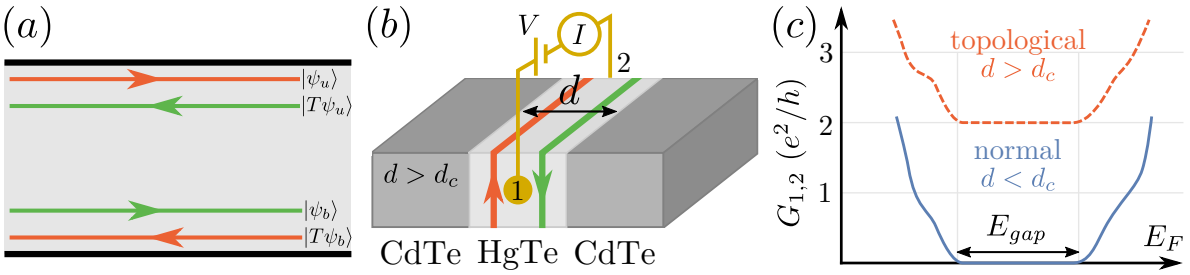

Figure 1.2: (*a*) Top view of a ribbon in the QSH phase where the bulk (middle) is insulating but the edge (top and bottom) supports a Kramers pair of conducting states. The color (green and red) indicates the spin polarization and the helical nature of the edge states: the spin of counterpropagating modes is opposite. (*b*) (Hg,Cd)Te quantum well in the QSH regime in a two-terminal setup where a voltage is applied between the front and back edge and a current I is measured. Here, d is the thickness of HgTe, which for $d > d_c$ is in the QSH regime, and the contacts are labeled by 1 and 2. (*c*) Two-terminal conductance $G_{1,2} = I/V$ of (Hg,Cd)Te quantum well in the normal (blue) and QSH (dashed red) regime as a function of the Fermi level E_F, which is tuned by a gate voltage, where E_{gap} is the confinement gap of HgTe.

Fermi level was inside the gap. The observed two-terminal conductance in both regimes is illustrated in Fig. 1.2 (*c*). All the observations could be explained if the edge supports a pair of counter-propagating dissipationless channels in the topological regime.

Remarkably, unlike the IQH state, the QSH state has a 3D generalization that cannot be adiabatically connected to a stack of QSH systems without closing the bulk energy gap. Therefore, this phase corresponds to a fundamentally different topological phase which was called *(strong) topological insulator* [2, 25]. Topological insulators in three spatial dimensions are characterized by four $\mathbb{Z}_2$ invariants $(\nu_0, \boldsymbol{\nu})$ where ν_0 distinguishes strong and weak topological insulator (STI and WTI). Similar to the QSH phase, the STI phase has gapless surface states on all surfaces, consisting of an odd number of Dirac cones at time-reversal-invariant momenta (Figs. 1.3 (*a*) and (*b*)). Time-reversal invariant perturbations can only couple Dirac points in pairs so that one Dirac cone always remains as long as TR is preserved and the bulk gap is not closed. Moreover, the surface states are protected against weak disorder because of the π Berry phase accumulated along a path that encircles the surface Fermi surface (weak antilocalization). This can also be understood from the helical nature of the surface states, which is called spin-momentum locking and is shown in Fig. 1.3 (*a*). In contrast, the WTIs are topologically equivalent to stacked QSH systems so that even in a clean system not all surfaces have gapless states necessarily. Consider for example a cubic system that consists of a stack of QSH systems in the z direction, shown in Fig. 1.3 (*c*): only four of the six faces have surface states. Both translation and time-reversal symmetry are required to prevent the helical edge states from being coupled in pairs and two Dirac cones remain in this case, as is

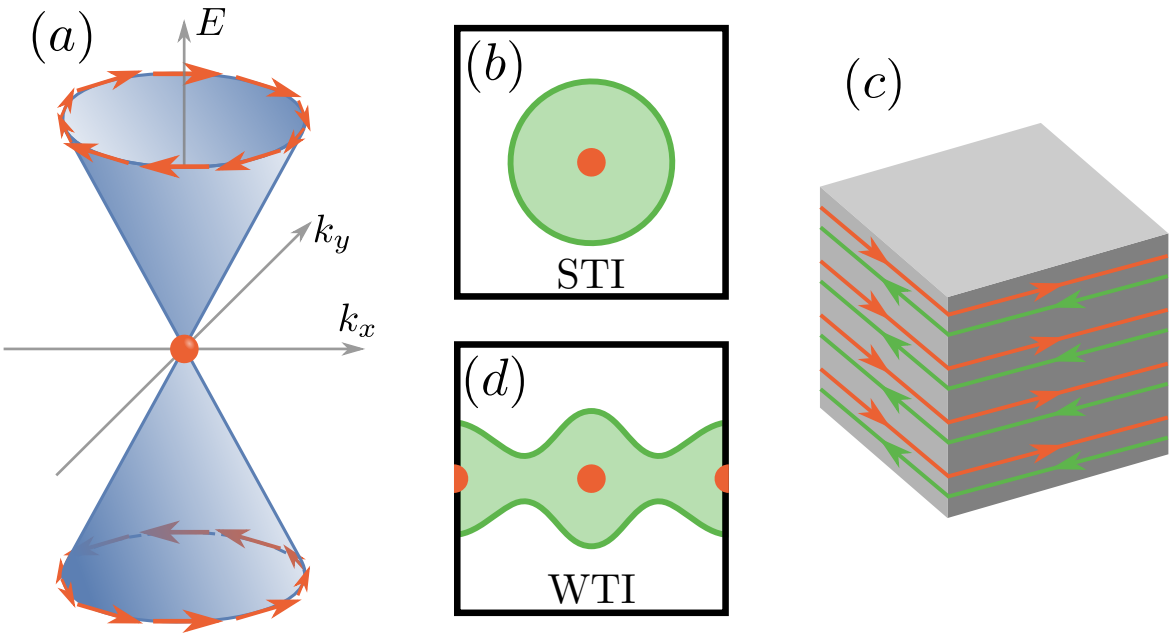

Figure 1.3: (*a*) Surface Dirac cone with spin-momentum locking (red arrows). (*b*) Surface Brillouin zone of STI where the surface Fermi surface (dark green) encloses a single Dirac point (red dot). (*c*) Surface Brillouin zone of WTI where the surface Fermi surface encloses two Dirac points. (*d*) Stack of QSH systems.

illustrated Fig. 1.3 (*d*). Hence, the WTIs are not protected by TR symmetry in general.

The first (strong) topological insulator was predicted in $Bi_{1-x}Sb_x$ alloys [3] which was soon confirmed experimentally with ARPES measurements [26]. However, this material is hard to study because of the complex surface states and alloy scattering. The second generation of topological insulators that were discovered are the thermoelectric semiconductors Bi_2Se_3, Bi_2Te_3, and Sb_2Te_3 which are stoichiometric and realize the simplest example of a topological insulator with a single surface Dirac cone at the $\bar{\Gamma}$ point of the surface Brillouin zone [27–30]. Since then, many more topological insulators have been discovered [31]. In addition, thin films of topological insulators have also been studied extensively since confinement can enhance the energy gap and reduces residual bulk conductivity due to impurities or vacancies [32, 33]. Moreover, in the ultrathin limit, the surface states on opposite surfaces hybridize, and for Bi_2Se_3 there is an oscillatory crossover between trivial and QSH phases when the thickness is reduced [34–36]. Furthermore, in magnetically doped topological insulator thin films, the quantum anomalous Hall effect or Chern insulator, an integer QH state without an external magnetic field, was demonstrated for the first time [10, 11].

Since the discovery of topological insulators, other symmetry-protected topological phases have been theoretically predicted and experimentally confirmed such as topologi-

cal crystalline insulators which have surface states that are protected by discrete crystal symmetries [37, 38]. One example is the mirror-symmetry-protected topological crystalline insulator, SnTe [39, 40]. For technical reviews on TIs, we refer to Refs. [5, 6, 41] and some popular overviews are given by Refs. [42, 43]. Potential applications of TIs can take advantage of the robust metallic nature of the surface states to build very efficient low-power electronics. Furthermore, the inherent spin polarization of the topological surface states has potential uses in spintronics [7, 8] and the switching of magnetic memory [9] to name a few. Lastly, when the surface is made superconducting by interfacing it with a superconductor, it can support so-called Majorana bound states which are robust against decoherence and have potential uses in quantum computing [44, 45].

We proceed by giving a more detailed look at the integer QH effect which is crucial to understand the QSH effect, which in turn can be extended to the 3D time-reversal-invariant topological insulators. Then, we discuss how the surface state can be confined by either breaking time reversal or by proximity-induced superconductivity and how this gives rise to exotic states of matter such as Majorana bound states. Finally, we present the structure of the thesis.

1.4 Quantum Hall effect

Consider a 2D electron gas, for example in a GaAs/AlAs quantum well, subjected to strong magnetic fields at low temperatures, i.e. when the Landau gap $\hbar\omega_c$ is much larger than the thermal energy $k_B T$. Experimentally, it is observed that the Hall conductance is quantized at plateaus given by

$$\sigma_{xy} = \frac{ne^2}{h}, \tag{1.1}$$

where n is integer, as a function of the magnetic field or electron density [15]. Moreover, the quantization is independent of the material or the sample quality and has been measured with a precision up to 10^{-10} [46]. The longitudinal conductance vanishes within each plateau but peaks at transitions between the plateaus (Fig. 1.1 (*b*)).

The different IQH states are labeled with the integer n which can be related to the number of occupied Landau levels. Note that, in the absence of disorder, the Hall conductance is always inversely proportional to the magnetic field, by Galilean invariance (within the effective-mass approximation) [46]. Disorder broadens the Landau levels and gives rise to a so-called mobility gap comprised of localized states around a peak of extended states in the density of states. When the Fermi level moves through the mobility gap, the Hall conductance is constant, giving rise to a plateau. On the other hand, when the Fermi level goes through a region of extended states, charge can flow from one edge to the other and the Hall conductance changes. Disorder extends the topological phase over a finite range of magnetic fields by providing a reservoir of localized states.

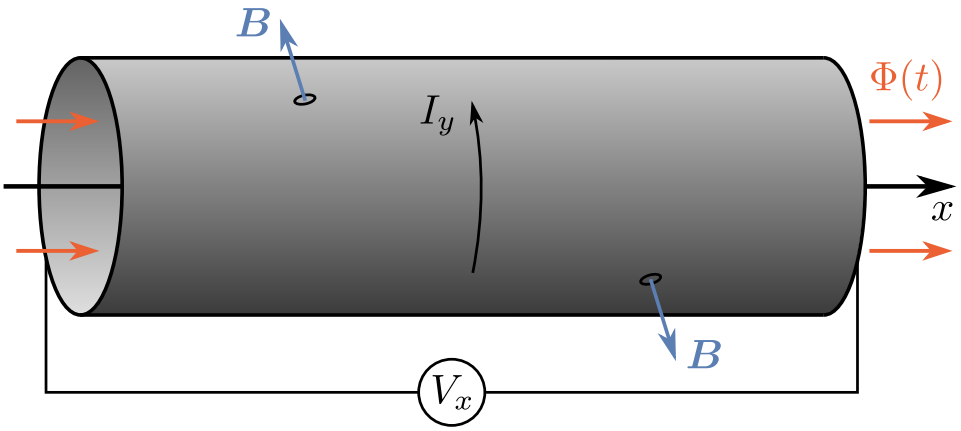

Figure 1.4: Laughlin cylinder. The magnetic field $\boldsymbol{B} = B\boldsymbol{e}_z$ that drives the IQH state is perpendicular to the sample and corresponds to the field of a constant line charge of magnetic monopoles along the central axis (x direction) of the cylinder. The fictional flux $\Phi(t)$ threading the cylinder originates from another magnetic field, $\boldsymbol{B}_\Phi(t) = 4\pi\Phi(t)/L_y^2\,\boldsymbol{e}_x$ where L_y is the cylinder circumference, and is used to control the k_y momentum.

1.4.1 Laughlin's gauge argument

In 1981, the quantization of the Hall conductance was explained by Laughlin in his famous thought experiment [16, 47, 48]. It is worth expounding since it illustrates the intimate relationship between a nonzero value of the Hall conductance and the existence of edge states, i.e. the bulk-boundary correspondence.

Consider a 2D (noninteracting) electron gas confined to a ribbon which is finite in the x direction and periodic in the y direction, and which is placed in a uniform magnetic field in the z direction, $\boldsymbol{B} = B\boldsymbol{e}_z$. Furthermore, we assume that n Landau levels are occupied and that the Fermi level is inside the mobility gap. Since the ribbon is periodic along one direction, it is equivalent to a cylinder and we can imagine *adiabatically* threading a fictional flux $\Phi(t)$ through the cylinder (Fig. 1.4). This flux differs from the external magnetic field $\boldsymbol{B}$ and is used to control the momentum k_y. It enters the Hamiltonian as $k_y \to k_y + \frac{2\pi}{L_y}\frac{\Phi}{\Phi_0}$ where $\Phi_0 = h/e$ is the flux quantum and L_y is the circumference of the cylinder. When a single flux quantum is threaded through the cylinder, the Hamiltonian returns to itself except that all momenta are shifted by one unit. Hence, the system can be in an excited state since the occupation of the electrons might have changed if there are states at the Fermi level. When the Fermi level is in the gap and the flux is threaded slowly, the bulk stays in the ground state so that the occupation can only change if there exist edge states at the Fermi level. These edge states act as reservoirs of electrons and originate from Landau levels whose dispersion bends upwards at the boundary due to the confining edge potential. Hence, when the Fermi level is in the mobility gap, the Laughlin cylinder acts as a charge pump when we thread a flux quantum: for every

occupied Landau level, one electron is transferred between the edges which can also be understood as a shift of the cyclotron centers $x_0 = -k_y l_B^2$. Because we have moved n electrons from one edge to the other, the resulting potential difference is given by

$$V_x = \frac{\Delta E}{ne}, \tag{1.2}$$

where ΔE is the energy difference due to the change in occupation. We now relate the potential V_x to the induced current I_y to obtain the Hall conductance. The current operator in the y direction is given by

$$\hat{I}_y = -\frac{e}{L_y}\hat{v}_y = -\frac{e}{L_y\hbar}\frac{\partial \hat{H}}{\partial k_y} = -\frac{\partial \hat{H}}{\partial \Phi}. \tag{1.3}$$

Hence, the average current in the y direction is given by

$$I_y = \langle\Psi|\,\hat{I}_y\,|\Psi\rangle = -\langle\Psi|\,\frac{\partial \hat{H}}{\partial \Phi}\,|\Psi\rangle = -\frac{\partial E}{\partial \Phi}, \tag{1.4}$$

where we used the Hellmann-Feynman theorem and $|\Psi\rangle\,(\Phi)$ is the many-body wave function. This current can only be carried by the chiral edge states because the Fermi level is inside a mobility gap. Furthermore, since the flux is threaded adiabatically,

$$I_y = -\frac{\Delta E}{\Delta \Phi}. \tag{1.5}$$

Returning to Laughlin's argument with $\Delta\Phi = \Phi_0$ and using (1.2), we find

$$I_y = -\frac{neV_x}{\Phi_0} = \left(-\frac{ne^2}{h}\right)V_x \Rightarrow \sigma_{xy} = \frac{ne^2}{h}. \tag{1.6}$$

The Laughlin argument is based solely on gauge invariance, i.e. that the Hamiltonian returns to itself after one flux quantum, and the fact that the Fermi level is in the mobility gap. If the Fermi level is inside a region of extended states, the pumped charge can relax back to the other edge through the bulk.

1.4.2 TKNN integer

We can further understand the robustness of the IQH state by considering a 2D periodic system in a perpendicular magnetic field [49]. If the number of flux quanta per unit cell is a rational number, the periodicity is preserved by taking a larger unit cell, the so-called magnetic unit cell [50]. This approach shows that the Hall conductance is given by a topological quantum number, the *TKNN integer*.

The Hall conductance can be obtained from the Kubo formula in the static ($\omega \to 0$) and low-temperature ($T \to 0$) limit [51]. In the famous TKNN paper [52], Thouless and

coworkers showed that when the Fermi level in the gap, the Hall conductance can be written as

$$\sigma_{xy} = \frac{e^2}{h} \sum_{E_\alpha < 0} n_\alpha, \tag{1.7}$$

where the sum runs over all occupied bands and n_α is the *Chern number* of the αth occupied band which is given by

$$n_\alpha = \frac{1}{2\pi} \int d^2k \, \mathcal{F}_\alpha, \tag{1.8}$$

with corresponding Berry curvature

$$\mathcal{F}_\alpha(\boldsymbol{k}) = i \left[\langle \partial_{k_x} u_{\alpha\boldsymbol{k}} | \partial_{k_y} u_{\alpha\boldsymbol{k}} \rangle - \langle \partial_{k_y} u_{\alpha\boldsymbol{k}} | \partial_{k_x} u_{\alpha\boldsymbol{k}} \rangle \right], \tag{1.9}$$

and where the integral runs over the magnetic Brillouin zone (BZ) and the $|u_{\alpha\boldsymbol{k}}\rangle$ are eigenstates of the Bloch Hamiltonian. Moreover, when the Berry curvature is integrated over a compact manifold like the BZ torus, the integral is an integer called the *Chern number* [16, 53]. Formula (1.8) is analogous to the *Gauss-Bonnet theorem* which states that the genus (number of holes) of a closed 2D surface (such as a sphere or a torus) is related to the integral of the Gaussian curvature over the surface [1]. It connects the geometry (curvature) to the topology (genus) since the genus is unchanged under continuous deformation of the surface. In the same way, since the Chern number is an integer, and integers cannot change continuously, the value of σ_{xy} is invariant under continuous changes in material parameters that do not close the bulk energy gap; it is a topological invariant.

1.4.3 Chiral edge states

In the IQH state, the existence of edge states is crucial for the quantization of the Hall conductance, as was demonstrated in Section 1.4.1. This is one example of the intimate relation between bulk topology and edge states. In general, gapless modes exist at the boundary between topological phases with a different topological invariant if the boundary conserves the symmetry that enables the topological phase. In case of the IQH phase, this symmetry is $U(1)$ charge conservation. We have previously discussed that the edge states of the IQH state can be thought of as skipping orbits which propagate in one direction only. Therefore, there can be no backscattering and the motion is dissipationless. Such edge states are called *chiral edge states*.

To demonstrate the emergence of chiral edge states, we consider a simple model by Jackiw and Rebbi [54]. When time reversal is broken, the bands near a gap closing point may be approximated with a two-band Dirac model where the mass m gives the energy gap [16]. We now consider an interface in the x direction between two regions with a different sign of $m(x)$:

$$\lim_{x \to \pm\infty} \operatorname{sign}\left[m(x)\right] = \pm 1, \tag{1.10}$$

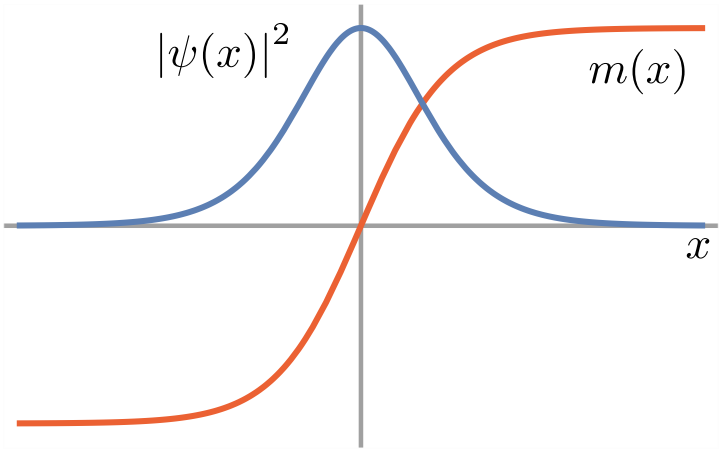

Figure 1.5: Mass domain wall, $m(x) = vm_0 \tanh x$, and the density of the corresponding bound state $|\psi(x)|^2 \propto (\cosh x)^{-2m_0}$.

which is illustrated in Fig. 1.5. Since the y direction is translational invariant, the wave function can be written as $\Psi(x, y) = e^{ik_y y}\psi(x)$ and the Hamiltonian becomes

$$\hat{h}(k_y) = -iv\partial_x\sigma_x + vk_y\sigma_y + m(x)\sigma_z, \tag{1.11}$$

where v is the Fermi velocity. Equation (1.10) tells us that the energy gap has to close somewhere between $x = -\infty$ and $x = +\infty$, and therefore we expect that there exists a zero-energy mode localized somewhere in between. Let us try to find a zero-energy solution at $k_y = 0$. We find

$$\hat{h}(0)\,\psi = 0 \quad \Leftrightarrow \quad \partial_x\psi = -\frac{m(x)}{v}\sigma_y\psi, \tag{1.12}$$

which yields a solution if ψ is an eigenstate of σ_y. There are two solutions but only one is normalizable, which is given by

$$\psi(x) = \exp\left[-\int_{x_0}^{x} dx'\,\frac{m(x')}{v}\right]\begin{pmatrix}1\\ i\end{pmatrix}, \tag{1.13}$$

where x_0 is chosen so that ψ is normalized. The density $|\psi(x)|^2$ of the bound state is shown in Fig. 1.5 for $m(x) = vm_0 \tanh x$. Moreover, since we have $\sigma_y\psi = \psi$, the dispersion is given by $E(k_y) = vk_y$ which is shown in Fig. 1.6 (a).

We have found that there exists a robust chiral mode, localized at the interface between two regions with a different sign of the gap, which is insensitive to the details of $m(x)$ as long as (1.10) is satisfied.

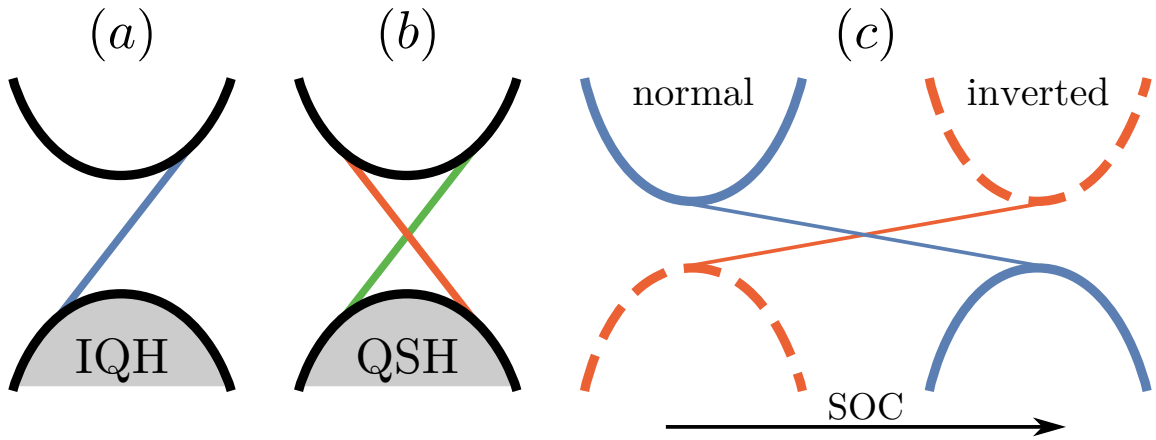

Figure 1.6: (a) Spectrum of a semi-infinite strip in the integer QH state with a single chiral edge state ($n = 1$). (b) Spectrum of a semi-infinite strip in the QSH state with a single Kramers pair of helical edge states. (c) Illustration of band inversion driven by the spin-orbit coupling (SOC).

1.5 Quantum spin Hall effect

In a time-reversal (TR) invariant system, the total Berry curvature $\sum_\alpha \mathcal{F}_\alpha$, where $\mathcal{F}_\alpha$ was defined in Section 1.4.2, is an odd function of the momentum so that the Hall conductance vanishes [16]. It was therefore believed that topological phases require broken TR symmetry. However, in 2005 Kane and Mele showed that the spin-orbit coupling can take on the role of a magnetic field with an opposite sign for opposite spins [19, 20]. This gives two IQH states, one for each spin, with opposite spin Chern numbers. Remarkably, when the spins are mixed, the phase persists as long as the bulk energy gap remains finite. This phase was called *quantum spin Hall* (QSH) insulator or 2D time-reversal-invariant topological insulator. In the QSH phase, each edge that preserves TR symmetry supports robust gapless states. Because of TR symmetry, the edge states necessarily come in Kramers pairs which have opposite momentum and spin (Fig. 1.6 (b)). Hence, these states were called *helical edge states*. In the QSH phase, there are always an odd number of Kramers pairs of edge states at a given edge, so that one pair always remains in the presence of TR-invariant perturbations that do not close the bulk energy gap or break charge conservation (we assume there are no superconducting terms). Moreover, the helical edge states cannot be localized by nonmagnetic disorder because elastic backscattering between Kramers partners is forbidden.

We start this section with a discussion of the implications of time-reversal symmetry in periodic quantum systems. We then discuss the QSH state from two complementary viewpoints: band inversion and the nature of the edge states. These two viewpoints are then combined through the bulk-boundary correspondence to establish the $\mathbb{Z}_2$ topological invariant. This section provides a stepping stone to the 3D topological insulators.

1.5.1 Kramers theorem

Time-reversal symmetry

Physical laws are said to be invariant under time-reversal (TR) symmetry if the resulting motion obeys the same laws when the motion is reversed. In quantum mechanics, TR symmetry is expressed as

$$[H, T] = 0, \tag{1.14}$$

where H is the Hamiltonian and T is the TR operator. Naturally, time reversal should change the sign of the momentum but leave the position unchanged. Hence, to preserve the fundamental commutator $[x, p] = i\hbar$, the time-reversal operator has to be antiunitary. An antiunitary operator is defined as $T = UK$ where U is unitary and K is complex conjugation. It follows that time reversal also flips the spin since the commutator $[\sigma_i, \sigma_j] = i\epsilon_{ijk}\sigma_k$ has to be preserved as well. Specifically, for a spin $\frac{1}{2}$ particle, we can take $T = i\sigma_y K$ which has the important property $T^2 = -1$ [55].

Kramers theorem

Consider a TR-invariant spin $\frac{1}{2}$ system. If $|\psi\rangle$ is an eigenstate, then $|T\psi\rangle$ is another distinct eigenstate with the same energy. Indeed, if $|T\psi\rangle = c\,|\psi\rangle$ where c is a phase factor, we find a contradiction: $-|\psi\rangle = |T^2\psi\rangle = |c|^2\,|\psi\rangle$. In general, *Kramers theorem* states that a TR-invariant system with an odd number of fermions is at least doubly degenerate. The eigenstates $|\psi\rangle$ and $|T\psi\rangle$ are called *Kramers partners* which together constitute a *Kramers pair*. Moreover, the Kramers partners cannot be coupled by a TR-invariant perturbation $V = TVT^{-1}$. This can be shown as follows:

$$\begin{aligned} \langle\psi|\, V\, |T\psi\rangle &= \langle\psi|\, TV\, |\psi\rangle && (1.15)\\ &= -\langle V\psi|T\psi\rangle && (1.16)\\ &= -\,\langle\psi|\, V\, |T\psi\rangle\,, && (1.17) \end{aligned}$$

where in the second step we used $\langle\psi|\phi\rangle = \langle T\phi|T\psi\rangle$ with $|\phi\rangle = TV|\psi\rangle$ (antiunitary property) and $T^2 = -1$. In the last step we used the fact that V is hermitian.

We now consider Kramers theorem in a periodic system. In a translational-invariant system, the eigenstates can be written as

$$|\psi_{\boldsymbol{k}}\rangle = e^{i\boldsymbol{k}\cdot\boldsymbol{r}}\,|u_{\boldsymbol{k}}\rangle\,, \tag{1.18}$$

where the Bloch functions $|u_{\boldsymbol{k}}\rangle$ have the same periodicity as the lattice and are eigenstates of the Bloch Hamiltonian

$$\mathcal{H}(\boldsymbol{k}) = e^{-i\boldsymbol{k}\cdot\boldsymbol{r}} H e^{i\boldsymbol{k}\cdot\boldsymbol{r}}, \tag{1.19}$$

with corresponding energy bands $E_\alpha(\boldsymbol{k})$. Time reversal gives

$$T\mathcal{H}(\boldsymbol{k})T^{-1} = \mathcal{H}(-\boldsymbol{k}), \tag{1.20}$$

since $[H, T] = 0$ when the system has TR symmetry.

So the Kramers partners have opposite momentum and the bands $E_\alpha(\boldsymbol{k})$ are even functions of $\boldsymbol{k}$. Moreover, the bands are degenerate at the TR-invariant momenta (TRIMs) defined by $-\boldsymbol{k} = \boldsymbol{k} + \boldsymbol{G}$ or $\boldsymbol{k} = \boldsymbol{G}/2$, where $\boldsymbol{G}$ is a reciprocal lattice vector. In one spatial dimension there are two TRIMs: $k = 0$ and $k = \pi/a$ where a is the lattice constant. In 2D there are four TRIMs:

$$\boldsymbol{\Gamma}_i = \frac{1}{2}\left(n_{i1}\boldsymbol{b}_1 + n_{i2}\boldsymbol{b}_2\right), \qquad (n_{i1}, n_{i2} = 0, 1), \tag{1.21}$$

where $\boldsymbol{b}_1$ and $\boldsymbol{b}_2$ are the reciprocal basis vectors, and in 3D there are eight TRIMs. Note that the number of bands in a (spinful) TR-invariant periodic system is always even and that the simplest model for a TR-invariant insulator has at least four bands.

1.5.2 Band inversion and edge states

One of the most important principles underlying the QSH state and 3D topological insulators is *band inversion*. Band inversion is the mechanism for the topological phase transition in TIs with inversion symmetry. Even though band inversion only occurs in systems with inversion symmetry, it is still an important concept. Band inversion occurs when the parity of the valence and conduction band at the TRIMs is opposite and changes sign an odd number of times between TRIMs so that the band ordering is twisted throughout the Brillouin zone. In inversion-asymmetric TIs, the topological phase transition does not generically occur at the TRIMs. Moreover, in 3D systems, the phase transition is necessarily accompanied with an intermediate (Weyl) semimetal phase [56, 57]. In most topological insulators, band inversion is driven by spin-orbit coupling, although in (Hg,Cd)Te quantum wells other relativistic corrections play an important role as well [58]. This is illustrated in Fig. 1.6 (*c*). When an insulator with an inverted band structure is placed next to one with a normal band ordering, the band gap has to close at some point to "untie" the twisted bands. Hence, we expect that there exists low-energy excitations localized at such an interface.

We now consider a generic TR-invariant 2D insulator with two edges, i.e. a strip that is periodic in one direction and finite in the other direction. In this case, there can be states at the Fermi level in the bulk energy gap that are localized at the edge. These edge states can be divided into two different types [2]. The generic band structure of the strip is illustrated in Fig. 1.7 for the two types of edge states. We assume that the strip is wide enough so that there is no coupling between opposite edges. Note that we only show one half of the strip Brillouin zone because the other half is identical due to TR symmetry and we only show edge states for one edge. In both cases, the edge states are Kramers degenerate at $k = 0$ and $k = \pi$. Moreover, in Fig. 1.7 (*a*), the edge states do not change their Kramers partners when they disperse away from $k = 0$ so that the same two branches meet up at $k = \pi$. This case corresponds to a trivial insulator because we can get rid of the edge states without closing the bulk energy gap

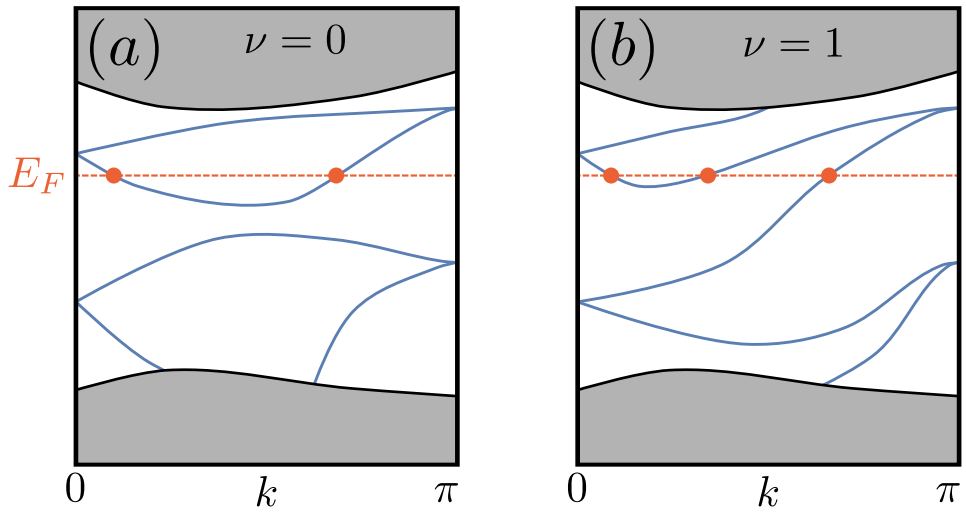

Figure 1.7: Band structure of a TR-invariant insulating strip; the edge states are only shown for a single edge. (a) Even number of Kramers pairs of edge states (blue) at the Fermi level (dashed red); edge states can be pushed into the projected bulk bands (gray) by an edge potential. (b) Odd number of Kramers pairs of edge states at the Fermi level; edge states are robust.

by pushing them into the bulk bands with an edge potential. On the other hand, in Fig. 1.7(b), the edge states switch Kramers partners between $k = 0$ and $k = \pi$. Clearly, this strip corresponds to the QSH phase since the edge states cannot be removed by an edge potential or any other TR-symmetric perturbation that does not close the bulk gap. In the QSH phase, there are always an odd number of Kramers pair of edge states at the Fermi level, while in the trivial case, there is an even number of Kramers pairs of edge states. The former is robust with one Kramers pair of edge states always surviving while the latter is connected to a system with no edge states. We can therefore write

$$(-1)^{\nu} = N_K \bmod 2, \tag{1.22}$$

where N_K is the number of Kramers pairs of edge states at the Fermi level for a given edge and $\nu = 0$ (1) corresponds to a trivial (QSH) insulator [5]. The number ν is called the $\mathbb{Z}_2$ topological invariant. It can only change when TR symmetry is intermittently broken or the bulk energy gap closes.

1.5.3 $\mathbb{Z}_2$ topological invariant

We saw that the physical interpretation of the $\mathbb{Z}_2$ invariant is given by the parity of the number of Kramers pairs of edge states at the Fermi level. However, the $\mathbb{Z}_2$ invariant is completely determined by the bulk topology alone. In their seminal paper, Kane and Mele showed that it could be written in terms of the zeros of a Pfaffian function

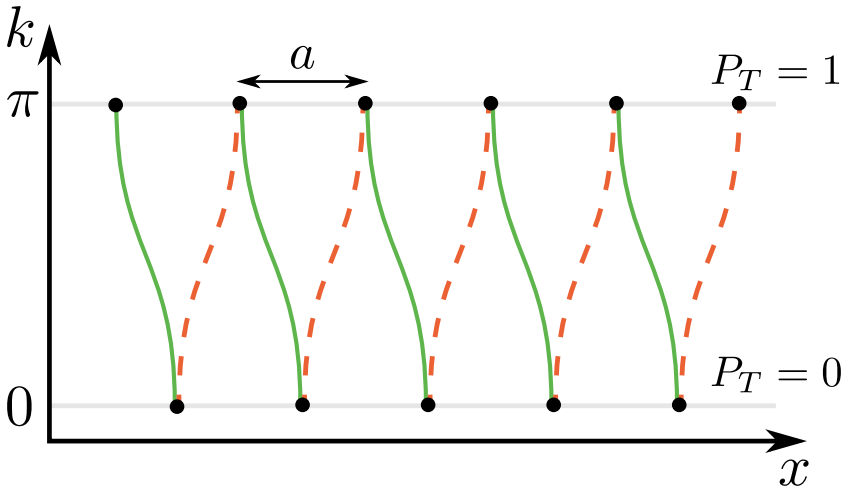

Figure 1.8: Evolutions of Kramers pairs (green and red) of Wannier charge centers of a finite 1D system with Hamiltonian $H(k_x)[k]$ as a function of k. The figure shows the case $\Delta P_T = 1$, where two singly-occupied Kramers pairs appear at each edge and the ground state becomes four-times degenerate.

determined from the bulk Bloch functions [19]. Later, Fu and Kane showed that it can also be written as the change in the difference of the Wannier charge centers of time-reversed occupied bands, which they called TR polarization, when half a flux quantum is threaded through a TR-invariant version of the Laughlin cylinder [2, 59]. This approach is analogous to the formulation of the Hall conductance in terms of the change in charge polarization (sum of Wannier centers) after one cycle of the Laughlin pump, which was discussed in Section 1.4.1 [60].

This argument goes as follows: Consider a 2D TR-invariant band insulator with Hamiltonian $H(k_x, k_y)$. Now construct a set of fictional 1D insulators parametrized by $k = k_y$ with Hamiltonians $H(k_x)[k]$. The TR polarization is defined for a 1D TR-invariant band insulator and is given by

$$P_T = e \sum_{\alpha} \left(\langle 0, \alpha, I | \, x \, | 0, \alpha, I \rangle - \langle 0, \alpha, II | \, x \, | 0, \alpha, II \rangle \right), \tag{1.23}$$

where the Wannier orbitals are given by

$$\langle x | R, \alpha, s \rangle = \frac{1}{2\pi} \int_{-\pi}^{\pi} dk_x \, e^{ik_x(x-R)} \langle x | u_{k_x,\alpha,s} \rangle, \tag{1.24}$$

and we have chosen the cell with lattice vector $R = 0$, $s = I, II$ indicate Kramers partners, $\alpha = 1, \ldots, N$ is a non-Kramers band index, and the number of occupied bands is given by $2N$ [2, 16, 59]. Note that the 1D insulators that we constructed are only TR symmetric for $k = 0$ and $k = \pi$ so that we can consider the change in TR polarization

between these two points:

$$\Delta P_T = P_T(k = \pi) - P_T(k = 0). \tag{1.25}$$

It is now claimed that $\nu \equiv \Delta P_T \mod 2$ defines the $\mathbb{Z}_2$ invariant. Let us assume that $\Delta P_T = 1$ and see if this indeed corresponds to the QSH phase. In this case, the time-reversed Wannier centers have changed partners with one of their neighbors. In the bulk, this only relabels the cell index of the Wannier centers. However, if we consider a finite system, a single occupied Wannier orbital appears at each of the two ends of the system whose Kramers partner is unoccupied. This is illustrated in Fig. 1.8 where we show the Wannier centers as a function of x and k. Hence, we find that the ground-state degeneracy changes in going from $k = 0$ to $k = \pi$: each end contributes a degeneracy of two. Moreover, the spectrum of these 1D finite systems as a function of k is given in Fig. 1.7 where each k now corresponds to a different system. For example, consider the case where a single Kramers pair of end states is occupied at $k = 0$. In Fig. 1.7 (a), which corresponds to a trivial insulator, the Kramers partners split up but return to each other so that the ground-state degeneracy is unchanged. However, in the QSH phase shown in Fig. 1.7 (b), one of the partners becomes degenerate with a previously unoccupied state at $k = \pi$ so that the ground state attains a degeneracy of two for each end. If only half a Kramers pair is occupied in (b), the ground state is degenerate at $k = 0$ and becomes nondegnerate at $k = \pi$. We have therefore shown that the QSH phase is characterized by a change in the ground-state degeneracy between $k = 0$ and $k = \pi$. This can be determined from ΔP_T which only requires knowledge of the bulk wave functions.

Furthermore, when the system has inversion symmetry, the bands have a definite parity at the TRIMs and Fu and Kane showed that the $\mathbb{Z}_2$ invariant can be written as the product of the parities of the occupied bands at the TRIMs [3]:

$$(-1)^\nu = \prod_{i=4} \left(\prod_{\alpha=1}^{N} \delta_\alpha(\mathbf{\Gamma}_i) \right), \tag{1.26}$$

where δ_α is the parity eigenvalue and α runs over one of the Kramers partners of each of the $2N$ occupied bands at the TRIMs. Note that Kramers partners have the same parity since time reversal and space inversion commute. Hence, the $\mathbb{Z}_2$ invariant determines if there are an even ($\nu = 0$) or odd ($\nu = 1$) number of band inversions. When the number of band inversions is even (odd) there will be an even (odd) number of gap closings at an interface with vacuum. Only an odd number is robust against time-reversal-invariant perturbations and therefore $\nu = 1$ corresponds to a topological insulator, while $\nu = 0$ corresponds to a trivial insulator. This method can also be used for systems without inversion symmetry if they can be adiabatically connected to a system with inversion symmetry without breaking TR and closing the bulk energy gap.

1.6 3D topological insulators

Remarkably, the QSH phase can be extended to a three-dimensional (3D) topological phase that is fundamentally different from stacked QSH phases, called *(strong) topological insulator* [2, 25]. To demonstrate this construction, we consider a simple cubic lattice with unit lattice constant. We can now calculate a $\mathbb{Z}_2$ invariant for each of the six time-reversal (TR) invariant planes in the 3D Brillouin zone cube, which are given by $k_i = 0$ and $k_i = \pi$ for $i = x, y, z$ [41]. For an inversion-symmetric system, the six $\mathbb{Z}_2$ invariants can be calculated with Eq. (1.26). We denote them as $i_0 = (-1)^{\nu_{(k_i=0)}}$ and $i_\pi = (-1)^{\nu_{(k_i=\pi)}}$ for $i = x, y, z$. However, because some planes share two TRIMs, not all invariants are independent. Observe that $x_0 x_\pi$, $y_0 y_\pi$, and $z_0 z_\pi$ are all given by the combined product of the parities of the occupied bands at all TRIMs. Hence,

$$x_0 x_\pi = y_0 y_\pi = z_0 z_\pi \equiv (-1)^{\nu_0}, \tag{1.27}$$

so that there are only four independent $\mathbb{Z}_2$ invariants. In case $\nu_0 = 1$, one goes from a trivial 2D insulator to a QSH insulator between opposite TR-invariant planes without closing the gap by effectively breaking TR symmetry when $k_i \neq 0, \pi$. This defines the (strong) topological insulator, since in this case there are an odd number of band inversions at the TRIMs in the 3D Brillouin zone. The remaining three $\mathbb{Z}_2$ invariants can be chosen as

$$\boldsymbol{\nu} = \left(\nu_{(k_x=0)}, \nu_{(k_y=0)}, \nu_{(k_z=0)}\right), \tag{1.28}$$

which further specify the band inversions. For example, the Bi_2Se_3 family of TIs has a single band inversion at the Γ point so that $(\nu_0, \boldsymbol{\nu}) = (1, 111)$ with this definition. In case $\nu_0 = 0$, there are an even number of band inversions which is equivalent to a stack of QSH systems. This is called a weak topological insulator (see Section 1.3).

Note that 3D topological insulator cannot exist when spin is conserved, since in that case, the $\mathbb{Z}_2$ invariants $\nu_{(k_i=0,\pi)}$ $(i = x, y, z)$ can be written in terms of the spin Chern numbers [19]. These are also defined if TR is broken and cannot change as long as the gap is not closed so that $\nu_0 = 0$. Spin-orbit coupling is therefore sufficient but not necessary to realize a 3D topological insulator.

1.6.1 Exotic gapped surface phases

In Section 1.3, we have already described the topological surface states of a strong topological insulator. In the simplest case, the surface state is given by a single surface Dirac cone characterized by spin-momentum locking, which is shown in Fig. 1.3 (a). Exotic gapped phases can emerge on the surface of a topological insulator by locally breaking time reversal or charge conservation by depositing magnetic or superconducting films on the surface, respectively. This is shown in Fig. 1.9.

Proximity to a magnetic film leads to an exchange potential which lifts the Kramers degeneracy and opens a gap at the Dirac point in the surface spectrum [12, 61]. Moreover, a magnetic domain wall, where the magnetization changes sign, supports a robust

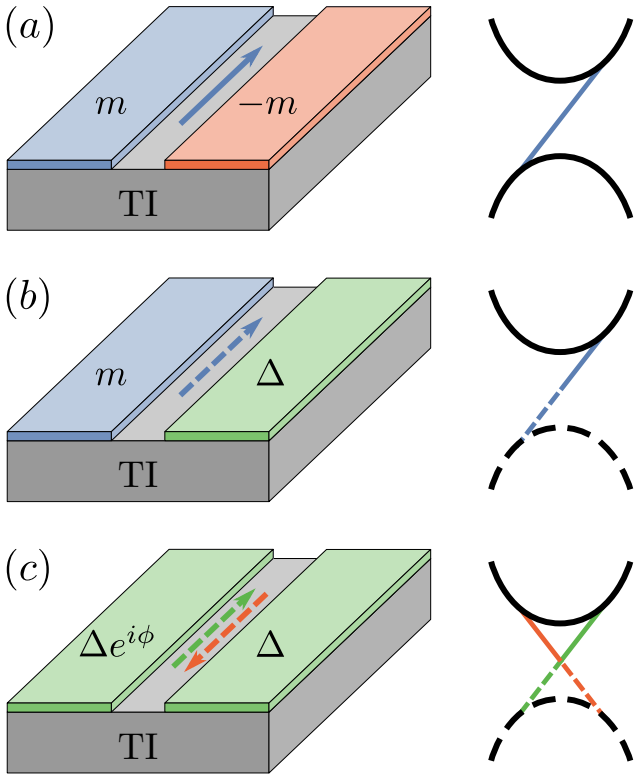

Figure 1.9: Domain wall between (a) two magnetic regions with opposite magnetization, which support a chiral fermion, (b) magnetic and superconducting regions, supporting a chiral Majorana, and (c) two superconducting regions with phase difference ϕ, which supports a helical Majorana for $\phi = \pi$. The right panels show the spectrum of the gapped surface state and the gapless interface state, where dashed lines indicate particle-hole redundancy.

chiral mode as we have shown in Section 1.4.3 (Fig. 1.9 (a)). Superconductivity can be induced in the surface by proximity to an ordinary s-wave superconductor, which opens a superconducting gap at the surface Fermi level [13, 62]. This breaks charge conservation since electrons can tunnel to and away from the surface as Cooper pairs. In this case, a domain wall between a magnetic and superconducting region exhibits a chiral Majorana mode (Fig. 1.9 (b)) and a domain wall between superconducting regions with a superconducting phase difference $\Delta\phi = \pi$ supports a Kramers pair of gapless Andreev bound states called helical Majorana modes (Fig. 1.9 (c)). Moreover, when $\Delta\phi = \pi - \epsilon$, a gap is opened and at a line junction between regions with $\epsilon > 0$ and $\epsilon < 0$, there exist robust zero-energy Majorana bound states (MBS) [13]. By adiabatically tuning the phase differences over a network of such line junctions, the (degenerate) MBSs can be exchanged in space which is equivalent to a rotation of the degenerate ground state subspace. Such operations can be exploited to perform topological quantum computations which are insensitive to local perturbations that normally cause decoherence [44, 45].

1.7 Structure of the thesis

In this doctoral thesis, we investigate hybrid quantum systems that combine topological insulators (TIs), magnetic films, superconductors, or graphene to give rise to new and interesting states of matter. There are three main subjects:

(1) Topological crystalline states in junctions of TIs (Chapter 2);

(2) Quantum dots on the surface of TIs (Chapters 3 and 4);

(3) Tunneling in graphene – TI heterostructures (Chapter 5).

In Chapter 2, we start by discussing a continuum model for TIs with a single band inversion, e.g. the Bi_2Se_3 family. We solve this model explicitly for a semi-infinite slab and we derive an effective surface Hamiltonian that we use in subsequent chapters to model the topological surface state. Then, we consider interface states localized at a junction of two topological insulators with mirror symmetry whose surface states have opposite helicity. Our initial motivation was the claim that this system exhibits tachyonlike excitations [63]. Here, we show that these solutions are spurious and we explicitly calculate the actual interface states and demonstrate how they are protected by the mirror symmetry.

In Chapters 3 and 4, we consider quantum dots on the surface of a topological insulator, where the surface state is confined with local exchange fields or superconducting proximity effect as we discussed in Section 1.6.1. These systems allow us to investigate the effect of confinement and electron-electron interactions on the topological surface state. In Chapter 3, we study a magnetic quantum dot created by depositing a perforated magnetic insulating film on top of the surface which traps the surface state within the hole. We also consider the effect of Coulomb interactions on the properties of the magnetic quantum dot, which leads to the formation of a *spin-polarized Wigner molecule*. We then consider hybrid quantum rings in Chapter 4. Specifically, we study two types of systems: an annulus region of the topological-insulator surface with a magnetic gap on the inside of the annulus and a superconducting gap on the outside, and an annulus bounded by two superconducting regions that have a different phase of the superconducting order parameter. These systems support Majorana bound states when half a flux quantum is threaded through the center of the ring.

Finally, in Chapter 5, we investigate heterostructures made from depositing graphene on the surface of a topological insulator. We discuss different commensurate structures and derive a low-energy model. The topological surface state migrates to the graphene and attains a cubic dispersion when the Dirac cones overlap in energy. Since these heterostructures can be probed by conductance measurements, we consider tunneling from the bare surface to steps and through nanoribbons of the deposited graphene.

2

Topological insulator junctions

We use a continuum model for a 3D strong topological insulator to find the topological surface state and obtain an effective surface Hamiltonian. We then consider a junction between two TIs whose surface states have opposite helicity and discuss how gapless states protected by mirror symmetry arise naturally at the interface both in terms of a scattering paradox and bulk topology. The interface states are then calculated explicitly with the continuum model for different cases. Finally, we consider spurious tachyonlike solutions which initially caused confusion in the community and we show their origin and how they can be resolved.

2.1 Model

First, we discuss the low-energy model of Bi_2Se_3, which also applies to other topological insulators (TIs) with the same crystal structure, shown in Fig. 2.1. For the Bi_2Se_3 class of TIs, there is one band inversion at the origin Γ of the Brillouin zone [27, 28]. Hence, it is sufficient to consider only bands near Γ to understand the topological properties. At the Γ point, the bands near the Fermi level are spanned by four states with angular momentum $m_j = \pm 1/2$ and parity $\mathcal{P} = \pm$ [64]. States with $\mathcal{P} = \pm$ arise from hybridization between the Bi (6p) and Se (4p) valence orbitals. However, because of the large energy difference between these orbitals, the hybridized states are mostly localized on Bi ($\mathcal{P} = +$) and Se atoms on the top and bottom of QLs ($\mathcal{P} = -$) [64]. On the other hand, states with $m_j = \pm 1/2$ are spin-orbit coupled superpositions of $|p_z \uparrow\rangle$ with $|p_+ \downarrow\rangle$ and $|p_z \downarrow\rangle$ with $|p_- \uparrow\rangle$, respectively. However, since the crystal-field splitting is much stronger than the spin-orbit coupling, these states are mainly p_z so that m_j is proportional to the electron spin. Therefore, the Hilbert space of the model is approximately spanned by p_z orbitals $\{|\text{Bi}\uparrow\rangle, |\text{Se}\uparrow\rangle, |\text{Bi}\downarrow\rangle, |\text{Se}\downarrow\rangle\}$.

We can construct the model on the basis of the symmetries of Bi_2Se_3 and how they act on the Bloch Hamiltonian $H(\boldsymbol{k}, k_z)$ where $\boldsymbol{k} = k_x \boldsymbol{e}_x + k_y \boldsymbol{e}_y$. These are given by time reversal ($\mathcal{T}$), space inversion ($\mathcal{P}$), a threefold rotation ($\mathcal{C}_3$) around the z axis which is

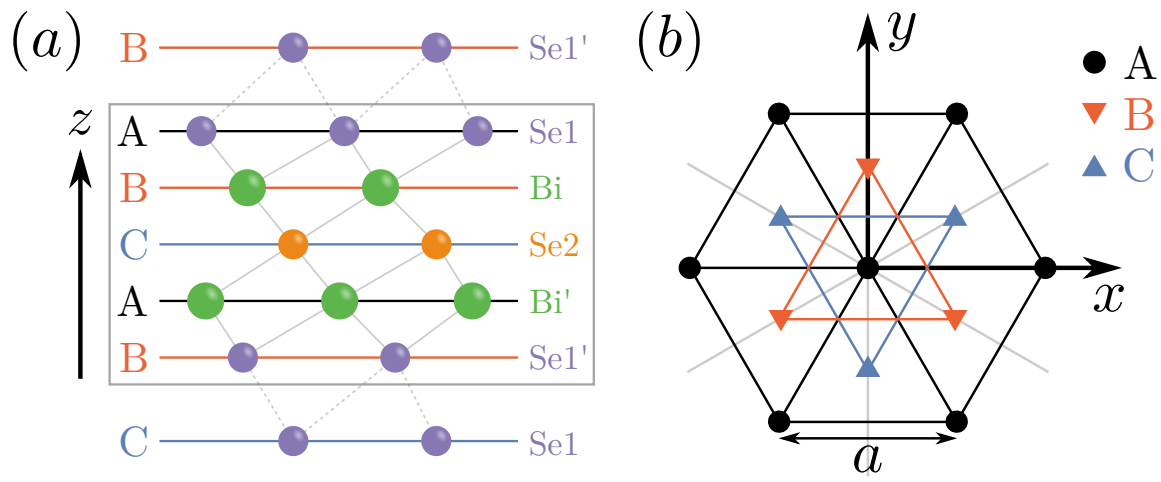

Figure 2.1: The crystal structure of Bi_2Se_3 (space group $R\bar{3}m$) is a layered structure consisting of units of five atomic layers, called quintuple layers (QLs), that are stacked on top of each other. (a) QL along the z axis where Se1 (Bi) and Se1′ (Bi′) are equivalent. The dotted gray lines represent van der Waals type bonds between QLs. (b) Each atomic layer is a trigonal lattice in the xy plane in consecutive positions A, B, and C that are offset by a distance $a/\sqrt{3}$ in the y direction where a is the in-plane lattice constant. The three mirror planes (e.g. yz plane) are shown as the gray lines.

perpendicular to the quintuple layers, and a mirror plane ($\mathcal{M}_x$) perpendicular to the x axis (Fig. 2.1). Time-reversal symmetry is expressed as

$$\mathcal{T}H(-\boldsymbol{k}, -k_z)\mathcal{T}^{-1} = H(\boldsymbol{k}, k_z), \tag{2.1}$$

where $\boldsymbol{k} = k_x\boldsymbol{e}_x + k_y\boldsymbol{e}_y$ and $\mathcal{T} = i\sigma_y\mathcal{K}$ is the time-reversal operator with $\mathcal{K}$ complex conjugation. Space inversion gives

$$\mathcal{P}H(-\boldsymbol{k}, -k_z)\mathcal{P}^\dagger = H(\boldsymbol{k}, k_z), \tag{2.2}$$

with $\mathcal{P} = \tau_z$ which acts on Bi ($\tau_z = +$) and Se ($\tau_z = -$). Together, time reversal and space inversion enforce doubly degenerate bands. Threefold rotation $\mathcal{C}_3$ around the z axis is expressed as

$$\mathcal{C}_3H(R(-\theta)\boldsymbol{k}, k_z)\mathcal{C}_3^\dagger = H(\boldsymbol{k}, k_z), \tag{2.3}$$

where $\mathcal{C}_3 = \exp(-i\theta\sigma_z/2)$ with $\theta = 0, 2\pi/3$ and $R(\theta)$ represents a rotation of the momentum in the xy plane. Finally, the mirror operation $x \to -x$, which is a combination of inversion and a twofold rotation around the x axis, is expressed as

$$\mathcal{M}_xH(-k_x, k_y, k_z)\mathcal{M}_x^\dagger = H(k_x, k_y, k_z), \tag{2.4}$$

with $\mathcal{M}_x = -i\sigma_x\tau_z$. Combined with the threefold rotation symmetry, there are three physical mirror planes, shown in Fig. 2.1 (b). Here, we have chosen the same spin basis

ε_1	ε_2	A_1	A_2	B_1	B_2	M
1.3 eVÅ^2	19.6 eVÅ^2	2.2 eVÅ	4.1 eVÅ	10 eVÅ^2	56.6 eVÅ^2	0.28 eV

Table 2.1: Parameter values of the Hamiltonian (2.6) for Bi_2Se_3 found from fitting the bulk energy spectrum to *ab initio* calculations [27].

as in Ref. [27] where the electron spin is given by

$$s_x = \sigma_x\tau_z, \qquad s_y = \sigma_y\tau_z, \qquad s_z = \sigma_z, \tag{2.5}$$

as can be seen from the form of $\mathcal{M}_x = -is_x$ since the mirror operation $x \to -x$ only affects the spin and leaves the p_z orbitals unchanged [64, 65].

With these symmetries, the Hamiltonian, up to quadratic order in the crystal momentum near Γ, becomes [27, 64]

$$H(\boldsymbol{k}, k_z) = \varepsilon(\boldsymbol{k}, k_z) + \mathcal{M}(\boldsymbol{k}, k_z)\tau_z + (A_1 k_z\sigma_z + A_2\boldsymbol{k}\cdot\boldsymbol{\sigma})\,\tau_x, \tag{2.6}$$

with

$$\varepsilon(\boldsymbol{k}, k_z) = \varepsilon_0 + \varepsilon_1 k_z^2 + \varepsilon_2 k^2, \tag{2.7}$$
$$\mathcal{M}(\boldsymbol{k}, k_z) = M - B_1 k_z^2 - B_2 k^2, \tag{2.8}$$

where $k = |\boldsymbol{k}|$. The values of the model parameters ε_1, ε_2, A_1, A_2, B_1, B_2, and M are given in Table 2.1 for Bi_2Se_3 and the energy shift ε_0 in (2.7) will be chosen such that the Dirac point of the topological surface state is at zero energy. Besides the diagonal term $\varepsilon(\boldsymbol{k}, k_z)$, the Hamiltonian (2.6) is identical to the 3D Dirac Hamiltonian with uniaxial anisotropy along the z direction and a momentum-dependent mass term given by $\mathcal{M}(\boldsymbol{k}, k_z)$ [27]. The anisotropy between the xy plane and the z axis is a reflection of the layered crystal structure of Bi_2Se_3. The diagonal term $\varepsilon(\boldsymbol{k}, k_z)$ breaks the particle-hole symmetry $\tau_y H \tau_y = -H$ so that the bands are not symmetric around zero.

Note that, in quadratic order, the Hamiltonian has continuous rotation symmetry around the z axis. This model symmetry is reduced to $\mathcal{C}_3$ by cubic warping terms [64, 66] which are not included in (2.6). Neglecting these terms does not affect the conclusions of this chapter. Furthermore, spectroscopic experiments show that the topological surface state of Bi_2Se_3 is almost an ideal Dirac cone, in contrast with Bi_2Te_3 which has a smaller energy gap and a substantial trigonal potential [67].

Bulk energy spectrum

The bulk spectrum can be easily found by noting that the square of the non-diagonal part of the Hamiltonian is diagonal:

$$(H - \varepsilon)^2 = \mathcal{M}^2 + (A_1 k_z\sigma_z + A_2\boldsymbol{k}\cdot\boldsymbol{\sigma})^2 = \mathcal{M}^2 + (A_1 k_z)^2 + (A_2 k)^2\,, \tag{2.9}$$

where the cross terms vanish because the Pauli matrices anticommute. Because the Hamiltonian matrix is four dimensional there are four eigenvalues, so that the energy bands are doubly degenerate as expected and given by

$$E_{\pm}(k,k_z) = \varepsilon_0 + \varepsilon_1 k_z^2 + \varepsilon_2 k^2 \pm \sqrt{\left(M - B_1 k_z^2 - B_2 k^2\right)^2 + \left(A_1 k_z\right)^2 + \left(A_2 k\right)^2}, \qquad (2.10)$$

which is shown in Fig. 2.2 for Bi_2Se_3. Note that the model describes an insulator only if $B_{1,2}^2 > \varepsilon_{1,2}^2$ which is the condition to have a band gap since otherwise the valence and conduction band have the same curvature.

$\mathbb{Z}_2$ topological nature

Because the model (2.6) has inversion symmetry, the topological nature can be understood from the change in the parity of the bulk wave function between zero and large momentum [3, 27]. Note that the eigenstates of (2.6) have definite parity only in those two cases as only then $\tau_z H \tau_z = H$. In case M, B_1, and B_2 have the same sign, the parity of the bands changes sign between zero and large momentum, which is called a *band inversion*. The phase with an inverted band structure is clearly topological as it cannot be connected continuously, i.e. without closing the band gap, to the atomic limit. Note that the sign of the gap itself is not enough to characterize the intrinsic band topology since it can be changed by the unitary transformation τ_x. In case inversion symmetry is broken, e.g. by a constant $\propto \tau_x$, the band inversion is no longer specified by parity, but as long as this extra term does not close the band gap, the system with broken inversion is topologically equivalent to the centrosymmetric system.

The band inversion can be undone by closing the gap at $k = k_z = 0$ and changing the sign of M which swaps the bands. Therefore, at an interface between an inverted insulator and a trivial insulator (or vacuum) the gap has to vanish at some point along the way so that there exist gapless modes at such an interface. Furthermore, if the interface respects time-reversal symmetry, these modes come in Kramers pairs that consist of two degenerate states at opposite momentum (Kramers theorem). At $k_\parallel = 0$, the two states that make up a Kramers pair form 2D Dirac points which are split at finite momentum due to the spin-orbit coupling. The surface or interface states are robust against perturbations that preserve time reversal, particle number or $U(1)$ gauge symmetry, and the bulk energy gap, only if the number of Dirac points is odd. Otherwise, the different Kramers pairs can pairwise couple and open an energy gap. Terms that break time reversal or particle number conservation can be used to confine the topological surface state and are discussed in Chapter 3 and 4, respectively.

This is an example of the *bulk-boundary correspondence* and it gives a physical interpretation of the $\mathbb{Z}_2$ (even or odd) topological invariant that classifies time-reversal invariant insulators such as model (2.6). Note that this discussion is restricted to the continuum model (2.6) which assumes that the relevant physics is contained in a small momentum region of the Brillouin zone near the Γ point and it should be supplemented with the general discussion on topological insulators given in the introduction.

2.1.1 Probability current density

Here, we derive the probability current density of the Hamiltonian (2.6) which is required to find the correct boundary conditions at the interface with vacuum or another insulator in the remainder of this chapter. The probability current density $\boldsymbol{j}$ is defined through the continuity equation

$$\partial_t \rho + \nabla \cdot \boldsymbol{j} = 0, \tag{2.11}$$

where $\rho(\boldsymbol{r}, z, t) = \Psi^\dagger \Psi$ is the probability density with $\boldsymbol{r} = x\boldsymbol{e}_x + y\boldsymbol{e}_y$. It can be found as follows: First, we write

$$i\partial_t \rho = i\partial_t \left(\Psi^\dagger \Psi\right) = \Psi^\dagger (i\partial_t \Psi) - c.c. = \Psi^\dagger \hat{H} \Psi - c.c., \tag{2.12}$$

where $\hat{H} = H(\hat{\boldsymbol{k}}, \hat{k}_z)$ with $\hat{\boldsymbol{k}} = -i\nabla_{\boldsymbol{r}}$ and $\hat{k}_z = -i\partial_z$. In the last step of (2.12) we made use of the time-dependent Schrödinger equation, $i\partial_t \Psi = \hat{H}\Psi$. As an example for the last step, consider the terms $\sigma_z \tau_x \hat{k}_z$ and $\tau_z \hat{k}_z^2$. The first term becomes

$$\Psi^\dagger \sigma_z \tau_x \hat{k}_z \Psi = \hat{k}_z (\Psi^\dagger \sigma_z \tau_x \Psi) + (\sigma_z \tau_x \hat{k}_z \Psi)^\dagger \Psi, \tag{2.13}$$

where we made use of $\hat{k}_z \Psi^\dagger = -(\hat{k}_z \Psi)^\dagger$. Similarly, the second term becomes

$$\Psi^\dagger \tau_z \hat{k}_z^2 \Phi = \hat{k}_z (\Psi^\dagger \tau_z \hat{k}_z \Psi) + (\tau_z \hat{k}_z \Psi)^\dagger \hat{k}_z \Psi \tag{2.14}$$

$$= \hat{k}_z [\Psi^\dagger \tau_z \hat{k}_z \Psi + (\tau_z \hat{k}_z \Psi)^\dagger \Psi] + (\tau_z \hat{k}_z^2 \Psi)^\dagger \Psi. \tag{2.15}$$

It therefore follows that

$$i\partial_t \rho = \hat{k}_x j_x + \hat{k}_y j_y + \hat{k}_z j_z, \tag{2.16}$$

where

$$j_z = \mathrm{Re}\left\{\Psi^\dagger \left[2\left(\varepsilon_1 - B_1 \tau_z\right) \hat{k}_z + A_1 \sigma_z \tau_x\right] \Psi\right\}, \tag{2.17}$$

$$j_{x,y} = \mathrm{Re}\left\{\Psi^\dagger \left[2\left(\varepsilon_2 - B_2 \tau_z\right) \hat{k}_{x,y} + A_2 \sigma_{x,y} \tau_x\right] \Psi\right\}, \tag{2.18}$$

are the components of the probability current density.

2.2 Surface state

Before we consider the interface between two topological insulators, we investigate the surface state of a topological insulator described by Hamiltonian (2.6). In this section we follow closely the approach of [68]. Since we are looking for a solution localized at the surface, we try the *ansatz*

$$\psi(\boldsymbol{r}, z) = \phi_\lambda e^{\lambda z} e^{i\boldsymbol{k}\cdot\boldsymbol{r}}. \tag{2.19}$$

If we plug this trial solution in the Schrödinger equation $\hat{H}\psi = E\psi$, we obtain

$$[H(\boldsymbol{k}, -i\lambda) - E]\,\phi_\lambda = 0, \tag{2.20}$$

which has a nontrivial solution for $|H(\boldsymbol{k}, -i\lambda) - E| = 0$. This yields an equation for the roots of the square of a biquadratic equation in λ which is given by

$$\begin{aligned} D_1 D_2 \lambda^4 + \left[A_1^2 + D_1\,(E - L_2) + D_2\,(E - L_1)\right] \lambda^2 \\ + (E - L_1)\,(E - L_2) - A_2^2 k^2 = 0, \end{aligned} \tag{2.21}$$

with

$$D_{1,2} = \varepsilon_1 \mp B_1, \tag{2.22}$$

$$L_{1,2}(k) = \varepsilon_0 \pm M + (\varepsilon_2 \mp B_2)\,k^2. \tag{2.23}$$

Solving (2.21) for λ^2 gives four distinct solutions in general, denoted as $\beta\lambda_\alpha(k, E)$ ($\alpha = 1, 2$ and $\beta = \pm$) which are doubly degenerate and where the labels are chosen such that $\operatorname{Re}\lambda_\alpha > 0$. The corresponding eigenvectors are found from (2.20) and can be written as

$$\phi_{\alpha\beta 1} = \begin{pmatrix} -iA_1\beta\lambda_\alpha \\ E - L_1 + D_1\lambda_\alpha^2 \\ A_2 k_+ \\ 0 \end{pmatrix}, \qquad \phi_{\alpha\beta 2} = \begin{pmatrix} 0 \\ A_2 k_- \\ E - L_2 + D_2\lambda_\alpha^2 \\ iA_1\beta\lambda_\alpha \end{pmatrix}, \tag{2.24}$$

where $k_\pm = k_x \pm ik_y$. The general solution is then given by $\Psi(\boldsymbol{r}, z) = \Phi(z)e^{i\boldsymbol{k}\cdot\boldsymbol{r}}$ with

$$\Phi(z) = \sum_{\alpha=1,2} \sum_{\beta=\pm} \sum_{\gamma=1,2} C_{\alpha\beta\gamma}\phi_{\alpha\beta\gamma} e^{\beta\lambda_\alpha z}, \tag{2.25}$$

where the coefficients $C_{\alpha\beta\gamma}(\boldsymbol{k}, E)$ are determined by the boundary conditions and the normalization.

For a semi-infinite system with a surface at $z = 0$ that extends in the negative z direction, the boundary conditions are given by

$$\Phi(z \to -\infty) = 0, \qquad \Phi(z = 0) = 0, \tag{2.26}$$

where the first boundary condition requires $\operatorname{Re}\lambda > 0$ so that the coefficients $C_{\alpha\beta\gamma}$ with $\beta = -1$ are zero and the λ_α have to be both real or complex conjugates. The second boundary condition makes the z component of the probability current density (2.17) vanish at the surface and becomes

$$\begin{pmatrix} \phi_{11} & \phi_{12} & \phi_{21} & \phi_{22} \end{pmatrix} \begin{pmatrix} C_{11} \\ C_{12} \\ C_{21} \\ C_{22} \end{pmatrix} = 0, \tag{2.27}$$

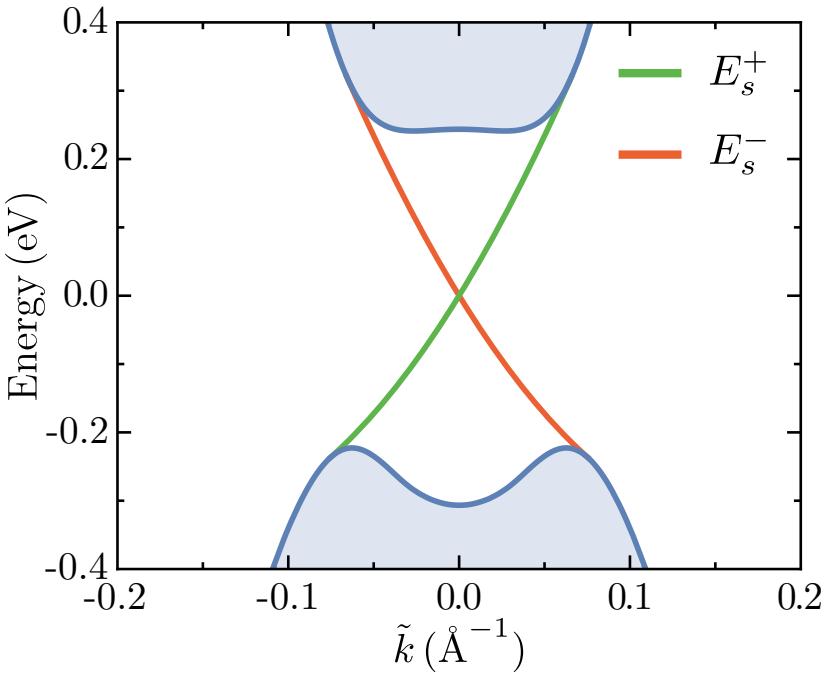

Figure 2.2: Projected bulk bands from (2.10) (blue) together with the dispersion of the surface states $E_s^{\pm}(k)$ (green and red) given in (2.29) for the Bi_2Se_3 parameters from Table 2.1 as a function of $\tilde{k} = \pm k$.

where we dropped the β index. A nonzero solution exists if $|\phi_{11}\ \phi_{12}\ \phi_{21}\ \phi_{22}| = 0$, which can be written as

$$(\lambda_1 + \lambda_2)^2 = \frac{A_1^2}{-D_1 D_2}. \tag{2.28}$$

So we find that a surface state exists if λ_1 and λ_2 are both real or complex conjugates and the above equation is satisfied. This is only possible if $D_1 D_2 < 0$ which is the condition to have a band gap in the k_z direction. Solving for the energy gives the spectrum of the surface states

$$E_s^{\pm}(k) = \pm |A_2| \sqrt{1 - \frac{\varepsilon_1^2}{B_1^2}}\, k + \left(\varepsilon_2 - \frac{B_2}{B_1}\varepsilon_1\right) k^2, \tag{2.29}$$

where we put $\varepsilon_0 = -(\varepsilon_1/B_1)\, M$ so that the Dirac point lies at zero energy. For the Bi_2Se_3 parameters listed in Table 2.1, we obtain $\varepsilon_0 \approx -0.0364$ eV. The dispersion of the surface state of Bi_2Se_3 is shown in Fig. 2.2.

Existence condition

Using the dispersion relation of the surface state, we can find an expression for $\lambda_\alpha^{\pm}(k)$ where $\pm$ corresponds with the energy branch $E_s^{\pm}(k)$. The existence condition of the

surface state is found from the behavior of (2.28) at $k = 0$. We obtain

$$\left(\lambda_1^{\pm} + \lambda_2^{\pm}\right)^2\Big|_{k=0} = -\frac{A_1^2}{D_1 D_2} + 2\left(\left|\frac{M}{B_1}\right| - \frac{M}{B_1}\right), \tag{2.30}$$

which can be found from the explicit expressions for $\lambda_\alpha^{\pm}(0)$ that are obtained from (2.21) with $k = 0$ and $E = 0$.

In order to have a valid surface-state solution, Eq. (2.28) should be satisfied, so that the second term in the above equation needs to vanish. We therefore find that a surface state only exists in the topological phase:

$$D_1 D_2 < 0 \qquad \text{: gap condition,} \tag{2.31}$$

$$\frac{M}{B_1} > 0 \qquad \text{: band inversion condition.} \tag{2.32}$$

Moreover, the surface state exists only in a finite momentum region around $k = 0$. At the edge of this region the surface state merges with the bulk bands as shown in Fig. 2.2.

Helicity

Furthermore, we find that the surface states are helical which means that the spin is locked to the momentum. We show this by calculating the spin expectation values. The wave functions for $k \neq 0$ are given by

$$\Phi_{\pm}(z) = \frac{C_{\pm}}{2}\begin{bmatrix} i\sqrt{\frac{D_2}{B_1}} \\ \operatorname{sign}(A_1 B_1)\sqrt{\frac{-D_1}{B_1}} \\ \pm \operatorname{sign}(A_1 A_2 B_1)\sqrt{\frac{D_2}{B_1}}\, e^{i\varphi_{\boldsymbol{k}}} \\ \pm i \operatorname{sign}(A_2)\sqrt{\frac{-D_1}{B_1}}\, e^{i\varphi_{\boldsymbol{k}}} \end{bmatrix}\left(e^{\lambda_1^{\pm} z} - e^{\lambda_2^{\pm} z}\right), \tag{2.33}$$

where $\varphi_{\boldsymbol{k}} = \arctan(k_y/k_x)$ and $C_{\pm}$ is a normalization constant. Note that the fraction of the density localized on the Bi (Se) atoms is $(1 \pm \varepsilon_1/B_1)/2$, respectively. The spin expectation values (in units $\hbar/2$) become

$$\langle S_x\rangle_{\pm} = \langle\Phi_{\pm}|\,\sigma_x\tau_z\,|\Phi_{\pm}\rangle = \pm\operatorname{sign}(A_1 A_2 B_1)\sin\varphi_{\boldsymbol{k}}, \tag{2.34}$$

$$\langle S_y\rangle_{\pm} = \langle\Phi_{\pm}|\,\sigma_y\tau_z\,|\Phi_{\pm}\rangle = \mp\operatorname{sign}(A_1 A_2 B_1)\cos\varphi_{\boldsymbol{k}}, \tag{2.35}$$

$$\langle S_z\rangle_{\pm} = \langle\Phi_{\pm}|\,\sigma_z\,|\Phi_{\pm}\rangle = 0. \tag{2.36}$$

2.2.1 Effective surface Hamiltonian

In this section, we derive an effective surface Hamiltonian by writing [64]

$$\hat{H} = H(0, -i\partial_z) + V(\boldsymbol{k}), \tag{2.37}$$

where we consider the second term as a perturbation in $\boldsymbol{k}$, given by

$$V(\boldsymbol{k}) = H(\boldsymbol{k}, k_z) - H(0, k_z) = A_2 \boldsymbol{k} \cdot \boldsymbol{\sigma} \tau_x + (\varepsilon_2 - B_2 \tau_z)\, k^2. \tag{2.38}$$

First, we solve the unperturbed problem for a semi-infinite system in the negative z direction. This amounts to solving for a surface state at $k = 0$. In this case the Hamiltonian is diagonal in spin and we only have to solve two smaller problems, one for each spin. Using the same *ansatz* as before, we find

$$[h_\sigma(-i\lambda) - E]\, \phi_\lambda = 0, \tag{2.39}$$

where the two blocks are given by

$$h_\sigma(k_z) = \varepsilon_0 + \varepsilon_1 k_z^2 + \left(M - B_1 k_z^2\right) \tau_z + \sigma A_1 k_z \tau_x, \tag{2.40}$$

where $\sigma = \pm$ for spin up and spin down, respectively. Note that $\tau_z h_\sigma \tau_z = h_{-\sigma}$ and we obtain two degenerate states which form a Kramers pair as required by time-reversal symmetry. Their wave functions can be written as

$$|\Phi_{0\uparrow}\rangle = \begin{pmatrix} \Phi_0 \\ 0 \end{pmatrix}, \qquad |\Phi_{0\downarrow}\rangle = \begin{pmatrix} 0 \\ \tau_z \Phi_0 \end{pmatrix}, \tag{2.41}$$

where

$$\Phi_0(z) = C_1 \phi_1 e^{\lambda_1^0 z} + C_2 \phi_2 e^{\lambda_2^0 z}, \tag{2.42}$$

with

$$\phi_\alpha = \begin{bmatrix} -iA_1 \lambda_\alpha^0 \\ E - L_1 + D_1 (\lambda_\alpha^0)^2 \end{bmatrix}, \tag{2.43}$$

and where $\lambda_\alpha^0 = \lambda_\alpha(k = 0, E)$. The coefficients C_α are again determined by the normalization and the boundary condition. The latter gives

$$\lambda_1^0 \lambda_2^0 = \frac{E - L_1}{D_1}, \tag{2.44}$$

$$\frac{C_2}{C_1} = -\frac{\lambda_1^0}{\lambda_2^0}. \tag{2.45}$$

If we shift the energy with the same factor ε_0 as before, we obtain two degenerate zero-energy solutions given by (2.41) with

$$\Phi_0(z) = C \begin{bmatrix} iA_1 \lambda_1^0 \\ L_1 - D_1 (\lambda_1^0)^2 \end{bmatrix} \left(e^{\lambda_1^0 z} - e^{\lambda_2^0 z}\right), \tag{2.46}$$

where C is a normalization coefficient and we redefine $\lambda_\alpha^0 = \lambda_\alpha(k=0, E=0)$. Furthermore, from (2.28) and (2.44) with $E=0$, we obtain

$$\lambda_{1,2}^0 = \begin{cases} a \pm b & \text{for} \quad \frac{M}{B_1} < \frac{A_1^2}{-4D_1D_2}, \\ a \pm ib & \text{for} \quad \frac{M}{B_1} > \frac{A_1^2}{-4D_1D_2}, \end{cases} \tag{2.47}$$

with

$$a = \frac{|A_1|}{2\sqrt{-D_1D_2}}, \qquad b = \sqrt{\left|\frac{M}{B_1} + \frac{A_1^2}{4D_1D_2}\right|}, \tag{2.48}$$

where the surface state only exists for $D_1D_2 < 0$ and $M/B_1 > 0$ so that a and b are positive real constants with $b < a$. The wave function becomes

$$\Phi_0(z) = C \begin{bmatrix} iA_1\lambda_1^0 \\ L_1 - D_1(\lambda_1^0)^2 \end{bmatrix} e^{az} \begin{cases} \sinh(bz) & \text{for} \quad \frac{M}{B_1} < \frac{A_1^2}{-4D_1D_2}, \\ \sin(bz) & \text{for} \quad \frac{M}{B_1} > \frac{A_1^2}{-4D_1D_2}, \end{cases} \tag{2.49}$$

where additional constants are absorbed in C. We see that there are two regimes for the decay of the wave function depending on the parameters. In both cases, the probability density $|\Phi_0(z)|^2$ first increases from its node at $z=0$ until it reaches a maximum and then decays exponentially into the bulk. However, when the $\lambda_{1,2}^0$ are complex, there are additional oscillations with period $b/(2\pi)$. The density is shown in Fig. 2.3 for both regimes and for Bi_2Se_3. We find that the zero-energy surface state for Bi_2Se_3 is localized near the bottom of the first quintuple layer.

The surface Hamiltonian is found by projecting the bulk Hamiltonian on the degenerate subspace formed by the zero-energy solutions from (2.41). We obtain

$$\mathcal{H}(\boldsymbol{k}) = A_2 \begin{pmatrix} 0 & -ik_- \langle\Phi_0|\,\tau_y\,|\Phi_0\rangle \\ ik_+ \langle\Phi_0|\,\tau_y\,|\Phi_0\rangle & 0 \end{pmatrix} + \left(\varepsilon_2 - B_2 \langle\Phi_0|\,\tau_z\,|\Phi_0\rangle\right) k^2, \tag{2.50}$$

where

$$\langle\Phi_0|\,\tau_y\,|\Phi_0\rangle = \frac{2A_1\left(D_1|\lambda_1^0|^2 - L_1\right)\operatorname{Re}\lambda_1^0}{\left|A_1\lambda_1^0\right|^2 + \left|L_1 - D_1(\lambda_1^0)^2\right|^2} \tag{2.51}$$

$$= \operatorname{sign}(A_1)\frac{2\sqrt{-D_1D_2}}{D_1 - D_2} = -\operatorname{sign}(A_1B_1)\sqrt{1 - \frac{\varepsilon_1^2}{B_1^2}}, \tag{2.52}$$

$$\langle\Phi_0|\,\tau_z\,|\Phi_0\rangle = \frac{\left|A_1\lambda_1^0\right|^2 - \left|L_1 - D_1(\lambda_1^0)^2\right|^2}{\left|A_1\lambda_1^0\right|^2 + \left|L_1 - D_1(\lambda_1^0)^2\right|^2} = \frac{D_2 + D_1}{D_2 - D_1} = \frac{\varepsilon_1}{B_1}. \tag{2.53}$$

We find

$$\mathcal{H}(\boldsymbol{k}) = \hbar v_F\,(\boldsymbol{\sigma} \times \boldsymbol{k}) \cdot \boldsymbol{e}_z + \frac{\hbar^2 k^2}{2m^*}, \tag{2.54}$$

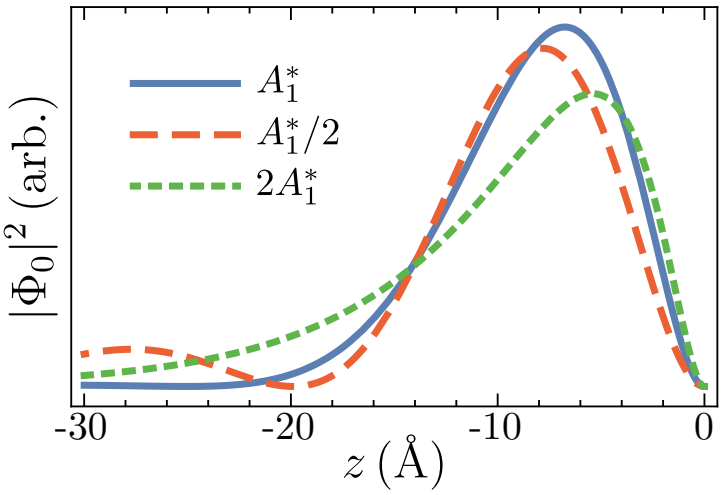

Figure 2.3: Normalized probability density $|\Phi_0(z)|^2$ of the surface state at $k = 0$ for the parameters given in Table 2.1. Here $A_1 = A_1^*$ corresponds to Bi_2Se_3 (blue) and we also show the oscillating regime with $A_1 = A_1^*/2$ (dashed red) and the exponential regime with $A_1 = 2A_1^*$ (dotted green).

in the basis $\{|\Phi_{0\uparrow}\rangle, |\Phi_{0\downarrow}\rangle\}$ which are symmetric and antisymmetric superpositions of $\mathcal{P} = +$ (Bi) and $\mathcal{P} = -$ (Se) states for $m_j = \pm 1/2$, respectively. The Fermi velocity v_F and the effective mass m^* are given by

$$m^* = \frac{\hbar^2}{2\left(\varepsilon_2 - \varepsilon_1 B_2/B_1\right)}, \tag{2.55}$$

$$v_F = \operatorname{sign}(A_1 A_2 B_1)\frac{|A_2|}{\hbar}\sqrt{1 - \frac{\varepsilon_1^2}{B_1^2}}. \tag{2.56}$$

Note that the perturbation theory is exact for the energy so that the contribution of the k_z continuum vanishes. Importantly, we find that the surface states are helical and that their helicity, i.e. the direction of the spin-momentum locking, is given by the relative sign of A_1 and A_2 since the sign of B_1 is already fixed by the gap M in the band inversion condition $M/B_1 > 0$. This agrees with the spin expectation values of the exact solution given in Eqs. (2.34)–(2.36). For the Bi_2Se_3 parameters from Table 2.1, we find $v_F \approx 6.176 \times 10^5\ \mathrm{m\,s^{-1}}$ and $m^* \approx 0.31 m_e$ where m_e is the electron mass. The former agrees well with the experimental value of approximately $5 \times 10^5\ \mathrm{m\,s^{-1}}$ [28].

Surface Hamiltonian from symmetry

The effective surface Hamiltonian can also be derived from symmetry. Remember that the xy surface has threefold rotational symmetry about the z axis and mirror symmetry

about the yz plane. In lowest order, the only combinations with time reversal and threefold rotational symmetry are $\boldsymbol{\sigma} \cdot \boldsymbol{k}$ and $(\boldsymbol{\sigma} \times \boldsymbol{k}) \cdot \boldsymbol{e}_z$. The mirror symmetry rules out the former and we obtain

$$\mathcal{H}_{xy}(k_x, k_y) = \mathcal{A}\left(k_y \sigma_x - k_x \sigma_y\right), \tag{2.57}$$

where $\mathcal{A}$ is a real constant that depends on the material. For completion, we also consider the xz and yz surface. On the xz plane, we only have mirror symmetry about the yz plane which gives

$$\mathcal{H}_{xz}(k_x, k_z) = \mathcal{A}_1 k_z \sigma_x + k_x \left(\mathcal{A}_2 \sigma_y + \mathcal{A}_3 \sigma_z\right), \tag{2.58}$$

where $\mathcal{A}_i$ $(i = 1, 2, 3)$ are real constants. In the model (2.6) we also have mirror symmetry about the xy plane so that $\mathcal{A}_2$ also vanishes in that case. The yz plane only has twofold rotational symmetry about the x axis (by combining space inversion and reflection about the yz plane) which gives

$$\mathcal{H}_{yz}(k_y, k_z) = \left(\mathcal{A}_{11} k_y + \mathcal{A}_{12} k_z\right) \sigma_y + \left(\mathcal{A}_{21} k_y + \mathcal{A}_{22} k_z\right) \sigma_z, \tag{2.59}$$

where $\mathcal{A}_{ij}$ $(i, j = 1, 2)$ are real constants. In the model, which also has mirror symmetry about the xy plane and the xz plane, we further have that $\mathcal{A}_{11} = \mathcal{A}_{22} = 0$.

Topological surface state

We have shown for a simple model (2.6) of a strong time-reversal invariant topological insulator with inversion symmetry that the existence of the pair of zero-energy surface states is insensitive to bulk parameters as long as the bulk gap is finite and the system is in the topological regime $M/B_1 > 0$. Because these states form a Kramers pair, no time-reversal invariant perturbation can hybridize them. For example, adding a constant τ_x term to the Hamiltonian breaks inversion symmetry, but it results only in a constant shift of the Dirac point. At finite momentum the surface states at a given energy and opposite momenta also constitute a Kramers pair so that a propagating mode on the surface cannot backscatter directly even in the presence of disorder as long as time-reversal symmetry is preserved. In the simple case of the (111) surface of Bi_2Se_3 which we have considered above, the topological surface state is given by a single Dirac cone at the Γ point. Furthermore, the topological surface state is helical which means that spin is locked to the momentum. In lowest order, the surface state is described by the effective surface Hamiltonian (2.57).

2.3 Interface states

In this section, we consider states localized at the xy interface ($z = 0$) between two topological insulators, labeled TI1 ($z < 0$) and TI2 ($z > 0$). An illustration of this setup

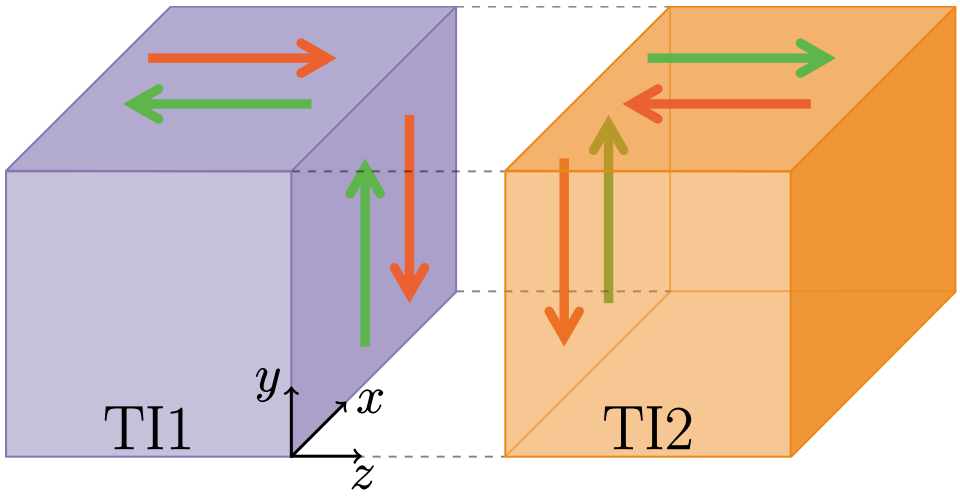

Figure 2.4: Interface between topological insulators TI1 and TI2 whose topological surface states have opposite helicity. The surface states are represented on the xz and xy surface for $k_x = 0$ by arrows where the color represents the spin-momentum locking $\sigma_x = \pm$ (green and red).

is shown in Fig. 2.4. In this case, the first two boundary conditions are given by the normalization condition:

$$\Phi^{(1)}(z \to -\infty) = 0, \qquad \Phi^{(2)}(z \to +\infty) = 0, \tag{2.60}$$

where $\Phi^{(1)}$ and $\Phi^{(2)}$ are the general solutions given in (2.25) that correspond to TI1 and TI2, respectively. It follows that the coefficients $C^{(1)}_{\alpha-\gamma}$ and $C^{(2)}_{\alpha+\gamma}$ vanish. The other two boundary conditions guarantee the continuity of the z component of the probability current density (2.17):

$$\Phi^{(1)}(z=0) = \Phi^{(2)}(z=0), \tag{2.61}$$

$$j_z^{(1)}(\hat{k}_z)\Phi^{(1)}(z)\Big|_{z=0} = j_z^{(2)}(\hat{k}_z)\Phi^{(2)}(z)\Big|_{z=0}, \tag{2.62}$$

with

$$j_z^{(n)}(\hat{k}_z) = 2\big(\varepsilon_1^{(n)} - B_1^{(n)}\tau_z\big)\hat{k}_z + A_1^{(n)}\sigma_z\tau_x, \tag{2.63}$$

where $n = 1, 2$ for TI1 and TI2, respectively. In case the parameters ε_1, B_1, and A_1 of the two TIs are equal, the condition (2.62) reduces to the continuity of the derivative of the wave function. The general solution becomes

$$\Phi^{(1)}(z) = \sum_{\alpha=1,2}\sum_{\gamma=1,2} C^{(1)}_{\alpha\gamma}\phi^{(1)}_{\alpha\gamma}e^{\lambda^{(1)}_\alpha z} \qquad \text{for} \quad z < 0, \tag{2.64}$$

$$\Phi^{(2)}(z) = \sum_{\alpha=1,2}\sum_{\gamma=1,2} C^{(2)}_{\alpha\gamma}\phi^{(2)}_{\alpha\gamma}e^{-\lambda^{(2)}_\alpha z} \qquad \text{for} \quad z > 0, \tag{2.65}$$

where we dropped the β index. Here the $\phi^{(n)}_{\alpha\gamma}$ are given by Eq. (2.24) with $\beta = \pm$ for TI1 and TI2, respectively, and the $\lambda^{(n)}_{\alpha}$ are obtained from (2.21) with the corresponding parameters for both TIs. The boundary conditions (2.61) and (2.62) become

$$\begin{vmatrix} \phi^{(1)}_{11} & \phi^{(1)}_{12} & \phi^{(1)}_{21} & \phi^{(1)}_{22} & -\phi^{(2)}_{11} & -\phi^{(2)}_{12} & -\phi^{(2)}_{21} & -\phi^{(2)}_{22} \\ j^{(1)}_1\phi^{(1)}_{11} & j^{(1)}_1\phi^{(1)}_{12} & j^{(1)}_2\phi^{(1)}_{21} & j^{(1)}_2\phi^{(1)}_{22} & -j^{(2)}_1\phi^{(2)}_{11} & -j^{(2)}_1\phi^{(2)}_{12} & -j^{(2)}_2\phi^{(2)}_{21} & -j^{(2)}_2\phi^{(2)}_{22} \end{vmatrix} = 0, \tag{2.66}$$

where $j^{(n)}_\alpha = j^{(n)}_z[(-1)^n i\lambda^{(n)}_\alpha]$. This equation has no analytical solution and must be solved numerically on a (k, E) grid.

2.3.1 Gapless interface states

In this section, we demonstrate the existence of gapless states at the interface between topological insulators whose surface states have opposite helicity [63, 69–71]. This setup is shown in Fig. 2.4. Unlike the topological surface states that we discussed in the previous section, these states are not robust against disorder. Instead they are protected by mirror symmetry but persist even if time-reversal symmetry is broken.

The existence of the gapless interface states can be understood by considering scattering of the topological surface state on the xz surface at the interface between TI1 and TI2 [69]. Mirror symmetry $\mathcal{M}_x$ enforces that the spin of the surface state on the xz (or xy) surface is locked perpendicular to the momentum for $k_x = 0$. This is also clear from the effective surface Hamiltonian given in (2.58). Now consider a right-moving mode on the xz surface of TI1 that scatters at the interface with TI2. At normal incidence, $k_x = 0$ so that σ_x is conserved due to the mirror symmetry. However, in case the helicity of the surface states of TI1 and TI2 is opposite, neither reflection or transmission conserves σ_x which is illustrated in Fig. 2.5. This paradox is resolved if the incoming state can scatter into the interface, so that there must exist helical gapless states localized at the xy interface for $k_x = 0$. The interface states originate from the coupling of the topological surface states of TI1 and TI2. If the helicity is opposite, the overlapping surface states at $k_x = 0$ have opposite σ_x so that any coupling that preserves σ_x cannot open a gap. In general, the gapless states exist only at an interface that preserves the mirror symmetry. Therefore these state are not robust against disorder unlike the $\mathbb{Z}_2$ topological surface states.

Mirror Chern number

The existence of the interface modes can also be understood from the mirror Chern number which is a weak topological invariant that gives an additional topological crystalline classification of topological insulators with mirror symmetry [4]. Hence, the Bi_2Se_3 class of TIs are both strong TIs and topological crystalline insulators protected by mirror symmetry [72]. We now calculate the mirror Chern number and show that it corresponds to the helicity of the surface states.

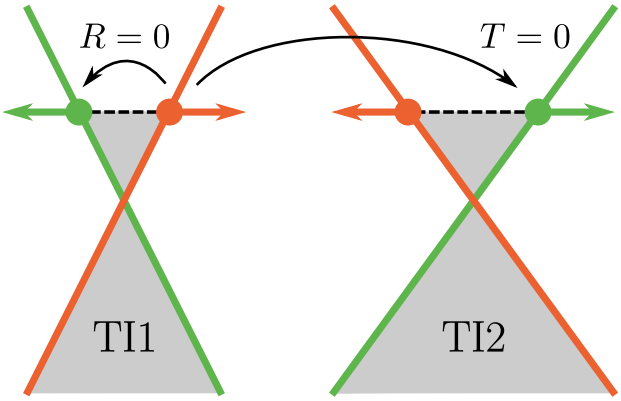

Figure 2.5: Scattering of surface states with opposite helicity on the xz surface at the interface between TI1 and TI2 at normal incidence ($k_x = 0$). In this case the mirror symmetry $\mathcal{M}_x$ about the yz plane ensures that the spin is locked perpendicular to the momentum with $\sigma_x = \pm$ (green and red). Both reflection (R) and transmission (T) are forbidden because σ_x is conserved. The dashed lines indicate the Fermi energy.

For $k_x = 0$, the Hamiltonian (2.6) commutes with the mirror operator $\mathcal{M}_x = -i\sigma_x\tau_z$ and the energy bands are labeled with the mirror eigenvalues $\pm i$. The occupied mirror eigenstates are obtained by first finding an eigenstate $|\psi_1\rangle$ of one of the occupied bands at $k_x = 0$. In this case, $|\psi_2\rangle = \mathcal{M}_x |\psi_1\rangle$ is also an eigenstate because $H(k_x = 0)$ commutes with $\mathcal{M}_x$. The mirror eigenstates are then given by $|\phi_\pm\rangle = |\psi_1\rangle \mp i |\psi_2\rangle$ since $\mathcal{M}_x |\phi_\pm\rangle = |\psi_2\rangle \pm i |\psi_1\rangle = \pm i (|\psi_1\rangle \mp i |\psi_2\rangle)$ where we used $\mathcal{M}_x^2 = -1$. In this way, we find that the normalized mirror eigenstates of the occupied bands are given by

$$|\phi_\pm(k_y, k_z)\rangle = \frac{1}{2\sqrt{d\left(d + M - B_1 k_z^2 - B_2 k_y^2\right)}} \begin{bmatrix} A_1 k_z \mp i A_2 k_y \\ -\left(d + M - B_1 k_z^2 - B_2 k_y^2\right) \\ \mp A_1 k_z + i A_2 k_y \\ \mp\left(d + M - B_1 k_z^2 - B_2 k_y^2\right) \end{bmatrix}, \tag{2.67}$$

where

$$d(k_y, k_z) = \sqrt{\left(M - B_1 k_z^2 - B_2 k_y^2\right)^2 + \left(A_1 k_z\right)^2 + \left(A_2 k_y\right)^2}. \tag{2.68}$$

Since we consider $k_x = 0$, the Hamiltonian is effectively two-dimensional and we can compute the Chern numbers of the mirror bands. The Chern number is defined as the integral over the Berry curvature [16, 52]. To obtain the Berry curvature we first calculate the Berry connection:

$$\boldsymbol{A}_\pm(k_y, k_z) = i \langle \phi_\pm | \nabla_{(k_y, k_z)} | \phi_\pm \rangle, \tag{2.69}$$

which can be written as $\boldsymbol{A}_\pm = \pm\boldsymbol{A}$ with

$$\boldsymbol{A} = \frac{(-A_1A_2)\left(M - B_1k_z^2 - B_2k_y^2 - d\right)}{2d\left[(A_1k_z)^2 + (A_2k_y)^2\right]}\begin{pmatrix} k_z \\ -k_y \end{pmatrix}. \tag{2.70}$$

The corresponding Berry curvature is then given by

$$F_{yz} = \partial_y A_z - \partial_z A_y = \frac{(-A_1A_2)\left(M + B_1k_z^2 + B_2k_y^2\right)}{2d^3}, \tag{2.71}$$

so that the mirror Chern numbers $n_\pm$ of the occupied bands $|\phi_\pm\rangle$ are given by

$$n_\pm = \pm\frac{1}{2\pi}\int_{-\infty}^{\infty}dk_y\int_{-\infty}^{\infty}dk_z\, F_{yz} \tag{2.72}$$

$$= \mp\frac{A_1A_2}{4\pi}\int_{-\infty}^{\infty}dk_y\int_{-\infty}^{\infty}dk_z\,\frac{M + B_1k_z^2 + B_2k_y^2}{d^3} \tag{2.73}$$

$$= \begin{cases} \mp\mathrm{sign}\,(A_1A_2M) & \text{for } M/B_{1,2} > 0 \\ 0 & \text{for } M/B_{1,2} < 0, \end{cases} \tag{2.74}$$

where we verified the integral numerically. In accordance with time-reversal symmetry the total Chern number of the occupied bands vanishes. However, the total mirror Chern number is nonzero in the inverted regime:

$$n_\mathcal{M} = (n_+ - n_-)/2 = -\mathrm{sign}\,(A_1A_2)\,, \tag{2.75}$$

for $M, B_1, B_2 > 0$ [4]. The mirror Chern number $n_\mathcal{M}$ is a weak topological invariant protected by mirror symmetry, which can only change its value when either A_1 or A_2 becomes zero in which case the gap vanishes as expected. For example, the bulk gap vanishes for $A_2 = 0$ along a circle in the Brillouin zone defined by $k_z = 0$ and $|\boldsymbol{k}| = \sqrt{M/B_2}$. However, this gap closing does not change the $\mathbb{Z}_2$ invariant because it does not undo the band inversion.

The gapless interface modes at $k_x = 0$ can be understood from a change $\Delta n_\mathcal{M} = 2$ across the interface shown in Fig. 2.4. The change in the Chern numbers $n_\pm$ gives rise to two left-moving and two right-moving modes in the y direction [16, 52, 69]. This is similar to the surface states of the topological crystalline insulator SnTe, which has $n_\mathcal{M} = -2$ [39]. Indeed, the number of surface Dirac points is given by $|n_\mathcal{M}|$ if the surface preserves the mirror symmetry. Moreover, in the presence of both time-reversal symmetry and mirror symmetry, the $\mathbb{Z}_2$ invariant is given by $n_\mathcal{M}$ mod 2 [4].

In the following, we take the Bi_2Se_3 parameters from Table 2.1 for TI1. Since the helicity of the surface states is determined by the relative sign of A_1 and A_2, we only consider changes in $A_1^{(2)}$ and $A_2^{(2)}$. First, we consider the case where $A_1^{(2)}/A_1^{(1)} > 0$ and $A_2^{(2)}/A_2^{(1)} < 0$ (opposite helicity) for which we find that the surface states are strongly coupled. Then we consider $A_1^{(2)}/A_1^{(1)} < 0$ with either $A_2^{(2)}/A_2^{(1)} > 0$ (opposite helicity) or $A_2^{(2)}/A_2^{(1)} < 0$ (same helicity) corresponding to weak coupling. In all cases, we set the energy shift ε_0 of the two TIs equal with $\varepsilon_0^{(1)} = \varepsilon_0^{(2)} = -(\varepsilon_1/B_1)\,M$.

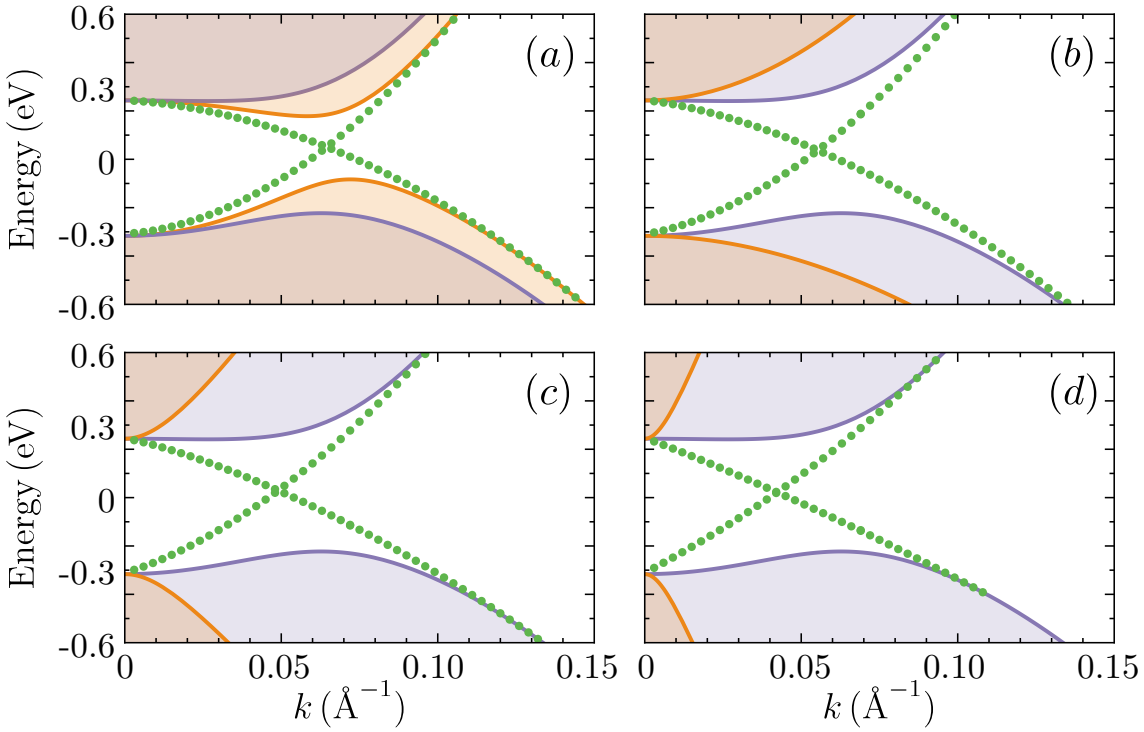

Figure 2.6: Interface spectrum (green) together with the projected bulk bands of TI1 (purple) and TI2 (orange) for $A_1^{(2)} = A_1^{(1)}$ and (*a*) $A_2^{(2)} = -A_2^{(1)}/2$, (*b*) $A_2^{(2)} = -2A_2^{(1)}$, (*c*) $A_2^{(2)} = -4A_2^{(1)}$, and (*d*) $A_2^{(2)} = -8A_2^{(1)}$.

Interface states: strong coupling

In this section, we consider the case where $A_2^{(2)}/A_2^{(1)} < 0$ and $A_1^{(2)} = A_1^{(1)}$. Some results are shown in Fig. 2.6. From the considerations above, we know that we should obtain gapless interface states for $k_x = 0$. However, we find that the gap closes on a circle in momentum space $|\boldsymbol{k}| = k_0$. This is because the model (2.6) has full rotation symmetry in the xy plane. The full rotation symmetry can be reduced to the physical threefold rotation symmetry by including cubic warping terms [64]. With cubic warping terms, which we include below, we only find six cones in the $\boldsymbol{k}$ plane given by $\{(0, \pm k_0), (\pm\sqrt{3}k_0/2, \pm k_0/2)\}$ in accordance with time reversal and threefold rotation symmetry [69]. Furthermore, if time-reversal symmetry is broken but the mirror symmetry is preserved, for example by a magnetic field along the x direction which breaks $\mathcal{C}_3$ symmetry as well, the two cones in the k_x direction survive regardless. Finally, we note that there are always two Kramers pairs consisting of states at opposite momentum at each energy in the gap so that the interface states are not stable against disorder even if time reversal is preserved.

We also show the probability density in Fig. 2.7 (*a*) and (*b*) for the states marked in Fig. 2.6 (*a*) and (*b*), respectively. The character of the individual surface states is lost

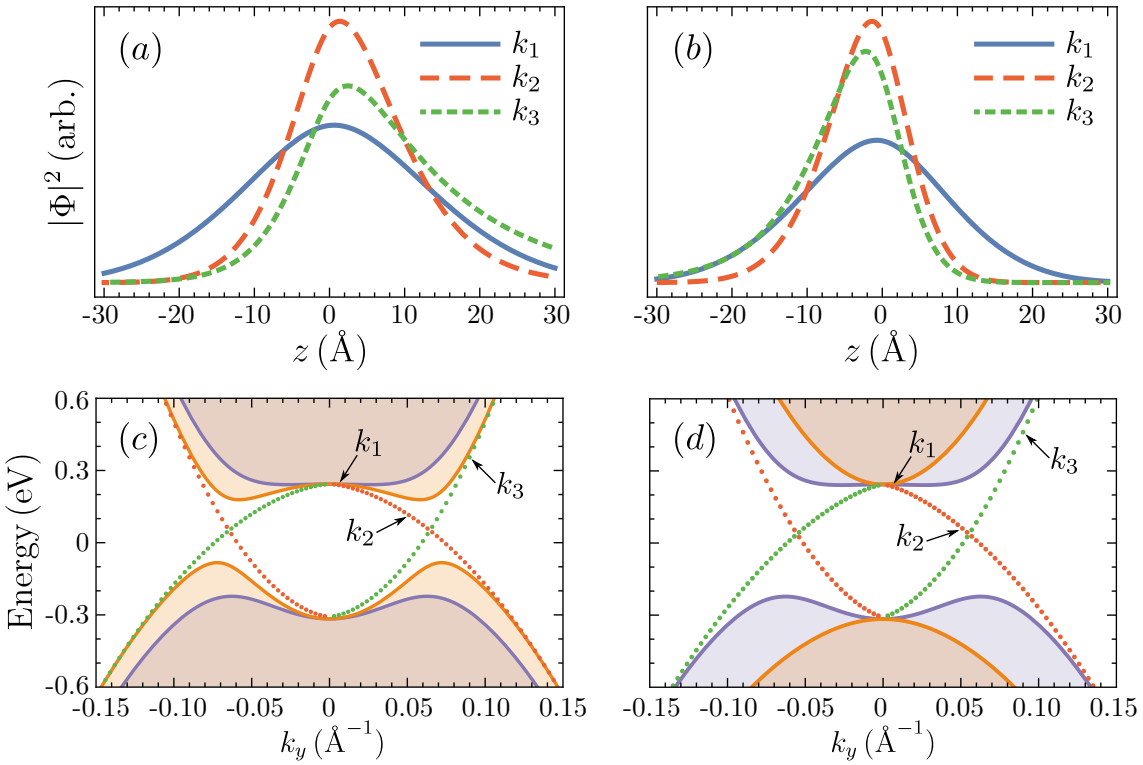

Figure 2.7: (a, b) Probability density of the interface states marked with arrows in (c, d), respectively. (c, d) Mirror eigenvalues $\pm i$ (red and green) of the interface states shown in Fig. 2.6 (a, b), respectively.

and the density of the interface states is spread over the entire junction. Moreover, at the crossing point in the dispersion, the density is localized more at the junction, and it spreads out more as the interface states merge with the bulk bands since the decay length diverges in the bulk. Also note that the density in (a) is localized more in TI2 while the density in (b) is localized more in TI1. This is because the corresponding energy gap is dominated by TI2 and TI1, respectively. The density is smooth at $z = 0$ because here we have $A_1^{(2)} = A_1^{(1)}$ so that the boundary condition (2.62) reduces to the continuity of the derivative of the wave function. Furthermore, the interface states at $k_x = 0$ are eigenstates of S_x, or equivalently, the mirror operator $\mathcal{M}_x$ with mirror eigenvalues $\pm i$ which are shown in Fig. 2.7 (c) and (d) for the interface states from Fig. 2.6 (a) and (b), respectively. Note that Kramers partners have opposite mirror eigenvalues: $\mathcal{M}_x \mathcal{T} |\phi_\pm\rangle = \mathcal{T} \mathcal{M}_x |\phi_\pm\rangle = \mp i \mathcal{T} |\phi_\pm\rangle$ where $\mathcal{T} = i\sigma_y K$ is the time-reversal operator. We see that the two branches of interface states have different mirror eigenvalues so that the crossing is protected by the mirror symmetry.

Finally, we note that changes in the magnitude of $A_1^{(2)}$ have very little impact on the spectrum of the interface states. This is to be expected since we showed in Section 2.2 that A_1 only controls the localization properties of the topological surface state.

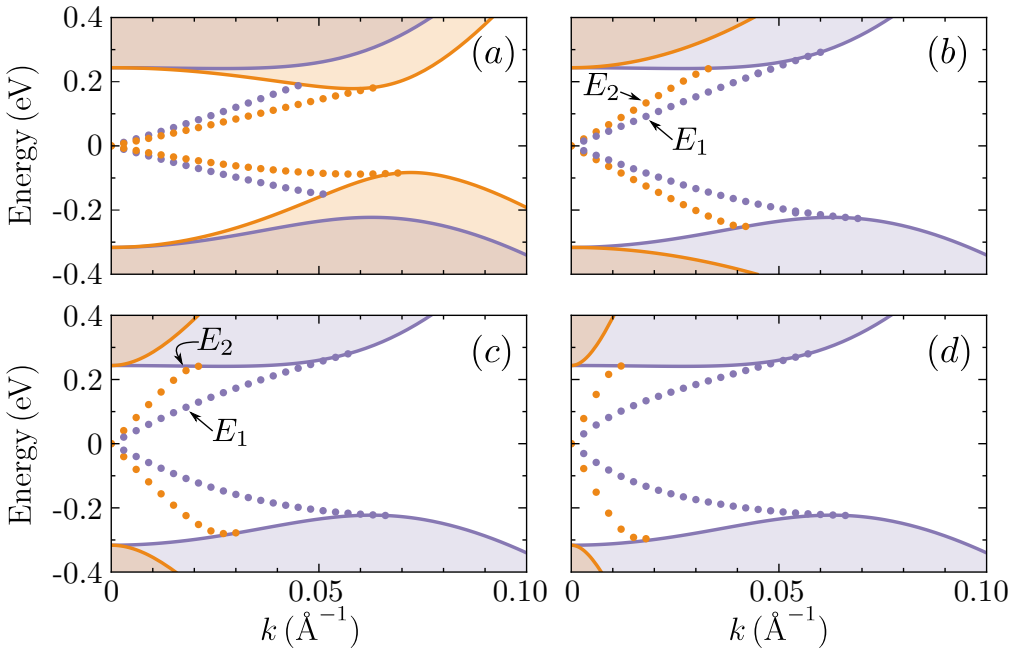

Figure 2.8: Interface spectrum together with the projected bulk bands of TI1 (purple) and TI2 (orange) for $A_1^{(2)} = -A_1^{(1)}$ and (a) $A_2^{(2)} = A_2^{(1)}/2$, (b) $A_2^{(2)} = 2A_2^{(1)}$, (c) $A_2^{(2)} = 4A_2^{(1)}$, and (d) $A_2^{(2)} = 8A_2^{(1)}$.

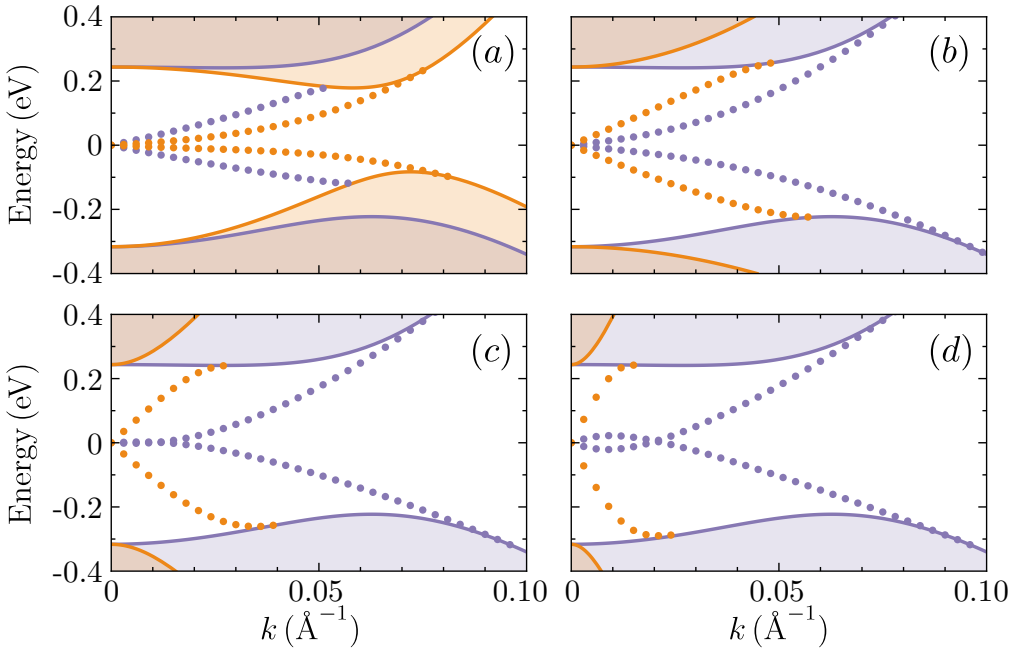

Figure 2.9: Interface spectrum together with the projected bulk bands of TI1 (purple) and TI2 (orange) for $A_1^{(2)} = -A_1^{(1)}$ and (a) $A_2^{(2)} = -A_2^{(1)}/2$, (b) $A_2^{(2)} = -2A_2^{(1)}$, (c) $A_2^{(2)} = -4A_2^{(1)}$, and (d) $A_2^{(2)} = -8A_2^{(1)}$.

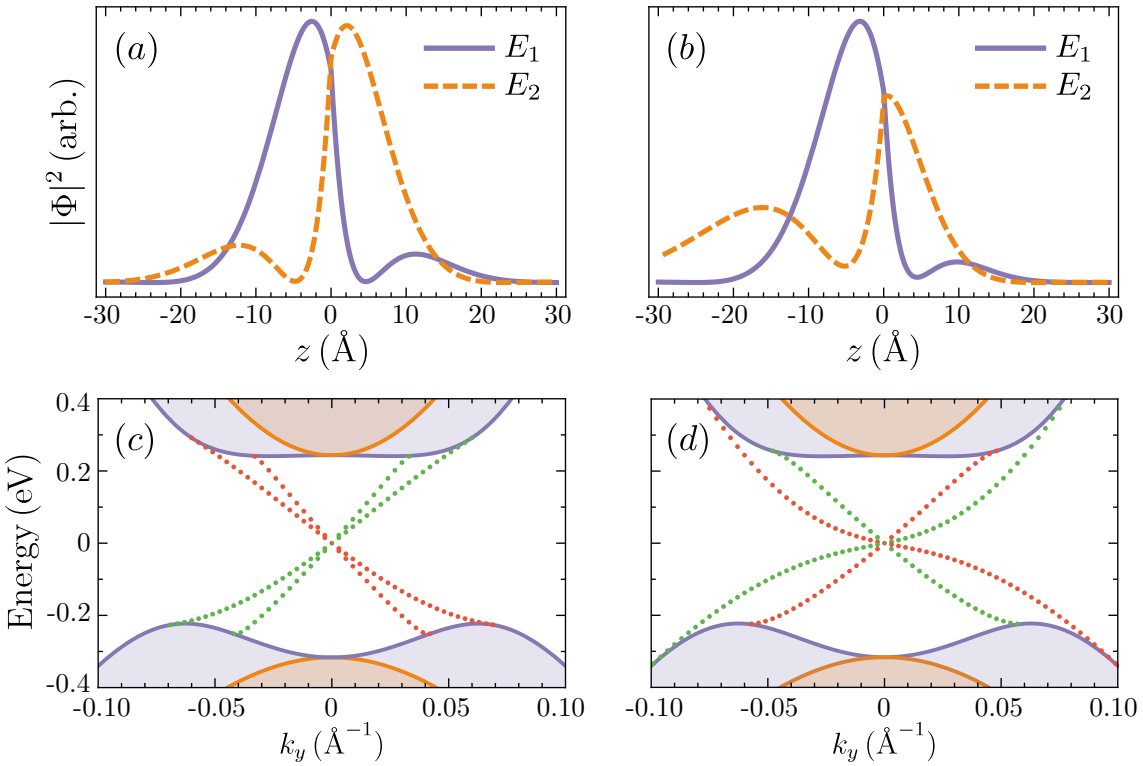

Figure 2.10: (a, b) Probability density of the interface states marked with arrows from Fig. 2.8 (b, c), respectively. (c, d) Mirror eigenvalues $\mathcal{M} = \pm i$ (red and green) of the interface states of Fig. 2.8 (b) and Fig. 2.9 (b), respectively.

Interface states: weak coupling

In this section, we always take $A_1^{(2)} = -A_1^{(1)}$ and we consider two cases: (1) $A_2^{(2)}/A_2^{(1)} > 0$ (opposite helicity) and (2) $A_2^{(2)}/A_2^{(1)} < 0$ (same helicity). Nevertheless, we find gapless interface states in both cases. The results are shown in Fig. 2.8 and Fig. 2.9 for the first and second case, respectively. In both cases, the coupling is weak and there are two Kramers pairs at $k_y = 0$ that are degenerate. This degeneracy is shifted towards finite momentum if M or ε_0 are different for the two TIs, for example. The crossing is protected by mirror symmetry only in the opposite helicity case, as we show below. Next we discuss the density which is shown in Fig. 2.10 (a) and (b) for opposite helicity. The surface states retain most of their original character and the two branches with different Fermi velocity correspond to interface states that are mostly localized in TI1 and TI2, respectively. Note that the density now has a kink at $z = 0$ due to the general boundary condition (2.62).

We now show that the gapless interface states are only robust in the first case where the helicity of the surface states is opposite. To this end, we use the fact that the interface states are eigenstates of $\mathcal{M}_x$ whose eigenvalues are shown in Fig. 2.10 for (c)

opposite helicity and (d) same helicity. We see that in (c) the gap will not open if the modes with the same mirror eigenvalue are coupled, for example by cubic terms in the Hamiltonian that conserve $\mathcal{M}_x$, while in (d) the gap will open. Therefore, we only find gapless interface states that are robust in the presence of the mirror symmetry $\mathcal{M}_x$ in the first case when the helicity of the surface states is opposite.

2.3.2 Warping terms

Here, we discuss the effect of the cubic warping terms on the interface spectrum. These terms are given by [64]

$$H_3 = \frac{R_1}{2}\left(k_+^3 + k_-^3\right)^3 \tau_y + \frac{R_2}{2i}\left(k_+^3 - k_-^3\right)^2 \sigma_z \tau_x, \tag{2.76}$$

which reduce the continuous rotation symmetry to $\mathcal{C}_3$ symmetry. In the following, we add H_3 to the quadratic Hamiltonian (2.6) which we now denote as H_0. The total Hamiltonian then becomes $H = H_0 + H_3$. Similar as before, we use the *ansatz*

$$\psi(\boldsymbol{r}, z) = \phi_\lambda e^{\lambda z} e^{i\boldsymbol{k}\cdot\boldsymbol{r}}, \tag{2.77}$$

from which we now obtain an equation for the roots of the square of a depressed quartic equation in λ which is given by

$$\begin{aligned} &D_1 D_2 \lambda^4 + \left[A_1^2 + D_1\left(E - L_2\right) + D_2\left(E - L_1\right)\right]\lambda^2 \\ &+ iA_1\left(N_1 + N_2\right)\lambda + \left(E - L_1\right)\left(E - L_2\right) \\ &- A_2^2 k^2 - N_1 N_2 = 0, \end{aligned} \tag{2.78}$$

where

$$D_{1,2} = \varepsilon_1 \mp B_1, \tag{2.79}$$

$$L_{1,2}(k) = \varepsilon_0 \pm M + \left(\varepsilon_2 \mp B_2\right)k^2, \tag{2.80}$$

$$N_{1,2}(\boldsymbol{k}) = k^3\left(R_2 \sin 3\theta_{\boldsymbol{k}} \pm iR_1 \cos 3\theta_{\boldsymbol{k}}\right) \tag{2.81}$$

with $\theta_{\boldsymbol{k}} = \arctan\left(k_y/k_y\right)$. Equation (2.78) gives four distinct λ in general, denoted as $\lambda_\alpha(\boldsymbol{k}, E)$ $(\alpha = 1, 2, 3, 4)$ which are doubly degenerate. Moreover, if λ_α is a solution of (2.78) then $-\lambda_\alpha^*$ is also a solution. Hence, if there are no imaginary solutions (in which case there would be no normalizable solutions), we can label the λ_α such that $\mathrm{Re}\,\lambda_{1,2} > 0$ and $\mathrm{Re}\,\lambda_{3,4} < 0$. The explicit expressions for the λ_α are omitted as they are not very informative. The corresponding eigenvectors can be written as

$$\phi_{\alpha 1} = \begin{bmatrix} -iA_1\lambda_\alpha + N_2 \\ E - L_1 + D_1\lambda_\alpha^2 \\ A_2 k_+ \\ 0 \end{bmatrix}, \qquad \phi_{\alpha 2} = \begin{bmatrix} 0 \\ A_2 k_- \\ E - L_2 + D_2\lambda_\alpha^2 \\ +iA_1\lambda_\alpha - N_2 \end{bmatrix}. \tag{2.82}$$

The interface states are then found in the same way as before, since the boundary conditions remain unchanged as H_3 does not change the probability current density in the z direction. In this case, we have to numerically solve the boundary conditions on a $(\boldsymbol{k}, E)$ grid. However, taking $\mathcal{T}$, $\mathcal{C}_3$, and $\mathcal{M}_x$ into account we can limit the $(\boldsymbol{k}, E)$ grid to one BZ slice, for example by taking $\theta_{\boldsymbol{k}} \in [\pi/2, 2\pi/3]$. The spectrum in the strong-coupling regime $A_2^{(2)}/A_2^{(1)} < 0$ is shown in Fig. 2.11.

Rotational mismatch

We have also investigated the effect of rotational mismatch between the two TIs. This breaks the mirror symmetry and thus opens a gap in the interface spectrum. The action of a rotation under an arbitrary angle φ on the Hamiltonian is given by

$$H' = e^{-i\frac{\varphi}{2}\sigma_z} H(\boldsymbol{k}', k_z) e^{i\frac{\varphi}{2}\sigma_z} = H_0 + H_3', \tag{2.83}$$

where $\boldsymbol{k}' = R(-\varphi)\boldsymbol{k}$. The rotation has no effect on H_0 since it preservers the full rotation symmetry. On the other hand, we have $H_3' = H_3(k, \theta_{\boldsymbol{k}} - \varphi)$ which can also be written as

$$H_3' = H_3(\boldsymbol{k}) \cos 3\varphi + V(\boldsymbol{k}) \sin 3\varphi, \tag{2.84}$$

where

$$V = \frac{R_1}{2i}\left(k_+^3 - k_-^3\right)\tau_y - \frac{R_2}{2}\left(k_+^3 + k_-^3\right)\sigma_z\tau_x. \tag{2.85}$$

which anticommutes with the mirror operator $\mathcal{M}_x = -i\sigma_x\tau_z$. The Hamiltonians of the two TIs with the rotational mismatch can then be written as

$$H^{(1)} = H_0^{(1)} + H_3^{(1)}(k, \theta_{\boldsymbol{k}}), \tag{2.86}$$

$$H^{(2)} = H_0^{(2)} + H_3^{(2)}(k, \theta_{\boldsymbol{k}} - \varphi). \tag{2.87}$$

Hence, the interface spectrum in the presence of rotational mismatch over an angle φ can be calculated in the same way as before with the substitution $\theta_{\boldsymbol{k}} \to \theta_{\boldsymbol{k}} - \varphi$ in all expressions that are related to TI2. In this way, we numerically obtain the energy gap induced by rotational mismatch at the interface, which is shown in Fig. 2.12 as a function of the rotational mismatch angle φ. As expected, we find that the energy gap has period $\pi/3$ and that it attains a maximum of approximately 107 meV at $\varphi = \pi/6$ when the rotational mismatch is maximal. It is clear that the magnitude of the energy gap depends on the parameters R_1 and R_2 and on the location of the crossing point $k_0 \approx 0.08$ Å^{-1} since the cubic terms are of the order of k_0^3 at the gap opening point.

Experimental signatures

An experimental realization requires topological insulators with opposite helicity, or equivalently, opposite mirror Chern number $n_{\mathcal{M}}$. Note that $n_{\mathcal{M}}$ cannot be determined

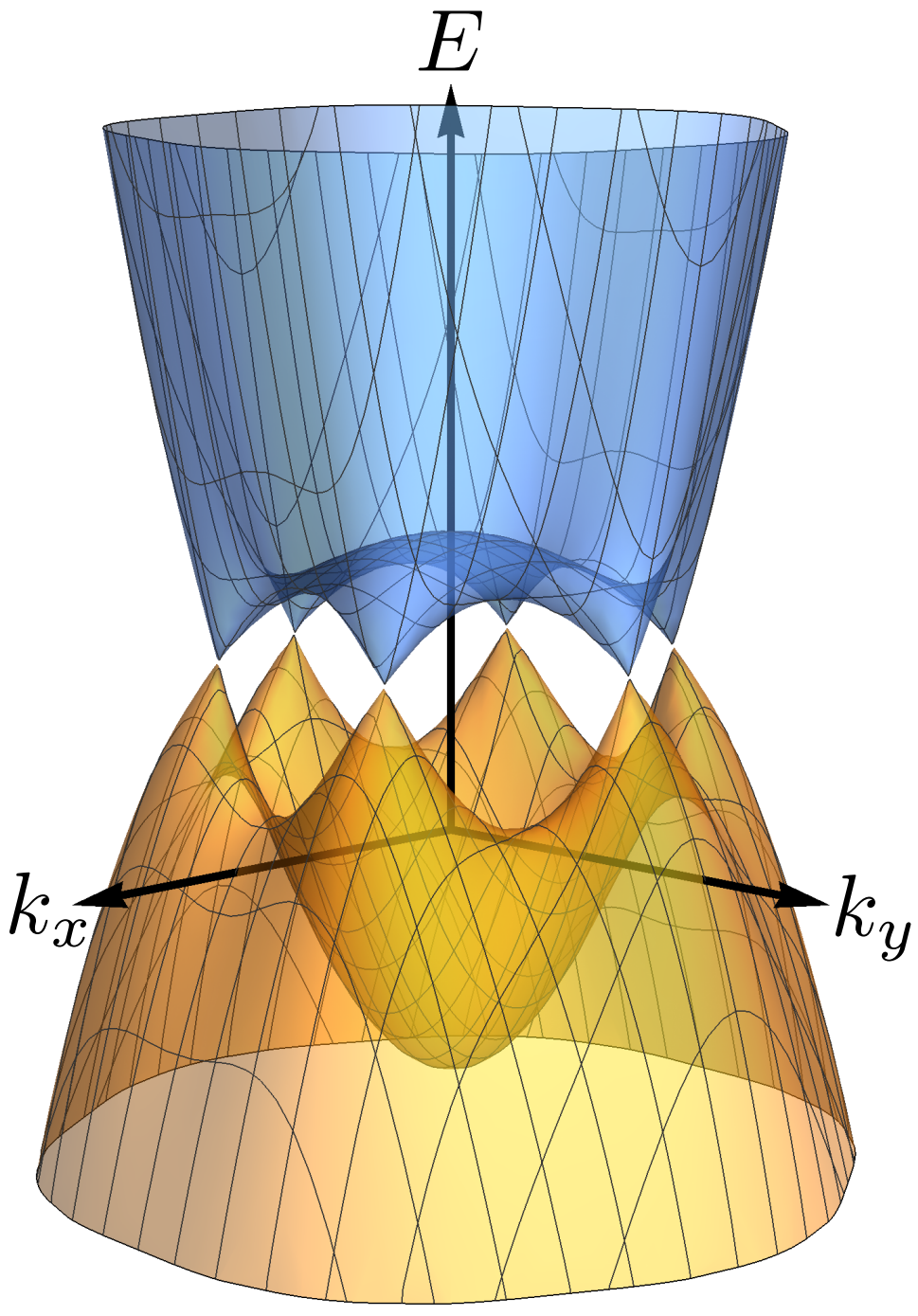

Figure 2.11: Spectrum of interface states for $A_2^{(2)} = -A_2^{(1)}$ in the 2D interface BZ where the parameters of TI1 correspond to Bi_2Se_3 and are taken from Ref. [73].

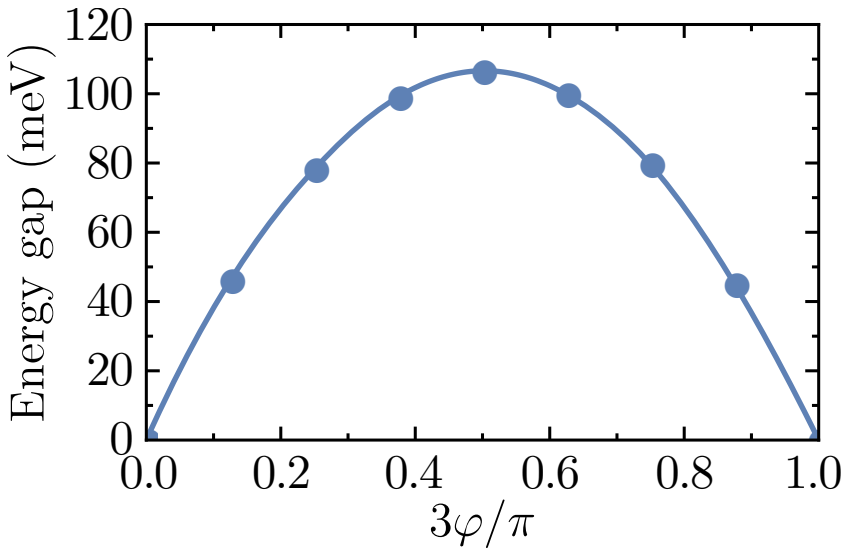

Figure 2.12: Energy gap of the interface spectrum as a function of the rotational mismatch angle φ for $A_2^{(2)} = -A_2^{(1)}$ where the parameters of TI1 correspond to Bi_2Se_3 and are taken from Ref. [73]. The interface spectrum for $\varphi = 0$ is shown in Fig. 2.11.

by fitting the energy bands [4]. Indeed, the bulk spectrum (2.10) is independent of the signs of A_1 and A_2. However, it is shown in Ref. [64] that sign(A_2) is determined by the spin-orbit coupling (SOC) constant, while sign(A_1) is not. For isolated atoms, the SOC constant is always positive because the potential is always attractive. However, in cubic binary materials, such as HgTe and HgS, the spin-orbit splitting can be effectively negative due to contributions from d orbitals [74]. In strained HgTe, this contribution is too small so that $n_{\mathcal{M}} = -1$ [75, 76]. In HgS, however, the p-d hybridization leads to an effective negative SOC constant for p orbitals and therefore $n_{\mathcal{M}} = 1$ [76, 77]. More generally, strained $HgTe_xS_{1-x}$ has been shown to exhibit (crystalline) topological phase transitions between strong TIs with $n_{\mathcal{M}} = \pm 1$ as a function of x and the strain with the limiting cases of strained HgTe ($n_{\mathcal{M}} = -1$) and unstrained HgS ($n_{\mathcal{M}} = 1$) [76]. Heterostructures of $HgTe_xS_{1-x}$ where the strain and x are tuned accordingly could therefore be a possible experimental realizations. Even though the mirror symmetry might be broken by disorder at the interface, e.g. due to lattice mismatch, the induced gap might be small. For example, in case of Bi_2Se_3-like TIs with rotational mismatch, we have shown that a small gap opens due to the terms of third order in the momentum.

In the Bi_2Se_3 family of TIs, orbitals normal to the surface favor clockwise ($n_{\mathcal{M}} = -1$) helicity while in-plane orbitals favor anticlockwise helicity ($n_{\mathcal{M}} = -1$) [78, 79]. Since the inverted bands at the Γ point are mostly p_z, the spin texture of the surface states depends strongly on the orientation of the surface [65, 80]. It should therefore in principle be possible to engineer the helicity of the topological surface state in Bi_2Se_3-like TIs.

A possible way to find signatures of these interface states is by applying a magnetic field along the x direction (mirror axis), which does not break the mirror symmetry $\mathcal{M}_x$ but does break the $\mathcal{C}_3$ symmetry in case of Bi_2Se_3-like TIs. This destroys four of the six cones and one could measure the conductance through the interface which should drop by a factor 3 when the magnetic field is applied. Moreover, if the sample is rotated around the z direction, the conductance oscillates with a period of $\pi/3$. This also gaps the Dirac cone on the transverse surface, which should enhance the signature.

2.3.3 Spurious tachyonlike interface states

In this section, we discuss the appearance of *spurious* tachyonlike interface states. In case the λ obtained from (2.21) have an additional degeneracy, i.e. when $\lambda_1 = \lambda_2$, the eigenvectors (2.24) are linearly dependent and we need a different trial solution. Even though this is a pathological case, it can lead to spurious solutions that resemble tachyonlike excitations with a diverging group velocity which initially caused some confusion in the community [63, 70]. The extra degeneracy of the λ occurs when the discriminant of the biquadratic equation (2.21) vanishes. This happens at specific points in the (k, E) plane determined by the "tachyonic dispersion"

$$E_t^{\pm}(k) = \varepsilon_0 + \frac{2MB_1 - A_1^2}{2B_1^2}\varepsilon_1 + \left(\varepsilon_2 - \frac{B_2}{B_1}\varepsilon_1\right)k^2 \pm \sqrt{\left(1 - \frac{\varepsilon_1^2}{B_1^2}\right)F(k)}, \tag{2.88}$$

where we introduced the function $F(k)$ given by

$$F(k) = \frac{A_1^2}{4B_1^2}\left(4MB_1 - A_1^2\right) + \left(A_2^2 - \frac{B_2}{B_1}A_1^2\right)k^2. \tag{2.89}$$

The "tachyonic momentum" k_t is defined as the momentum where the group velocity of the tachyonic dispersion diverges [63]. This happens when $F(k_t) = 0$ and the square root in (2.88) vanishes. We obtain

$$k_t = \frac{1}{2|B_1|}\sqrt{\frac{A_1^2 - 4MB_1}{(A_2/A_1)^2 - B_2/B_1}}. \tag{2.90}$$

Note that the group velocity can only diverge when k_t is real. In general, we find that the degeneracy occurs at energies $E_t^{\pm}(k)$ under the conditions

$$k^2 > k_t^2 \qquad \text{for} \quad \frac{A_2^2}{A_1^2} > \frac{B_2}{B_1}, \tag{2.91}$$

$$k^2 < k_t^2 \qquad \text{for} \quad \frac{A_2^2}{A_1^2} < \frac{B_2}{B_1}. \tag{2.92}$$

We find that condition (2.92) is satisfied for the Bi_2Se_3 parameters given in Table 2.1 with $k_t \approx 0.0853$ Å^{-1} and $E_t^{\pm}(k_t) \approx 0.0575$ eV. Therefore, the extra λ degeneracy occurs

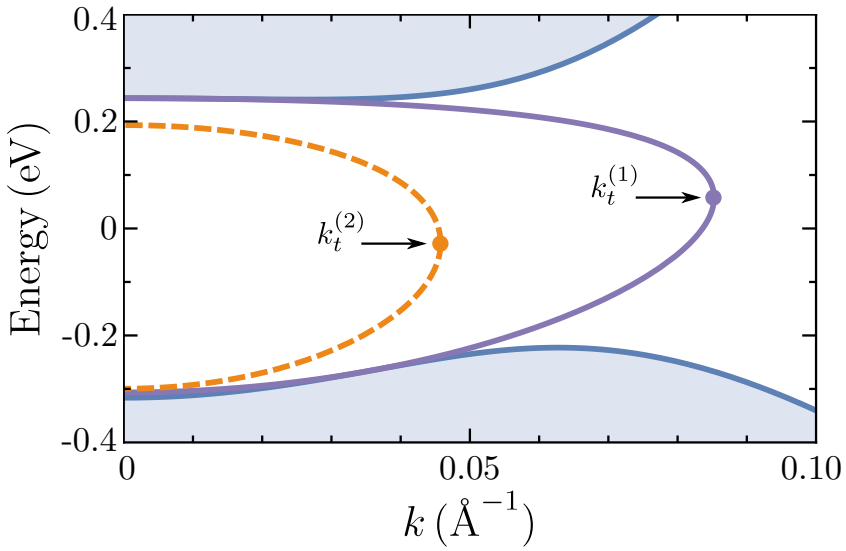

Figure 2.13: The functions $E_t^{\pm}(k)$ given in (2.88) for TI1 (purple) and TI2 (dashed orange) with $A_1^{(2)} = \pm 1.3 A_1^{(1)}$ and $A_2^{(2)} = \pm A_2^{(1)}$ together with the bulk bands (blue) where the tachyonic point is marked with a dot. The tachyonic momenta are given by $k_t^{(1)} \approx 0.0853$ Å^{-1} and $k_t^{(2)} \approx 0.0458$ Å^{-1}.

inside the energy gap for those parameters giving rise to spurious interface states whose tachyonlike spectrum is shown in Fig. 2.13.

Next, we demonstrate how to resolve this case by finding the correct general solution when the λ are four times degenerate. However, in the actual calculation, we simply superimpose the tachyonic dispersion on our results to identify the spurious solutions.

General solution

For the Hamiltonian (2.6), the Schrödinger equation $H(-i\partial_z, \boldsymbol{k})\phi = E\phi$ is a system of four homogeneous second-order differential equations with constant coefficients. In general such a system can be written as

$$P\phi + Q\phi' - \phi'' = 0, \tag{2.93}$$

with P and Q constant $n \times n$ matrices. The trial solution $\phi(z) = e^{\lambda z}\eta_\lambda$ gives

$$\left(P + \lambda Q - \lambda^2 I\right)\eta_\lambda = 0, \tag{2.94}$$

where I is the $n \times n$ unit matrix. This equation has a nonzero solution for η_λ if and only if $|P + \lambda Q - \lambda^2 I| = 0$, so that the λ are given by the roots of a polynomial of order $2n$. Now consider the case where there is a repeated root. If there are two linearly independent η_λ for the repeated root, the trial solution remains valid. Otherwise, we try

the *ansatz* $\phi(z) = ze^{\lambda z}\eta_\lambda + e^{\lambda z}\rho_\lambda$ and we obtain

$$z\left[P + \lambda Q - \lambda^2 I\right]\eta_\lambda + \left[\left(P + \lambda Q - \lambda^2 I\right)\rho_\lambda + \left(Q - 2\lambda I\right)\eta_\lambda\right] = 0. \tag{2.95}$$

Putting terms of equal power in z to zero, we again find Eq. (2.94) together with

$$\left(P + \lambda Q - \lambda^2 I\right)\rho_\lambda + \left(Q - 2\lambda I\right)\eta_\lambda = 0. \tag{2.96}$$

Observe that this equation is obtained from (2.94) by taking the partial derivative with respect to λ. We identify $\rho_\lambda = \partial_\lambda \eta_\lambda$ and the solution becomes $\phi(z) = e^{\lambda z}\left(z + \partial_\lambda\right)\eta_\lambda$ where η_λ is found from (2.94).

We now apply this solution to our problem. We find that the correct general solution along the "tachyonic dispersion" (2.88) is given by

$$\Phi(z) = \sum_{\beta=\pm}\sum_{\gamma=1,2} e^{\beta\lambda z}\left[C_{1\beta\gamma} + C_{2\beta\gamma}\left(z + \beta\partial_\lambda\right)\right]\phi_{\beta\gamma}. \tag{2.97}$$

2.4 Summary

In this chapter, we first discussed the minimal continuum model for a three-dimensional time-reversal-invariant strong topological insulator (TI) with inversion symmetry where we used the well-studied case of Bi_2Se_3 as an example. We showed that the topological regime is characterized by band inversion and protected by time-reversal symmetry by invoking the *bulk-boundary correspondence* which relates the parity of the number of Kramers pairs of surface states to the $\mathbb{Z}_2$ invariant. Next, we considered a semi-infinite system with open boundary conditions and demonstrated the existence and robustness of the topological surface state. For the Bi_2Se_3 family of TIs, the surface state consists of a single Dirac cone located at the $\bar{\Gamma}$ point of the surface Brillouin zone. We then derived the effective surface Hamiltonian, both from perturbation theory and from symmetry principles. This effective surface Hamiltonian is used in the upcoming chapters to model the topological-insulator surface. In the last section, we considered junctions between two TIs and explicitly calculated the dispersion and wave functions of gapless interface states that are protected by mirror symmetry. We demonstrated that their existence can be understood from the properties of the surface as the resolution of a scattering paradox, or alternatively, from the bulk properties as a change across the junction of the *mirror Chern number*, which is given by $n_{\mathcal{M}} = -\mathrm{sign}(A_1 A_2)$ where A_1 and A_2 are the spin-orbit parameters in the z direction and the xy plane, respectively. The mirror Chern number is a weak topological invariant that gives an additional classification of topological insulators with mirror symmetry. We then calculated the gapless interface states for three cases: in the first case A_2 changes sign across the junction, in the second case A_1 changes sign, and both change sign in the third case. We showed that the interface states are robust only for the first two cases where the helicity of the topological surface state is opposite for the two TIs and demonstrated their existence when the Hamiltonian commutes with the mirror operator for $k_x = 0$. Next, we included cubic terms to the Hamiltonian which reduce the full rotation symmetry of the interface to the physical threefold rotation symmetry and showed that the interface states survive as long as mirror symmetry is present. Moreover, we considered rotational mismatch at the junction and calculated the resulting energy gap in the interface spectrum as a function of the mismatch. Furthermore, we proposed a possible experimental realization in strained $HgTe_xS_{1-x}$ systems and a specific experiment to find signatures of the interface states. Finally, we discussed the appearance of spurious tachyonlike interface states in the continuum model and how they can be resolved.

3

Helical quantum dots

We investigate the properties of a quantum dot on the surface of a 3D strong topological insulator. The surface state is confined with a patterned magnetic insulator that breaks time-reversal symmetry which leads to backscattering of the surface state. First, we obtain the general solution for a circular-symmetric system from which we obtain the hard-wall boundary conditions. We then discuss the single-particle properties of the quantum dot for different boundary conditions. Next, we include Coulomb interactions with the configuration-interaction method and show that the few-particle system evolves to a spin-polarized Wigner molecule when the interaction strength is increased.

3.1 Model

In Section 2.2.1, we derived the effective Hamiltonian (2.54) for the (111) surface of a Bi_2Se_3-like strong topological insulator. In lowest order, the surface Hamiltonian in second-quantized form, in the presence of external potentials, becomes

$$\hat{H}_0 = \int d^2r\, \hat{\psi}^\dagger(\boldsymbol{r}) \left[-iv_F\, (\boldsymbol{\sigma} \times \boldsymbol{e}_z) \cdot \nabla + V(\boldsymbol{r}) + m(\boldsymbol{r})\sigma_z\right] \hat{\psi}(\boldsymbol{r}), \tag{3.1}$$

where $V(\boldsymbol{r})$ is the electrostatic potential and $\boldsymbol{m}(\boldsymbol{r})$ is the exchange field. Note that we do not consider the coupling of the magnetic field to the momentum via the vector potential. Moreover, we put $\hbar = 1$ in the remainder of this chapter unless otherwise stated. The spinor field operator given by

$$\hat{\psi}(\boldsymbol{r}) = \begin{bmatrix} \hat{\psi}_\uparrow(\boldsymbol{r}) \\ \hat{\psi}_\downarrow(\boldsymbol{r}) \end{bmatrix}, \tag{3.2}$$

where $\hat{\psi}^\dagger_\sigma(\boldsymbol{r})$ ($\hat{\psi}_\sigma(\boldsymbol{r})$) is the electron field operator which creates (destroys) an electron with spin σ at position $\boldsymbol{r}$ and satisfies the anticommutation relations

$$\{\hat{\psi}^\dagger_\sigma(\boldsymbol{r}), \hat{\psi}_{\sigma'}(\boldsymbol{r}')\} = \delta_{\sigma\sigma'}\delta(\boldsymbol{r} - \boldsymbol{r}'), \tag{3.3}$$

$$\{\hat{\psi}_\sigma(\boldsymbol{r}), \hat{\psi}_{\sigma'}(\boldsymbol{r}')\} = \{\hat{\psi}^\dagger_\sigma(\boldsymbol{r}), \hat{\psi}^\dagger_{\sigma'}(\boldsymbol{r}')\} = 0. \tag{3.4}$$

The Hamiltonian is diagonalized with the basis transformation

$$\hat{\psi}(\boldsymbol{r}) = \sum_a \psi_a(\boldsymbol{r})\, \hat{c}_a, \tag{3.5}$$

where $\hat{c}_a^\dagger$ ($\hat{c}_a$) are the creation (destruction) operators that create (destroy) an electron in the state a, which satisfy $\{\hat{c}_a^\dagger, \hat{c}_b\} = \delta_{ab}$ and $\{\hat{c}_a, \hat{c}_b\} = \{\hat{c}_a^\dagger, \hat{c}_b^\dagger\} = 0$. These relations follow from the inverse transformation

$$\hat{c}_a = \int d^2r\, \psi_a^\dagger(\boldsymbol{r})\hat{\psi}(\boldsymbol{r}), \tag{3.6}$$

and the anticommutators of (3.3) and (3.4), respectively. The spinors $\psi_a(\boldsymbol{r})$ and corresponding energies E_a are obtained from the wave equation $\hat{\mathcal{H}}_0\psi_a = E_a\psi_a$ with

$$\hat{\mathcal{H}}_0 = -iv_F\,(\boldsymbol{\sigma} \times \boldsymbol{e}_z)\cdot\nabla + V(\boldsymbol{r}) + \boldsymbol{m}(\boldsymbol{r})\cdot\boldsymbol{\sigma}. \tag{3.7}$$

Symmetries

Depending on the potentials, the Dirac Hamiltonian $\hat{\mathcal{H}}_0$ can possess three discrete non-spatial symmetries: time reversal $\mathcal{T} = i\sigma_y\mathcal{K}$, charge conjugation $\mathcal{C} = \sigma_x\mathcal{K}$, and the combination of $\mathcal{T}$ and $\mathcal{C}$ which is the chiral symmetry $\mathcal{S} = \mathcal{T}\mathcal{C} = \sigma_z$. Time-reversal symmetry is expressed as

$$\sigma_y\, \hat{\mathcal{H}}_0^*\sigma_y = \hat{\mathcal{H}}_0, \tag{3.8}$$

which is only satisfied if $\boldsymbol{m}(\boldsymbol{r})$ vanishes. In this case, the energy is doubly degenerate where the degenerate states form a Kramers pair. In a periodic system, the Kramers pairs consists of states at opposite momentum. Charge conjugation

$$\sigma_x\, \hat{\mathcal{H}}_0^*\sigma_x = -\hat{\mathcal{H}}_0, \tag{3.9}$$

requires $V(\boldsymbol{r}) = 0$ and $\boldsymbol{m}(\boldsymbol{r}) = m(\boldsymbol{r})\,\boldsymbol{e}_z$. It follows that the energy is symmetric around zero where charge conjugation connects states at opposite momentum and energy. Chiral symmetry σ_z is the combination of time reversal and charge conjugation and connects states at the same momentum but opposite energy.

3.1.1 Wave equation

Here, we first find the general solution of the wave equation $\hat{\mathcal{H}}_0\psi = E\psi$ when the system has circular symmetry. Finally, we give the solution to the wave equation for a free particle in polar coordinates.

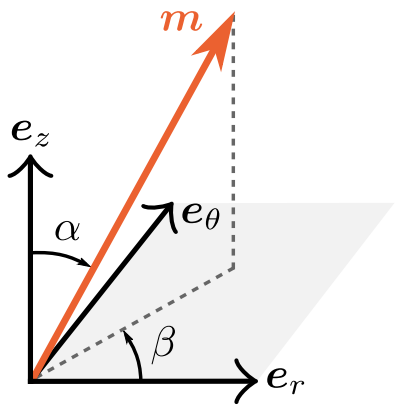

Figure 3.1: The angles α and β that define the direction of the circular-symmetric exchange field $\boldsymbol{m}$.

General solution

In polar coordinates (r, θ) the wave equation (3.7) transforms into

$$\left[-iv_F\left(\sigma_\theta\partial_r - \frac{1}{r}\sigma_r\partial_\theta\right) + V(\boldsymbol{r}) + \boldsymbol{m}(\boldsymbol{r})\cdot\boldsymbol{\sigma}\right]\psi(\boldsymbol{r}) = E\psi(\boldsymbol{r}), \tag{3.10}$$

where we used $\nabla = \boldsymbol{e}_r\partial_r + \boldsymbol{e}_\theta r^{-1}\partial_\theta$ and $\boldsymbol{\sigma} = \sigma_r\boldsymbol{e}_r + \sigma_\theta\boldsymbol{e}_\theta + \sigma_z\boldsymbol{e}_z$ with

$$\sigma_r = \boldsymbol{\sigma}\cdot\boldsymbol{e}_r = \begin{pmatrix} 0 & e^{-i\theta} \\ e^{i\theta} & 0 \end{pmatrix}, \qquad \sigma_\theta = \boldsymbol{\sigma}\cdot\boldsymbol{e}_\theta = \begin{pmatrix} 0 & -ie^{-i\theta} \\ ie^{i\theta} & 0 \end{pmatrix}. \tag{3.11}$$

If the system has circular symmetry, the general form of the potentials are

$$V(\boldsymbol{r}) = V(r), \tag{3.12}$$

$$\boldsymbol{m}(\boldsymbol{r}) = m(r)\left(\sin\alpha\cos\beta\,\boldsymbol{e}_r + \sin\alpha\sin\beta\,\boldsymbol{e}_\theta + \cos\alpha\,\boldsymbol{e}_z\right), \tag{3.13}$$

where α and β specify the direction of $\boldsymbol{m}$ which is shown in Fig. 3.1. The angular part of the wave equation (3.10) is solved with the *ansatz*

$$\psi(r,\theta) = e^{i\left(j-\frac{\sigma_z}{2}\right)\theta}\phi(r), \tag{3.14}$$

which is an eigenstate of the angular momentum along the z direction $\hat{j}_z = -i\partial_\theta + \sigma_z/2$ with eigenvalues $j = \pm 1/2, \pm 3/2, \ldots$. If we plug in the *ansatz* and multiply both sides of (3.10) with $\exp\left[-i\left(j-\sigma_z/2\right)\theta\right]$, the kinetic term becomes

$$e^{-i\left(j-\frac{\sigma_z}{2}\right)\theta}\left(\sigma_\theta\partial_r - \frac{1}{r}\sigma_r\partial_\theta\right)e^{i\left(j-\frac{\sigma_z}{2}\right)\theta} = e^{i\sigma_z\theta}\left[\sigma_\theta\partial_r - \frac{1}{r}i\sigma_r\left(j-\frac{\sigma_z}{2}\right)\right] \tag{3.15}$$

$$= \sigma_y\partial_r - \frac{1}{r}i\sigma_x\left(j-\frac{\sigma_z}{2}\right), \tag{3.16}$$

and the remaining terms give

$$e^{-i\left(j-\frac{\sigma_z}{2}\right)\theta}\left[E-V(r)-\boldsymbol{m}(\boldsymbol{r})\cdot\boldsymbol{\sigma}\right]e^{i\left(j-\frac{\sigma_z}{2}\right)\theta}=E-V(r)-m(r)\sigma_m, \tag{3.17}$$

with $\sigma_m=\sin\alpha\left(\cos\beta\,\sigma_x+\sin\beta\,\sigma_y\right)+\cos\alpha\,\sigma_z$. Now, we only need to solve an equation for the radial spinor:

$$\partial_r\phi(r)=\left[\frac{E-V(r)}{v_F}i\sigma_y+\frac{m(r)}{v_F}\tilde{\sigma}_m+\frac{1}{r}\left(j\sigma_z-\frac{1}{2}\right)\right]\phi(r), \tag{3.18}$$

where $\tilde{\sigma}_m=-i\sigma_y\sigma_m$. This is formally solved by

$$\begin{aligned}\phi(r)&=\phi(r_0)+\int_{r_0}^{r}dr'A(r')\phi(r') &(3.19)\\ &=\left(1+\int_{r_0}^{r}dr'A(r')+\int_{r_0}^{r}dr'\int_{r_0}^{r'}dr''A(r')A(r'')+\cdots\right)\phi(r_0) &(3.20)\\ &=\mathcal{S}\exp\left(\int_{r_0}^{r}dr'A(r')\right)\phi(r_0), &(3.21)\end{aligned}$$

where $r_0\geq r$, $A(r)$ is the matrix working on ϕ on the right side of (3.18), and $\mathcal{S}$ is a path-ordering operator that orders operators with their radial coordinate increasing from right to left [81]. We obtain

$$\phi(r)=\mathcal{S}\exp\left\{\int_{r_0}^{r}dr'\left[\frac{E-V(r')}{v_F}i\sigma_y+\frac{m(r')}{v_F}\tilde{\sigma}_m+\frac{1}{r'}\left(j\sigma_z-\frac{1}{2}\right)\right]\right\}\phi(r_0). \tag{3.22}$$

Free particle

The free-particle solution of the wave equation (3.10) can be easily found by taking the square of the kinetic term. We obtain two decoupled equations

$$-\nabla^2\psi(\boldsymbol{r})=k^2\psi(\boldsymbol{r}), \tag{3.23}$$

where $k=E/v_F$. First, we consider solutions for $k\neq 0$. In this case, the radial solution for the spin-up component becomes

$$\phi_\uparrow(r)=aJ_{j-1/2}(kr)+bY_{j-1/2}(kr), \tag{3.24}$$

where a,b are constants and $J_{j-1/2}(kr)$ and $Y_{j-1/2}(kr)$ are Bessel functions of the first and second kind, respectively. The spin-down component is then obtained from the radial wave equation (3.18):

$$\left[\partial_r-\frac{1}{r}\left(\pm j-\frac{1}{2}\right)\right]\phi_{\uparrow,\downarrow}(r)=\pm k\phi_{\downarrow,\uparrow}(r). \tag{3.25}$$

Hence, the free-particle solution for $k \neq 0$ is given by

$$\psi(r,\theta) = e^{i\left(j-\frac{\sigma_z}{2}\right)\theta}\phi(r), \qquad \phi(r) = \begin{pmatrix} \phi_{j-1/2}(kr) \\ -\phi_{j+1/2}(kr) \end{pmatrix}, \tag{3.26}$$

where $\phi_{j\pm1/2}(kr) = aJ_{j\pm1/2}(kr) + bY_{j\pm1/2}(kr)$. There are also two zero-energy solutions which follow from (3.25) with $k = 0$. We find that the two-dimensional degenerate subspace is spanned by

$$\psi_{0\uparrow}(r,\theta) = ar^{j-1/2}e^{i(j-1/2)\theta}\begin{pmatrix}1\\0\end{pmatrix}, \qquad \psi_{0\downarrow}(r,\theta) = br^{-j-1/2}e^{i(j+1/2)\theta}\begin{pmatrix}0\\1\end{pmatrix}. \tag{3.27}$$

3.1.2 Helical quantum dot

We now consider a circular quantum dot with radius R on the surface of a topological insulator. Confinement of the surface state is realized by depositing a magnetic insulator on the surface which is illustrated in Fig. 3.2 (a). The magnetic covering can be achieved by first depositing a trivial insulator, which prevents leaking of the topological surface state, followed by depositing a ferromagnetic layer. Alternatively, one could consider a slab of topological insulator that is placed between the north and south pole of a cylindrical array of magnets, shown in Figs. 3.2 (b) and (c). This setup might be favorable since the magnetic field of the magnetic film only falls off as $1/R$ in the center of the dot. This system was already considered as a possible realization for a qubit [82]. If the magnetization points in the z direction, the resulting exchange field is given by

$$\boldsymbol{m}(r) = v_F m_0 \Theta(R-r)\,\boldsymbol{e}_z, \tag{3.28}$$

which opens a mass gap $|2v_F m_0|$ everywhere, besides in the region occupied by the quantum dot. This confines the surface states whose energies lie within the gap because the corresponding wave functions decay exponentially outside the quantum dot with decay length v_F/m_0. Particles inside the quantum dot are reflected by the exchange gap at the edge and pick up a time-reversal breaking phase which opens the gap inside the dot [83]. When the radius of the dot is much larger than the decay length, it is a good approximation to send $m_0 \to \infty$. This is called an infinite-mass boundary. In this case, the wave function of the bound states vanishes outside the dot and we only need to consider the wave function inside the dot.

Boundary condition

Here we derive all possible hard-wall boundary conditions for a system with circular symmetry. Hence, we consider a circular delta barrier with

$$m(r) = v_F m_0\,\delta(r-R), \tag{3.29}$$

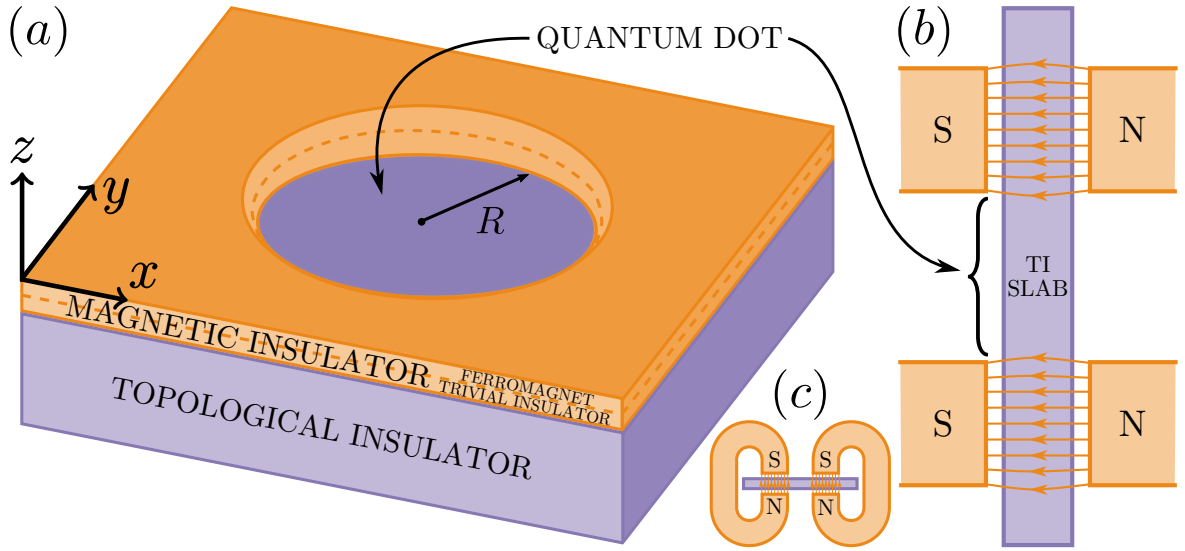

Figure 3.2: (*a*) Quantum dot on the surface of a topological insulator defined by a patterned magnetic insulator. The magnetic covering can be achieved by depositing a two-layer structure consisting of a ferromagnetic metal on top of a trivial insulator. (*b*) Quantum dot on the surface of a topological insulator defined by placing a slab of topological insulator between the north and south pole of a cylindrical array of magnets. (*c*) Lateral view of (*b*).

where m_0 determines the strength of the barrier. The boundary condition on the radial part of the spinor is found from the general solution (3.22) with $r_0 = R_-$ and $r = R_+$ where $R_\pm = R \pm \epsilon$. In the limit $\epsilon \to 0$, we find

$$\phi(R_+) = \exp\left(m_0 \tilde{\sigma}_m\right) \phi(R_-) \tag{3.30}$$

$$\propto \left[\cosh\left(m_0\gamma\right) + \frac{\sinh\left(m_0\gamma\right)}{\gamma}\left(\cos\alpha\,\sigma_x - \sin\alpha\cos\beta\,\sigma_z\right)\right]\phi(R_-), \tag{3.31}$$

where the proportionality constant is a phase factor and

$$\gamma = \sqrt{1 - \sin^2\alpha\,\sin^2\beta}. \tag{3.32}$$

In case $\gamma \neq 0$, we can divide both sides of (3.31) with the hyperbolic cosine and take the hard-wall limit $m_0 \to \infty$. We obtain

$$\left(\gamma - \sin\alpha\cos\beta\,\sigma_z + \cos\alpha\,\sigma_x\right)\phi(R_-) = 0, \tag{3.33}$$

which always has a nonzero solution. When the exchange field lies in the z direction ($\alpha = \beta = 0$ and $\gamma = 1$), the hard-wall boundary condition is reduced to the infinite-mass boundary condition [83].

Quantum dot

We now take an exchange field with direction $\hat{\boldsymbol{m}} = \sin\alpha\,\boldsymbol{e}_r + \cos\alpha\,\boldsymbol{e}_z$. Inside the quantum dot, the general solution is given by the free-particle solution (3.26). However, because the wave function has to be normalizable, we have to set $b = 0$ for finite-energy bound states and for zero energy we need the spin-up solution for $j > 0$ and the spin-down solution for $j < 0$. The hard-wall boundary condition is given by

$$\begin{cases} \cos\alpha\,\phi_\uparrow = -(1+\sin\alpha)\,\phi_\downarrow, & \alpha \neq \pm\frac{\pi}{2}, \\ \phi_{\downarrow,\uparrow} = 0, & \alpha = \pm\frac{\pi}{2}, \end{cases} \tag{3.34}$$

where the components are evaluated at $r = R$. Hence, a zero-energy solution exists only for $\alpha = +\pi/2$ with $j > 0$ and $\alpha = -\pi/2$ with $j < 0$. For bound states with a finite energy, the wave function inside the disk is given by

$$\psi_{jn}(r,\theta) = A_{jn} \begin{pmatrix} e^{i(j-1/2)\theta} J_{j-1/2}(k_{jn} r) \\ -e^{i(j+1/2)\theta} J_{j+1/2}(k_{jn} r) \end{pmatrix}, \tag{3.35}$$

with $n = \pm 1, \pm 2, \ldots$ the radial quantum number where negative values correspond to states with negative energy. The energies $E_{jn} = v_F k_{jn}$ are determined from the boundary conditions which become

$$\begin{cases} \cos\alpha\, J_{j-1/2}(kR) = (1+\sin\alpha)\, J_{j+1/2}(kR), & \alpha \neq \pm\frac{\pi}{2}, \\ J_{j\pm1/2}(kR) = 0, & \alpha = \pm\frac{\pi}{2}, \end{cases} \tag{3.36}$$

and the normalization constant A_{jn} is given by

$$A_{jn}^{-2} = 2\pi R^2 \begin{cases} \left(J_{j-1/2}(k_{jn}R)\right)^2 \frac{2}{1+\sin\alpha} \left(1 - \frac{j\cos\alpha}{k_{jn}R}\right), & \alpha \neq \pm\frac{\pi}{2}, \\ \left(J_{j\mp1/2}(k_{jn}R)\right)^2, & \alpha = \pm\frac{\pi}{2}. \end{cases} \tag{3.37}$$

Spectrum

In Fig. 3.3, we show the energy spectrum of the quantum dot as a function of the angle α which is obtained numerically from (3.36). As the direction of the exchange field is reversed, some energy levels evolve into zero-energy states when the field lies in the radial direction ($\alpha = \pm\pi/2$). Zero-energy states exist only for $j > 0$ when $\alpha = +\pi/2$ and $j < 0$ when $\alpha = -\pi/2$ which was already shown above. Furthermore, the energy spectrum is symmetric around zero energy only when the field lies in the z direction ($\alpha = 0, \pi$) or the radial direction ($\alpha = \pm\pi/2$). In the first case, this is due to charge-conjugation symmetry $\mathcal{C} = \sigma_x \mathcal{K}$ where the charge-conjugated pairs have opposite angular momentum

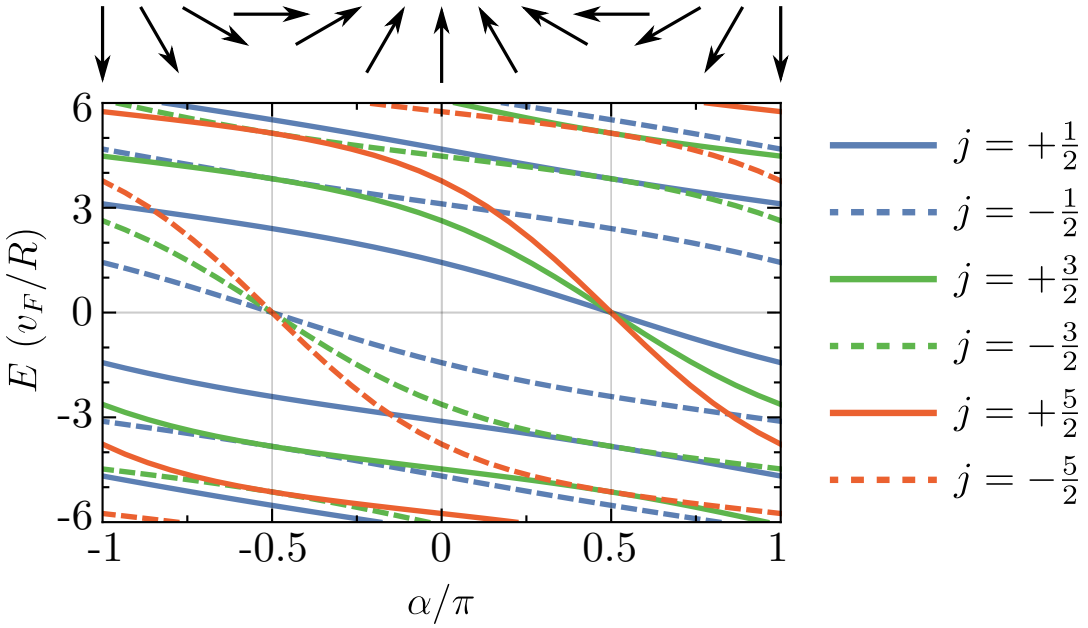

Figure 3.3: Several low-lying energy levels of the quantum dot for the hard-wall boundary conditions with $\beta = 0$ as a function of the angle α between the z direction and the exchange field which is shown above the plot.

j and opposite radial quantum number n with energies $E_{jn} = -E_{-j-n}$. On the other hand, when the field is radial, this is instead caused by the chiral symmetry $\mathcal{S} = \sigma_z$ which leads to $E_{jn} = E_{j-n}$. Moreover, now there is also an accidental degeneracy given by $E_{jn} = E_{-j-1n}$ for $|n| > 0$ and $j \neq \pm 1/2$ for $\alpha = \mp\pi/2$, respectively. These results all follow from the boundary conditions (3.36) and the properties of Bessel functions.

Note that the confinement gap Δ_c reaches a maximum when $\hat{\boldsymbol{m}}$ points in the z direction, which is given by $\Delta_c \approx 2.87\ v_F/R$.

Spin polarization

The spin expectation values are obtained from the expression of the wave function (3.35) and are given by (in units $\hbar$)

$$\langle S_z \rangle = \pi A_{jn}^2 \int_0^R dr\, r \left[\left(J_{j-1/2}(k_{jn} r) \right)^2 - \left(J_{j+1/2}(k_{jn} r) \right)^2 \right] \tag{3.38}$$

$$= \pi R^2 A_{jn}^2 \, \frac{J_{j-1/2}(k_{jn}R) J_{j+1/2}(k_{jn}R)}{k_{jn}R}, \tag{3.39}$$

$$\langle S_r \rangle = -\pi A_{jn}^2 \int_0^R dr\, r J_{j-1/2}(k_{jn} r) J_{j+1/2}(k_{jn} r), \tag{3.40}$$

$$\langle S_\theta \rangle = 0, \tag{3.41}$$

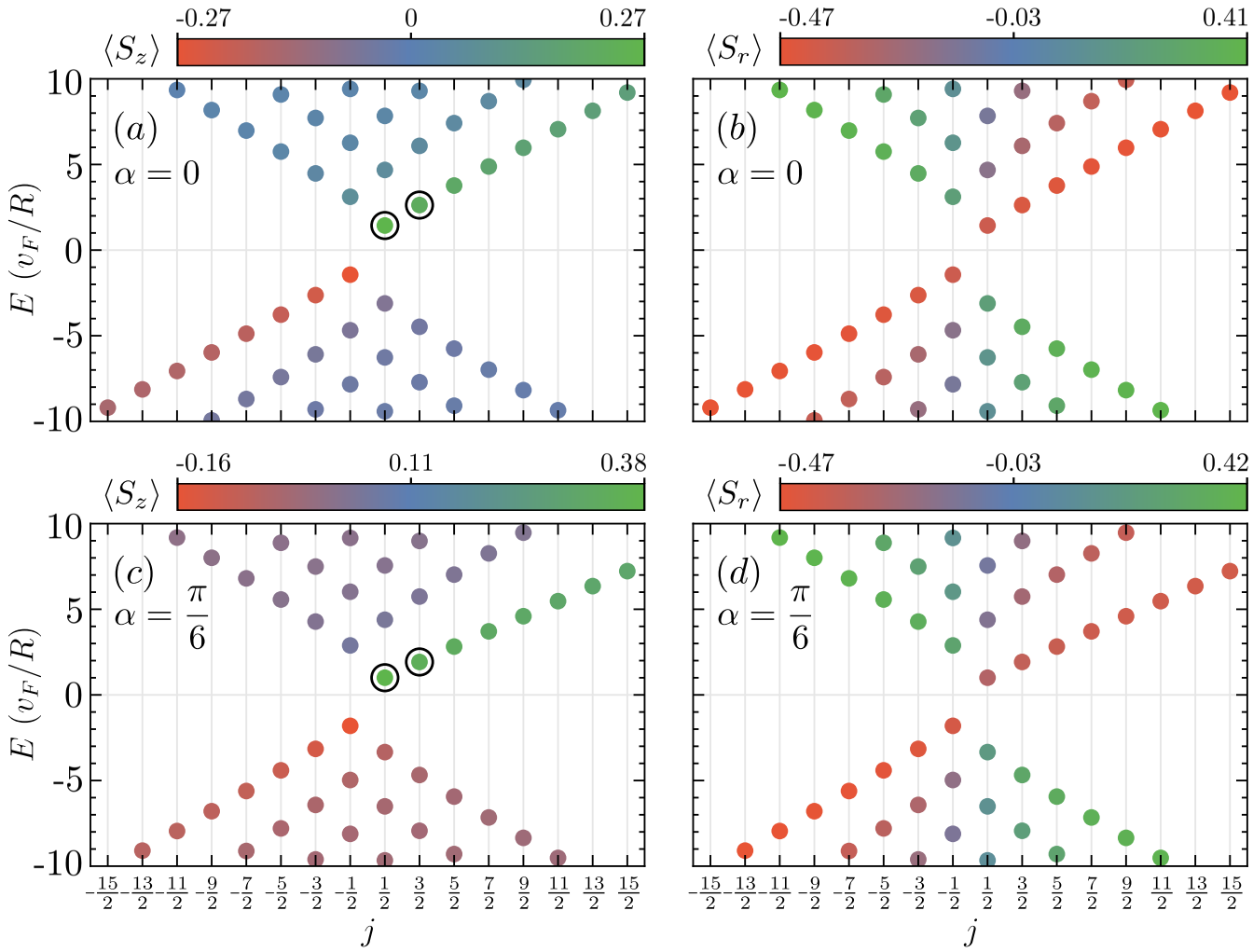

Figure 3.4: Energy spectrum and spin expectation values $\langle S_z \rangle$ and $\langle S_r \rangle$ (in units $\hbar$) of the quantum dot with (a, b) $\hat{\boldsymbol{m}} = \boldsymbol{e}_z$ $(\alpha = 0)$ and (c, d) $\hat{\boldsymbol{m}} = (1/2)\boldsymbol{e}_r + (\sqrt{3}/2)\boldsymbol{e}_z$ $(\alpha = \pi/6)$ as a function of the angular momentum j for several low-energy states.

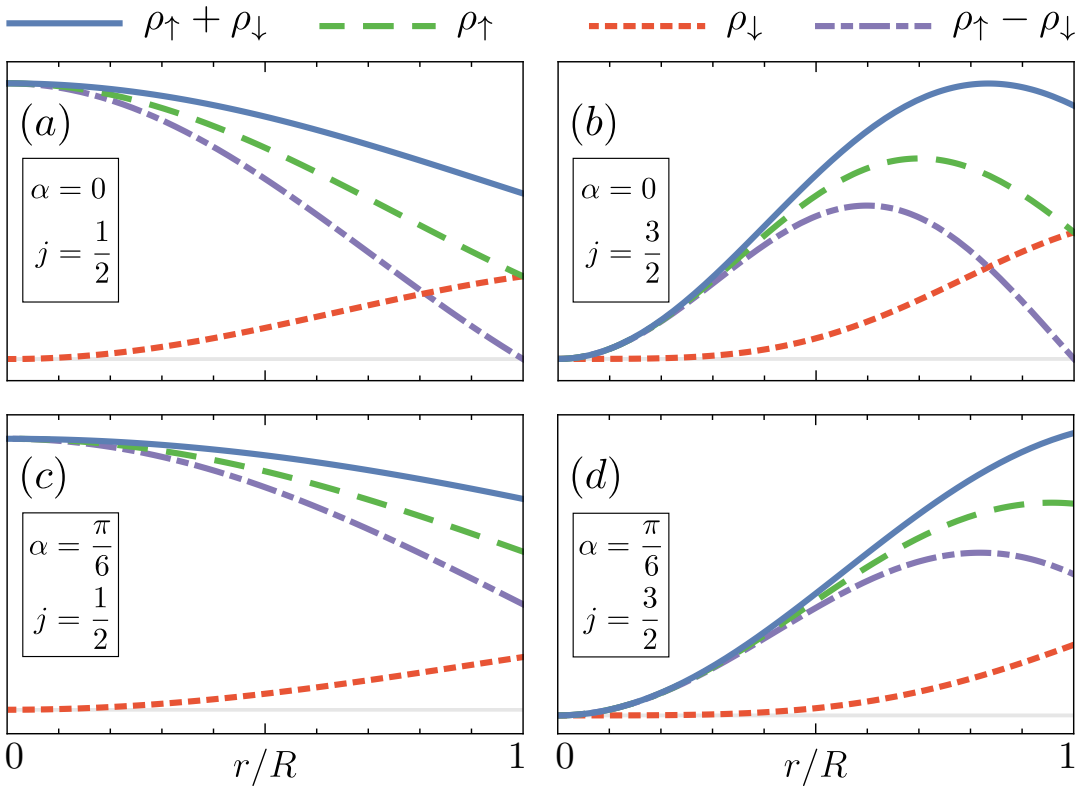

Figure 3.5: Probability density $\rho = \rho_\uparrow + \rho_\downarrow$, spin-up density $\rho_\uparrow$, spin-down density $\rho_\downarrow$, and spin density $\sigma = \rho_\uparrow - \rho_\downarrow$ for (a, b) $\alpha = 0$ and (c, d) $\alpha = \pi/6$ of the states with radial quantum number $n = 1$ that are encircled in Fig. 3.4.

where $\langle S_r \rangle$ yields no simple expression. Both $\langle S_z \rangle$ and $\langle S_r \rangle$ are shown in Fig. 3.4 (a, b) and (c, d) for $\alpha = 0$ and $\alpha = \pi/6$, respectively, as a function of j. In the first case, the exchange field points in the z direction and charge conjugation is preserved. We see that $\langle S_z \rangle$ is opposite for charge-conjugated stated and only appreciable for two charge-conjugated branches. Moreover, in Fig. 3.4 (b) we see that $\langle S_r \rangle \propto j$, so that the confined surface state remains helical except for the two branches that are S_z polarized. This is also the case for the quantum dot with $\alpha = \pi/6$. However, now the exchange field is tilted in the radial direction and we have no charge-conjugation symmetry. The S_z polarization is reduced in general but increases for a single branch. This branch evolves towards zero energy when the field becomes radial and is then completely polarized in the z direction as can be seen from the zero-energy solutions given in (3.27).

Charge and spin density

The spin densities follow from (3.35) and are given by

$$\rho_\sigma(r) = \left(A_{jn} J_{j-\sigma/2}(k_{jn} r)\right)^2, \tag{3.42}$$

where $\sigma = \pm$ for spin up and spin down, respectively. The charge and spin densities of the S_z-polarized branch of the quantum dot with magnetization $\alpha = 0$ and $\alpha = \pi/6$ are shown in Fig. 3.5. As the angle α increases, these states evolve into zero-energy states when the exchange field is radial and the density shifts towards the edge. This can also be seen from the density of the zero-energy states which is localized at the edge and increasingly so with increasing $|j|$. For $\alpha = \pi/2$, for example, the density of the zero-energy states which are spin-up states in this case, is given by

$$|\psi_{0j}|^2 = \frac{2j}{\pi R^{2j}} r^{2j-1}, \qquad j = \frac{1}{2}, \frac{3}{2}, \ldots . \tag{3.43}$$

In the following, we only consider the infinite-mass boundary condition for which the exchange field points in the z direction ($\alpha = \beta = 0$) because the confinement gap is largest in this case and because it is the most experimentally relevant case.

3.2 Coulomb interaction

Here, we investigate the few-particle properties of the infinite-mass quantum dot whose single-particle levels are shown in Fig. 3.4 (a). Similar to previous studies, we assume that the quantum dot is initially filled up to the charge-neutrality point so that all negative-energy states are occupied [84]. We then only consider interactions between particles that are added to the system. Thus we neglect electron-hole excitations. However, electron-hole excitations have an energy that is larger or equal to the confinement gap. Therefore this approximation is valid only if the energy scale of the interaction is smaller than the confinement gap which is approximately given by $2.87\ v_F/R$.

The effective Hamiltonian becomes

$$\hat{H} = \frac{v_F}{R} {\sum_a}' \varepsilon_a \hat{c}_a^\dagger \hat{c}_a + \hat{H}'_{e-e}, \tag{3.44}$$

where $a = (j_a, n_a)$ labels the quantum numbers, $\varepsilon_a = (R/v_F)E_a$ are the dimensionless single-particle energies of the infinite-mass quantum dot, and the primed sum runs only over states with positive energy. The electron-electron interaction term is given by

$$\hat{H}_{e-e} = \frac{1}{2} \int d^2r \int d^2r'\, V\left(|\boldsymbol{r} - \boldsymbol{r}'|\right) \hat{\psi}^\dagger(\boldsymbol{r}) \hat{\psi}^\dagger(\boldsymbol{r}') \hat{\psi}(\boldsymbol{r}') \hat{\psi}(\boldsymbol{r}), \tag{3.45}$$

which becomes

$$\hat{H}'_{e-e} = \frac{1}{2} {\sum_{a,b,a',b'}}' V_{aa'b'b} \hat{c}_a^\dagger \hat{c}_{a'}^\dagger \hat{c}_{b'} \hat{c}_b, \tag{3.46}$$

where we used the basis transformation (3.5) and excluded negative-energy states. In the following, we omit the primes for simplicity and remember that the sums only run

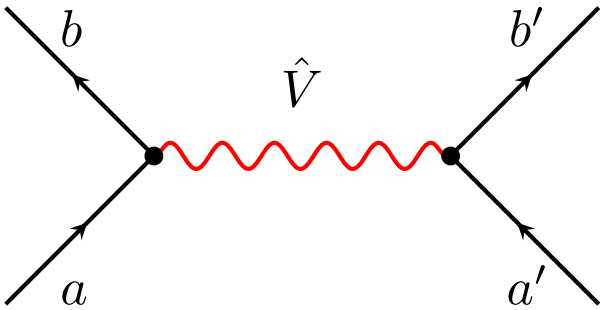

Figure 3.6: Diagram of the process $aa' \to bb'$ whose amplitude is given by $V_{aa'b'b}$.

over states with positive energy. The interaction integrals are given by

$$V_{aa'b'b} = \langle aa' | \hat{V} | b'b \rangle \tag{3.47}$$

$$= \int d^2r \int d^2r' \, V\left(|\boldsymbol{r} - \boldsymbol{r}'|\right) \left(\psi_a^\dagger(\boldsymbol{r})\psi_b(\boldsymbol{r})\right)\left(\psi_{a'}^\dagger(\boldsymbol{r}')\psi_{b'}(\boldsymbol{r}')\right), \tag{3.48}$$

with $V\left(|\boldsymbol{r} - \boldsymbol{r}'|\right)$ the interaction potential. This is the amplitude for the process where two particles in the state $|aa'\rangle$ interact and scatter to the state $|bb'\rangle$ which is shown in Fig. 3.6. Since the Hamiltonian should be hermitian, the matrix elements satisfy the relation $V_{aa'b'b} = V^*_{bb'a'a}$. We also have $V_{aa'b'b} = V_{a'abb'}$ because the interaction potential only depends on the distance between the particles.

Interaction integrals

We calculate the interaction integrals $V_{aa'b'b}$ for the unscreened Coulomb potential

$$V\left(|\boldsymbol{r} - \boldsymbol{r}'|\right) = \frac{e^2}{4\pi\epsilon\,|\boldsymbol{r} - \boldsymbol{r}'|}, \tag{3.49}$$

where e is the electron charge and ϵ is the permittivity of the topological-insulator surface. To solve the angular integrals, we make use of the expansion [85]

$$\frac{1}{|\boldsymbol{r} - \boldsymbol{r}'|} = \frac{1}{\pi\sqrt{rr'}} \sum_{m=-\infty}^{\infty} Q_{m-1/2}\left(\chi\right) e^{im(\theta-\theta')}, \tag{3.50}$$

where $Q_{m-1/2}$ is a Legendre function of the second kind of half-integer degree and

$$\chi = \frac{r^2 + r'^2}{2rr'}. \tag{3.51}$$

With this expansion and the single-particle wave function from (3.35), the interaction integrals become

$$V_{aa'b'b} = \frac{v_F}{R}\frac{e^2}{4\pi^2\epsilon v_F}\mathcal{N}_{aa'b'b}\sum_{m=-\infty}^{\infty}\int_0^{2\pi} d\theta\, e^{i(j_b-j_a+m)\theta}\int_0^{2\pi} d\theta'\, e^{i(j_{b'}-j_{a'}-m)\theta'} \tag{3.52}$$

$$\times\int_0^1 dt\int_0^1 dt'\, Q_{m-1/2}(\chi)G_{ab}(t)G_{a'b'}(t') \tag{3.53}$$

$$= \frac{v_F}{R}\left[4\pi\alpha\,\delta_{j_a+j_{a'},j_b+j_{b'}}\,\mathcal{N}_{aa'b'b}\int_0^1 dt\int_0^1 dt'\, Q_{\tau_{ab}-1/2}(\chi)G_{ab}(t)G_{a'b'}(t')\right], \tag{3.54}$$

where $\mathcal{N}_{aa'b'b} = R^4 A_{j_a n_a} A_{j_{a'} n_{a'}} A_{j_{b'} n_{b'}} A_{j_b n_b}$, $\tau_{ab} = j_a - j_b = -(j_{b'} - j_{a'})$ is the angular-momentum exchange, and we defined

$$G_{ab}(t) = \sqrt{t}\left[J_{j_a-1/2}(\varepsilon_{j_a n_a}t)J_{j_b-1/2}(\varepsilon_{j_b n_b}t) + J_{j_a+1/2}(\varepsilon_{j_a n_a}t)J_{j_b+1/2}(\varepsilon_{j_b n_b}t)\right]. \tag{3.55}$$

The effective fine-structure constant α gives the strength of the Coulomb interaction relative to the kinetic energy scale v_F/R and is given by

$$\alpha = \frac{e^2}{4\pi\epsilon\hbar v_F} \approx \frac{2.2\times 10^6\ \mathrm{m\,s^{-1}}}{\epsilon_r v_F}, \tag{3.56}$$

where we restored $\hbar$ and ϵ_r is the relative permittivity. Note that α is determined only by the material constants v_F and ϵ_r and not by the charge density as is the case for the standard electron gas. The remaining radial integrals in (3.54) presumably have no analytical solution and have to be solved numerically.

3.2.1 Configuration interaction

The many-body problem is solved if we diagonalize the total Hamiltonian (3.44). We therefore construct a complete basis for the Fock space from the eigenstates of the single-particle Hamiltonian $\hat{H}_0$. The basis states are given by the configurations

$$|\mu\rangle = \hat{c}^\dagger_{\mu_1}\hat{c}^\dagger_{\mu_2}\cdots\hat{c}^\dagger_{\mu_N}|0\rangle, \tag{3.57}$$

where $|0\rangle$ is the vacuum state given here by the state in which all negative-energy levels of the quantum dot are filled. In position representation, the configurations are given by Slater determinants. The number of interacting fermions in the dot is given by N which is a conserved quantity because each term in the Hamiltonian contains an equal amount of creation and destruction operators. Moreover, we order the fermions such that $\varepsilon_{\mu_1} < \varepsilon_{\mu_2} < \cdots < \varepsilon_{\mu_N}$. The matrix elements of the Hamiltonian in this basis can then be written as

$$H_{\mu\nu} = \langle\mu|\hat{H}|\nu\rangle = \frac{v_F}{R}\varepsilon_\mu\delta_{\mu\nu} + V_{\mu\nu}, \tag{3.58}$$

where ε_μ is the total single-particle energy of the configuration $|\mu\rangle$ and $V_{\mu\nu}$ is the interaction matrix element between the configurations $|\mu\rangle$ and $|\nu\rangle$.

In practice, we take a finite number of configurations for which $\varepsilon_\mu < \varepsilon_T$ where ε_T is a threshold energy; all configurations whose total single-particle energy exceeds the threshold are discarded. The threshold is increased until the many-body ground state energy for a given value of the interaction strength α converges. This numerical diagonalization method is called *configuration interaction*, which can be thought of as an extension of the *Hartree-Fock* method where one tries to minimizes the ground-state energy with only a single many-body configuration [86].

3.2.2 Matrix elements

Our next goal is to calculate the matrix elements (3.58). The first term is the total single-particle energy of $|\mu\rangle$ which is given by

$$\varepsilon_\mu = \langle\mu|\,\hat{H}_0\,|\mu\rangle = \sum_a \varepsilon_a \langle\mu|\,\hat{c}_a^\dagger \hat{c}_a\,|\mu\rangle = \sum_{i=1}^{N} \varepsilon_{\mu_i}, \tag{3.59}$$

since the matrix element

$$\begin{aligned}
\langle\mu|\,\hat{c}_a^\dagger \hat{c}_a\,|\mu\rangle &= \langle\mu|\,\hat{c}_a^\dagger \hat{c}_a \hat{c}_{\mu_1}^\dagger \cdots \hat{c}_{\mu_N}^\dagger\,|0\rangle && (3.60)\\
&= \langle\mu|\,\hat{c}_a^\dagger \left(\delta_{a\mu_1} - \hat{c}_{\mu_1}^\dagger \hat{c}_a\right) \hat{c}_{\mu_2}^\dagger \cdots \hat{c}_{\mu_N}^\dagger\,|0\rangle && (3.61)\\
&= \delta_{a\mu_1} + \langle\mu|\,\hat{c}_{\mu_1}^\dagger \hat{c}_a^\dagger \hat{c}_a \hat{c}_{\mu_2}^\dagger \cdots \hat{c}_{\mu_N}^\dagger\,|0\rangle && (3.62)\\
&= \sum_{i=1}^{N} \delta_{a\mu_i}, && (3.63)
\end{aligned}$$

is nonzero only if the state a is contained in the configuration $|\mu\rangle$. The second term of (3.58) is the interaction matrix element

$$V_{\mu\nu} = \langle\mu|\,\hat{H}_{e-e}\,|\nu\rangle = \frac{1}{2} \sum_{a,b,a',b'} V_{aa'b'b} \langle\mu|\,\hat{c}_a^\dagger \hat{c}_{a'}^\dagger \hat{c}_{b'} \hat{c}_b\,|\nu\rangle\,. \tag{3.64}$$

Note that the matrix element $\langle\mu|\,\hat{c}_a^\dagger \hat{c}_{a'}^\dagger \hat{c}_{b'} \hat{c}_b\,|\nu\rangle$ is nonzero only if $|\mu\rangle$ and $|\nu\rangle$ are equal or differ by one or two states. We now consider these three cases separately.

Case 1: Configurations differ by two states

If the configurations differ by two states, there are only four possible sets of quantum numbers $\{a, a', b, b'\}$ which give a nonzero result. In this case, we can write $|\nu\rangle$ in terms of $|\mu\rangle$ as follows:

$$|\nu\rangle = (-1)^{s_\alpha + s_\beta} \hat{c}_{\nu_\beta}^\dagger \hat{c}_{\mu_\beta} \hat{c}_{\nu_\alpha}^\dagger \hat{c}_{\mu_\alpha}\,|\mu\rangle\,, \tag{3.65}$$

where α and β label the states that differ and s_α (s_β) is the number of fermion swaps necessary to destroy the state μ_α (μ_β) and create the state ν_α (ν_β) in the correct order such that $\varepsilon_{\nu_1} < \varepsilon_{\nu_2} < \cdots < \varepsilon_{\nu_N}$. To proceed, we find

$$\hat{c}_b |\nu\rangle = (-1)^{s_\alpha+s_\beta} \left(\delta_{b\nu_\beta} - \hat{c}^\dagger_{\nu_\beta}\hat{c}_b\right) \hat{c}_{\mu_\beta}\hat{c}^\dagger_{\nu_\alpha}\hat{c}_{\mu_\alpha} |\mu\rangle \tag{3.66}$$

$$= (-1)^{s_\alpha+s_\beta} \left(\delta_{b\nu_\beta}\hat{c}_{\mu_\beta}\hat{c}^\dagger_{\nu_\alpha}\hat{c}_{\mu_\alpha} + \delta_{b\nu_\alpha}\hat{c}^\dagger_{\nu_\beta}\hat{c}_{\mu_\beta}\hat{c}_{\mu_\alpha}\right) |\mu\rangle + \cdots , \tag{3.67}$$

where we omitted the last term because it corresponds to a term that gives zero in the end result. Similarly, we obtain

$$\hat{c}_{b'}\hat{c}_b |\nu\rangle = (-1)^{s_\alpha+s_\beta} \left(\delta_{b\nu_\alpha}\delta_{b'\nu_\beta} - \delta_{b\nu_\beta}\delta_{b'\nu_\alpha}\right) \hat{c}_{\mu_\beta}\hat{c}_{\mu_\alpha} |\mu\rangle + \cdots , \tag{3.68}$$

and

$$\langle\mu| \hat{c}^\dagger_a\hat{c}^\dagger_{a'}\hat{c}_{b'}\hat{c}_b |\nu\rangle = (-1)^{s_\alpha+s_\beta} \left(\delta_{a\mu_\alpha}\delta_{a'\mu_\beta} - \delta_{a\mu_\beta}\delta_{a'\mu_\alpha}\right) \left(\delta_{b'\nu_\beta}\delta_{b\nu_\alpha} - \delta_{b'\nu_\alpha}\delta_{b\nu_\beta}\right) . \tag{3.69}$$

We find that the interaction matrix element between configurations that differ by two states labeled by α and β is given by

$$V^{(2)}_{\mu\nu} = (-1)^{s_\alpha+s_\beta}\frac{1}{2}\sum_{a,b,a',b'} V_{aa'b'b} \left(\delta_{a\mu_\alpha}\delta_{a'\mu_\beta} - \delta_{a\mu_\beta}\delta_{a'\mu_\alpha}\right) \left(\delta_{b'\nu_\beta}\delta_{b\nu_\alpha} - \delta_{b'\nu_\alpha}\delta_{b\nu_\beta}\right) \tag{3.70}$$

$$= (-1)^{s_\alpha+s_\beta} \left(V_{\mu_\alpha\mu_\beta\nu_\beta\nu_\alpha} - V_{\mu_\alpha\mu_\beta\nu_\alpha\nu_\beta}\right) , \tag{3.71}$$

where we used the property $V_{aa'b'b} = V_{a'abb'}$ in the last step.

Case 2: Configurations differ by one state

In this case, we can write

$$|\nu\rangle = (-1)^{s_\alpha}\hat{c}^\dagger_{\nu_\alpha}\hat{c}_{\mu_\alpha} |\mu\rangle , \tag{3.72}$$

where α labels the state that is different and s_α is the number of fermion swaps necessary to destroy μ_α and create ν_α in the correct order. We find

$$\hat{c}_{b'}\hat{c}_b |\nu\rangle = (-1)^{s_\alpha}\hat{c}_{b'} \left(\delta_{b\nu_\alpha} - \hat{c}^\dagger_{\nu_\alpha}\hat{c}_b\right) \hat{c}_{\mu_\alpha} |\mu\rangle = (-1)^{s_\alpha} \left(\delta_{b\nu_\alpha}\hat{c}_{b'}\hat{c}_{\mu_\alpha} - \delta_{b'\nu\alpha}\hat{c}_b\hat{c}_{\mu_\alpha}\right) |\mu\rangle + \cdots , \tag{3.73}$$

and

$$\langle\mu| \hat{c}^\dagger_a\hat{c}^\dagger_{a'}\hat{c}_{b'}\hat{c}_b |\nu\rangle = (-1)^{s_\alpha} \sum_{i\neq\alpha} \left(\delta_{a\mu_\alpha}\delta_{a'\mu_i} - \delta_{a\mu_i}\delta_{a'\mu_\alpha}\right) \left(\delta_{b'\mu_i}\delta_{b\nu_\alpha} - \delta_{b'\nu_\alpha}\delta_{b\mu_i}\right) . \tag{3.74}$$

We find that the interaction matrix element between configurations that differ by one state labeled by α is given by

$$V^{(1)}_{\mu\nu} = (-1)^{s_\alpha}\frac{1}{2}\sum_{i\neq\alpha}\sum_{a,b,a',b'} V_{aa'b'b} \left(\delta_{a\mu_\alpha}\delta_{a'\mu_i} - \delta_{a\mu_i}\delta_{a'\mu_\alpha}\right) \left(\delta_{b'\mu_i}\delta_{b\nu_\alpha} - \delta_{b'\nu_\alpha}\delta_{b\mu_i}\right) \tag{3.75}$$

$$= (-1)^{s_\alpha} \sum_{i\neq\alpha} \left(V_{\mu_\alpha\mu_i\mu_i\nu_\alpha} - V_{\mu_\alpha\mu_i\nu_\alpha\mu_i}\right) . \tag{3.76}$$

Case 3: Equal configurations

When the configurations are equal, we find

$$\langle\mu|\,\hat{c}_a^\dagger\hat{c}_{a'}^\dagger\hat{c}_{b'}\hat{c}_b\,|\mu\rangle = \sum_{i\neq j}\left(\delta_{a\mu_i}\delta_{a'\mu_j}-\delta_{a\mu_j}\delta_{a'\mu_i}\right)\left(\delta_{b'\mu_j}\delta_{b\mu_i}-\delta_{b'\mu_i}\delta_{b\mu_j}\right), \tag{3.77}$$

which is obtained in the same way as a above. The interaction matrix element becomes

$$V_{\mu\nu}^{(0)} = V_{\mu\mu} = \frac{1}{2}\sum_{i\neq j}\sum_{a,b,a',b'} V_{aa'b'b}\left(\delta_{a\mu_i}\delta_{a'\mu_j}-\delta_{a\mu_j}\delta_{a'\mu_i}\right)\left(\delta_{b'\mu_j}\delta_{b\nu_i}-\delta_{b'\nu_i}\delta_{b\mu_j}\right) \tag{3.78}$$

$$= \sum_{i\neq j}\left(V_{\mu_i\mu_j\mu_j\mu_i}-V_{\mu_i\mu_j\mu_i\mu_j}\right). \tag{3.79}$$

3.3 Helical Wigner molecule

In a regular electron gas, at low temperatures, the Coulomb interaction becomes dominant in the low-density limit. This is because the average (noninteracting) kinetic energy of the ground state scales as r_s^{-2}, where r_s is proportional to the average distance between electrons, while the Coulomb potential energy scales as r_s^{-1} [86]. Hence, the ground state is dominated by interactions in the limit $r_s \to \infty$ and there is a crossover to a Wigner crystal where the electrons are localized and form a periodic lattice structure in the ground state [87].

However, for Dirac fermions, the kinetic energy also scales as r_s^{-1} so that there is no competition between energy scales and Wigner crystallization is absent in bulk Dirac systems [88]. Nevertheless, in finite Dirac systems, Wigner crystallization can occur at sufficiently high values of the interaction strength α, which only depends on material properties [84]. This phase is called a *Wigner molecule*. Because of the induced magnetic confinement gap, the dispersion of the confined Dirac electrons becomes effectively quadratic at low energies. Hence, the energetics are those of a regular electron gas and the Wigner molecule can emerge in a quantum dot on the surface of a topological insulator albeit with a nontrivial spin texture.

In this section, we discuss our results for interacting particles in the infinite-mass quantum dot where Coulomb interactions are included with the configuration-interaction method for up to seven particles in the dot. Circular symmetry considerably simplifies the calculation because in this case the Hamiltonian is block diagonal in the total angular momentum $J = \sum_{i=1}^{N} j_i$. First, we give an overview of the observables that are used to characterize the Wigner molecule. Besides the few-particle energy, we also investigate the spin-resolved densities and pair-correlation functions as a function of the interaction strength α.

3.3.1 Observables

Here, we give an overview of the observables used to probe the real-space properties of the few-particle system. For a given eigenstate of the interacting quantum dot, the many-body wave function can be written as

$$|\Phi\rangle = \sum_{\mu} C_{\mu} |\mu\rangle \,, \tag{3.80}$$

where the coefficients C_μ are given by the eigenvectors of the matrix $H_{\mu\nu}$ and are obtained numerically with the configuration-interaction method described above. The probability density of spin σ fermions is given by

$$\rho_\sigma(\boldsymbol{r}) = \frac{\langle \hat{\psi}^\dagger_\sigma(\boldsymbol{r})\hat{\psi}_\sigma(\boldsymbol{r})\rangle}{N} \tag{3.81}$$

$$= \frac{1}{N}\sum_{a,b} \psi^*_{\sigma a}(\boldsymbol{r})\psi_{\sigma b}(\boldsymbol{r})\langle \hat{c}^\dagger_a \hat{c}_b\rangle, \tag{3.82}$$

where the expectation value is taken with respect to (3.80) and N is the number of fermions in the dot. Hence, the remaining matrix element becomes

$$\langle \hat{c}^\dagger_a \hat{c}_b\rangle = \sum_{\mu,\nu} C^*_\mu C_\nu \langle \mu| \, c^\dagger_a \hat{c}_b \, |\nu\rangle \tag{3.83}$$

$$= \delta_{ab}\sum_{\mu} |C_\mu|^2 \sum_{i=1}^{N} \delta_{a\mu_i} + \sum_{\mu,\nu}^{(1)} C^*_\mu C_\nu (-1)^{s_\alpha} \delta_{a\mu_\beta}\delta_{b\nu_\beta}, \tag{3.84}$$

where the second sum in the last line only runs over configurations that differ by one state labeled by β. Thus, we obtain

$$\rho_\sigma(\boldsymbol{r}) = \frac{1}{N}\left[\sum_{\mu} |C_\mu|^2 \sum_{i=1}^{N} |\psi_{\sigma\mu_i}(\boldsymbol{r})|^2 + \sum_{\mu,\nu}^{(1)} C^*_\mu C_\nu (-1)^{s_\alpha}\, \psi^*_{\sigma\mu_\beta}(\boldsymbol{r})\psi_{\sigma\nu_\beta}(\boldsymbol{r})\right], \tag{3.85}$$

and the total charge and spin probability density are then given by

$$\rho(\boldsymbol{r}) = \sum_\sigma \rho_\sigma(\boldsymbol{r}), \qquad s_z(\boldsymbol{r}) = \frac{1}{2}\sum_\sigma \sigma\rho_\sigma(\boldsymbol{r}), \tag{3.86}$$

respectively. In a system with circular symmetry, these functions only depend on the radius. The crossover to the Wigner molecule phase is best captured with the *spin-resolved pair-correlation functions* $g_{\sigma\sigma'}(\boldsymbol{r},\boldsymbol{r}')$. This is the joint probability of having a particle with spin σ at position $\boldsymbol{r}$ and another particle with spin σ' at position $\boldsymbol{r}'$:

$$g_{\sigma\sigma'}(\boldsymbol{r},\boldsymbol{r}') = \frac{\langle \hat{\psi}^\dagger_\sigma(\boldsymbol{r})\hat{\psi}^\dagger_{\sigma'}(\boldsymbol{r}')\hat{\psi}_{\sigma'}(\boldsymbol{r}')\hat{\psi}_\sigma(\boldsymbol{r})\rangle}{N\,(N-1)} \tag{3.87}$$

$$= \frac{1}{N\,(N-1)}\sum_{a,b,a',b'} \psi^*_{\sigma a}(\boldsymbol{r})\psi_{\sigma b}(\boldsymbol{r})\psi^*_{\sigma' a'}(\boldsymbol{r}')\psi_{\sigma' b'}(\boldsymbol{r}')\langle \hat{c}^\dagger_a \hat{c}^\dagger_{a'}\hat{c}_{b'}\hat{c}_b\rangle, \tag{3.88}$$

where the remaining expectation value was already calculated in Section 3.2.2. Note that $g_{\sigma\sigma'}(\boldsymbol{r},\boldsymbol{r}') = g_{\sigma'\sigma}(\boldsymbol{r}',\boldsymbol{r})$. The total pair-correlation function is then given by

$$g(\boldsymbol{r},\boldsymbol{r}') = \sum_{\sigma,\sigma'} g_{\sigma\sigma'}(\boldsymbol{r},\boldsymbol{r}'), \tag{3.89}$$

which is normalized as $\int d^2r \int d^2r'\, g(\boldsymbol{r},\boldsymbol{r}') = 1$. Moreover, since

$$\rho_\sigma(\boldsymbol{r}) = \sum_{\sigma'} \int d^2r'\, g_{\sigma\sigma'}(\boldsymbol{r},\boldsymbol{r}'), \tag{3.90}$$

the conditional probability of finding a particle with spin σ at position $\boldsymbol{r}$ given that there is a particle with spin σ' at position $\boldsymbol{r}'$ is defined as

$$P(\boldsymbol{r}\sigma|\boldsymbol{r}'\sigma') \equiv \frac{g_{\sigma\sigma'}(\boldsymbol{r},\boldsymbol{r}')}{\rho_{\sigma'}(\boldsymbol{r}')}. \tag{3.91}$$

3.3.2 Results

The energy of the ground state together with some excited states of the two-particle ($N = 2$) dot $E_2(\alpha)$ are shown in Fig. 3.7 as a function of α. We do not show the energy for other N because it is not very informative. Instead, we consider the total angular momentum J of the ground state which is shown in Fig. 3.8 (a). Note that, except for $N = 2$ and $N = 4$, there are level crossings towards higher J when the interaction strength α increases. This can be understood from the density $\rho(r)$ which is shown together with the spin densities $\rho_\sigma(r)$ and the spin density $s_z(r)$ in Fig. 3.9 for $\alpha = 0, 1, 2$. For all cases, expect for $N = 2$ and $N = 4$, the charge density is not peaked at the edge of the dot for $\alpha = 0$, which is not energetically favorable when α increases. Hence, the system transitions to a higher angular momentum which increases the kinetic energy but decreases the total energy overall because it significantly lowers the interaction energy. Intuitively speaking, this is because the particles have more room to spread out closer to the edge. In terms of the single-particle spectrum, as the angular momentum of the ground state increases, the spin-polarized branch, which is shown in Fig. 3.4, is being occupied. Hence, the spin polarization

$$\langle S_z\rangle = \frac{\hbar}{2} N \int d^2r\, [\rho_\uparrow(r) - \rho_\downarrow(r)] = \frac{\hbar}{2}\left(N_\uparrow - N_\downarrow\right), \tag{3.92}$$

where $N_\sigma = \int d^2r\, \rho_\sigma$ is the average number of spin σ fermions, jumps at every level crossing, which shown in Fig. 3.8 (b). The physical significance of the spin polarization is the following. With increasing interaction strength, the system evolves toward a classical state: the Wigner molecule. In nontopological systems, the classical nature, and the consequent loss of the spin degree of freedom, is realized by the fact that many states tend to become degenerate in the limit of infinite interaction strength. The presence

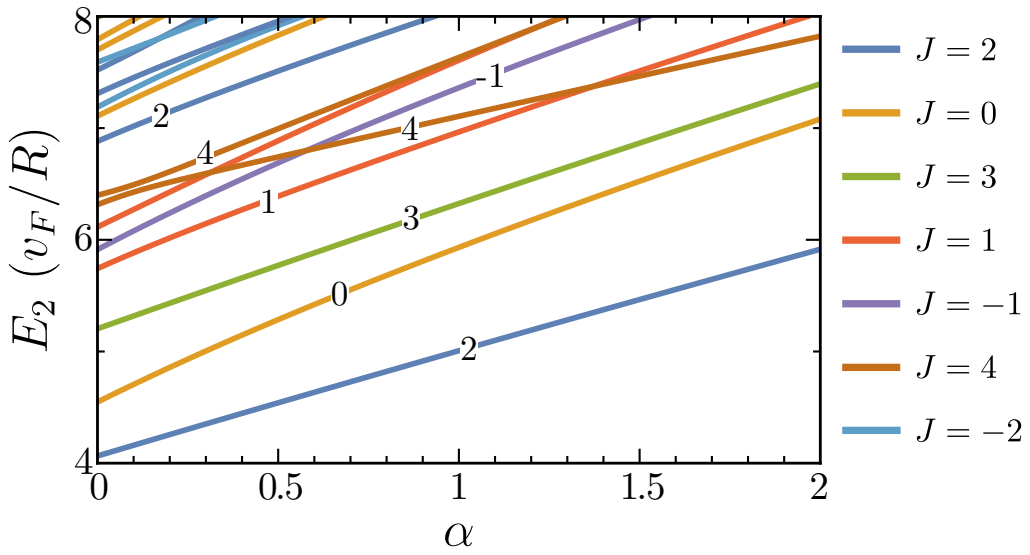

Figure 3.7: Several few-particle energy levels of the interacting infinite-mass quantum dot with $N = 2$ as a function of the interaction strength α.

of a single Dirac cone with spin-momentum locking, however, prevents our system from developing this degeneracy. Increasing the spin polarization is therefore a natural way to approach the classical limit of a collective spinless (or spin-polarized) system in the helical quantum dot. The quantum phase transitions shown in Fig. 3.8 (*b*) indicates that the effect is generic for $2 < N < 7$ and $0 < \alpha < 2$. Moreover, it contains further peculiarities: In ordinary 2DEG quantum dots, $\langle S_z \rangle$ does not change with interaction strength and the total spin is fixed by an applied magnetic field which itself can induce quantum phase transitions toward states with a higher spin imbalance [89, 90].

Next, we address the chemical potential of the quantum dot,

$$\mu_N = E_{N+1} - E_N, \tag{3.93}$$

which is the energy that is required to add an additional particle to a quantum dot with N particles. These energies correspond to peaks in the current flowing through the quantum dot as a function of gate voltage in a Coulomb blockade experiment [91]. The distance between consecutive current peaks is given by the addition energy

$$\Delta_N = \mu_N - \mu_{N-1} = E_{N+1} + E_{N-1} - 2E_N, \tag{3.94}$$

which is shown in Fig. 3.8 (*b*).

Spin-resolved correlations

To directly probe the crossover to the Wigner molecule, we consider the spin-resolved pair-correlation functions $g_{\sigma\sigma'}(\boldsymbol{r}, \boldsymbol{r}')$ which are shown in Fig. 3.10 as a function of the

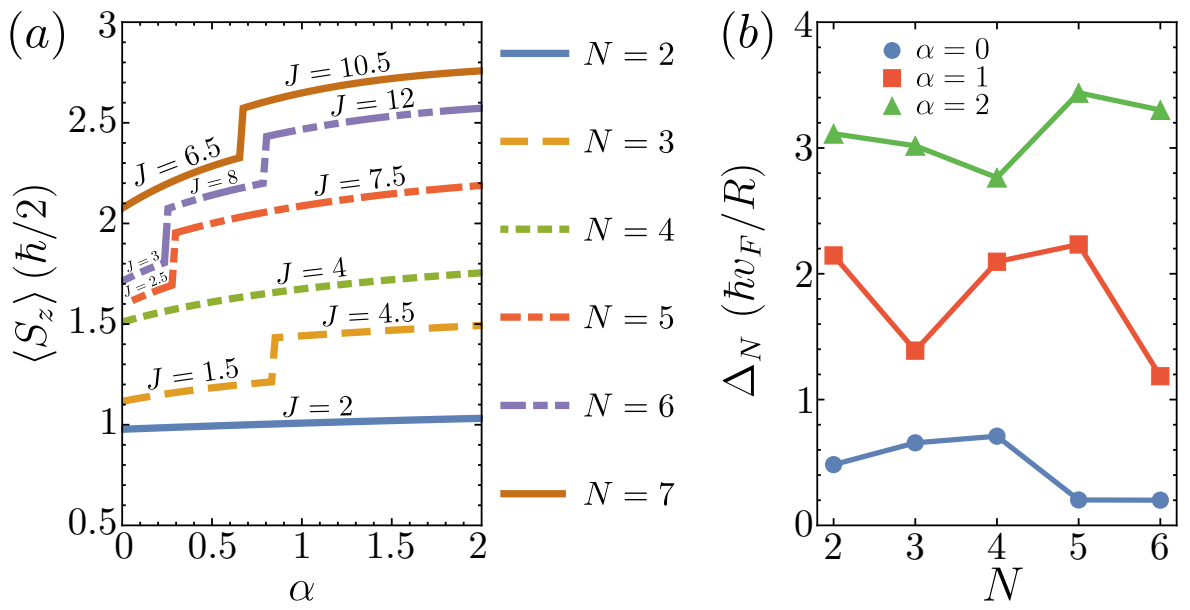

Figure 3.8: (a) Spin expectation value $\langle S_z \rangle$ for $N = 2, \ldots, 7$. The ground-state angular momentum is given in the figure and the discontinuities correspond to level crossings. (b) Addition energy Δ_N for $\alpha = 0$ (blue), $\alpha = 1$ (red), and $\alpha = 2$ (green) as a function of the number of particles N in the dot.

angle $\theta - \theta'$ where $r = r' = r_0$ with r_0 the radius where the probability density ρ is maximal. This path is shown for $\alpha = 2$ as the dashed blue circle in the contour plots of the pair-correlation functions shown in Figs. 3.12 – 3.17 for $N = 2, \ldots, 7$. Here, there are only four distinct curves since

$$g_{\downarrow\uparrow}(r, \theta; r', \theta') = g_{\uparrow\downarrow}(r', \theta'; r, \theta) = g_{\uparrow\downarrow}(r', \theta; r, \theta'), \tag{3.95}$$

where we used $g_{\sigma\sigma'}(\boldsymbol{r}, \boldsymbol{r}') = g_{\sigma'\sigma}(\boldsymbol{r}', \boldsymbol{r})$ in the first step and the circular symmetry of the quantum dot in the last step. In all cases, when α increases, we clearly see the crossover to the Wigner molecule where the particles are localized in a regular N-polygon. Note, however, that the Wigner molecule is rotating since the ground state has finite J. We found no shell formation which might occur for $N > 7$ [84]. In the noninteracting case, only shown for $N = 2$ and $N = 4$, we see that $g_{\uparrow\uparrow}$ dominates due to the spin polarization induced by the boundary. Consistent with the Pauli principle, $g_{\uparrow\uparrow}$ and $g_{\downarrow\downarrow}$ is zero for $\theta = \theta'$, while $g_{\uparrow\downarrow}$ and $g_{\downarrow\uparrow}$ can be nonzero as is the case for $N = 4$ and $\alpha = 0$. However, at finite α all correlation functions become zero for $\theta = \theta'$, indicating that the system is in the interacting regime. However, the spin-down correlations remain suppressed (liquidlike) even for $\alpha = 2$. Therefore, the system is characterized by a crossover to a spin-selective Wigner molecule. This is consistent with both the increase in spin polarization and the radial dependence of the spin-resolved density. Intuitively speaking, one of the effects of interactions in this system is to push the particles closer to

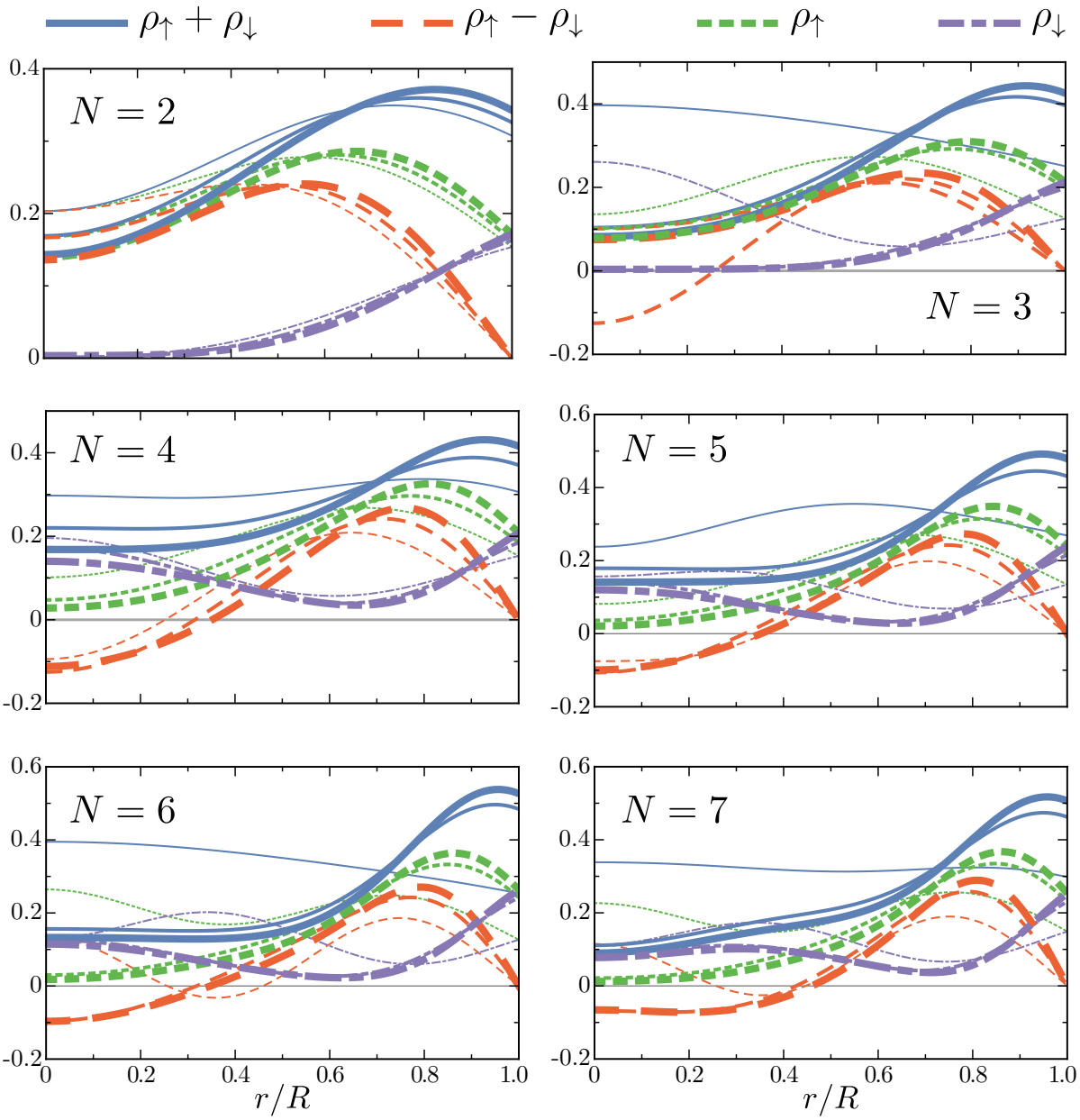

Figure 3.9: Spin-resolved probability densities $\rho_\sigma(r)$ together with the total charge and spin probability density $\rho(r)$ and $S_z(r)$ of the ground state of the few-particle infinite-mass dot for $N = 2, 3, \ldots, 7$ and $\alpha = 0$ (thin line), $\alpha = 1$ (medium thick line), and $\alpha = 2$ (thick line).

the boundaries to minimize the interaction energy. Particles that remain near the center when interactions are increased (the spin-down density in this case) do not minimize the interaction energy, and their spatial distribution and correlations are still mostly determined by kinetic energy and confinement. Hence, a more strongly polarized state is favored with increasing interaction strength. The emergence of the correlation peaks is shown in more detail in Fig. 3.10 where we show $g_{\sigma\sigma'}(\boldsymbol{r}, \boldsymbol{r}')$ as a function of r for $\theta = 2\pi/N$ with $\boldsymbol{r}'$ fixed at the maximum of the density with $r' = r_0$ and $\theta' = 0$. This path is shown as the dotted green line in Figs. 3.12 – 3.17. In this case, $g_{\uparrow\downarrow}$ and $g_{\downarrow\uparrow}$ are different in general, but cross at $r = r_0$. Furthermore, we see that $g_{\uparrow\uparrow}$ ($g_{\downarrow\downarrow}$) and $g_{\downarrow\uparrow}$ ($g_{\uparrow\downarrow}$) become equal at the boundary ($r = R$) which is a consequence of the infinite-mass boundary condition.

On the other hand, the formation of a spin-polarized state might be counterintuitive if we keep the infinite-mass boundary condition in mind. Indeed, for few particles in the dot, in the limit of very strong interactions, the particles will be localized almost entirely at the edge. Because of the infinite-mass boundary condition, however, the spin densities are equal at the edge, so that eventually the spin polarization should reduce again with increasing interaction strength. However, in reality, the mass barrier is finite and in the limit $\alpha \gg mR/(\hbar v_F)$, the particles will leak out of the quantum dot. The critical mass m is given by

$$m_c = \frac{\hbar v_F}{R}\alpha = \frac{e^2}{4\pi\epsilon R}, \tag{3.96}$$

where we restored $\hbar$. Since $m = g\mu_B B/2$ with g the g-factor of the topological surface state and μ_B the Bohr magneton, we find that the field B required to keep the particles confined in the presence of electron-electron interactions, should be of the order of

$$B_c = \frac{2\hbar v\alpha}{g\mu_B R} \approx 227 \times \frac{v\alpha}{gR}\ \mathrm{T}, \tag{3.97}$$

where R is given in units of 100 nm and v is given in units $10^6\ \mathrm{m\,s^{-1}}$. For Bi_2Se_3, we find $g \approx 18$ [92] and $v \approx 0.5 \times 10^6\ \mathrm{m\,s^{-1}}$ [28], so that

$$B_c \approx \frac{6.3\alpha}{R}\ \mathrm{T}. \tag{3.98}$$

for a quantum dot with radius R given in units of 100 nm.

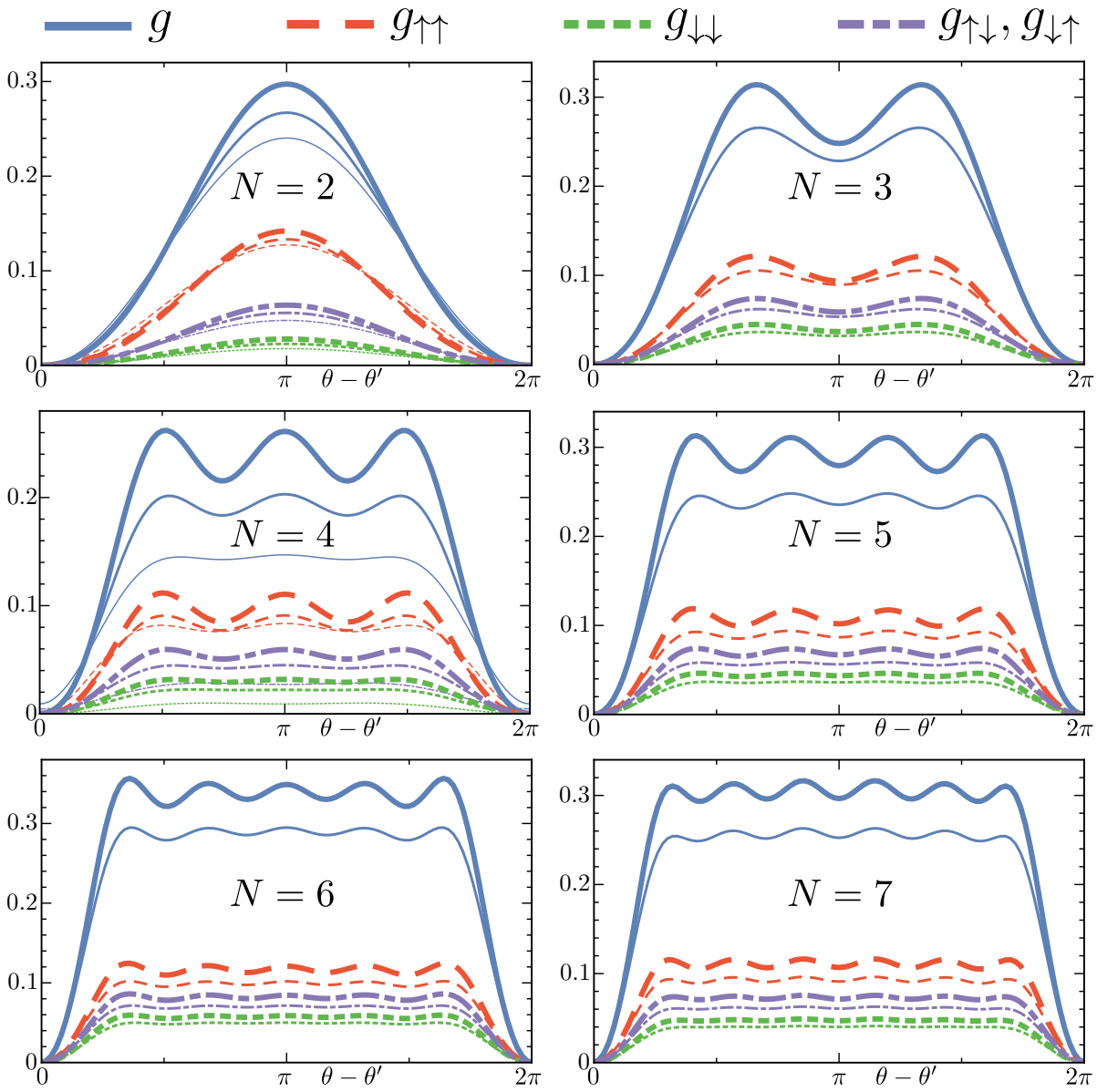

Figure 3.10: Pair-correlation functions $g_{\sigma\sigma'}(\boldsymbol{r}, \boldsymbol{r}')$ of the ground state of the few-particle infinite-mass dot for $N = 2, 3, \ldots, 7$ and $\alpha = 0$ (thin line), $\alpha = 1$ (medium thick line), and $\alpha = 2$ (thick line) as a function of $\theta - \theta'$ with $r = r' = r_0$ which corresponds to the maximum of $\rho(r)$. This path is shown for $\alpha = 2$ as the dashed blue circle in Figs. 3.12 – 3.17.

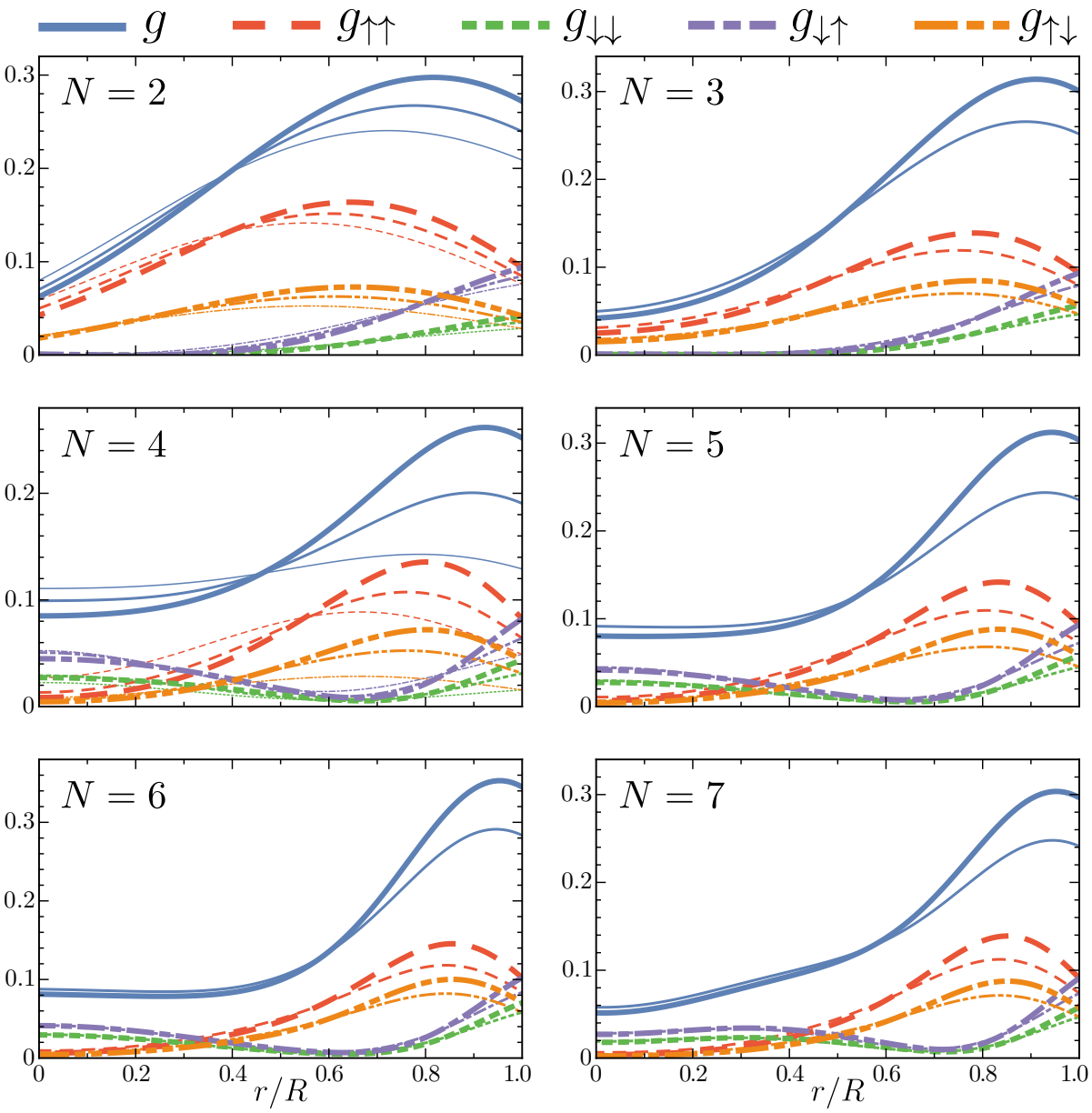

Figure 3.11: Pair-correlation functions $g_{\sigma\sigma'}(\boldsymbol{r}, \boldsymbol{r}')$ of the ground state of the few-particle infinite-mass dot for $N = 2, 3, \ldots, 7$ and $\alpha = 0$ (thin line), $\alpha = 1$ (medium thick line), and $\alpha = 2$ (thick line) as a function of r with $\theta = 2\pi/N$, $r' = r_0$, and $\theta' = 0$ where r_0 corresponds to the maximum of $\rho(r)$. This path is shown as the dotted green line in Figs. 3.12 – 3.17.

Wigner molecules

In Figs. 3.12 – 3.17, we show the pair-correlation functions $g_{\sigma\sigma'}(\boldsymbol{r}, \boldsymbol{r}')$ together with the total pair-correlation function $g(\boldsymbol{r}, \boldsymbol{r}')$ as a function of r and θ, where we have fixed $\boldsymbol{r}'$ at the maximum of the charge density, for $N = 2, \ldots, 7$, respectively. These figures are given for completeness and lead to the same conclusions as the above discussion.

Experiments

As far as the experimental observations of our predictions are concerned, different issues might arise. The realization of quantum dots on the surface of topological insulators remains a challenge but it should be possible in principle and the surface is readily accessible to experimental probes. For example, the spin polarization can be accessed by coupling the dot to spin-polarized local probes such as spin-resolved ARPES [93, 94]. On the other hand, since the Wigner molecule is rotating, there is an associated persistent current which produces a magnetic moment that can be detected with nitrogen-vacancy (NV) centers in diamonds or superconducting quantum interference devices (nanoSQUIDs) [95–97]. For example, for a dot with radius $R = 500$ nm, a classical finite-element calculation shows that the typical variations of the resulting magnetic field are of the order of 0.2 μT, which is measurable by both techniques [98]. In smaller dots, the signal, which scales as $1/R^2$, is larger, but in that case the required spatial resolution favors the use of NV centers.

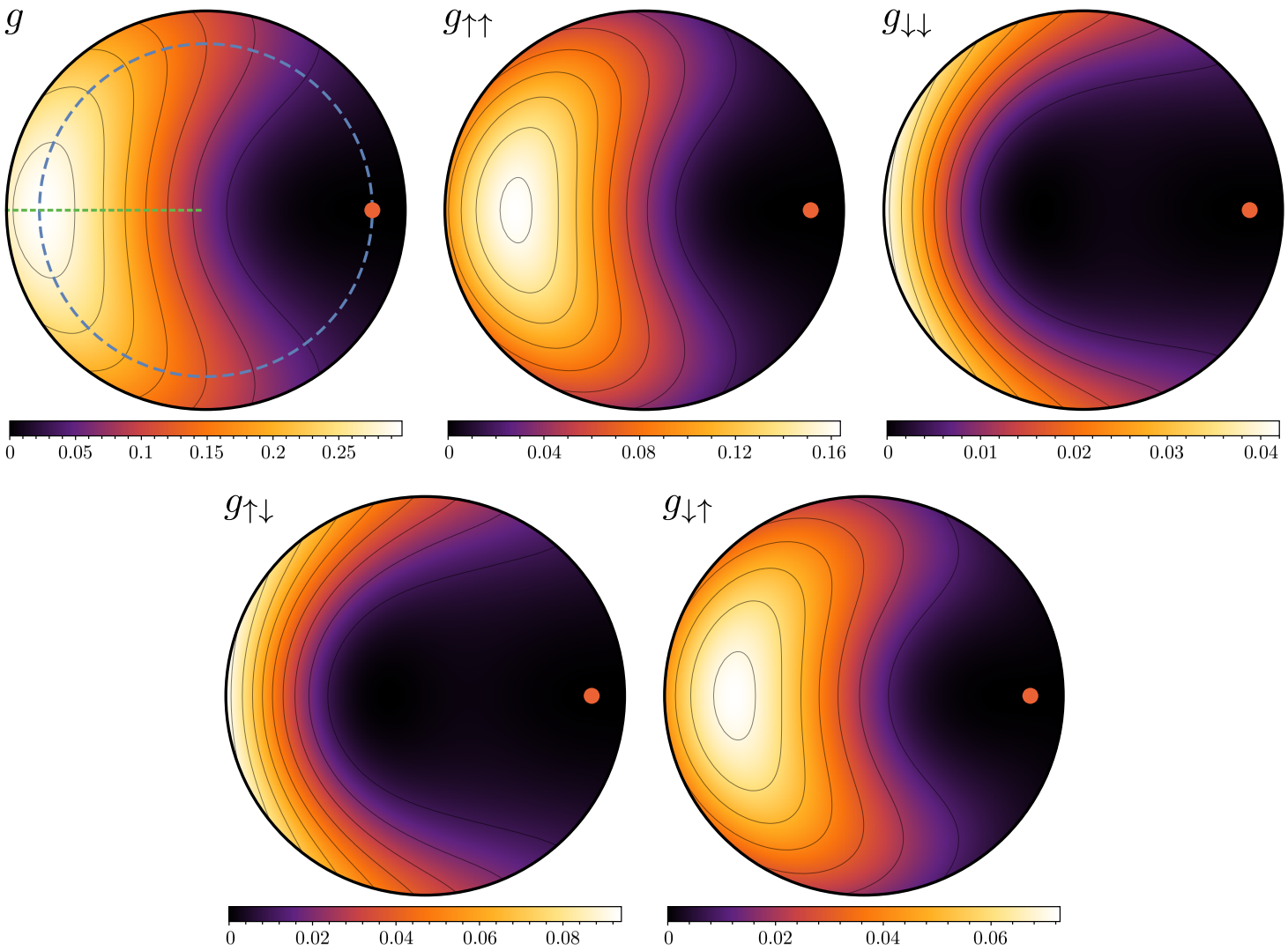

Figure 3.12: Pair-correlation functions $g_{\sigma\sigma'}(\boldsymbol{r}, \boldsymbol{r}')$ of the $N = 2$ infinite-mass dot for the ground state at $\alpha = 2$ ($J = 2$) as a function of $\boldsymbol{r}$. We have taken $\boldsymbol{r}' = (r_0, 0)$ which indicated with a red dot and where r_0 corresponds to the maximum of the total probability density $\rho(r)$.

Figure 3.13: Pair-correlation functions $g_{\sigma\sigma'}(\boldsymbol{r}, \boldsymbol{r}')$ of the $N = 3$ infinite-mass dot for the ground state at $\alpha = 2$ ($J = 4.5$) as a function of $\boldsymbol{r}$. We have taken $\boldsymbol{r}' = (r_0, 0)$ which indicated with a red dot and where r_0 corresponds to the maximum of the total probability density $\rho(r)$.

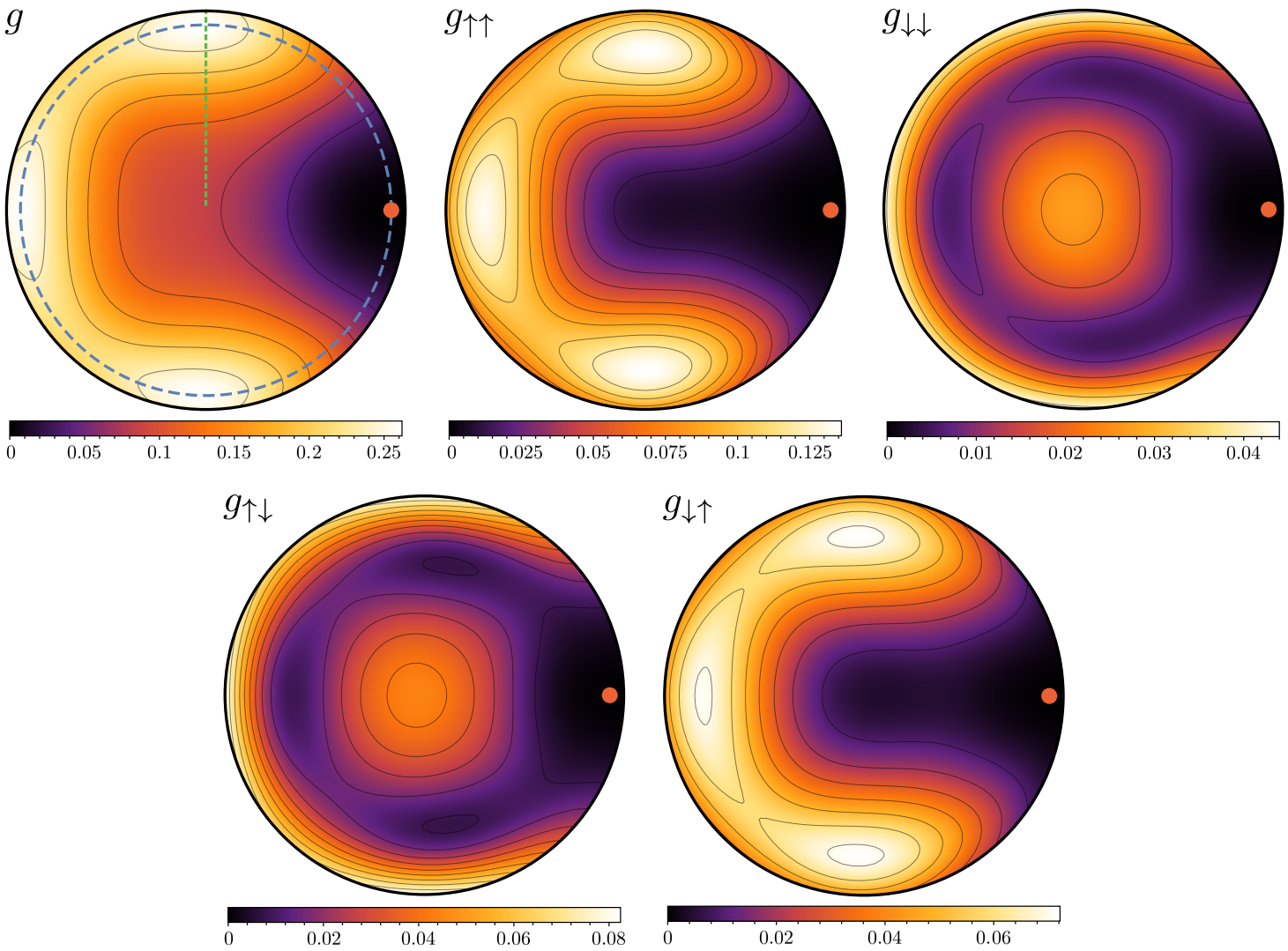

Figure 3.14: Pair-correlation functions $g_{\sigma\sigma'}(\boldsymbol{r}, \boldsymbol{r}')$ of the $N = 4$ infinite-mass dot for the ground state at $\alpha = 2$ ($J = 4$) as a function of $\boldsymbol{r}$. We have taken $\boldsymbol{r}' = (r_0, 0)$ which indicated with a red dot and where r_0 corresponds to the maximum of the total probability density $\rho(r)$.

Figure 3.15: Pair-correlation functions $g_{\sigma\sigma'}(\boldsymbol{r}, \boldsymbol{r}')$ of the $N = 5$ infinite-mass dot for the ground state at $\alpha = 2$ ($J = 7.5$) as a function of $\boldsymbol{r}$. We have taken $\boldsymbol{r}' = (r_0, 0)$ which indicated with a red dot and where r_0 corresponds to the maximum of the total probability density $\rho(r)$.

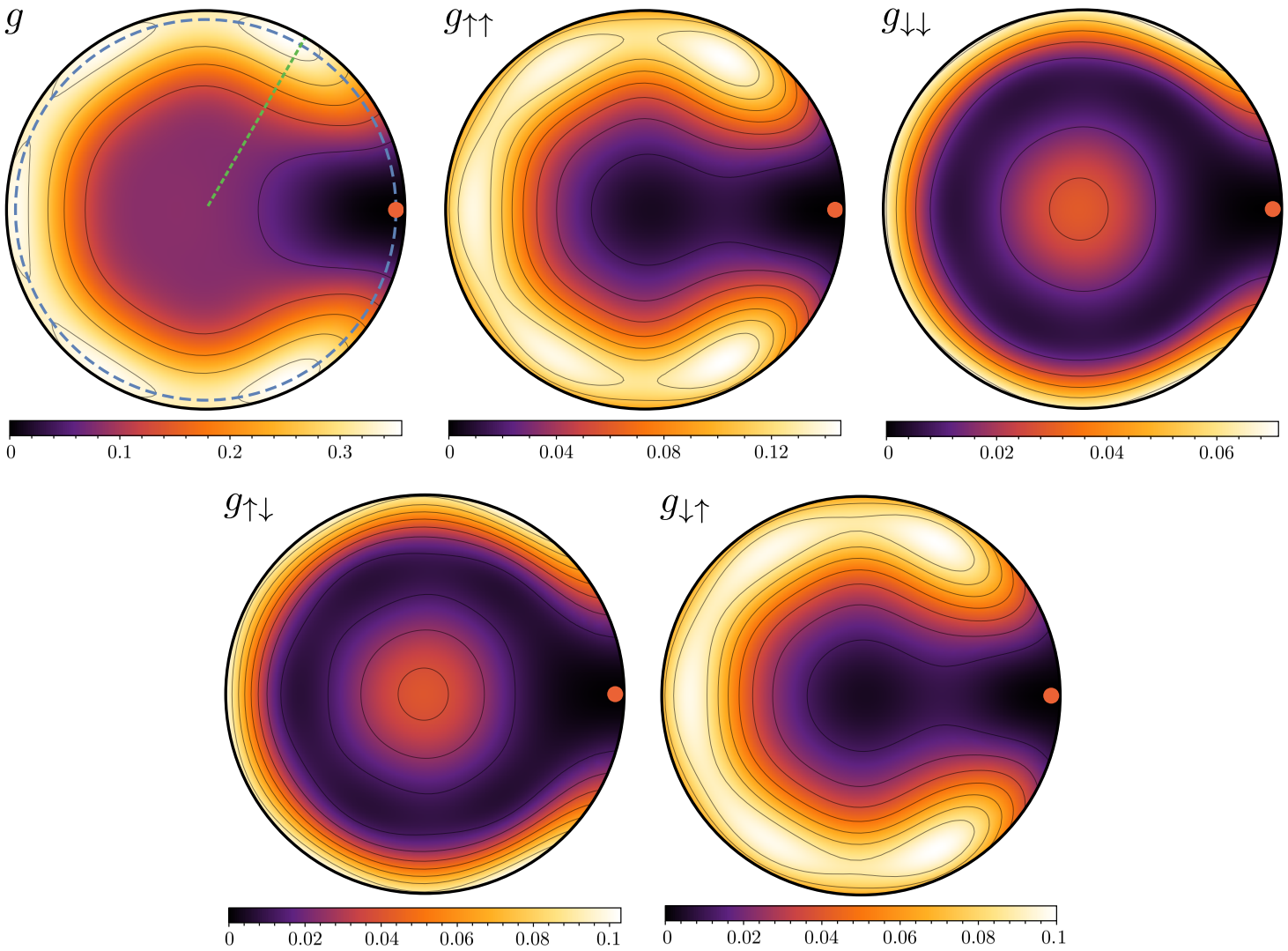

Figure 3.16: Pair-correlation functions $g_{\sigma\sigma'}(\boldsymbol{r}, \boldsymbol{r}')$ of the $N = 6$ infinite-mass dot for the ground state at $\alpha = 2$ ($J = 12$) as a function of $\boldsymbol{r}$. We have taken $\boldsymbol{r}' = (r_0, 0)$ which indicated with a red dot and where r_0 corresponds to the maximum of the total probability density $\rho(r)$.

Figure 3.17: Pair-correlation functions $g_{\sigma\sigma'}(\boldsymbol{r}, \boldsymbol{r}')$ of the $N = 7$ infinite-mass dot for the ground state at $\alpha = 2$ ($J = 10.5$) as a function of $\boldsymbol{r}$. We have taken $\boldsymbol{r}' = (r_0, 0)$ which indicated with a red dot and where r_0 corresponds to the maximum of the total probability density $\rho(r)$.

3.4 Summary

In this chapter, we studied quantum dots on the surface of a topological insulator where the surface state is confined with an insulating magnetic film that is deposited on the surface or with a cylindrical array of magnets. Specifically, we considered a system consisting of a disk of the bare surface surrounded by a magnetic field. This opens a magnetic gap on the surface everywhere except in the disk region which confines particles in the disk. The surface state was modeled with the Dirac Hamiltonian, derived in Chapter 2, where the magnetic field acts as a local exchange potential. First, we derived the general single-particle solution for a circular symmetric system and we obtained the hard-wall boundary conditions which couple the spin components and break time reversal. We then investigated the single-particle properties of the quantum dot as a function of the magnetization direction of the surrounding film. We found that the single-particle spectrum is characterized by a spin-polarized branch which evolves to a zero-energy branch when the magnetization direction lies in the surface plane. We also showed how the properties of the spectrum can be understood in terms of symmetries. We proceeded by including electron-electron interactions with the configuration-interaction method for which we explicitly calculated the matrix elements. Here, we assumed that all negative-energy states were filled and only considered interactions between positive-energy states. This approximation is justified as long as the interaction scale is smaller than the confinement gap. Besides the many-body spectrum, we calculated the spin-resolved densities and spin-resolved pair correlation functions of the ground state for up to seven fermions in the dot. The latter were used to study the crossover to a spin-polarized Wigner molecule with increasing interaction strength. During the crossover to the Wigner molecule, the majority spin crystallizes in a regular N-polygon localized near the edge while the minority spin remains liquidlike. This can be understood in terms of the occupation of the spin-polarized branch in the single-particle spectrum since it is energetically favorable for particles to occupy higher angular-momentum states. The crossover is thus accompanied with transitions of the ground state towards higher angular momentum.

4

Hybrid quantum dots

We investigate the properties of hybrid quantum dots on the surface of a strong 3D time-reversal invariant topological insulator. The system consists of an annulus region of the clean surface bounded by gapped regions. On the inside, the annulus is bounded by a region with proximity-induced superconductivity. For the outer region, we either consider a ferromagnetic insulator or another superconductor with a different superconducting phase. First, we derive the general solution for a system with circular symmetry and obtain the hard-wall boundary conditions at the inner and outer edge of the annulus. We calculate the spectrum and show that the quantum rings support robust Majorana bound states when half a flux quantum is threaded trough the inner region.

4.1 Motivation

It is well known that the surface of a strong 3D time-reversal invariant topological insulator (TI) in proximity to an ordinary s-wave superconductor can support Majorana bound states (MBSs). Similar to the $p_x + ip_y$ superconductor, each $h/(2e)$ vortex in the phase angle of the condensate wave function supports a MBS [44, 99]. Moreover, MBSs can also exist at the ends of line junctions by tuning the superconducting phase differences across the junctions which gives one possible way of adiabatically exchanging MBSs to exploit their non-abelian statistics for topological quantum computing [13, 45].

In this chapter, we investigate the interplay between confinement and MBSs. We consider two types of quantum rings on the surface of a topological insulator that can support either a chiral MBS or a Kramers pair of MBSs. We start by introducing the model for the surface states in the presence of both a ferromagnetic insulator and proximity-induced superconductivity.

4.2 Model

The Hamiltonian for the bare surface is given by

$$\hat{H}_0 = \int d^2r\, \hat{\psi}^\dagger(\boldsymbol{r}) \left[-i\hbar v_F \left(\boldsymbol{\sigma} \times \boldsymbol{e}_z\right) \cdot \nabla - \mu\right] \hat{\psi}(\boldsymbol{r}), \tag{4.1}$$

where $\hat{\psi} = (\hat{\psi}_\uparrow, \hat{\psi}_\downarrow)^t$, v_F is the Fermi velocity, $\boldsymbol{\sigma} = \sigma_x \boldsymbol{e}_x + \sigma_y \boldsymbol{e}_y$ are Pauli matrices, and μ is the chemical potential. The exchange coupling due to a ferromagnetic insulator deposited on the surface, can be written as

$$\hat{H}_M = \int d^2r\, \hat{\psi}^\dagger(\boldsymbol{r}) m(\boldsymbol{r}) \sigma_z \hat{\psi}(\boldsymbol{r}), \tag{4.2}$$

here m is the exchange potential. This term opens a gap on the surface by breaking time-reversal symmetry. The surface can also be gapped with a superconducting term which breaks particle number conservation because a Cooper pair of electrons can always be added or removed from the surface. However, the fermion number parity $(-1)^N$ is still conserved. If an s-wave superconductor is deposited on the surface, Cooper pairs can tunnel into the surface states and induce superconductivity [13]. This is called *proximity effect* and can be described with the mean-field Hamiltonian

$$\hat{H}_\Delta = \int d^2r \left[\Delta(\boldsymbol{r}) \hat{\psi}^\dagger_\uparrow(\boldsymbol{r}) \hat{\psi}^\dagger_\downarrow(\boldsymbol{r}) + \Delta(\boldsymbol{r})^* \hat{\psi}_\downarrow(\boldsymbol{r}) \hat{\psi}_\uparrow(\boldsymbol{r})\right], \tag{4.3}$$

where $\Delta = \Delta_0 e^{i\phi}$ is the pairing potential (order parameter) that is induced through the proximity effect with ϕ the superconducting phase. The microscopic details of Δ depend on the type of superconductor and the interface [100].

4.2.1 BdG Hamiltonian

The total Hamiltonian can be written as

$$\hat{H} = \hat{H}_0 + \hat{H}_M + \hat{H}_\Delta \tag{4.4}$$

$$= \frac{1}{2} \int d^2r\, \hat{\Psi}^\dagger\, \hat{\mathcal{H}}\, \hat{\Psi}, \tag{4.5}$$

with

$$\hat{\mathcal{H}} = \begin{bmatrix} \hat{\mathcal{H}}_0 + \hat{\mathcal{H}}_M & \Delta \\ \Delta^* & -\mathcal{T}(\hat{\mathcal{H}}_0 + \hat{\mathcal{H}}_M)\mathcal{T}^{-1} \end{bmatrix}, \tag{4.6}$$

in the Nambu basis $\hat{\Psi} = (\hat{\psi}_\uparrow, \hat{\psi}_\downarrow, \hat{\psi}^\dagger_\downarrow, -\hat{\psi}^\dagger_\uparrow)^t$ and where $\mathcal{T} = i\sigma_y \mathcal{K}$ is the time-reversal operator and $\mathcal{K}$ is complex conjugation. The matrix $\hat{\mathcal{H}}$ is called the *Bogoliubov-de Gennes*

(BdG) Hamiltonian. In this formalism, the pairing effectively acts as a coupling between electrons and holes. Since $\mathcal{T}\hat{\mathcal{H}}_0\mathcal{T}^{-1} = \hat{\mathcal{H}}_0$ and $\mathcal{T}\hat{\mathcal{H}}_M\mathcal{T}^{-1} = -\hat{\mathcal{H}}_M$, we find

$$\hat{\mathcal{H}} = \tau_z\left(-i\hbar v_F \boldsymbol{\sigma}\cdot\nabla - \mu\right) + m\sigma_z + \Delta_0\left(\tau_x\cos\phi - \tau_y\sin\phi\right), \tag{4.7}$$

where the Pauli matrices $\boldsymbol{\tau}$ act on the electron and hole degree of freedoms. Time reversal sends $\phi \to -\phi$ and is preserved only for $m = 0$.

The Hamiltonian is diagonalized with the transformation

$$\hat{\Psi} = \sum_n \psi_n \hat{\gamma}_n, \tag{4.8}$$

where ψ_n are the eigenstates of the BdG Hamiltonian with $\hat{\mathcal{H}}\psi_n = E_n\psi_n$ and $\hat{\gamma}_n$ are the quasiparticle operators. If we define $\psi_n = (u_n,\, i\sigma_y v_n)^t$ we can write

$$\hat{\gamma}_n^\dagger = \int d^2r\, \hat{\Psi}^\dagger\psi_n = \int d^2r\, (\hat{\psi}^\dagger u_n + v_n^t\hat{\psi}), \tag{4.9}$$

which are called Bogoliubov quasiparticles. Note that the quasiparticles consist of superpositions of electrons and holes. This expresses the fact that an excitation can be created by either adding or removing one electron from the condensate.

Particle-hole symmetry

In the Nambu basis, the degrees of freedom are artificially doubled in order to diagonalize the Hamiltonian. Hence, the BdG Hamiltonian has an inherent redundancy which is expressed in terms of the particle-hole symmetry,

$$\mathcal{C}\hat{\mathcal{H}}\mathcal{C}^{-1} = -\hat{\mathcal{H}}, \tag{4.10}$$

where $\mathcal{C} = \tau_y\sigma_y\mathcal{K}$ is the charge-conjugation operator. If ψ_n is an eigenstate of $\hat{\mathcal{H}}$ with energy E_n, then $\psi_{-n} \equiv \mathcal{C}\psi_n$ is also an eigenstate with energy $E_{-n} = -E_n$ so that the BdG spectrum is symmetric with respect to zero energy. Furthermore,

$$\begin{pmatrix} u_{-n} \\ v_{-n} \end{pmatrix} = \begin{pmatrix} v_n^* \\ u_n^* \end{pmatrix}, \tag{4.11}$$

and therefore

$$\hat{\gamma}_{-n}^\dagger = \int d^2r\, (\hat{\psi}^\dagger u_{-n} + v_{-n}^t\hat{\psi}) \tag{4.12}$$

$$= \int d^2r\, (\hat{\psi}^\dagger v_n^* + u_n^\dagger\hat{\psi}) = \hat{\gamma}_n, \tag{4.13}$$

so that creating a quasiparticle with energy E is the same as destroying a quasiparticle with energy $-E$. This prompts us to adopt the following interpretation. In the ground

state, which is given by the Cooper-pair condensate, all the quasiparticle states with negative energy are occupied. Indeed, the Hamiltonian can be written as

$$\hat{H} = \frac{1}{2}\sum_n E_n \hat{\gamma}_n^\dagger \hat{\gamma}_n = \sum_n{}' E_n \hat{\gamma}_n^\dagger \hat{\gamma}_n + E_g, \tag{4.14}$$

where $E_g = -\Sigma_n' E_n/2$ is the energy of the ground state and the primed sum runs only over states with positive energy.

Homogeneous pairing

In case the pairing potential Δ is constant in space, the spatial dependence is solved with a plane wave and the corresponding Bloch Hamiltonian is given by

$$\mathcal{H}(\boldsymbol{k}) = e^{-i\boldsymbol{k}\cdot\boldsymbol{r}}\hat{\mathcal{H}}e^{i\boldsymbol{k}\cdot\boldsymbol{r}}, \tag{4.15}$$

where particle-hole symmetry is now expressed as

$$\mathcal{C}\mathcal{H}(\boldsymbol{k})\mathcal{C}^{-1} = -\mathcal{H}(-\boldsymbol{k}). \tag{4.16}$$

Diagonalizing $\mathcal{H}(\boldsymbol{k})$ for $m = 0$ gives the quasiparticle excitation spectrum,

$$E_{\boldsymbol{k}\pm} = \sqrt{(v|\boldsymbol{k}| \pm \mu)^2 + \Delta_0^2}, \tag{4.17}$$

which is shown in Fig. 4.1 together with the excitation spectrum of a clean surface. The superconducting excitation gap Δ_0 opens at the surface Fermi surface which is given by a circle with radius $k_F = \mu/v_F$.

4.2.2 Wave equation

Here, we find the general solution of the BdG wave equation $\hat{\mathcal{H}}\psi = E\psi$ when the system has circular symmetry and we give the explicit solution for a free particle in polar coordinates. In the next section, we use the general solution to obtain the boundary conditions at the edges of the hybrid quantum dot.

General solution

In polar coordinates (r, θ) the BdG wave equation transforms into

$$\left[-iv_F\tau_z\left(\sigma_\theta\partial_r - \frac{1}{r}\sigma_r\partial_\theta\right) - \mu\tau_z + m\sigma_z + \Delta_0\left(\tau_x\cos\phi - \tau_y\sin\phi\right)\right]\psi = E\psi, \tag{4.18}$$

where we put $\hbar = 1$ and m, Δ_0, and ϕ can be functions of r but not of θ. In this case, the angular dependence of the wave function is solved with the *ansatz*

$$\psi_j(r,\theta) = e^{i\left(j-\frac{\sigma_z}{2}\right)\theta}\varphi_j(r), \tag{4.19}$$

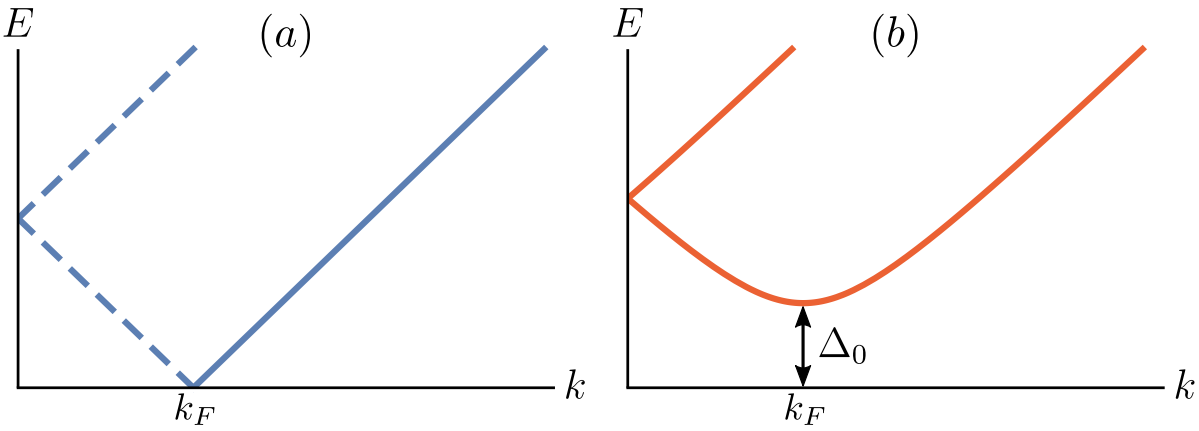

Figure 4.1: (a) Excitation spectrum of the clean TI surface where the dashed curves correspond to holes. (b) Excitation spectrum of the TI surface with proximity-induced superconductivity where the excitations are now superpositions of electrons and holes. In both cases, the chemical potential $\mu > 0$.

where $\varphi(r)$ is the radial part of the wave function. Because the wave function has to be single valued, we have $j = \pm\frac{1}{2}, \pm\frac{3}{2}, \ldots$ which is the total angular momentum quantum number. The radial Hamiltonian becomes

$$\hat{\mathcal{H}}(j) = e^{-i\left(j-\frac{\sigma_z}{2}\right)\theta}\hat{\mathcal{H}}e^{i\left(j-\frac{\sigma_z}{2}\right)\theta}, \tag{4.20}$$

and we have

$$\mathcal{C}\hat{\mathcal{H}}(j)\mathcal{C}^{-1} = -\hat{\mathcal{H}}(-j), \tag{4.21}$$

so that the charge-conjugated partners have opposite j. The remaining radial wave equation $\hat{\mathcal{H}}(j)\varphi_j = E\varphi_j$ is given by

$$\left[-iv_F\tau_z\left(\sigma_y\partial_r - \frac{i\sigma_x}{r}\left(j-\frac{\sigma_z}{2}\right)\right) - \mu\tau_z + m\sigma_z + \Delta_0\left(\tau_x\cos\phi - \tau_y\sin\phi\right)\right]\varphi_j = E\varphi_j. \tag{4.22}$$

Similar to Eq. (3.22) of Chapter 3, the general solution becomes

$$\varphi_j(r) = \mathcal{S}\exp\left\{\frac{1}{v_F}\int_{r_0}^{r}dr'\left[\frac{v_F}{r'}\left(j\sigma_z - \frac{1}{2}\right) + \left[E\tau_z + \mu(r')\right]i\sigma_y + m(r')\tau_z\sigma_x \right.\right. \\ \left.\left. + \Delta_0(r')\left[\tau_y\cos\phi(r') + \tau_x\sin\phi(r')\right]\sigma_y\right]\right\}\varphi_j(r_0), \tag{4.23}$$

where $\mathcal{S}$ is the path-ordering operator.

Free particle

The solution for a free particle ($\Delta = m = 0$) in polar coordinates can be obtained in the same way as in Chapter 3. The radial spinor can be written as

$$\varphi_j = \begin{pmatrix} u_j \\ i\sigma_y v_j \end{pmatrix}, \tag{4.24}$$

where u_j and v_j are the electron and hole spinors which are given by

$$u_j = \begin{pmatrix} u_{j-1/2} \\ -u_{j+1/2} \end{pmatrix}, \qquad v_j = \begin{pmatrix} -v_{j+1/2} \\ v_{j-1/2} \end{pmatrix}, \tag{4.25}$$

with

$$u_{j\pm1/2}(r) = a\, J_{j\pm1/2}\left[(k+k_F)\, r\right] + b\, Y_{j\pm1/2}\left[(k+k_F)\, r\right], \tag{4.26}$$
$$v_{j\pm1/2}(r) = c\, J_{j\pm1/2}\left[(k-k_F)\, r\right] + d\, Y_{j\pm1/2}\left[(k-k_F)\, r\right], \tag{4.27}$$

where $k = E/v_F$ and $k_F = \mu/v_F$. Here J and Y are Bessel functions of the first and second kind, respectively, and a, b, c, and d are constants. We note that this solution is not valid for $k = \pm k_F$. However, in this case the solution can be obtained by expanding the above solutions up to lowest order in $k \pm k_F$.

4.3 Hybrid quantum dots

We consider two types of hybrid quantum dots which are illustrated in Fig. 4.2. Both systems consist out of an annulus region ($R_o < r < R_i$) on the clean surface of the topological insulator, bounded by gapped regions due to either the exchange coupling of a magnetic insulator film or proximity-induced superconductivity. The first type, shown in Fig. 4.2 (a), is an annulus bounded by an s-wave superconductor on the inside and a magnetic insulator on the outside. The second type consists of an annulus bounded by two superconducting regions that have a phase difference $\Delta\phi = \phi_o - \phi_i$. In the region with a magnetic or superconducting gap, the wave function of the surface state decays with characteristic length v_F/m and v_F/Δ_0, respectively. Hence, the surface state is confined within the annulus for energies that lie within the gaps. In the limit where the decay length is much smaller than the radius of the quantum dot, it is a good approximation to send both m and Δ_0 to infinity. These boundary conditions are called the infinite mass and infinite pairing boundary condition, respectively. In this case, the problem is simplified since the wave function vanishes immediately inside the gapped region and we only need to consider the solution inside the annulus.

Here, we first derive these boundary conditions from the general solution (4.23) and implement them for our two systems. We subsequently obtain the Andreev bound states

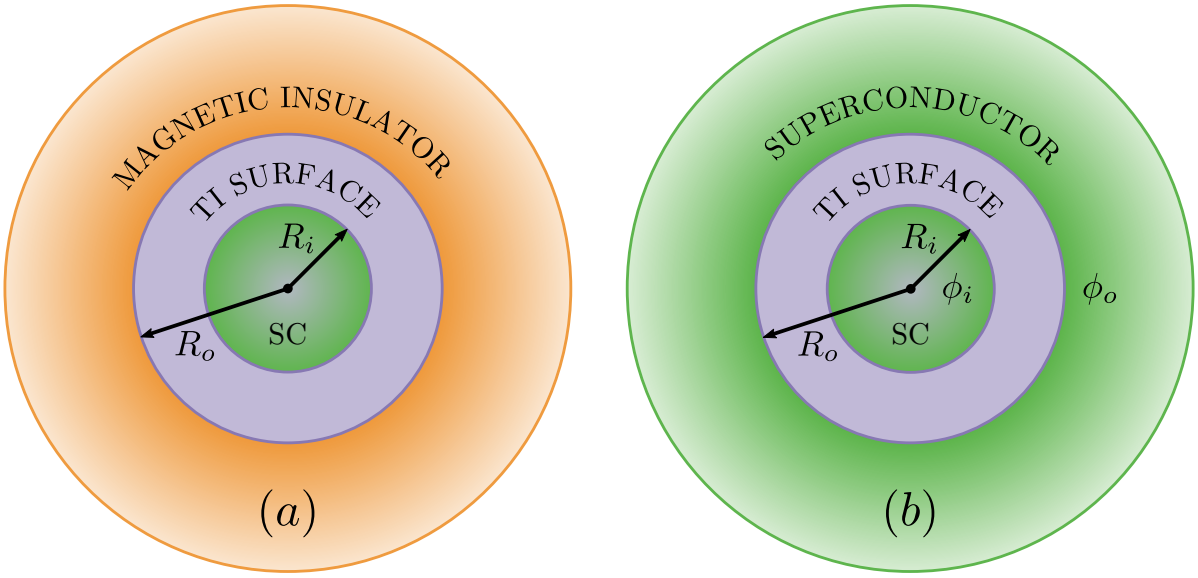

Figure 4.2: Top view of the hybrid quantum rings. (a) Annulus with a superconductor (SC) inside and a ferromagnetic insulator outside. (b) Annulus with both a superconductor inside and outside with a phase difference $\Delta\phi = \phi_i - \phi_o$.

of the hybrid quantum rings. Moreover, when the inner superconductor contains an odd number of $h/(2e)$ vortices, we obtain either a chiral Majorana bound state or a Kramers pair of helical Majorana bound states that are delocalized over the annulus.

4.3.1 Infinite mass boundary

Consider a circular delta barrier

$$m(r) = v_F m_0 \, \delta\left(r - R\right), \tag{4.28}$$

where m_0 controls the height of the barrier. In case Δ and μ are smooth at $r = R$, the boundary condition at the barrier can be found from plugging (4.28) in the general solution (4.23) with $r_0 = R_-$ and $r = R_+$ where $R_\pm = R \pm \epsilon$. In the limit $\epsilon \to 0$, we find

$$\varphi(R_+) = \exp\left(m_0 \tau_z \sigma_x\right) \varphi(R_-) \tag{4.29}$$

$$= \left(\cosh m_0 + \tau_z \sigma_x \sinh m_0\right) \varphi(R_-). \tag{4.30}$$

We can now obtain the infinite-mass boundary condition by first dividing both sides with the hyperbolic cosine and taking the limit $m_0 \to \infty$. This gives

$$\left(1 \pm \tau_z \sigma_x\right) \varphi(R_\mp) = 0, \tag{4.31}$$

where $\pm$ corresponds to the outer and inner region, respectively. These equations are linearly dependent, so in the end we obtain only two separate equations for the electron

and hole components at the edge:

$$u_\uparrow \pm u_\downarrow|_{edge} = 0, \qquad v_\uparrow \mp v_\downarrow|_{edge} = 0. \tag{4.32}$$

4.3.2 Infinite pairing boundary

If we perform the same calculation for the pairing barrier

$$\Delta_0(r) = v_F \Delta_0 \, \delta\left(r - R\right), \tag{4.33}$$

we find

$$\begin{aligned} \varphi(R_+) &= \exp\left[\Delta_0 \left(\tau_y \cos\phi + \tau_x \sin\phi\right) \sigma_y\right] \varphi(R_-) && (4.34)\\ &= \left[\cosh\Delta_0 + \left(\tau_y \cos\phi + \tau_x \sin\phi\right) \sigma_y \sinh\Delta_0\right] \varphi(R_-). && (4.35) \end{aligned}$$

In the limit $\Delta_0 \to \infty$, we obtain the infinite-pairing boundary condition

$$\left[1 \pm \left(\tau_y \cos\phi + \tau_x \sin\phi\right) \sigma_y\right] \varphi(R_\mp) = 0, \tag{4.36}$$

where $\pm$ corresponds to the outer and inner region, respectively. In terms of the electron and hole components u and v, which are defined by $\varphi = (u,\, i\sigma_y v)^t$, the infinite-pairing boundary condition becomes

$$u \pm e^{i\phi} v\big|_{edge} = 0. \tag{4.37}$$

We see that the electron and hole components are coupled. Physically, this boundary condition expresses that electrons are perfectly Andreev reflected at the boundary.

4.4 Results

In this section, we implement the hard-wall boundary conditions that we derived above for the two systems shown in Fig. 4.2. We present our results for several values of the chemical potential μ, the ratio between the inner and outer radius $\lambda = R_i/R_0$, and the phase difference $\Delta\phi$ for the annulus bounded by two superconductors. We show the spectrum of the Andreev bound states together with the average charge

$$\langle\psi|\, \tau_z \,|\psi\rangle = \langle u|u\rangle - \langle v|v\rangle, \tag{4.38}$$

and the average spin

$$\begin{aligned} \langle\psi|\, S_r \,|\psi\rangle &= \frac{\hbar}{2} \left(\langle u|\, \sigma_x \,|u\rangle - \langle v|\, \sigma_x \,|v\rangle\right), && (4.39)\\ \langle\psi|\, S_\theta \,|\psi\rangle &= 0, && (4.40)\\ \langle\psi|\, S_z \,|\psi\rangle &= \frac{\hbar}{2} \left(\langle u|\, \sigma_z \,|u\rangle - \langle v|\, \sigma_z \,|v\rangle\right), && (4.41) \end{aligned}$$

where $S_r = \boldsymbol{S}\cdot\boldsymbol{e}_r = S_x\cos\theta + S_y\sin\theta$ and we restored $\hbar$. For example,

$$\langle\psi|\, S_r\,|\psi\rangle = \frac{\hbar}{2}\int_{annulus} d^2r\,\varphi^\dagger(r)\left[e^{-i\left(j-\frac{\sigma_z}{2}\right)\theta}\sigma_r e^{i\left(j-\frac{\sigma_z}{2}\right)\theta}\right]\varphi(r) \tag{4.42}$$

$$= \frac{\hbar}{2}\langle\varphi|\,\sigma_x\,|\varphi\rangle \tag{4.43}$$

$$= \frac{\hbar}{2}\left(\langle u|\,\sigma_x\,|u\rangle - \langle v|\,\sigma_x\,|v\rangle\right). \tag{4.44}$$

These observables are opposite for charge conjugates since $\mathcal{C}^\dagger\tau_z\mathcal{C} = -\tau_z$ and $\mathcal{C}^\dagger S_{r,z}\mathcal{C} = -S_{r,z}$. Furthermore, in case $\mu = 0$, the BdG Hamiltonian (4.7) has an extra symmetry given by $(\tau_x\cos\phi - \tau_y\sin\phi)\,\sigma_z$. In this case, and in the absence of any accidental degeneracy, we find

$$\begin{pmatrix} u \\ v \end{pmatrix} \propto \begin{pmatrix} \sigma_x v \\ \sigma_x u \end{pmatrix}, \tag{4.45}$$

so that $\langle\tau_z\rangle = \langle S_r\rangle = 0$ for $\mu = 0$. Hence, we always consider $\mu > 0$ since this symmetry connects solutions at μ and $-\mu$.

The energy is always given with respect to the chemical potential μ and all energies are given in units of $\hbar v_F/R_o$. For Bi_2Se_3, we can assume $\hbar v_F \approx 330$ nm meV so that the energy scale ranges between 33 meV and 3 meV for R_o between 10 nm and 100 nm. This is well within the bulk energy gap, where the surface states reside, which is approximately 300 meV for Bi_2Se_3 [28].

4.4.1 Chiral annulus

First, we consider the quantum ring, shown in Fig. 4.2 (a), that is bounded by a ferromagnetic insulator on the outside and a superconductor on the inside. Using (4.32) together with (4.25) we obtain the boundary conditions for the outer edge:

$$\begin{bmatrix} J_{j+1/2} - J_{j-1/2} & 0 \\ 0 & Y_{j+1/2} - Y_{j-1/2} \end{bmatrix}^+ \begin{bmatrix} a \\ b \end{bmatrix} = 0, \tag{4.46}$$

$$\begin{bmatrix} J_{j+1/2} + J_{j-1/2} & 0 \\ 0 & Y_{j+1/2} + Y_{j-1/2} \end{bmatrix}^- \begin{bmatrix} c \\ d \end{bmatrix} = 0, \tag{4.47}$$

where the $+$ and $-$ indicate that the functions are evaluated at $(k \pm k_F)\,R_o$. Similarly, using (4.37), we obtain the boundary condition at the inner edge:

$$\begin{bmatrix} J^+_{j-1/2} & Y^+_{j-1/2} & J^-_{j+1/2} & Y^-_{j+1/2} \\ J^+_{j+1/2} & Y^+_{j+1/2} & J^-_{j-1/2} & Y^-_{j-1/2} \end{bmatrix} \begin{bmatrix} a \\ b \\ c \\ d \end{bmatrix} = 0, \tag{4.48}$$

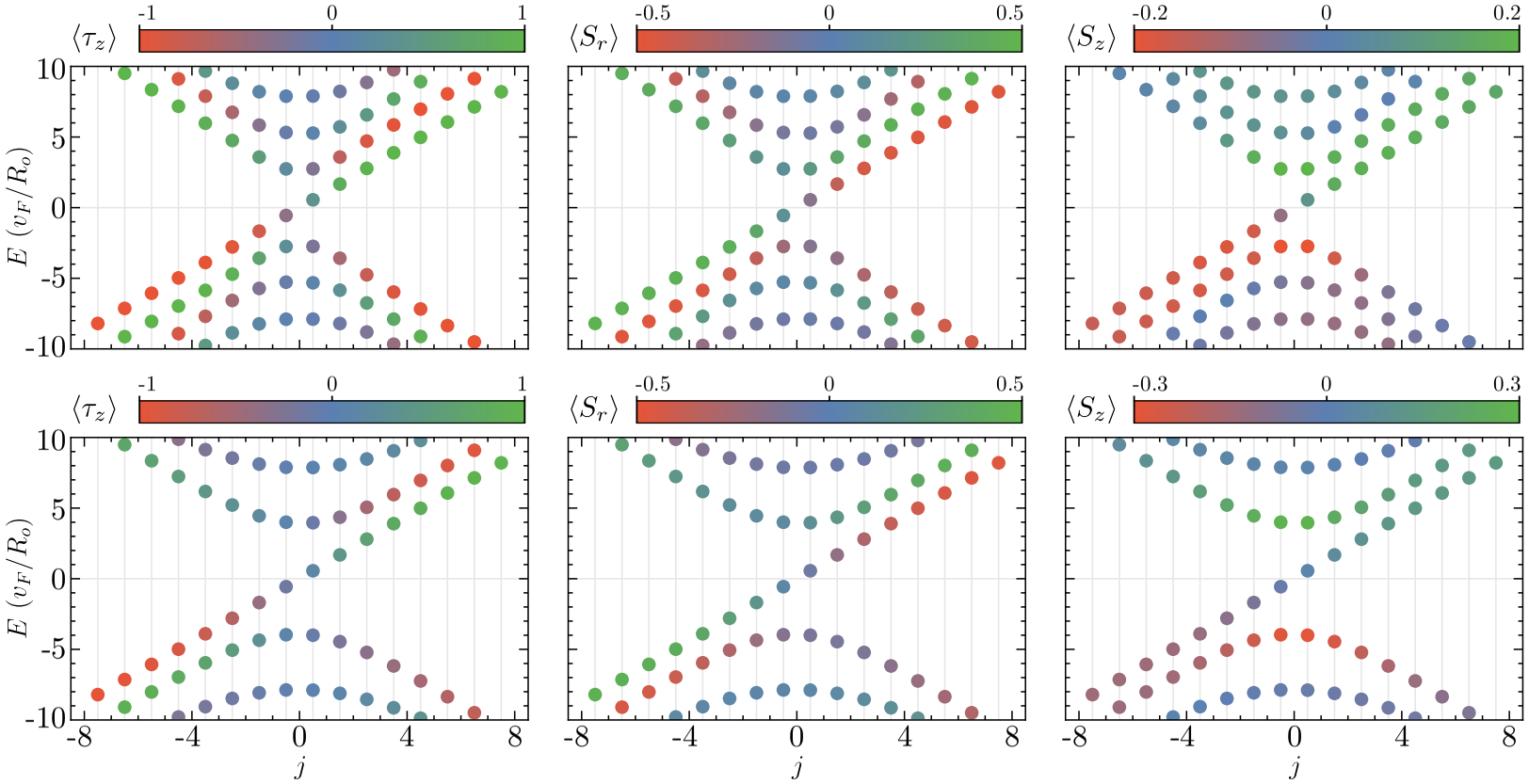

Figure 4.3: Spectrum of the hybrid quantum ring bounded by an infinite mass gap on the outside and an infinite pairing gap on the inside for $\mu = 1$ with $\lambda = 0.4$ (top row) and $\lambda = 0.6$ (bottom row). The color gives the expectation values of the charge (left column), the radial spin S_r (middle column), and the normal spin S_z (right column) where the latter two are given in units $\hbar$.

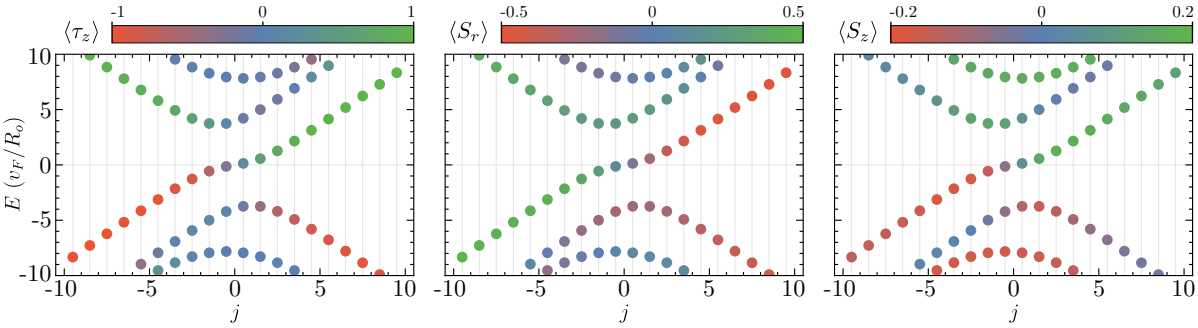

Figure 4.4: Spectrum of the annulus bounded by an infinite mass gap on the outside and an infinite pairing gap on the inside for $\lambda = 0.6$ and $\mu = 3$. The color gives the expectation value of the charge in (a) and spin S_z (in units $\hbar$) in (b).

where now the $+$ and $-$ indicate that the functions are evaluated at $(k \pm k_F)\, R_i$. We have set the superconducting phase to zero since we only have one superconductor for this system and a global phase can be gauged away.

In Fig. 4.3, we show the spectrum of the Andreev bound states for $\mu = 1$ and $\lambda = 0.4$ and 0.6. From the average charge $\langle \tau_z \rangle$, we see that there is an alternation between electronlike and holelike bands and that states for small j become more mixed as the energy increases. This can be understood as follows. Roughly speaking, the spectrum resembles the excitation spectrum of the infinite-mass dot. In this case, the hole states are mapped very close to the electron states, leading to a much stronger coupling between them. Furthermore, we find that the radial projection of the spin $\langle S_r \rangle$ remains correlated with j and that the helicity is opposite for electronlike and holelike bands. Nevertheless, we see that the bound states have a finite $\langle S_z \rangle$ induced by the boundary with the ferromagnetic insulator which breaks time reversal, i.e. it is not locked to the momentum.

In both cases with different λ, there is a single gapless chiral branch independent of the width. On the other hand, the energy of the other bound states increases as the width is reduced as expected for confined states. The existence of this chiral mode is topologically protected. Remember that the annulus acts as a domain wall between two regions with a different gap. If we start from the magnetic insulator on the outer side and move towards the superconductor, the magnetic gap has to close and reopen as a superconducting gap. Since there is no way around this gap closing, there exist gapless modes at the boundary. Importantly, in the topological insulator case, there will be an odd amount of such modes. However, because we have put the system on a ring, the energy levels are now discrete. Consequently, the existence of the chiral mode is also insensitive to μ. This is illustrated in Fig. 4.4 where we show our results for $\lambda = 0.6$ and $\mu = 3$. We see that μ only modifies the group velocity of the chiral branch.

However, because a Majorana bound states (MBS) is its own charge conjugate, the lowest-energy bound state is not a MBS since it has finite energy, j, charge, and spin.

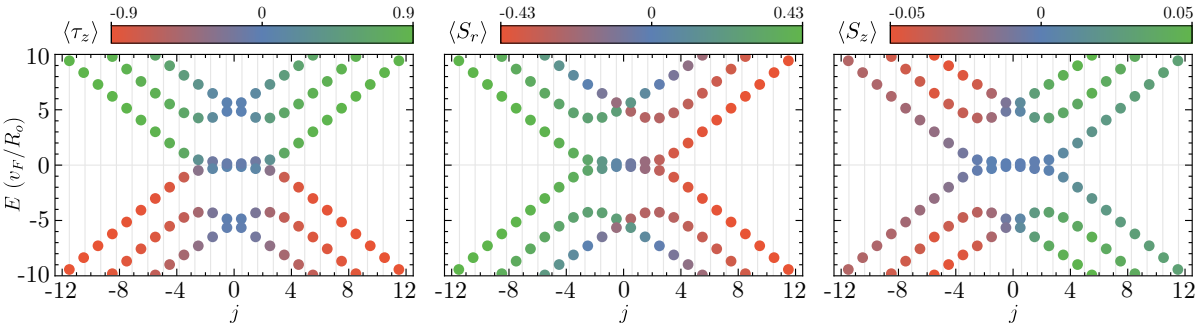

Figure 4.5: Spectrum of the hybrid quantum ring bounded by an infinite pairing gap on the inside and outside with $\Delta\phi = \pi$ for $\lambda = 0.4$ and $\mu = 6$. The color gives the expectation value of the charge (left), radial spin (middle) and normal spin (right) where the latter two are given in units $\hbar$.

4.4.2 Helical annulus

We now consider an annulus bounded by a superconductor on the outside and a superconductor on the inside. This system is illustrated in Fig. 4.2 (b). We set the global phase so that $\phi_i = 0$ and therefore the phase difference between the superconductors is given by $\Delta\phi = \phi_o$. The boundary condition for the inner edge is the same as before and the for the outer edge, we find

$$\begin{bmatrix} J^+_{j-1/2} & Y^+_{j-1/2} & -e^{i\Delta\phi}J^-_{j+1/2} & -e^{i\Delta\phi}Y^-_{j+1/2} \\ J^+_{j+1/2} & Y^+_{j+1/2} & -e^{i\Delta\phi}J^-_{j-1/2} & -e^{i\Delta\phi}Y^-_{j-1/2} \end{bmatrix} \begin{bmatrix} a \\ b \\ c \\ d \end{bmatrix} = 0, \tag{4.49}$$

where here the $+$ and $-$ indicate that the functions are evaluated at $(k \pm k_F)\, R_o$.

The spectrum of the annulus is shown in Fig. 4.5 for $\Delta\phi = \pi$, $\lambda = 0.4$, and $\mu = 6$. We see that the spectrum is symmetric with respect to $j \to -j$ because the infinite pairing boundary condition (4.37) does not break TR symmetry for $\phi = 0, \pi$: If $\psi(\phi)$ obeys the boundary condition then $\mathcal{T}\psi(-\phi)$ also obeys it. Consequently, the bound states are spin-momentum locked because even though they have a finite $\langle S_z \rangle$, it is opposite for opposite j. This can also been seen from

$$\begin{aligned} \langle \psi_j | \, S_{r,z} \, | \psi_j \rangle &= \langle \mathcal{T} S_{r,z} \psi_j | \mathcal{T} \psi_j \rangle & (4.50) \\ &= \langle \mathcal{T} S_{r,z} \mathcal{T}^{-1} \mathcal{T} \psi_j | \mathcal{T} \psi_j \rangle & (4.51) \\ &= - \langle \psi_{-j} | \, S_{r,z} \, | \psi_{-j} \rangle \, , & (4.52) \end{aligned}$$

where we used the antiunitary property of $\mathcal{T}$ and $|\psi_{-j}\rangle \propto \mathcal{T}\,|\psi_j\rangle$ for $\phi = 0, \pi$. For this choice of μ, the helical Majorana mode has a very flat dispersion for $|j| < 4$. The helical Majorana mode is only stable for $\Delta\phi = \pi$ since in this case the change of the nature

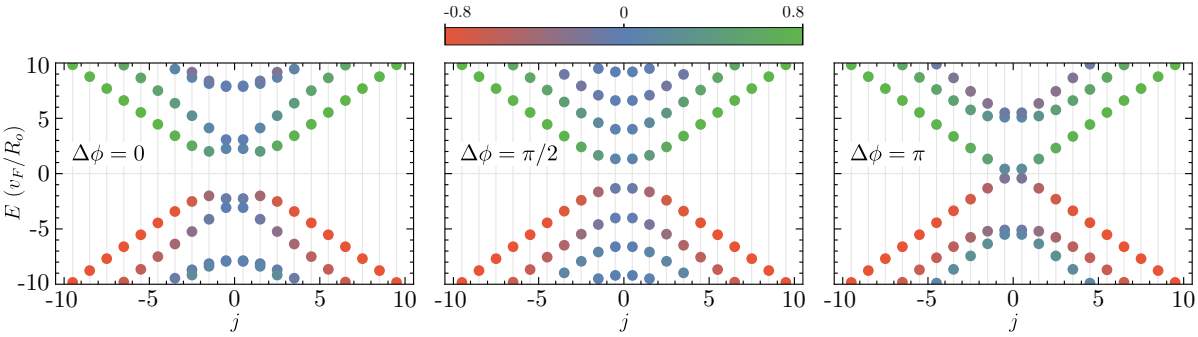

Figure 4.6: Spectrum of the hybrid quantum ring bounded by an infinite pairing gap on the inside and outside with $\lambda = 0.4$ and $\mu = 3$ for $\Delta\phi = 0$, $\pi/2$, and π. The color gives the expectation value of the charge.

of the pairing gap over the annulus is accompanied with a Kramers theorem. This is illustrated in Fig. 4.5 where we show the bound-state spectrum of a quantum ring with $\lambda = 0.4$ and $\mu = 3$ for $\Delta\phi = 0$, $\pi/2$, and π.

4.5 Majorana bound states

In the results that we have shown until now, there are no zero-energy bound states and hence no Majorana bound states. This can be understood as follows. If we put a chiral or helical Majorana mode on a circle with radius R, the wave function picks up a minus sign if we go around the circle because it picks up a π Berry phase inherited from the topological surface state. Equivalently, the spin is rotated by 2π if you go around a circle giving a minus sign. Hence, the boundary condition becomes *antiperiodic* which gives $k = j/R$ where j is half-integer. However, if we thread half a flux quantum $\Phi = \Phi_0/2$ through the circle there is an additional Aharanov-Bohm phase of π which cancels the π Berry phase [101]. This can be achieved if the inner superconductor is a type-II superconductor with a single $h/(2e)$ vortex.

4.5.1 Flux threading

We now consider threading a flux Φ through the inner region of the hybrid quantum rings. Outside of the inner region, the vector potential is given by

$$\boldsymbol{A}(r) = \frac{\Phi}{2\pi r}\boldsymbol{e}_\theta, \tag{4.53}$$

where

$$\Phi = \int_{inner\ disk} \boldsymbol{B} \cdot d\boldsymbol{a}, \tag{4.54}$$

is the flux through the inner disk. In this case, the flux only corresponds to a gauge transformation. Hence, the eigenstates and the pairing potential are transformed as

$$\psi(\boldsymbol{r}) \to \exp\left[-i\tau_z\left(\Phi/\Phi_0\right)\theta\right]\psi(\boldsymbol{r}), \tag{4.55}$$

$$\Delta(\boldsymbol{r}) \to \exp\left[-i2\left(\Phi/\Phi_0\right)\theta\right]\Delta(\boldsymbol{r}), \tag{4.56}$$

where $\Phi_0 = h/e$ is the flux quantum. Because the pairing potential has to be single valued, the flux in the inner superconductor has to be quantized in units $\Phi_0/2$ which correspond to $h/(2e)$ vortices. We now consider the case when there are an odd number of $h/(2e)$ vortices in the inner superconductor. The only thing that has changed is that the single valuedness of the wave function now demands that j is an integer. So we find that we can effectively change the boundary condition around the ring with the number parity of $h/(2e)$ vortices in the inner region of the annulus.

Note that threading half a flux quantum does not break TR symmetry. This is because $-\Phi_0/2$ is equivalent to $\Phi_0/2$ up to a flux quantum which can be gauged away since it only amounts to a relabelling of j.

4.5.2 Majorana bound states

In Fig. 4.7, we show our results for the hybrid quantum dots which have a single $h/(2e)$ vortex in the inner superconductor. As we discussed above, the flux changes the quantization condition from half-integer to integer j. For the chiral annulus, we obtain a single chiral Majorana bound state (MBS). Because MBSs always come in pairs as they constitute a nonlocal fermion, the other MBS is trapped at the vortex core. We can see that the chiral MBS has zero energy, j, charge, and spin. On the other hand, for the helical annulus, we obtain a Kramers pair of helical MBSs for $\Delta\phi = \pi$. As long as time-reversal symmetry is preserved, the helical MBSs are stable and cannot hybridize. In case $\Delta\phi \neq \pi$ they will hybridize and move away from zero energy in opposite directions.

We also show the spin-resolved electron densities of the MBSs in Fig. 4.8. The densities of the hole component are not shown since the electron and hole wave functions of MBSs are identical up to a phase. Consequently, particle-hole symmetry (see Section 4.2.1) now gives

$$\hat{\gamma}_0^\dagger = \int d^2r\,(\hat{\psi}^\dagger u_0 + v_0^t\hat{\psi}) \tag{4.57}$$

$$= \int d^2r\,(\hat{\psi}^\dagger v_0^* + u_0^\dagger\hat{\psi}) = \hat{\gamma}_0, \tag{4.58}$$

so that Majorana bound states can be viewed as excitations that are equal to their own anti-particle. Two Majoranas can then be paired into a fermion as follows:

$$\hat{c} = \frac{1}{2}\left(\hat{\gamma}_0^{(1)} + i\,\hat{\gamma}_0^{(2)}\right), \qquad \hat{c}^\dagger = \frac{1}{2}\left(\hat{\gamma}_0^{(1)} - i\,\hat{\gamma}_0^{(2)}\right). \tag{4.59}$$

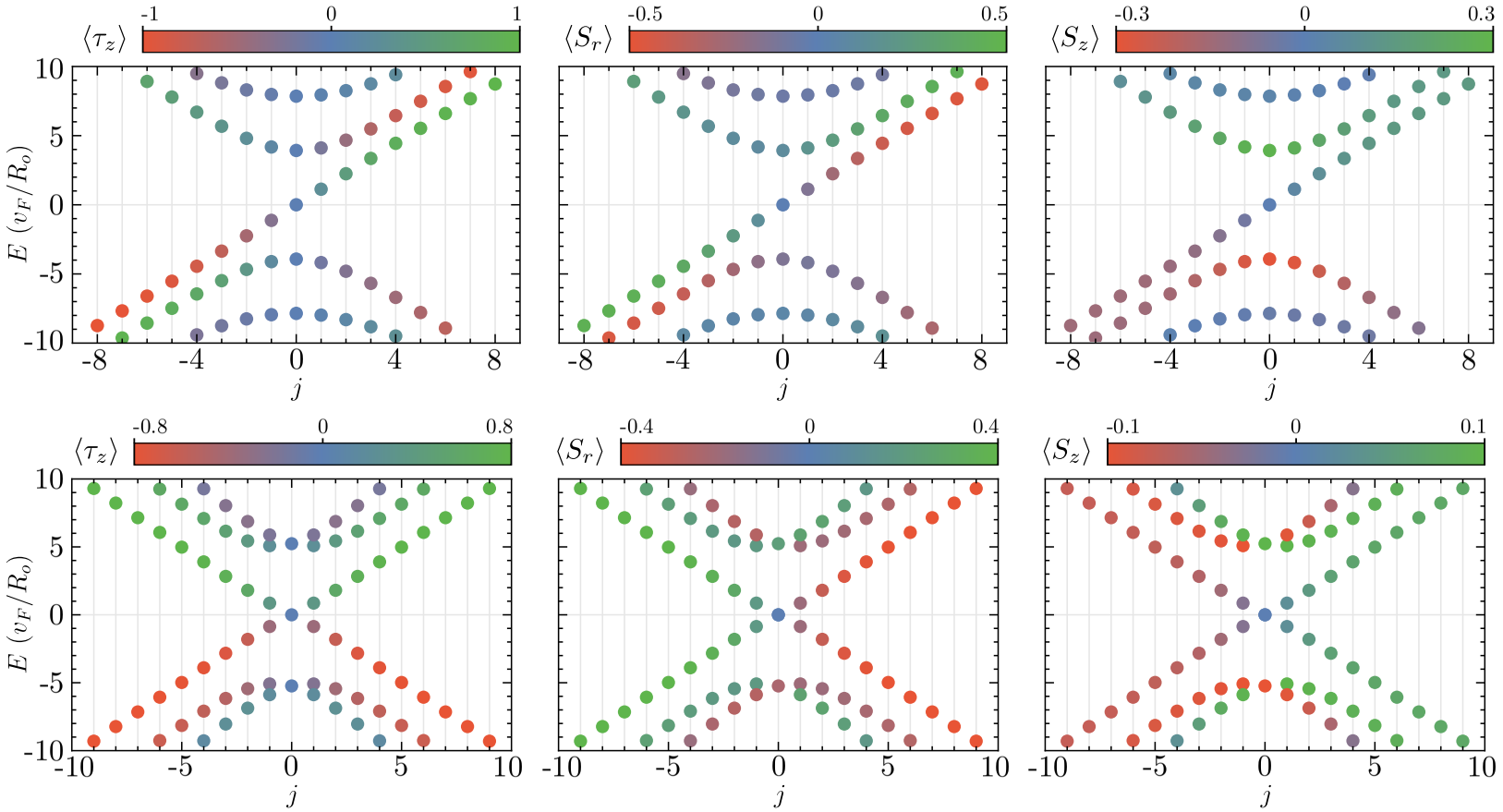

Figure 4.7: Spectrum of the chiral annulus for $\mu = 1$ and $\lambda = 0.6$ (top row) and helical annulus for $\mu = 3$, $\lambda = 0.4$, and $\Delta\phi = \pi$ (bottom row) when half a flux quantum is threaded through the inner region of the annulus. The color gives the expectation values of the charge (left column), the radial spin S_r (middle column), and the normal spin S_z (right column) where the latter two are given in units $\hbar$.

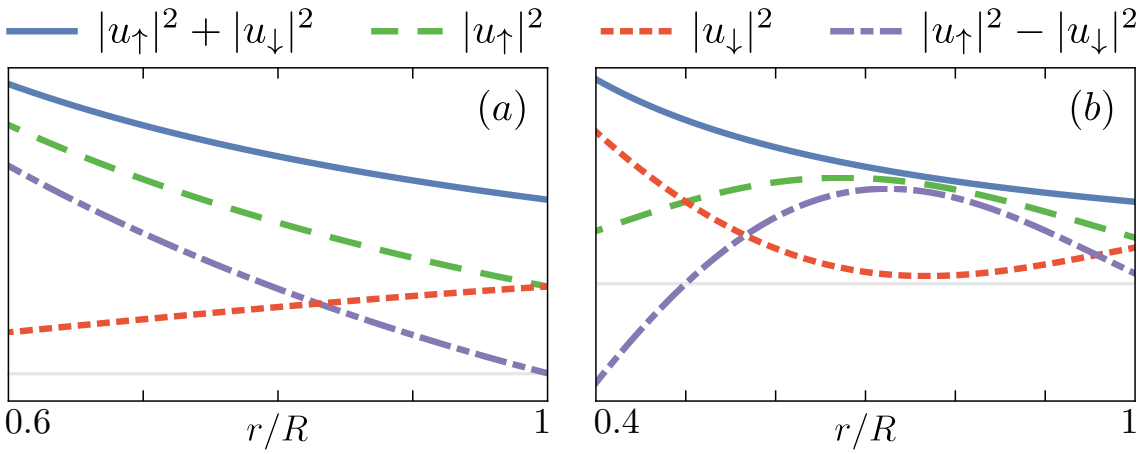

Figure 4.8: (a) Electron density $|u_\uparrow|^2 + |u_\downarrow|^2$, spin-up electron density $|u_\uparrow|^2$, spin-down electron density $|u_\downarrow|^2$ and spin electron density $|u_\uparrow|^2 - |u_\downarrow|^2$ for (a) the chiral Majorana bound state (MBS) and (b) one of the helical MBSs shown in the first and second row of Fig. 4.7, respectively. The corresponding hole densities are identical. The gray line corresponds to zero in both figures.

4.6 Summary

In Chapter 4, we investigated two types of confined hybrid quantum systems on the surface of a topological insulator consisting of deposited insulating magnetic films or s-wave superconductors in an annulus geometry. Specifically, we considered an annulus region of the clean surface bounded either by a magnetic region outside and a superconducting region inside (chiral annulus) or by superconducting regions both inside and outside with a superconducting phase difference (helical annulus). Because these regions are gapped, the surface state is confined within the annulus. The annulus region is effectively a domain wall between regions with a different type of gap. We therefore expected that the quantum rings could support robust low-energy excitations whose properties depend on the type of boundaries. First, we obtained the general solution in the BdG formalism for the surface state in the presence of exchange and pairing potentials with circular symmetry. Subsequently, we obtained the hard-wall boundary conditions at the edges of the annulus and calculated the spectrum of the Andreev bound states. Because of the π Berry phase inherited from the topological surface state, the angular boundary condition gaps the bound-state spectrum (half-integer j) and hence there are no zero-energy bound states. However, the boundary condition can be shifted to integer j by threading half a flux quantum through the inner region, for example with a single $h/(2e)$ vortex if the inner region is a type-II superconductor. Therefore, when half a flux quantum is threaded through the inner disk, the bound states are spectrally shifted and Majorana bound states (MBSs) appear. In case of the chiral annulus, we obtained a single MBS while for the helical annuls we obtained a Kramers pair of MBSs.

5

Graphene topological insulator heterostructure

In the final chapter, we consider hybrid structures made from depositing a monolayer of graphene on the surface of a topological insulator. First, we discuss the low-energy model for the graphene and topological insulator heterostructures. Next, we investigate the electronic transport through steps and barriers of the deposited graphene: We calculate the transmission probability at zigzag and armchair edges of the deposited graphene and we show that the longitudinal conductance through graphene nanoribbon barriers can be understood from antiresonances in the transmission probability.

5.1 Motivation

It is desirable to tailor the properties of the topological surface states both for potential applications and the possibility of new physics. For example, by modifying their dispersion relation, the kinetic energy near the Dirac point can be suppressed [102, 103] so that the topological surface state becomes more susceptible towards interactions which could lead to novel strongly correlated phases. One possibility consists of depositing a thin film of a non-topological metal on the topological-insulator surface (TIS) which effectively changes the boundary conditions at the surface [104–106]. The topological surface state migrates to the new surface obtaining different properties depending on the type of deposited thin film. In particular, graphene is a very interesting candidate for several reasons. Graphene has been studied extensively in the last decade and its properties are well known: It hosts four Dirac cones whose Dirac structure act on the sublattice pseudospin of the honeycomb lattice [107]. When graphene is deposited on the TIS, the interplay between the Dirac cones of graphene and the topological Dirac cone drastically change the properties of the topological surface state [108, 109]. Moreover, the lattice mismatch between graphene and the natural surface of several TIs is very small, from a few percent to near perfect matching.

	mismatch (%)	gap (eV)	v_t/v_g
Bi_2Se_3	2.7 [120]	0.3 [28]	0.5 [28], 0.3 [118]
Sb_2Te_3	0.1 [121]	0.3 [121]	0.4 [121]
Bi_2Te_2Se	0.9 [120]	0.3 [122]	0.5 [122]
$TlBiSe_2$	0.2 [119]	0.35 [116], 0.3 [117], 0.2 [118]	0.3 [116], 0.4 [117], 0.7 [118]

Table 5.1: Lattice mismatch of the graphene and TI heterostructure, band gap, and Fermi velocity v_t for some TIs with a single surface Dirac cone. Here, we have taken $a = 2.46$ Å and $v_g = 10^6$ m/s for the lattice constant and Fermi velocity of graphene, respectively [107].

In this chapter, we investigate transmission in heterostructures made from depositing graphene on top of the (111) surface of a Bi_2Se_3-like TI. This setup was recently experimentally realized [110–115]. The archetypal topological insulator, Bi_2Se_3, has a layered crystal structure where each layer has trigonal symmetry and the layers are generally only weakly coupled by van der Waals-like bonding (see Figure 2.1). The (111) surface is parallel to these layers and hosts a single Dirac cone at the center of the surface Brillouin zone (BZ). If graphene is placed on the (111) surface in the commensurate $\sqrt{3}\times\sqrt{3}$ R30 stacking configuration, the graphene Dirac cones are folded onto the topological Dirac cone so that even weak coupling can strongly affect the low-energy physics if the chemical potential difference is tuned accordingly [108]. In this configuration, the trigonal lattice of graphene and the TIS are rotated by 30° with respect to each other and the surface unit cell contains six carbon atoms from graphene and one atom from the TIS.

The most promising currently known TIs for realizing such a heterostructure are Sb_2Te_3, which has recently been fabricated [113], and $TlBiSe_2$ [116–118]. The corresponding lattice mismatch is only about 0.1% for both materials [118, 119]. Moreover, while the interlayer coupling of Sb_2Te_3 is van der Waals-like, that of $TlBiSe_2$ is more covalent [116] and hence the coupling between graphene and the TIS is stronger in this case. In Table 5.1, we show a list of potential TIs for the heterostructure together with the lattice mismatch, the band gap, and the Fermi velocity of the topological Dirac cone.

5.2 Model

We consider the surface of a Bi_2Se_3-like time-reversal invariant strong topological insulator on which a monolayer of graphene is deposited. The Hamiltonian reads

$$H = H_G + H_{TIS} + V, \tag{5.1}$$

where H_G and H_{TIS} are, respectively, the Hamiltonians of graphene and the topological-insulator surface (TIS) and V is the coupling between them.

For commensurate $\sqrt{3}\times\sqrt{3}$ R30 stacking, illustrated in Fig. 5.1 (a), the Dirac cones at the K and K' point of graphene are folded onto the zone center $\bar{\Gamma}$ of the TIS BZ which harbors the topological Dirac cone. Hence, the low-energy Bloch Hamiltonian becomes

$$h(\boldsymbol{k}) = \begin{pmatrix} h_K & 0 & \mathcal{V}^\dagger, \\ 0 & h_{K'} & \mathcal{V}^\dagger, \\ \mathcal{V} & \mathcal{V} & h_{TIS} \end{pmatrix}, \tag{5.2}$$

where $\mathcal{V}$ are the coupling matrix elements of V between the p_z orbitals of graphene and the TIS. More details and a derivation of Eq. (5.2) are given in Appendix 5.6.1. In the coordinate system shown in Fig. 5.1 (a), we have

$$h_K = \hbar v_g \left[s_0 \otimes (\boldsymbol{\sigma}\cdot\boldsymbol{k})\right], \tag{5.3}$$
$$h_{K'} = \hbar v_g \left[s_0 \otimes (-\boldsymbol{\sigma}^*\cdot\boldsymbol{k})\right], \tag{5.4}$$
$$h_{TIS} = \hbar v_t \left(\hat{\boldsymbol{z}}\times\boldsymbol{s}\right)\cdot\boldsymbol{k} - \mu s_0, \tag{5.5}$$

where v_g and v_t are respectively the Fermi velocity of graphene and the bare TIS, μ is the chemical potential difference between graphene and the TIS, and $\boldsymbol{\sigma}$ and $\boldsymbol{s}$ are the Pauli matrices corresponding to pseudospin and spin, respectively. In the remainder of this chapter, we put $\hbar = 1$ unless otherwise stated.

In our basis, the time-reversal operator becomes

$$\mathcal{T} = (\tau_x \otimes is_y \otimes \sigma_0) \oplus is_y\mathcal{K}, \tag{5.6}$$

where $\mathcal{K}$ denotes complex conjugation and τ_x is the Pauli matrix in valley space. Time-reversal symmetry, $\mathcal{T}h(-\boldsymbol{k})\mathcal{T}^{-1} = h(\boldsymbol{k})$, constrains the coupling $\mathcal{V}$:

$$\mathcal{V}(\boldsymbol{k}) = \begin{pmatrix} t_A(\boldsymbol{k}) & t_B(\boldsymbol{k}) & \lambda_A(\boldsymbol{k}) & \lambda_B(\boldsymbol{k}) \\ -\lambda_A(-\boldsymbol{k})^* & -\lambda_B(-\boldsymbol{k})^* & t_A(-\boldsymbol{k})^* & t_B(-\boldsymbol{k})^* \end{pmatrix}, \tag{5.7}$$

where t_A and t_B correspond to couplings between the same spins, and λ_A and λ_B to couplings between different spins. It is to be expected that the former is stronger than the latter, which is due to spin-orbit effects, and hence we put $\lambda_A = \lambda_B = 0$. The specific form of t_A and t_B depends on the stacking: In Fig. 5.1 (a), we show the three most symmetric stacking configurations. *Ab initio* studies on graphene deposited on thin films of Sb_2Te_3 show that the binding energy of these structures only differ by a few meV with H the most stable configuration [123].

For the T and B structure, coupling is given by

$$\mathcal{V} = \begin{pmatrix} t_A & t_B & 0 & 0 \\ 0 & 0 & t_A & t_B \end{pmatrix}, \tag{5.8}$$

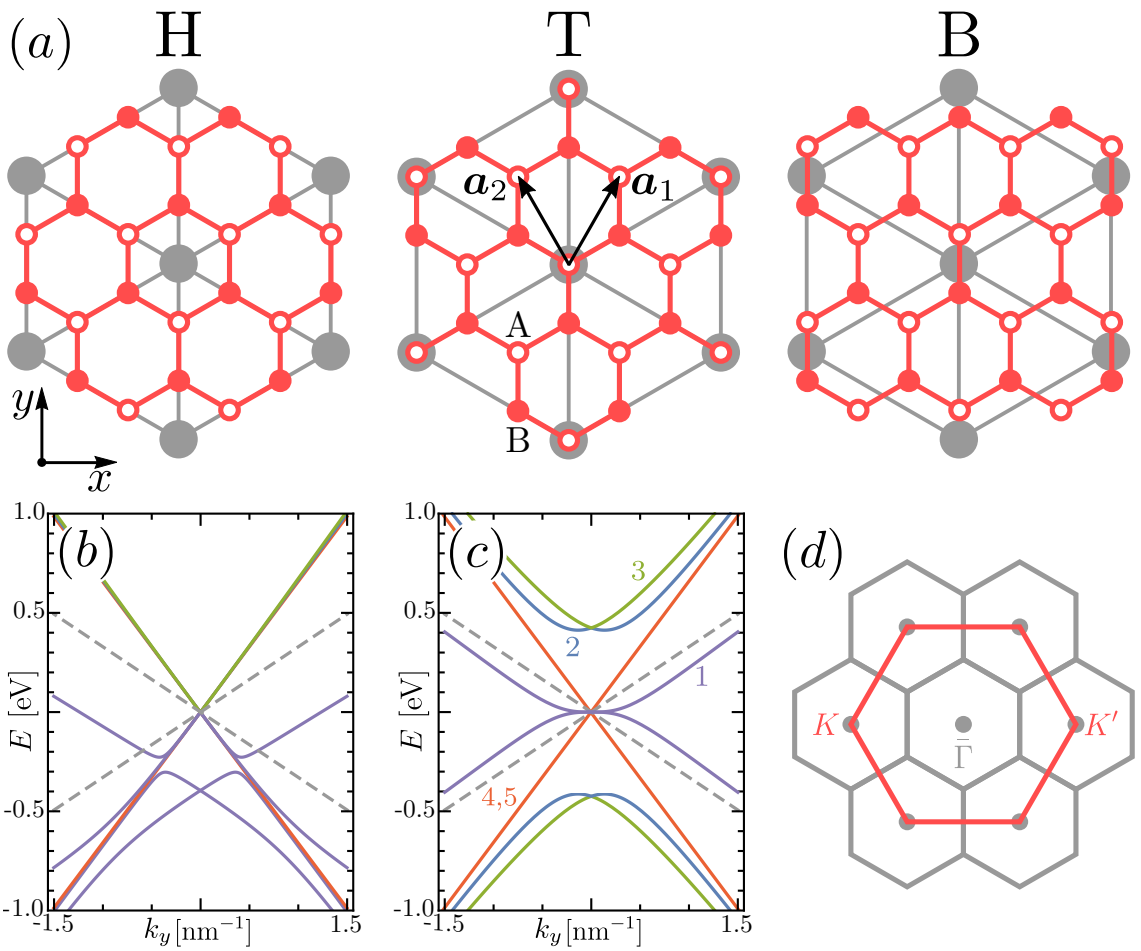

Figure 5.1: (a) Top view of symmetric commensurate $\sqrt{3}\times\sqrt{3}$ R30 stackings of the graphene (small red dots) and TIS (large gray dots) heterostructure. The structures differ by the position of the TIS atom in the unit cell: (H) the center of a graphene hexagon, (T) one sublattice on top, and (B) bond on top. (b, c) Energy spectrum of the (b) H and (c) T structure for $\mu = 0$ and $v_t = v_g/2$. In both cases, the dashed curve is the original topological Dirac cone of the TIS. For (b), the spectrum is shown for $t'' = 0.6$ eV, while for (c) $t = t_A = 0.3$ eV, $t_B = 0$, and the index $n = 1, \ldots, 5$ labels the scattering channel. The spectrum shown in (c) also corresponds to B stacking with $t' = t/\sqrt{2}$. (d) Momentum space of the commensurate $\sqrt{3}\times\sqrt{3}$ R30 stacking configurations shown in (a) in the extended zone scheme. The small gray hexagons correspond to the TIS. The dots are reciprocal lattice points and the large red hexagon is the first BZ of graphene; the K and K' point of graphene are folded to the $\bar{\Gamma}$ point of the surface BZ of the TI.

where t_A (t_B) represents the coupling between the TIS and the A (B) sublattice. In lowest order, we have $t_B = 0$ for T stacking and $t_A = t_B$ for B stacking. However, for the H structure, the lowest-order coupling vanishes at $\boldsymbol{k} = 0$ and the high-energy graphene band at the origin cannot be neglected (see Appendix 5.6.1). Hence, in this case, (5.2) does not describe the low-energy physics.

The energy spectrum of the T structure is shown in Fig. 5.1 (c) for $\mu = 0$. A similar energy spectrum is obtained for the B structure. For the H structure, shown in Fig 5.1 (b), the topological Dirac cone is only shifted in energy and the Fermi velocity is modified (see Appendix 5.6.1). The spectrum shown in Fig. 5.1 (c) is thus generic for any $\sqrt{3}\times\sqrt{3}$ R30 stacking configuration at low energies with the exception of H stacking for which the lowest-order coupling to the TIS vanishes due to C_3 symmetry. Since we are interested in strong coupling between the Dirac cones of graphene and the TIS, we restrict ourselves to the T structure with $\mu = 0$. Thus, we put $t \equiv t_A$ and $t_B = 0$ in the remainder of the chapter.

5.2.1 Valley exchange

From the energy spectrum, shown in Fig. 5.1 (c), we observe that two of the four Dirac cones of graphene do not couple at all with the TIS. This suggests that the graphene Dirac cones partly decouple. The symmetry responsible is *valley exchange*: $K \leftrightarrow K'$ such that states that are even under valley exchange couple to the TIS, while states that are odd under valley exchange do not. Formally, we can write

$$UhU^\dagger = h_+ \oplus h_-, \tag{5.9}$$

where the unitary transformation $U = U_{\boldsymbol{k}}$ is explicitly given in Appendix 5.6.2. This is illustrated in Fig. 5.2. For T stacking, the two blocks h_+ and h_- can be written as

$$h_+ = \begin{pmatrix} 0 & -v_g k_- & & & & \\ -v_g k_+ & 0 & \sqrt{2}t & & & \\ & \sqrt{2}t & 0 & v_t i k_- & & \\ & & -v_t i k_+ & 0 & \sqrt{2}t & \\ & & & \sqrt{2}t & 0 & v_g k_- \\ & & & & v_g k_+ & 0 \end{pmatrix}, \tag{5.10}$$

$$h_- = v_g \left(\boldsymbol{\sigma} \cdot \boldsymbol{k} \oplus -\boldsymbol{\sigma}^* \cdot \boldsymbol{k}\right), \tag{5.11}$$

with $k_\pm = k_x \pm i k_y$. We find that h_+ is equivalent to spinless ABC-stacked trilayer graphene for which the middle layer is triaxially strained, while h_- resembles the Hamiltonian of spinless graphene [124]. We can understand the decoupling as follows: The matrix elements between the odd subspace and the topological surface state pick up a

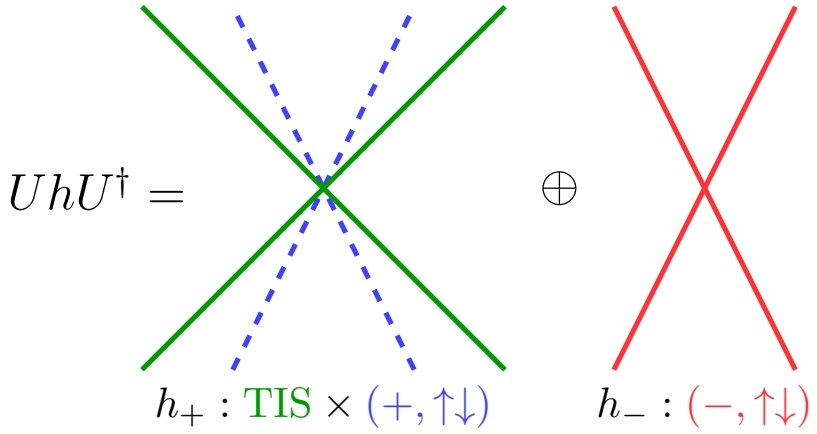

Figure 5.2: Representation of the block diagonalization of h into subspaces that are even ($+$, dashed blue cone) and odd ($-$, red cone) under valley exchange. The spectra are shown for $t = 0$ and $2v_t = v_g$. Only the even subspace couples to the topological-insulator surface (green cone).

minus sign under time reversal, so that they have to be zero because the coupling is time-reversal invariant.

In analogy with ABC trilayer graphene, the energy dispersion is cubic at low energies ($vk/t \ll 1$) [124]. Moreover, we find that the topological surface state migrates to the graphene. The effective low-energy Hamiltonian close to the $\bar{\Gamma}$ point becomes

$$\frac{v_g^2 v_t}{2t^2} \begin{pmatrix} 0 & k_-^3 \\ k_+^3 & 0 \end{pmatrix} \oplus h_-, \tag{5.12}$$

with corresponding dispersion relations $\pm v_g^2 v_t/(2t^2)k^3$ and $\pm v_g k$, respectively, where the latter is spin degenerate. The basis of the first 2×2 block of the effective Hamiltonian is $\{i\left|\psi_B^+ \uparrow\right\rangle, \left|\psi_B^+ \downarrow\right\rangle\}$. Here, the $+$ indicates that these states are symmetric-like superposition of K and K'. Note that these states correspond to the sublattice that does not couple directly to the TIS in lowest order of vk/t. Accordingly, the low-energy physics is understood in terms of an intermediate virtual process: In lowest order, the spin states of the B^+ sublattice couple to each other via the A^+ sublattice and the original topological surface state, leading to the cubic dispersion. Apart from the cubic dispersion, two valley-odd cones from graphene remain uncoupled. The presence of boundaries, however, can induce coupling to these cones and they are not robust against time-reversal invariant perturbations in general. Similarly, an AB-stacked graphene bilayer that is suitably deposited on the TIS leads to a quintic dispersion at low energies, now localized on a single sublattice of the top layer of the bilayer, together with two quadratic cones corresponding to the odd subspace of the bilayer [108].

In Fig. 5.3, we show the two-dimensional bands obtained from h_+ together with the corresponding spin expectation values, which are shown as arrows. While the decoupled

Dirac cones from h_- remain s_z eigenstates, the other bands inherit their spin structure from the original topological surface state. Besides the cubic Dirac bands, there are two bands originating from the valley-even states that have a Rashba-like dispersion with opposite spin-momentum locking. These states arise from proximity-induced Rashba coupling as reflection symmetry about the graphene plane is broken when it is deposited on the TIS. By expanding the dispersion relation to second order in k, we find that the Rashba momentum and energy splitting are approximately given by $(2\sqrt{2}tv_t)/(4v_g^2+v_t^2)$ and $(tv_t^2)/[\sqrt{2}\left(4v_g^2+v_t^2\right)]$.

5.3 Transmission

In this section, we consider elastic scattering of the topological surface state at the graphene-topological insulator heterostructure for T stacking. First, we consider scattering at a graphene step terminated by zigzag or armchair edges, where an incident wave on the bare TIS coming in from the left ($x<0$) is transmitted to the right ($x>0$) into a semi-infinite region of the heterostructure. Next, we consider transmission through a graphene nanoribbon barrier of finite width. We work in the original basis in which the Hamiltonian takes the form given in Eq. (5.2). In the basis where the Hamiltonian is block diagonal, the boundary conditions at a graphene edge can couple the two blocks and we prefer to work in the original basis where the boundary conditions are straightforward.

Since the y direction is translational invariant, the wave function can be written as $\Psi(x,y)=e^{ik_y y}\Phi(x)$. If we take the coordinate system shown in Fig. 5.4, the scattering state for the bare TIS is given by an incident and reflected wave

$$\Phi_I(x)=\phi_i e^{ik_x x}+r\phi_r e^{-ik_x x}, \tag{5.13}$$

where r is the reflection coefficient and

$$\phi_i=\begin{pmatrix} E/v_t \\ k_y-ik_x \end{pmatrix}, \qquad \phi_r=\begin{pmatrix} E/v_t \\ k_y+ik_x \end{pmatrix}, \tag{5.14}$$

are the corresponding spinors with E the Fermi energy, measured relative to the Dirac point. We have left out normalization constants because they are irrelevant for the calculation. The longitudinal and transverse momentum are given by k_x and k_y, respectively. The latter is conserved because of translation symmetry in the y direction. The longitudinal momentum is given by

$$k_x=\mathrm{sign}(E)\sqrt{(E/v_t)^2-k_y^2}, \tag{5.15}$$

where $E=v_t k$ for the Dirac cone of the TIS. The sign of k_x makes sure that the incident wave propagates to the right and the reflected wave propagates to the left.

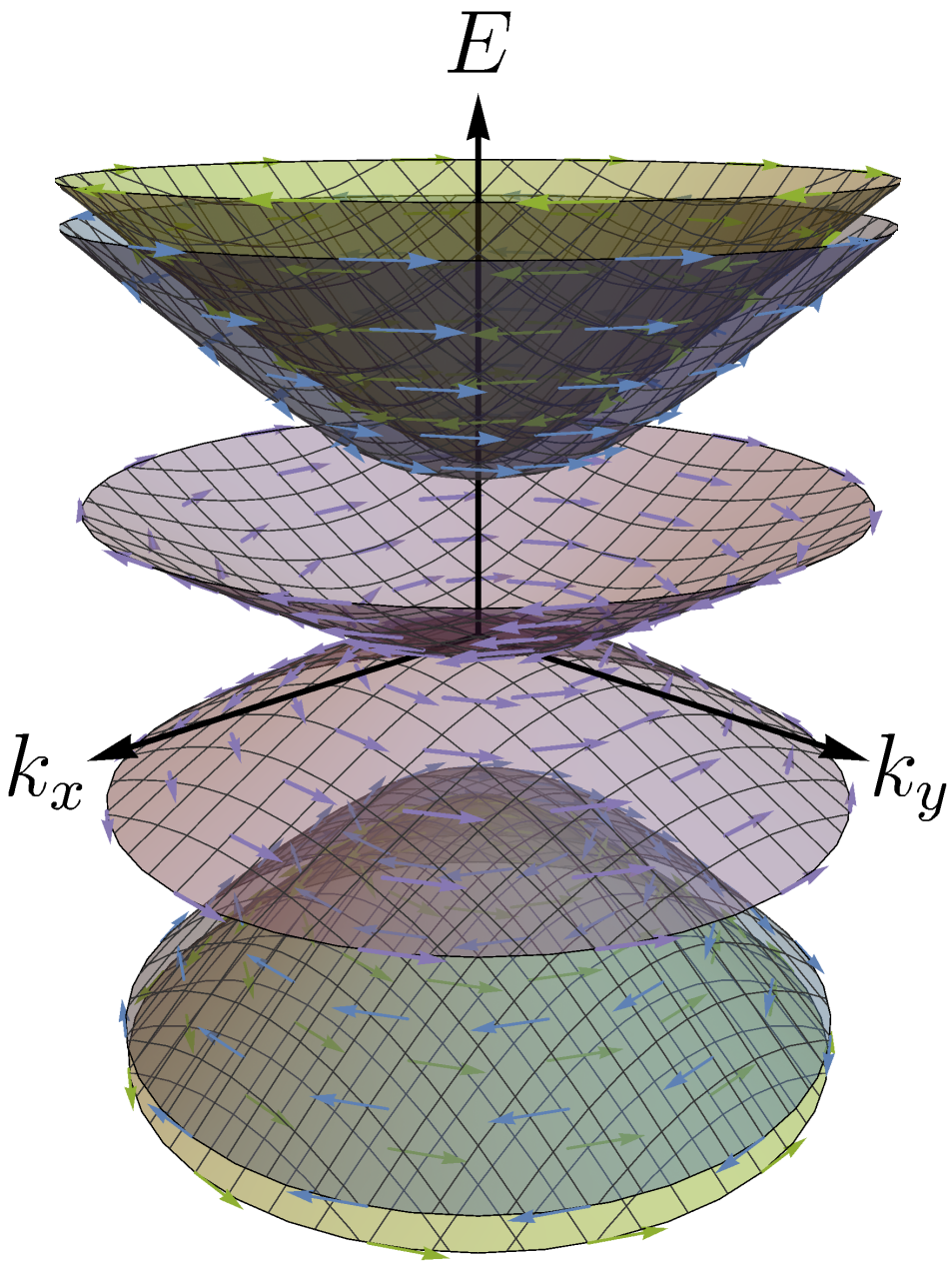

Figure 5.3: Low-energy spectrum for T (or B) stacking where the corresponding spin expectation values are shown as arrows. All bands except the two valley-odd Dirac cones that are decoupled in the bulk heterostructure are shown. The explicit expressions of the spectrum are given in Appendix 5.6.3.

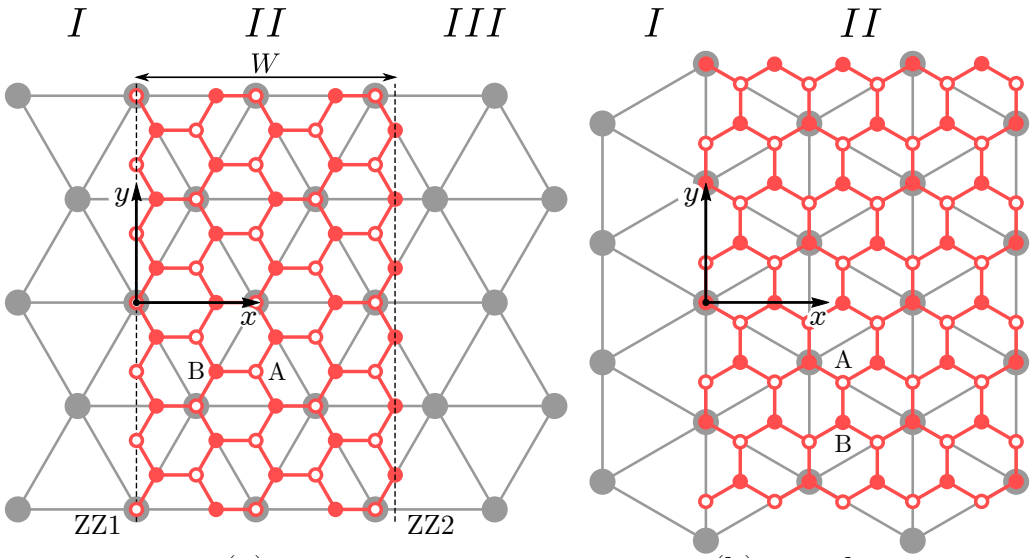

(a) zigzag (b) armchair

Figure 5.4: Edge geometries of graphene (red, small dots) on top of the TIS (gray, large dots) for T stacking. The Roman numerals indicate different scattering regions. (a) Zigzag edges: two types depending on whether the edge is terminated by the A (ZZ1) or B (ZZ2) sublattice. (b) One of the three physically-distinct armchair edges which the continuum model cannot distinguish.

5.3.1 Graphene step

Scattering states

In the semi-infinite T region, the wave function can be written as

$$\Phi_{II}(x) = \sum_{n=1}^{5} t_n \psi_n e^{iq_{nx}x}, \tag{5.16}$$

where t_n, ψ_n, $\boldsymbol{q}_n = q_{nx}\hat{\boldsymbol{x}} + k_y\hat{\boldsymbol{y}}$ are, respectively, the transmission coefficient, the spinor, and the momentum of the nth scattering channel. The sign of q_{nx} is chosen such that the group velocity for scattering modes is positive and the wave propagates to the right, while for evanescent modes it is chosen such that the imaginary part is positive since otherwise the solution from Eq. (5.16) would blow up for $x \to \infty$. The bands corresponding to the different transmission channels are shown in Fig. 5.1 (*c*): ψ_1 corresponds to the cubic dispersion, ψ_2 and ψ_3 to the Rashba-like bands, while ψ_4 and ψ_5 correspond to the two decoupled Dirac cones. Transmission can occur only if q_x is real since otherwise the corresponding wave function is evanescent. Furthermore, we expect there is no transmission to the channels ψ_4 and ψ_5 because they are decoupled from the TIS in the bulk heterostructure. The presence of certain boundaries, however, allows for transmission to ψ_4 and ψ_5, as we show below.

The spinors ψ_4 and ψ_5 can be explicitly written as

$$\psi_4 = \begin{pmatrix} E/v_g & q_{4x} + ik_y & 0 & 0 & -E/v_g & q_{4x} - ik_y & 0 & 0 & 0 & 0 \end{pmatrix}^t, \tag{5.17}$$

$$\psi_5 = \begin{pmatrix} 0 & 0 & E/v_g & q_{5x} + ik_y & 0 & 0 & -E/v_g & q_{5x} - ik_y & 0 & 0 \end{pmatrix}^t, \tag{5.18}$$

with

$$q_{4x} = q_{5x} = \text{sign}(E)\sqrt{(E/v_g)^2 - k_y^2}. \tag{5.19}$$

It is clear that the spinors ψ_4 and ψ_5 are s_z eigenstates and have odd valley parity since they are antisymmetric superpositions of states at K and K'. The remaining spinors are given by ψ_1, ψ_2, and ψ_3 and the corresponding wave vectors are found with the secular equation $|h_+(q_x, k_y) - E| = 0$ which yields two cubic equations:

$$2t^2 E + \left(E^2 - v_g^2 q^2\right)(\pm v_t q - E) = 0, \tag{5.20}$$

where $q_x = (\pm)\sqrt{q^2 - k_y^2}$ with solutions

$$q_m = \pm\frac{E}{3v_t}\left(1 + C_m + \frac{\Delta_0}{C_m}\right), \tag{5.21}$$

for $m = 1, 2, 3$ and where

$$\Delta_0 = 1 + 3\left(v_t/v_g\right)^2, \tag{5.22}$$

$$\Delta_1 = 1 + 9\left(v_t/v_g\right)^2\left[3(t/E)^2 - 1\right], \tag{5.23}$$

$$C_m = e^{\frac{2mi\pi}{3}}\sqrt[3]{\Delta_1 + \sqrt{\Delta_1^2 - \Delta_0^3}}. \tag{5.24}$$

Again, for the graphene step, the sign $(\pm)$ of q_{mx} is chosen such that scattering modes propagate towards positive x and evanescent modes decay inside the T region.

Boundary conditions

The boundary conditions at $x = 0$ are given by the continuity of the TIS spinor,

$$\Phi_I(0) = \Phi_{II}(0)|_{\text{TIS}}\,, \tag{5.25}$$

together with the appropriate open boundary conditions for the graphene components depending on the type of edge [125, 126]. We consider three edge geometries, shown in Fig. 5.4. For the T structure there are two distinct types of zigzag edges. One is terminated by sublattice A (ZZ1) and the other one is terminated by sublattice B (ZZ2). For the armchair edge (AC) there are three different edge configurations, but the continuum model cannot distinguish any of them because the armchair edge contains both sublattices. In case of B stacking, shown in Fig. 5.1 (a), there is also no distinction

between the ZZ1 and ZZ2 edges within the continuum model. For the zigzag edge shown in Fig. 5.4 (a), the boundary condition is satisfied if we put the component of the relevant sublattice equal to zero at the edge for the two valleys separately [127]. For a zigzag edge at $x = 0$, this gives

$$\Phi_{II}(0)|_{\alpha\uparrow(\downarrow)} = \Phi_{II}(0)|_{\alpha'\uparrow(\downarrow)} = 0, \tag{5.26}$$

where $\alpha = A, B$ for the ZZ2 and ZZ1 boundary conditions, respectively. For the armchair edge, shown in Fig. 5.4 (b), we can only obtain a nontrivial solution if the boundary conditions couple the K and K' valleys of graphene because an armchair edge contains both sublattices [127]. Thus, the boundary condition for the armchair edge is

$$\Psi_K e^{i\boldsymbol{K}\cdot\boldsymbol{r}} + \Psi_{K'} e^{i\boldsymbol{K'}\cdot\boldsymbol{r}}\Big|_{\text{edge}} = 0, \tag{5.27}$$

where Ψ_K and $\Psi_{K'}$ are the graphene spinors. For the coordinates in Fig. 5.4 (b) and $\boldsymbol{K'} = -\boldsymbol{K} = 4\pi/(3a)\hat{\boldsymbol{x}}$ where a is the graphene lattice constant, the spinors are

$$\Psi_K = \begin{pmatrix} \psi_A \\ \psi_B \end{pmatrix}, \qquad \Psi_{K'} = \begin{pmatrix} \psi_{A'} \\ \psi_{B'} \end{pmatrix}, \tag{5.28}$$

for both spin components. Note that we have chosen the Hamiltonian (5.2) in such a way that no phase factors arise in the components. In the zigzag case, relative phase factors between valleys drop out of the boundary condition. Hence, it does not matter that we used rotated coordinates for the zigzag case, as shown in Fig. 5.4 (a). Thus, we find that the armchair boundary condition at $x = 0$ is given by

$$\Phi_{II}(0)|_{\alpha\uparrow(\downarrow)} + \Phi_{II}(0)|_{\alpha'\uparrow(\downarrow)} = 0, \quad \alpha = A, B. \tag{5.29}$$

In general, the combined boundary conditions from (5.25) and (5.26) or (5.29) result in six equations that are solved numerically and yield the reflection coefficient r and the five transmission coefficients t_n.

Transmission channels

In the heterostructure region for the graphene step, there are five scattering channels while there is only one reflection channel for the bare TIS. In order to obtain the transmission probability of the different scattering channels, we consider the probability current in the x direction. The probability-current operator in the x direction is given by

$$j = (v_g s_0 \otimes \sigma_x) \oplus (-v_g s_0 \otimes \sigma_x) \oplus (-v_t s_y)\,. \tag{5.30}$$

By definition, the transmission probability of the nth scattering channel is given by

$$T_n = \frac{\psi_n^\dagger j \psi_n}{\phi_i^\dagger j \phi_i} |t_n|^2 = \frac{\psi_n^\dagger j \psi_n}{2Ek_x} |t_n|^2\,, \tag{5.31}$$

and the total transmission probability $T = \sum_{n=1}^{5} T_n$. For scattering modes of the graphene Dirac cones with odd valley parity ($E^2 > v_g^2 k_y^2$) (5.17) gives

$$T_4 = \frac{2q_{4x}}{k_x} |t_4|^2 , \qquad T_5 = \frac{2q_{5x}}{k_x} |t_5|^2 , \tag{5.32}$$

while the transmission vanishes for evanescent modes ($E^2 < v_g^2 k_y^2$). The reflection probability R is given by

$$R = -\frac{\phi_r^\dagger j \phi_r}{\phi_i^\dagger j \phi_i} |r|^2 = |r|^2 , \tag{5.33}$$

where conservation of the probability current density gives $R+T = 1$. This is guaranteed by the boundary conditions. Before we discuss our results for the step geometry, we consider the boundary conditions for the nanoribbon barrier.

5.3.2 Graphene nanoribbon barrier

Now we consider a barrier composed of a graphene nanoribbon deposited on the TIS in the T stacking configuration. The ribbon is infinite along the y direction and finite in the x direction with width W. This is illustrated for the zigzag barrier in Fig. 5.4 (a).

Scattering states

The scattering state of the TIS for $x < 0$ is again given by Eq. (5.13). In the barrier region ($0 < x < W$), the wave function can be written as

$$\Phi_{II}(x) = \sum_{n=1}^{5} a_n \psi_{n+} e^{iq_{nx}x} + b_n \psi_{n-} e^{-iq_{nx}x}, \tag{5.34}$$

where the wave vectors q_{nx} are found from Eqs. (5.19) and (5.20). Note that we do not need to worry about the correct sign of the wave vector because both are admissible in the finite barrier. Behind the barrier ($x > W$), the solution becomes

$$\Phi_{III}(x) = t\phi_t e^{ik_x x}, \tag{5.35}$$

where t is the reflection coefficient, the spinor $\phi_t = \phi_i$ is given in Eq. (5.14), and k_x is given in Eq. (5.15).

Boundary conditions

In case of the barrier, the boundary conditions consist of the continuity of the TIS spinor components and the appropriate open boundary conditions for the graphene spinor components at $x = 0$ and $x = W$. The former are

$$\Phi_I(0) = \Phi_{II}(0)|_{\text{TIS}} , \tag{5.36}$$

$$\Phi_{III}(W) = \Phi_{II}(W)|_{\text{TIS}} . \tag{5.37}$$

Next, we discuss the open boundary conditions for the graphene components. For the zigzag ribbon, we take the ZZ1 edge at $x = 0$ so that the edge at $x = W$ is automatically ZZ2. So the boundary conditions for the zigzag ribbon are given by

$$\Phi_{II}(0)|_{B\uparrow(\downarrow)} = \Phi_{II}(0)|_{B'\uparrow(\downarrow)} = 0, \tag{5.38}$$
$$\Phi_{II}(W)|_{A\uparrow(\downarrow)} = \Phi_{II}(W)|_{A'\uparrow(\downarrow)} = 0. \tag{5.39}$$

Analogous to the discussion on the armchair edge above, we find that the boundary conditions for the armchair ribbon are given by

$$\Phi_{II}(0)|_{\alpha\uparrow(\downarrow)} + \Phi_{II}(0)|_{\alpha'\uparrow(\downarrow)} = 0, \tag{5.40}$$
$$\Phi_{II}(W)|_{\alpha\uparrow(\downarrow)} + e^{i\Delta K W}\, \Phi_{II}(W)|_{\alpha'\uparrow(\downarrow)} = 0, \tag{5.41}$$

for $\alpha = A, B$, where $\Delta K = 8\pi/(3a)$.

The boundary conditions for the graphene nanoribbon barrier give twelve equations that are solved numerically and yield the reflection coefficient r, the ten barrier coefficients a_n and b_n, and the transmission coefficient t.

Bound states

Solutions of the TIS for which $E^2 < v_t^2 k_y^2$ are evanescent and therefore there possibly exist bound states, localized in the graphene nanoribbon. In this case, the wave functions outside the ribbon can be written as

$$\Phi_I(x) = c \begin{pmatrix} E/v_t \\ k_y - \kappa \end{pmatrix} e^{\kappa x}, \qquad \Phi_{III}(x) = d \begin{pmatrix} E/v_t \\ k_y + \kappa \end{pmatrix} e^{-\kappa x}, \tag{5.42}$$

where $\kappa = \sqrt{k_y^2 - (E/v_t)^2}$. The wave function inside the ribbon is given by (5.34) and the boundary conditions and the normalization give twelve independent equations for the coefficients a_n, b_n, c, and d.

5.4 Results

In this section, we discuss our results for transmission through a graphene step and a nanoribbon barrier deposited on the TIS in the T stacking configuration. For the parameters, we always take $v_t = v_g/2$ which is representative for the TIs listed in Table 5.1. Furthermore, we take $t = 0.3$ eV as a qualitative example which is of the same order as the interlayer coupling in bilayer graphene [124], unless stated explicitly.

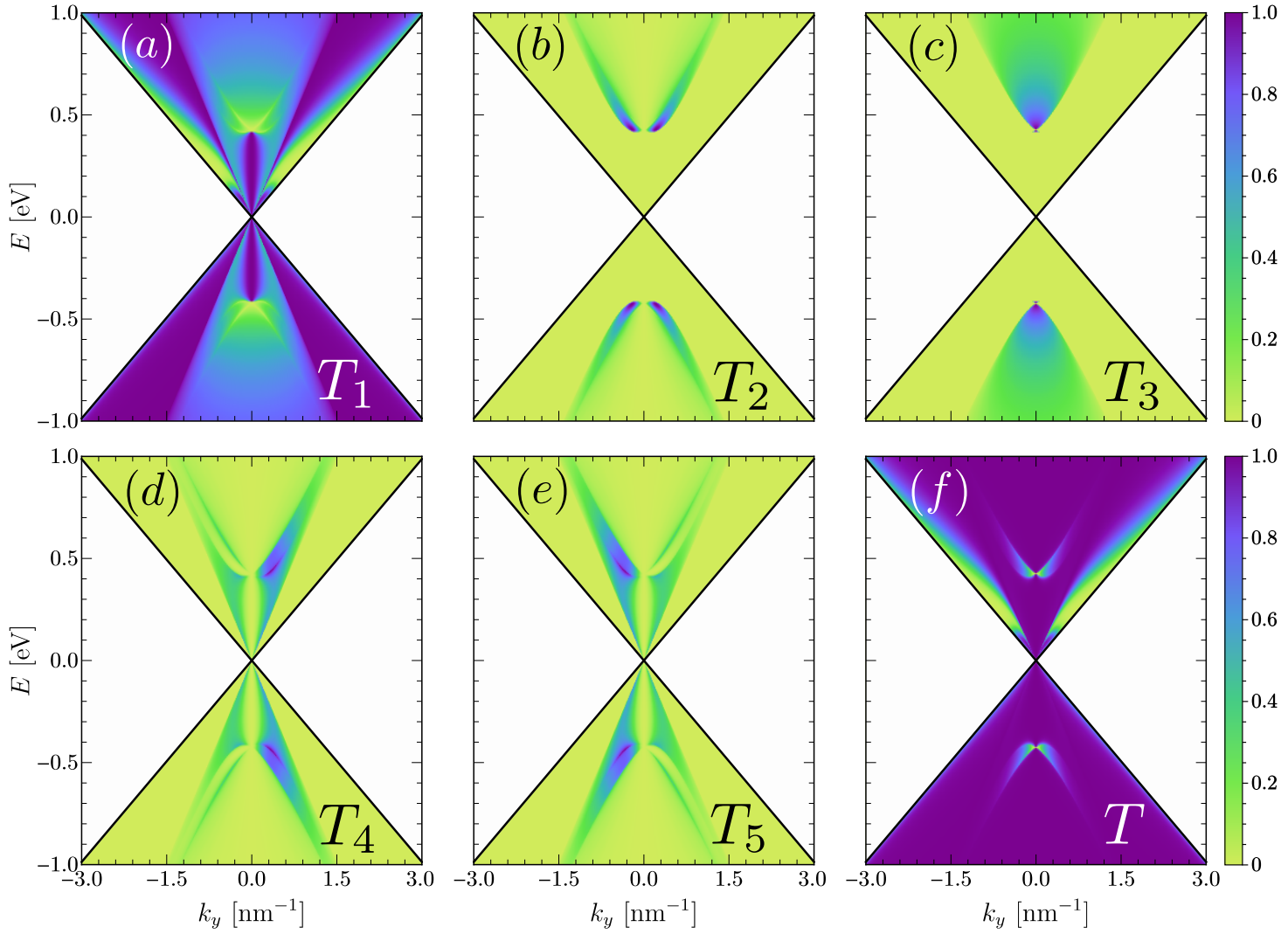

Figure 5.5: (a)–(e) Transmission probabilities T_n for scattering at the ZZ1 step with $t = 0.3$ eV for the scattering channels $n = 1, \ldots, 5$, respectively, and (f) the total transmission probability $T = \sum_{n=1}^{5} T_n$.

5.4.1 Graphene step

Out of the three edges we have considered for the graphene step, only one of the zigzag edges, ZZ1, shows interesting features in the transmission probability $T(E, k_y)$. Interestingly, the result for the ZZ2 and AC edges is exactly the same and shows near perfect transmission, even at oblique angles. As seen in Fig. 5.4, the terminated graphene edge only couples directly to the TIS lattice for the ZZ1 boundary. Furthermore, we find that only the ZZ1 edge induces coupling to the valley-odd cones that are decoupled in the bulk heterostructure. The transmission probability of the different scattering channels at the ZZ1 edge is shown in Fig. 5.5, together with the total transmission probability. For $E \lesssim \sqrt{2}t$, the main transmission channel is T_1, and the ZZ1 edge allows for some transmission to channels 4 and 5, corresponding to the valley-odd cones. At higher energies, the Rashba channels T_2 and T_3 become available and the transmission via T_1 reduces inside the region $E^2 < v_g^2 k_y^2$ defined by the graphene Dirac cone. The transmittance of the channels T_4 and T_5, which are s_z eigenstates and completely localized in the graphene for the bulk heterostructure, are mirrored with respect to $k_y = 0$ which is due to TR symmetry. Moreover, they show a preference for either left or right moving states for both electrons and holes, creating a bulk spin-momentum locked state localized on the deposited graphene. Note that only T_1, and therefore also the total transmission probability, is not symmetric with respect to zero energy. This asymmetry originates from the fact that a step graphene-TIS system has only one interface which breaks the symmetry of the lattice structure, resulting in an asymmetric transmission for electrons and holes, in contrast to the graphene-TIS barrier structure discussed below.

5.4.2 Graphene nanoribbon barrier

Here, we discuss our results for the transmission across the graphene nanoribbon deposited on the TIS in the T stacking configuration. The results for the barrier are symmetric with respect to zero energy and therefore we only show results for positive energy. The width of the graphene ribbons, including dangling bonds, is given by

$$W_{ZZ} = \frac{a}{2\sqrt{3}} (3N + 2) , \tag{5.43}$$

$$W_{AC} = \frac{a}{2} (N + 1) , \tag{5.44}$$

where a is the graphene lattice constant and N is the number of two-atom unit cells along the finite x direction.

In Figs. 5.6 and 5.7, we show the transmission probability for the zigzag and armchair barrier, respectively. The transmission probability is always equal to unity at normal incidence for both zigzag and armchair ribbons, which is what we expect for a nonmagnetic scatterer on the TIS. Moreover, we observe two resonances at low energies for the zigzag ribbon and antiresonances for both zigzag and armchair ribbons. The low-energy resonances for the zigzag ribbons, shown in Fig. 5.6, are caused by edge states, that are

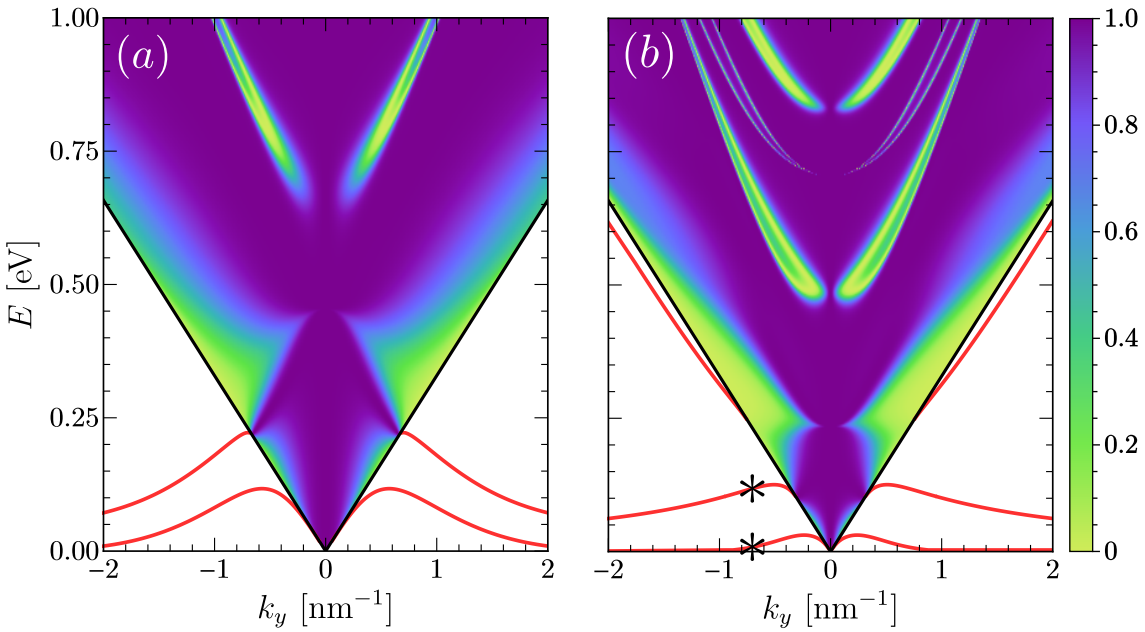

Figure 5.6: Transmission probability $T(E, k_y)$ for a zigzag ribbon with $t = 0.3$ eV, and (a) $N = 10$ and (b) $N = 20$. The red curves are bound states and the density corresponding to the states marked with an asterisk is shown in Fig. 5.9.

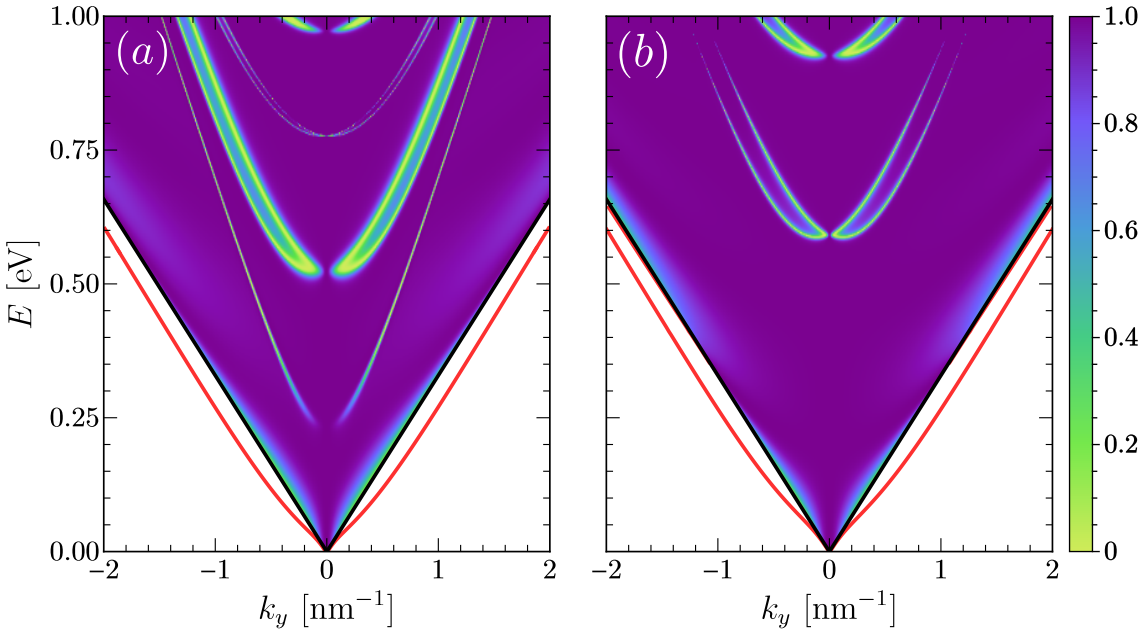

Figure 5.7: Transmission probability $T(E, k_y)$ for an armchair ribbon with $t = 0.3$ eV and (a) $N = 30$ (insulating) and (b) $N = 41$ (metallic). The red lines outside the cone are bound states.

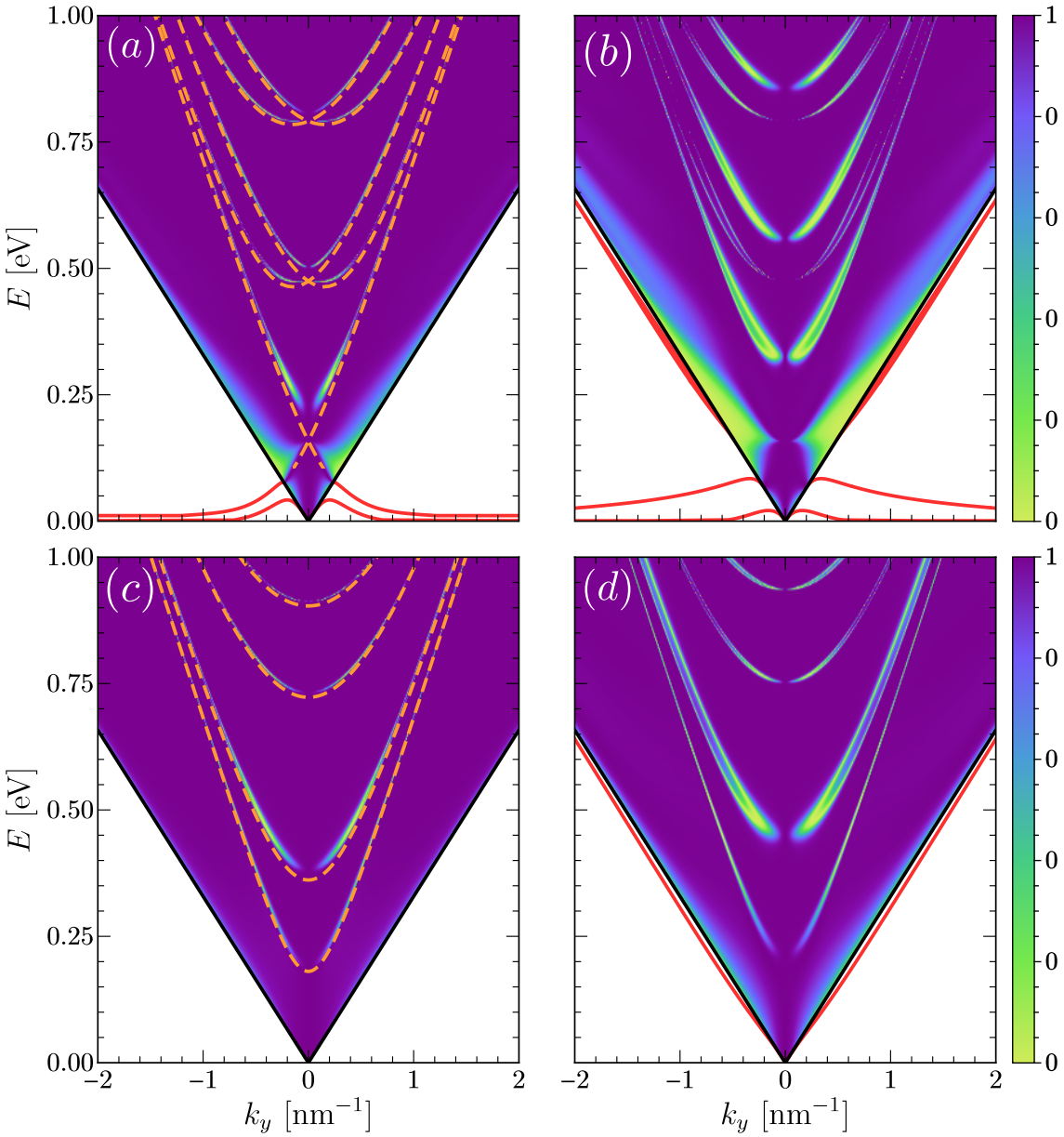

Figure 5.8: Transmission probability $T(E, k_y)$ for the nanoribbon barrier. (a)–(b) Zigzag ribbon with $N = 30$ for (a) $t = 0.1$ eV and (b) $t = 0.2$ eV. (c)–(d) Armchair ribbon with $N = 30$ for (c) $t = 0.1$ eV and (d) $t = 0.2$ eV. The red lines are bound states, localized in the barrier, while the orange dashed lines in (a) and (c) are the bound states of a bare graphene nanoribbon.

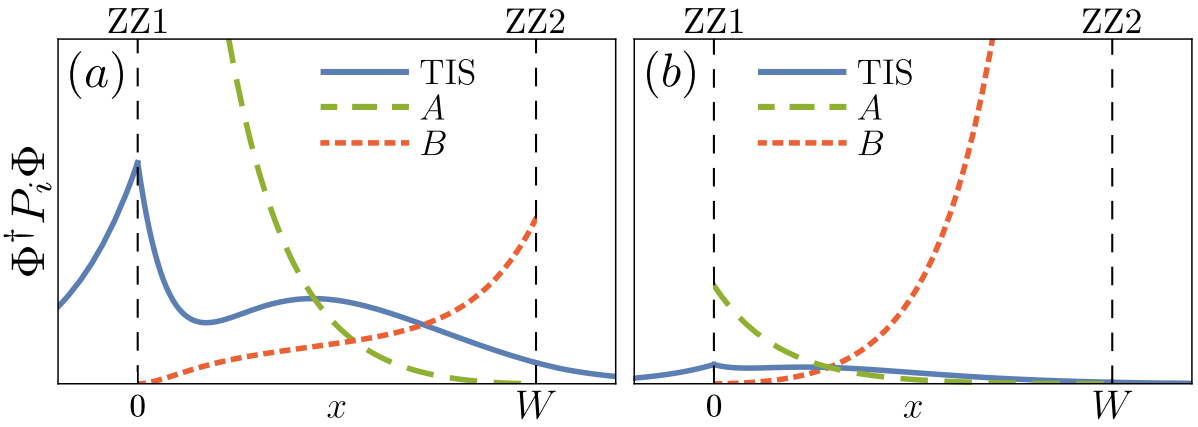

Figure 5.9: Projected densities of the (a) upper and (b) lower branch of edge states for the zigzag ribbon with $N = 20$ and $t = 0.3$ for $k_y = 0.7$ nm^{-1} which are marked with an asterisk in Fig. 5.6. Here, P_i ($i = \text{TIS}, A, B$) is the projection operator on the TIS and the A/B sublattices of graphene. We see that the edge state shown in (a) is mostly localized on the A sublattice (ZZ2 edge) while (b) is mostly localized on the B sublattice (ZZ1 edge).

absent for an armchair ribbon. To understand the nature of these edge states and the antiresonances, we consider the evolution of the transmission probability as a function of the coupling t between graphene and the TIS. In Fig. 5.8, we show the transmission probability for zigzag and armchair ribbons with $t = 0.1$ eV and $t = 0.2$ eV. We see that the dispersion of the two branches of edge states of the zigzag ribbon split with increasing t since the upper branch is localized on the ZZ1 edge which couples directly to the TIS, while the lower branch is localized on the ZZ2 edge which has no direct coupling to the TIS. The electron density of the edge states corresponding to Fig. 5.6 (b) is shown in Fig. 5.9 for a fixed value of k_y. Note that the upper branch is actually a hybridized state of graphene and the TIS, localized near the ZZ1 edge. The cusp in the projected density of the TIS is due to the fact that the boundary conditions only require that the spinor components are continuous.

The energy splitting of the edge states is shown in Fig. 5.10 as a function of t for $N = 10$ and $N = 20$. For $N = 10$, there is a confinement effect near $t = 0$ which is absent for $N = 20$. However, the confinement splitting is lifted when t increases because the energy difference of edge states localized at different edges increases, and the lower branch returns to zero energy. The energy of the upper branch grows linearly with t, as the coupling with the TIS splits the two edge states, that are originally s_z eigenstates, localized on the ZZ1 edge. Moreover, if the barrier is wide enough or the coupling strong enough, there are bound states, delocalized over the ribbon, both in the zigzag and armchair case, as is shown in Figs. 5.6, 5.7, and 5.8.

Furthermore, in Fig. 5.8 (a) and (c), we have superimposed the bound states of a bare graphene ribbon on the transmission probability for $t = 0.1$ eV for both an armchair

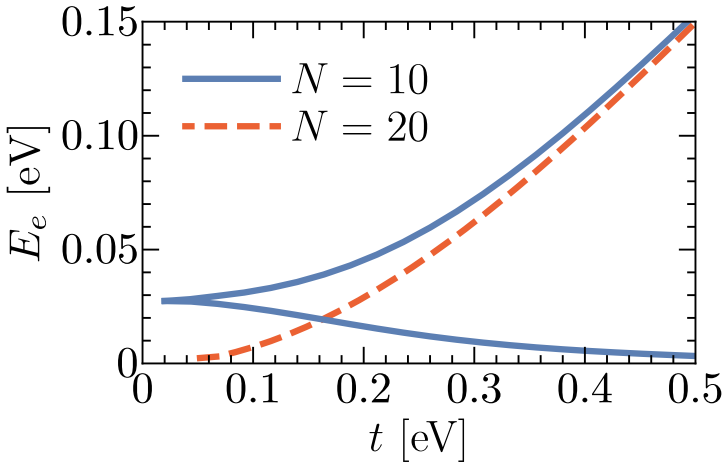

Figure 5.10: Energy of the zigzag edge states at $k_y = 2$ nm^{-1} as a function of t for $N = 10$ and $N = 20$. We only show one state for $N = 20$, since the other state remains at zero energy for all t.

and zigzag barrier. In this case, the antiresonances are very sharp and coincide almost perfectly with the bound states of the bare ribbon. These antiresonances are quasibound states originating from both valley-even and valley-odd states. With increasing t, the quasibound states split into two classes: Those that broaden and move in energy with increasing t correspond to the Rashba-split bands while those that remain very sharp and almost at the same energy correspond to the valley-odd cones. Indeed, the latter are missing for the armchair barrier because the AC edge does not induce coupling to these states. Note that due to the ZZ1 edge, some spin splitting is induced into the quasibound states originating from the valley-odd states. At these energies, the wave function is either strongly hybridized for the Rashba-like states, or completely localized in the graphene for the valley-odd states. In the latter case, which only occurs for zigzag ribbons, tunneling is impossible since the ribbon contains at least one edge that does not allow tunneling to these states. On the other hand, the Rashba-like bound states of the graphene ribbon, induced by the ribbon confinement, can only lead to more possibilities for backscattering, and thus antiresonances. As a last remark, we see that the antiresonances in Figs. 5.6 and 5.7 are broadened compared to Fig. 5.8 because the coupling to the TIS is stronger in this case.

Conductance

Finally, we calculate the zero-temperature longitudinal conductance through a barrier of width W and length L. It is given by

$$G(E) = G_0 \frac{L}{2\pi} \int_{-\frac{|E|}{\hbar v_t}}^{\frac{|E|}{\hbar v_t}} dk_y \, T(E, k_y), \tag{5.45}$$

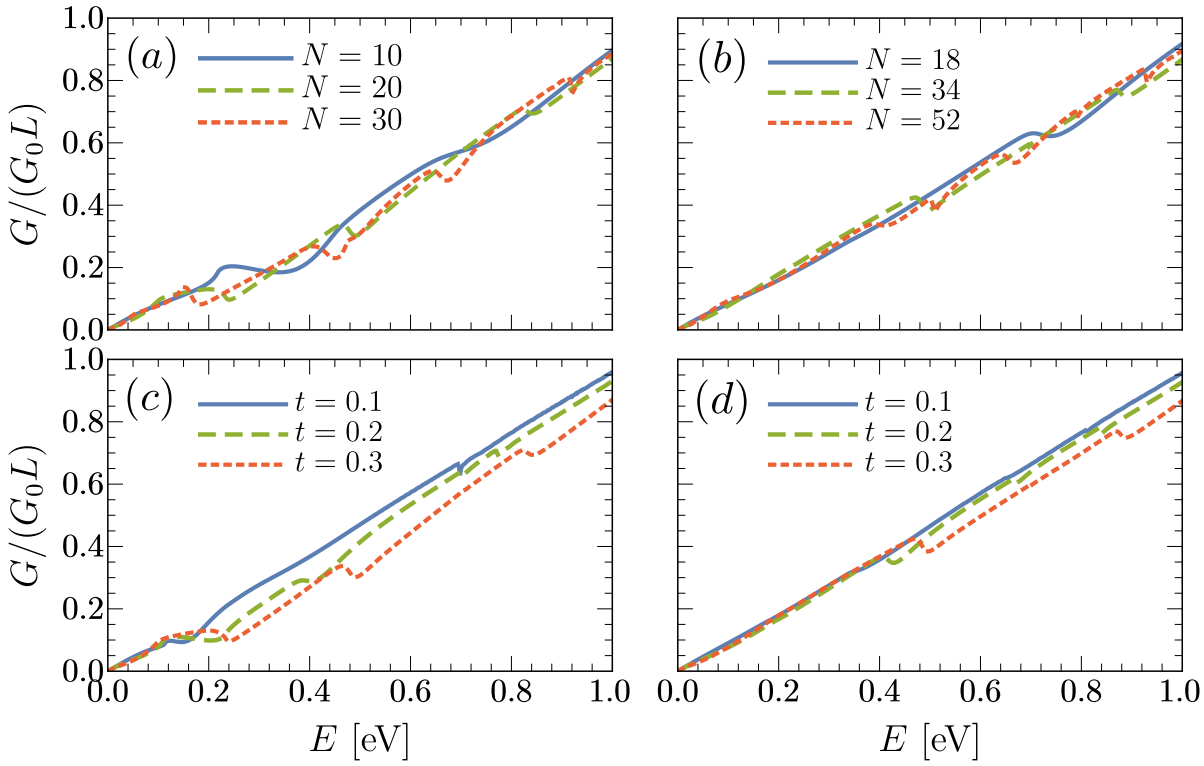

Figure 5.11: (a, b) Conductance for the (a) zigzag and (b) armchair barrier for several widths with $t = 0.3$ eV as a function of the Fermi energy E. The widths of the armchair ribbon are chosen so that it is insulating and matches the corresponding widths in the zigzag case. (c, d) Conductance for the (c) zigzag barrier with $N = 20$ and (d) armchair barrier with $N = 34$ for several t, whose values are shown in eV.

where $G_0 = 2e^2/h$ is the conductance quantum and where we have used dimensionful units. The conductance through zigzag and armchair nanoribbons on the TIS in the T stacking configuration are shown in Fig. 5.11 for several values of the width W and the coupling t.

The plateaus in the conductance are caused by the antiresonances in the transmission probability discussed above. They are more pronounced for the zigzag barrier than the armchair barrier. With increasing N, the number of plateaus increase and they move towards zero energy because of the reduced confinement. On the other hand, if we increase t, more plateaus appear and the conductance is suppressed overall due to increased backscattering at oblique angles.

5.5 Summary

In Chapter 5, we studied electronic transport of the topological surface state through heterostructures that consist of the surface of a topological insulator on which a monolayer of graphene is deposited. We investigated several commensurate stacking configurations and derived a low-energy model. The topological surface state migrates to the graphene layer and generically attains a cubic energy dispersion. We then focused on a single stacking and studied transmission through a semi-infinite graphene step and graphene nanoribbon barriers with both zigzag and armchair boundaries and we obtained the transmission probability by imposing that the current density is continuous. We found that the transmission depends strongly on the type of edge: for the ZZ1 graphene step, the transmission probability has many features and exhibits electron-hole asymmetry, while the transmission for armchair and ZZ2 graphene steps is close to unity independent of the angle of incidence. Moreover, our results show that the conductance through a graphene nanoribbon exhibits plateaus as a function of the Fermi energy, which are caused by antiresonances in the transmission probability corresponding to quasibound states of the deposited nanoribbon. Furthermore, the stackings we considered are commensurate by less than one percent with at least two well-known TIs, Sb_2Te_3 and $TlBiSe_2$. The proposed graphene and topological insulator hybrid structures could for example be fabricated using a mechanical transfer method where the chemical potential difference and electron density can be tuned by gate voltages. Further studies are required to address the effect of a difference in the chemical potential between graphene and the TIS, an external magnetic field, and the number of deposited graphene layers on the transport properties.

5.6 Appendix

5.6.1 Hamiltonian

Here, we derive the low-energy Bloch Hamiltonian of the graphene-topological insulator heterostructure shown in Fig. 5.1. The Hamiltonian is given by

$$H = H_G + H_{TIS} + V, \tag{5.46}$$

where H_G and H_{TIS} are, respectively, the Hamiltonians of graphene and the topological-insulator surface (TIS) and V is the coupling between them. Now consider the basis of Bloch states

$$\left|\Psi^{\alpha,s}_{\boldsymbol{k}+\boldsymbol{G}}\right\rangle = \frac{1}{\sqrt{N_1}} \sum_{\boldsymbol{r}_1} e^{i(\boldsymbol{k}+\boldsymbol{G})\cdot\boldsymbol{r}_1} \left|\boldsymbol{r}_1; \alpha, s\right\rangle, \tag{5.47}$$

$$\left|\Phi^{s}_{\boldsymbol{k}}\right\rangle = \frac{1}{\sqrt{N_2}} \sum_{\boldsymbol{r}_2} e^{i\boldsymbol{k}\cdot\boldsymbol{r}_2} \left|\boldsymbol{r}_2; s\right\rangle, \tag{5.48}$$

for graphene and the TIS, respectively, where $\alpha = A, B$, $s = \uparrow, \downarrow$, and $\boldsymbol{r}_1$ ($\boldsymbol{r}_2$) runs over the graphene (TIS) unit cells. The wave vector $\boldsymbol{k}$ lies inside the folded Brillouin zone (BZ) shown in Fig. 5.1 (*d*) and $\boldsymbol{G}$ are the reciprocal vectors of the heterostructure contained in the graphene BZ. They are given by $\bar{\Gamma}$ and the two inequivalent Dirac points of graphene $\boldsymbol{K'} = -\boldsymbol{K} = 4\pi/(3a)\hat{\boldsymbol{x}}$. In this basis, the Hamiltonian becomes

$$\mathcal{H}_{\boldsymbol{k}} = \begin{pmatrix} h^{(g)}_{\boldsymbol{k}} & 0 & 0 & V_{\boldsymbol{k}} \\ 0 & h^{(g)}_{\boldsymbol{k}+\boldsymbol{K}} & 0 & V_{\boldsymbol{k}+\boldsymbol{K}} \\ 0 & 0 & h^{(g)}_{\boldsymbol{k}+\boldsymbol{K'}} & V_{\boldsymbol{k}+\boldsymbol{K'}} \\ V^{\dagger}_{\boldsymbol{k}} & V^{\dagger}_{\boldsymbol{k}+\boldsymbol{K}} & V^{\dagger}_{\boldsymbol{k}+\boldsymbol{K'}} & h^{(tis)}_{\boldsymbol{k}} \end{pmatrix}, \tag{5.49}$$

where, in the nearest-neighbor approximation, we have

$$h^{(g)}_{\boldsymbol{k}} = \gamma \begin{pmatrix} 0 & f(\boldsymbol{k}) \\ f^*(\boldsymbol{k}) & 0 \end{pmatrix}, \tag{5.50}$$

and

$$h^{(tis)}_{\boldsymbol{k}} = \hbar v_t \left(\hat{\boldsymbol{z}} \times \boldsymbol{s}\right) \cdot \boldsymbol{k}. \tag{5.51}$$

Here, the parameter $\gamma \approx 3.12$ eV is the nearest-neighbor hopping parameter of graphene and $f(\boldsymbol{k}) = 1 + e^{i\boldsymbol{k}\cdot\boldsymbol{a}_1} + e^{i\boldsymbol{k}\cdot\boldsymbol{a}_2}$ with $\boldsymbol{a}_{1,2} = \frac{a}{2}\left(\pm 1, \sqrt{3}\right)$ the graphene lattice vectors, shown in Fig. 5.1 (*a*). Up to first order in $|\boldsymbol{k}|$, we have

$$f(\boldsymbol{k} + \boldsymbol{K}) \simeq \frac{\sqrt{3}\, a}{2} \left(k_x - i k_y\right), \tag{5.52}$$

$$f(\boldsymbol{k} + \boldsymbol{K'}) \simeq -\frac{\sqrt{3}\, a}{2} \left(k_x + i k_y\right), \tag{5.53}$$

$$f(\boldsymbol{k}) \simeq 3. \tag{5.54}$$

On the other hand, the coupling matrix elements are

$$[V_{\boldsymbol{k}+\boldsymbol{G}}]_{\alpha,ss'} = \langle \Psi^{\alpha,s}_{\boldsymbol{k}+\boldsymbol{G}} | V | \Phi^{s'}_{\boldsymbol{k}} \rangle \tag{5.55}$$

$$= \frac{1}{\sqrt{3}} \sum_{\boldsymbol{r}_1} e^{-i(\boldsymbol{k}+\boldsymbol{G})\cdot\boldsymbol{r}_1} V_{\alpha,ss'}(r_1), \tag{5.56}$$

with

$$V_{\alpha,ss'}(r_1) = \langle \boldsymbol{r}_1; \alpha, s | V | \boldsymbol{0}; s' \rangle, \tag{5.57}$$

where we assumed that the matrix elements only depend on the separation $r_1 = |\boldsymbol{r}_1|$.

Next we calculate the coupling matrix elements in lowest order for the three stacking configurations shown in Fig. 5.1. Moreover, we ignore couplings between different spins and drop the spin indices. For the T and B structure, we find

$$[V^{(T)}_{\boldsymbol{k}+\boldsymbol{G}}]_{\alpha} = \delta_{\alpha A} t, \qquad [V^{(B)}_{\boldsymbol{k}+\boldsymbol{G}}]_{\alpha} = t', \tag{5.58}$$

where $t = V_A^{(T)}(0)/\sqrt{3}$ and $t' = V_\alpha^{(B)}(0)/\sqrt{3}$. In addition, the two high-energy graphene bands at the origin of the unfolded BZ, also couple to the topological Dirac cone. However, because they have energy $\pm 3\gamma$ at $\bar{\Gamma}$, they can be neglected for T and B stacking as long as the coupling to the TIS is much smaller than γ.

On the other hand, for the H structure, we obtain

$$[V_{\boldsymbol{k}+\boldsymbol{G}}^{(H)}]_\alpha = t'' \left[\delta_{\alpha A} e^{-i\boldsymbol{q}\cdot\boldsymbol{a}_1} f(\boldsymbol{q}) + \delta_{\alpha B} e^{i\boldsymbol{q}\cdot\boldsymbol{a}_2} f^*(\boldsymbol{q})\right]_{|\boldsymbol{q}=\boldsymbol{k}+\boldsymbol{G}}, \tag{5.59}$$

where $t'' = V_\alpha^{(H)}(0)/\sqrt{3}$. We see that the coupling to the high-energy graphene band in the origin dominates for H stacking. In lowest order of $|\boldsymbol{k}|$ and t''/γ, we find that the spectrum for the H structure is given by the graphene Dirac cones superimposed on

$$\varepsilon_H(\boldsymbol{k}) = -\frac{6t''^2}{\gamma} \pm \hbar v_t \left(1 - \frac{2t''^2}{\gamma^2}\right) k, \tag{5.60}$$

where $\gamma = 2\hbar v_g/(\sqrt{3}a)$. Hence, for H stacking, the coupling to the parabolic bands of graphene at the $\bar{\Gamma}$ point cannot be neglected. This is because the lowest-order coupling between the TIS and the graphene cones vanishes due to C_3 symmetry. This results in much weaker coupling for H stacking compared to T and B stacking: The topological Dirac cone is only shifted in energy and the Fermi velocity is slightly modified.

5.6.2 Unitary transformation

Here, we give the expression for the unitary transformation $U_{\boldsymbol{k}}$ that transforms the Hamiltonian (5.2) for the case $t_B = 0$ (T structure) into the block diagonal form shown in (5.9), (5.10), and (5.11). We find

$$U_{\boldsymbol{k}} = \begin{pmatrix} A_{\boldsymbol{k}} & B_{\boldsymbol{k}} & 0 \\ A_{\boldsymbol{k}} & -B_{\boldsymbol{k}} & 0 \\ 0 & 0 & 1 \end{pmatrix}, \tag{5.61}$$

with

$$A_{\boldsymbol{k}} = \frac{1}{\sqrt{2}} \mathrm{diag}\left(1, -e^{-2i\mathcal{T}_{\boldsymbol{k}}}, 1, 1\right), \tag{5.62}$$

$$B_{\boldsymbol{k}} = \frac{1}{\sqrt{2}} \mathrm{diag}\left(1, 1, 1, -e^{2i\mathcal{T}_{\boldsymbol{k}}}\right), \tag{5.63}$$

where $\mathcal{T}_{\boldsymbol{k}} = \arctan(k_y/k_x)$. The new basis states are

$$|\psi_{A^\pm\uparrow(\downarrow)}\rangle = \frac{1}{\sqrt{2}} \left(|\psi_{A\uparrow(\downarrow)}\rangle \pm |\psi_{A'\uparrow(\downarrow)}\rangle\right), \tag{5.64}$$

$$|\psi_{B^\pm\uparrow}\rangle = \frac{1}{\sqrt{2}} \left(\mp e^{-2i\mathcal{T}_{\boldsymbol{k}}} |\psi_{B\uparrow}\rangle + |\psi_{B'\uparrow}\rangle\right), \tag{5.65}$$

$$|\psi_{B^\pm\downarrow}\rangle = \frac{1}{\sqrt{2}} \left(|\psi_{B\downarrow}\rangle \mp e^{2i\mathcal{T}_{\boldsymbol{k}}} |\psi_{B'\downarrow}\rangle\right), \tag{5.66}$$

where $\pm$ corresponds to the even or the odd valley subspace. Under time reversal, the new basis transforms as

$$\mathcal{T}\left|\psi_{A^{\pm}\uparrow(\downarrow)}\right\rangle = \mp(\pm)\left|\psi_{A^{\pm}\downarrow(\uparrow)}\right\rangle, \tag{5.67}$$
$$\mathcal{T}\left|\psi_{B^{\pm}\uparrow(\downarrow)}\right\rangle = -(+)\left|\psi_{B^{\mp}\downarrow(\uparrow)}\right\rangle. \tag{5.68}$$

Moreover, if $\left|\phi_{\uparrow(\downarrow)}\right\rangle$ is a spin-up (down) basis state of the TIS, we find

$$\left\langle\psi_{A^{-}\uparrow(\downarrow)}\right| V \left|\phi_{\uparrow(\downarrow)}\right\rangle = \left\langle\psi_{A^{-}\uparrow(\downarrow)}\right| \mathcal{T}^{-1} V \mathcal{T} \left|\phi_{\uparrow(\downarrow)}\right\rangle \tag{5.69}$$
$$= -\left\langle\psi_{A^{-}\downarrow(\uparrow)}\right| V \left|\phi_{\downarrow(\uparrow)}\right\rangle \tag{5.70}$$
$$= -\left\langle\psi_{A^{-}\uparrow(\downarrow)}\right| V \left|\phi_{\uparrow(\downarrow)}\right\rangle, \tag{5.71}$$

and the matrix elements between the odd subspace and the TIS vanish.

5.6.3 Spectrum for T stacking

The low-energy energy spectrum of the T-stacked heterostructure at $\mu = 0$ is obtained from the secular equation $|h_+(\boldsymbol{k}) - E| = 0$, where $h_+(\boldsymbol{k})$ is given in (5.10). Similarly to Eq. (5.20), this yields two cubic equations,

$$2t^2 E + \left(E^2 - v_g^2 k^2\right)(\pm v_t k - E) = 0, \tag{5.72}$$

where $k = |\boldsymbol{k}|$. Note that, at $t = 0$, we obtain the low-energy spectrum of graphene superimposed on the topological Dirac cone of the TIS. At finite t, the spectrum is explicitly given by

$$E_m(\boldsymbol{k}) = \pm\frac{v_t k}{3}\left|1 + C_m(k) + \frac{\Delta_0(k)}{C_m(k)}\right|, \tag{5.73}$$

for $m = 1, 2, 3$, which matches the notation of Fig. 5.1 (c), and where

$$\Delta_0(k) = 1 + 6\left[t/\left(v_t k\right)\right]^2 + 3\left(v_g/v_t\right)^2, \tag{5.74}$$
$$\Delta_1(k) = 1 + 9\left[t/\left(v_t k\right)\right]^2 - 9\left(v_g/v_t\right)^2, \tag{5.75}$$
$$C_m(k) = e^{-\frac{2mi\pi}{3}}\sqrt[3]{\Delta_1 + \sqrt{\Delta_1^2 - \Delta_0^3}}. \tag{5.76}$$

The low-energy spectrum for B stacking is obtained by substituting $t \to \sqrt{t_A^2 + t_B^2}$.

6 Conclusion

In the last chapter of my doctoral thesis, I summarize my results that were extensively discussed in the previous chapters and I present several proposals for future research.

6.1 Summary

In this doctoral thesis, I have studied the electronic properties of confined quantum systems in heterostructures made from time-reversal-invariant strong topological insulators (TIs), magnetic films, superconductors, and graphene. In these studies, we used effective continuum models to describe the low-energy physics of bulk TIs and the topological surface state. Electron-electron interactions and proximity-induced superconductivity were included with the configuration-interaction and BdG mean-field method, respectively. My work consisted of three main parts:

(1) Topological crystalline states in junctions of TIs (Chapter 2);

(2) Quantum dots on the surface of TIs (Chapters 3 and 4);

(3) Tunneling in graphene – TI heterostructures (Chapter 5).

In Chapter 2, we first discussed the minimal continuum model for a three-dimensional time-reversal-invariant strong topological insulator with inversion symmetry where we used the well-studied case of Bi_2Se_3 as an example. We showed that the topological regime is characterized by band inversion and protected by time-reversal symmetry by invoking the *bulk-boundary correspondence* which relates the parity of the number of Kramers pairs of surface states to the $\mathbb{Z}_2$ invariant. Next, we considered a semi-infinite system with open boundary conditions and demonstrated the existence and robustness of the topological surface state. For the Bi_2Se_3 family of TIs, the surface state consists of a single Dirac cone located at the $\bar{\Gamma}$ point of the surface Brillouin zone. We then derived the effective surface Hamiltonian, both from perturbation theory and from symmetry principles. This effective surface Hamiltonian was used in all subsequent chapters

to model the topological-insulator surface. In the last section, we considered junctions between two TIs and explicitly calculated the dispersion and wave functions of gapless interface states that are protected by mirror symmetry. We demonstrated that their existence can be understood from the properties of the surface as the resolution of a scattering paradox, or alternatively, from the bulk properties as the change of the *mirror Chern number* across the junction. We explicitly showed that the interface states are robust only when the helicity of the topological surface state is opposite for the two TIs and demonstrated that they only occur when the Hamiltonian commutes with the mirror operator. We then included cubic momentum terms to the Hamiltonian which reduce the full rotation symmetry of the interface to the physical threefold rotation symmetry and showed that the interface states survive as long as mirror symmetry is present. Moreover, we considered rotational mismatch at the junction and calculated the resulting energy gap in the interface spectrum. Furthermore, we proposed a possible experimental realization in strained $HgTe_xS_{1-x}$ systems and a specific experiment to find signatures of the interface states. Finally, we discussed the appearance of spurious tachyonlike interface states in the continuum model and how they can be resolved.

In Chapter 3, we studied quantum dots on the surface of a topological insulator where the surface state is confined with an insulating magnetic film that is deposited on the surface or with a cylindrical array of magnets. Specifically, we considered a system consisting of a disk of the bare surface surrounded by a magnetic field. This opens a magnetic gap on the surface everywhere except in the disk region which confines particles in the disk. The surface state was modeled with the Dirac Hamiltonian where the magnetic field acts as a local exchange potential. First, we derived the general single-particle solution for a circular symmetric system and we obtained the hard-wall boundary conditions which couple the spin components and break time reversal. We then investigated the single-particle properties of the quantum dot as a function of the magnetization direction of the surrounding film. We found that the single-particle spectrum is characterized by a spin-polarized branch which evolves to a zero-energy branch when the magnetization direction lies in the surface plane. We also showed how the properties of the spectrum can be understood in terms of symmetries. We proceeded by including electron-electron interactions with the configuration-interaction method. Here, we assumed that all negative-energy states were filled and only considered interactions between positive-energy states. This approximation is justified as long as the interaction energy scale is smaller than the confinement gap. Besides the many-body spectrum, we calculated the spin-resolved densities and spin-resolved pair correlation functions of the ground state for up to seven fermions in the dot. The latter were used to study the crossover to a spin-polarized Wigner molecule with increasing interaction strength. During this crossover, the majority spin crystallizes in a regular N-polygon localized near the edge while the minority spin remains liquidlike. This can be understood in terms of the occupation of the spin-polarized branch in the single-particle spectrum since it is energetically favorable for particles to occupy higher angular-momentum states. The crossover is thus accompanied with transitions of the ground state towards higher angu-

lar momentum.

In Chapter 4, we investigated two types of confined hybrid quantum systems on the surface of a topological insulator consisting of deposited insulating magnetic films or s-wave superconductors in an annulus geometry. Specifically, we considered an annulus region of the clean surface bounded either by a magnetic region outside and a superconducting region inside (chiral annulus) or by superconducting regions both inside and outside with a superconducting phase difference (helical annulus). Because these regions are gapped, the surface state is confined within the annulus. The annulus region is effectively a domain wall between regions with a different type of gap. We therefore expected that the quantum rings could support robust low-energy excitations whose properties depend on the type of boundaries. First, we obtained the general solution in the BdG formalism for the surface state in the presence of exchange and pairing potentials with circular symmetry. Subsequently, we obtained the hard-wall boundary conditions at the edges of the annulus and calculated the spectrum of the Andreev bound states. Because of the π Berry phase inherited from the surface state, the angular boundary condition gaps the bound-state spectrum (half-integer j) and hence there are no zero-energy bound states. However, the boundary condition can be shifted to integer j by threading half a flux quantum through the inner region, for example with a single $h/(2e)$ vortex if the inner region is a type-II superconductor. Therefore, when half a flux quantum is threaded through the inner disk, the bound states are spectrally shifted and Majorana bound states (MBSs) appear. In case of the chiral annulus, we obtained a single MBS while for the helical annuls we obtained a Kramers pair of MBSs.

In Chapter 5, we studied electronic transport of the topological surface state through heterostructures that consist of the surface of a topological insulator on which a monolayer of graphene is deposited. We investigated several commensurate stacking configurations and derived a low-energy model. The topological surface state migrates to the graphene layer and generically attains a cubic energy dispersion. We then focused on a single stacking and studied transmission through a semi-infinite graphene step and graphene nanoribbon barriers with both zigzag and armchair boundaries and we obtained the transmission probability by imposing that the current density is continuous. We found that the transmission depends strongly on the type of edge: for the ZZ1 graphene step, the transmission probability has many features and exhibits electron-hole asymmetry, while the transmission for armchair and ZZ2 graphene steps is close to unity independent of the angle of incidence. Moreover, our results show that the conductance through a graphene nanoribbon exhibits plateaus as a function of the Fermi energy, which are caused by antiresonances in the transmission probability corresponding to quasibound states of the deposited nanoribbon. Furthermore, the stackings we considered are commensurate by less than one percent with at least two well-known TIs, Sb_2Te_3 and $TlBiSe_2$. The proposed graphene and topological insulator hybrid structures could for example be fabricated using a mechanical transfer method where the chemical potential difference and electron density can be tuned by gate voltages.

6.2 Research prospects

In general, I would like to transition my research more towards subjects that are currently subject to intense study in the field of topological phases such as hybrid structures in Weyl semimetals [56, 128], symmetry-protected topological phases of interacting fermions [129], or the recently discovered topological insulators with quantized electric multipoles [130]. For example, it would be interesting to investigate hybrid quantum systems on the surface of Weyl semimetals to engineer new topological states from the Fermi surface arcs and to consider the implications of electron-electron interactions in these systems. On the other hand, in the graphene–topological insulator heterostructure that we considered, the surface state attains a cubic dispersion which makes it more susceptible to interactions since the kinetic energy is suppressed at low energies. New strongly-correlated topological states could therefore emerge in these heterostructures. It could also be interesting to further investigate the effects of proximity-induced superconductivity on the Wigner crystallization in quantum dots on the surface of a topological insulator.

6.3 Nederlandse versie

6.3.1 Samenvatting

In deze doctoraatsthesis heb ik de elektronische eigenschappen van ingeperkte kwantumsystemen bestudeerd in heterostructuren gemaakt van tijdsomkeerinvariante sterke topologische isolatoren (TIs), magnetische films, supergeleiders en grafeen. In dit onderzoek werden effectieve continuummodellen gebruikt om de lage-energie eigenschappen van bulk TIs en de topologische oppervlaktetoestand te beschrijven. Elektron-elektron interacties en nabijheid-geïnduceerde supergeleiding werden behandeld met respectievelijk de configuratie-interactie en de BdG gemiddelde-veld methode. Mijn werk bestond uit drie delen:

(1) Topologische kristallijne toestanden in juncties van TIs (Hoofdstuk 2);

(2) Kwantumstippen op het oppervlak van TIs (Hoofdstukken 3 en 4);

(3) Tunnelen in grafeen – TI heterostructuren (Hoofdstuk 5).

In Hoofdstuk 2 hebben we eerst het essentiële continuummodel voor een driedimensionale tijdsomkeerinvariante sterke topologische isolator met inversiesymmetrie besproken waar we het veelbestudeerde geval van Bi_2Se_3 gebruikt hebben als voorbeeld. We toonden aan dat het topologische regime gekarakteriseerd is door bandinversie en beschermd door tijdsomkeersymmetrie door beroep te doen op de bulk-rand relatie dat de pariteit van het aantal Kramersparen van oppervlaktetoestanden verbindt met de $\mathbb{Z}_2$ invariant. Vervolgens beschouwden we een halfoneindig systeem met open randvoorwaarden en toonde we het bestaan en de robuustheid van de topologische oppervlaktetoestand aan. Voor de Bi_2Se_3 familie van TIs bestaat de topologische oppervlaktetoestand uit een enkele Dirackegel in het $\bar{\Gamma}$ punt van de oppervlakte Brillouin zone. Daarna hebben we een effectieve oppervlakte-hamiltoniaan afgeleid, zowel met storingsrekening als met symmetrieprincipes. Deze effectieve oppervlakte-hamiltoniaan werd gebruikt in de volgende hoofdstukken om het oppervlak van een topologische isolator te beschrijven. In de laatste sectie hebben we juncties tussen twee TIs beschouwd en de dispersie en golffuncties van de kloofloze interfacetoestanden, die beschermd zijn door spiegelsymmetrie, expliciet berekend. Hun bestaan kon begrepen worden uit de eigenschappen van het oppervlak als de oplossing van een verstrooiingsparadox of alternatief door de verandering van het bulk *spiegel-Cherngetal* over de junctie. We toonden aan dat interfacetoestanden enkel robuust zijn wanneer de heliciteit van de topologische oppervlaktetoestand tegengesteld is voor de twee TIs en demonstreerden dat ze enkel voorkomen wanneer de Hamiltoniaan commuteert met de spiegeloperator. Daarna hebben we kubische termen toegevoegd aan de Hamiltoniaan die de volledige rotatiesymmetrie van de interface reduceren naar de fysische drievoudige rotatiesymmetrie en we toonden aan dat de interfacetoestanden overleven zo lang als de spiegelsymmetrie behouden is. Ook hebben we rotationele mismatch aan de junctie beschouwd en de resulterende energiekloof in het

interfacespectrum berekend. Voorts hebben we een mogelijke experimentele realisatie in vervormde $HgTe_xS_{1-x}$ systemen en een specifiek experiment om sporen van de interfacetoestanden te vinden, voorgesteld. Tenslotte hebben we de verschijning van valse tachyonachtige interfacetoestanden in het continuummodel, en hoe deze kunnen worden vermeden, besproken.

In Hoofdstuk 3 bestudeerden we kwantumstippen op het oppervlak van een topologische isolator waar de oppervlaktetoestand ingeperkt wordt door een isolerende magnetische film die op het oppervlak gelegd wordt of door een cilindervormige reeks van magneten. Specifiek hebben we een systeem beschouwd dat bestaat uit een schijf van het naakte oppervlak, omringd door een magnetische veld. Dit opent een magnetische kloof op het oppervlak overal behalve in de schijf zodat de deeltjes ingeperkt worden in de schijf. De oppervlaktetoestand werd beschreven met de Dirac-hamiltoniaan waar het magnetische veld optreedt als een lokale uitwisselingspotentiaal. Allereerst hebben we de ééndeeltjesoplossing voor een cirkelsymmetrisch systeem afgeleid waarmee we de harde-muur randvoorwaarden, die de spin componenten koppelen en tijdsomkeersymmetrie breken, verkregen hebben. Daarna hebben we de ééndeeltjeseigenschappen van de kwantumstip bestudeerd als functie van de richting van de magnetisatie van de omliggende film. We vonden dat het ééndeeltjesspectrum gekarakteriseerd is door een spingepolariseerde tak die naar een energie-nul tak evolueert wanneer de magnetisatierichting in het vlak van het oppervlak ligt en dat de eigenschappen van het spectrum begrepen kunnen worden met symmetrieën. Vervolgens hebben we elektron-elektron interacties toegevoegd met de configuratie-interactie methode. Hier namen we aan dat alle toestanden met negatieve energie gevuld waren en we beschouwden enkel interacties tussen toestanden met positieve energie. Deze benadering is verantwoord zolang als de interactieschaal kleiner is dan de inperkingskloof. Naast het veeldeeltjesspectrum hebben we ook de spindichtheden en spinpaarcorrelatiefuncties van de grondtoestand berekend voor maximaal zeven fermionen in de stip. De laatstgenoemden werden gebruikt om de crossover naar een spingepolariseerde Wigner molecule te karakteriseren naarmate de interactiesterkte toeneemt. Tijdens deze crossover kristalliseert de meerderheidspin in een regelmatige N-hoek in de buurt van de rand, terwijl de minderheidspin vloeistofachtig blijft. Dit kon begrepen worden als de bezetting van de spingepolariseerde tak in het ééndeeltjesspectrum aangezien het energetisch gunstig is voor de deeltjes om toestanden te bezetten met een hoger draaimoment. Vandaar dat de crossover samengaat met overgangen van de grondtoestand naar hoger draaimoment.

In Hoofdstuk 4 hebben we twee types van ingeperkte hybride kwantumsystemen op het oppervlak van een topologische isolator onderzocht. De heterostructuren bestaan uit gedeponeerde isolerende magnetische films of s-golf supergeleiders in een ringvormige opstelling. We beschouwden een ringvormig gebied van het schone oppervlak begrensd door ofwel een magnetisch gebied buiten en een supergeleidend gebied binnen de ring (chirale ring) of supergeleidende gebieden binnen en buiten de ring met een verschillende supergeleidende fase (helische ring). Omdat deze gebieden een energiekloof hebben, wordt de oppervlaktetoestand ingeperkt in de ring. Het ringvormig gebied is effectief een domein-

muur tussen gebieden met een verschillend soort kloof. We verwachtten daarom dat deze kwantumringen robuuste laagenergetische excitaties kunnen ondersteunen waarvan de eigenschappen afhangen van de randen. Eerst hebben we de algemene oplossing voor de oppervlaktetoestand in het BdG formalisme afgeleid in de nabijheid van paar- en uitwisselingspotentialen met cirkelvormige symmetrie. Hiermee hebben we de harde-muur randvoorwaarden aan de binnen- en buitenkant van de ring verkregen en hebben we het spectrum van de Andreev gebonden toestanden berekend. Echter omwille van de π Berry fase van de oppervlaktetoestand, zorgt de randvoorwaarde in de hoekrichting voor een kloof in het spectrum van de gebonden toestanden (halftallige j) en daarom zijn er geen toestanden met energie gelijk aan nul. De randvoorwaarden kunnen echter verschoven worden naar gehele j door een half flux kwantum door het binnenste van de ring te sturen, bv. met een $h/(2e)$ vortex als het binnenste een type-II supergeleider is. In dit geval worden de gebonden toestanden spectraal verschoven en verschijnen er Majorana gebonden toestanden (MGTs). Voor de chirale ring geeft dit één MGT, terwijl we voor de helische ring een Kramers paar MGTs bekomen.

In Hoofdstuk 5 beschouwden we het elektronisch transport van de topologische oppervlaktetoestanden doorheen heterostructuren die bestaan uit het oppervlak van een topologische isolator waarop een monolaag grafeen gelegd is. We onderzochten verschillende commensurabele stapelconfiguraties en we hebben een laagenergetisch model afgeleid. De topologische oppervlaktetoestand migreert naar het grafeen en verkrijgt in het algemeen een kubische dispersie. Daarna beschouwden we een specifieke stapeling en bestuurden we transmissie doorheen een halfoneindige grafeenstap en een grafeennanostrookbarrière met zowel zigzag als armstoel randen. Vervolgens verkregen we de transmissiewaarschijnlijkheid door continuïteit van de stroomdichtheid te eisen. We vonden dat de transmissie sterk afhing van het type van rand: voor de ZZ1 grafeenstap vertoont de transmissie elektron-holte asymmetrie terwijl voor ZZ2 en armstoel stappen de transmissie steeds perfect is onafhankelijk van de invalshoek. Bovendien toonden onze resultaten aan dat de conductantie door grafeennanostroken, plateaus vertoont als functie van de Fermi-energie die veroorzaakt worden door antiresonanties in de transmissiewaarschijnlijkheid die overeenkomen met quasigebonden toestanden van de gedeponeerde nanostrook. Daarenboven zijn de stapelconfiguraties die we beschouwden commensurabel tot minder dan één percent voor minstens twee bekende topologische isolatoren, Sb_2Te_3 and $TlBiSe_2$. De voorgestelde grafeen en topologische-isolator hybride structuren kunnen bijvoorbeeld gemaakt worden met een mechanische transfermethode waar het verschil in chemische potentiaal en de elektronendichtheid afgestemd kunnen worden met poortvoltages.

6.3.2 Onderzoeksvooruitzichten

In het algemeen zou ik graag de overgang maken naar meer actuele onderzoeksgebieden binnen het gebied van topologische toestanden zoals hybride structuren in Weyl semimetalen [56, 128], symmetriebeschermde topologische fasen van interagerende fermionen [129] of de recent ontdekte topologische isolatoren met gekwantiseerde elektrische multipolen. Het zou bijvoorbeeld interessant zijn om hybride kwantumsystemen op het oppervlak van Weyl semimetalen te bestuderen om zo nieuwe topologische toestanden op te bouwen uit de oppervlakte Fermiboog en de gevolgen van elektron-elektron interacties in deze systemen te beschouwen. Anderzijds, in de grafeen–topologische isolator heterostructuren die we beschouwd hebben, verkrijgt de oppervlaktetoestand een kubische dispersie wat het meer vatbaar maakt voor elektron-elektron interacties aangezien de kinetische energie onderdrukt wordt bij lage energieën. Er zouden dus nieuwe sterk gecorreleerde topologische toestanden kunnen opduiken in deze heterostructuren. Het kan ook interessant zijn om verder de effecten van nabijheid-geïnduceerde supergeleiding op de Wigner kristallisatie in kwantumstippen op het oppervlak van een topologische isolator te onderzoeken.

Bibliography

(*DOIs are clickable in the PDF version*)

[1] M. Nakahara, *Geometry, Topology and Physics*, Taylor and Francis (2003).

[2] L. Fu, C. L. Kane, and E. Mele, *Topological Insulators in Three Dimensions*, Phys. Rev. Lett. **98**, 106803 (2007). doi:10.1103/PhysRevLett.98.106803.

[3] L. Fu and C. L. Kane, *Topological insulators with inversion symmetry*, Phys. Rev. B **76**, 045302 (2007). doi:10.1103/PhysRevB.76.045302.

[4] J. Teo, L. Fu, and C. L. Kane, *Surface states and topological invariants in three-dimensional topological insulators: Application to* $Bi_{1-x}Sb_x$, Phys. Rev. B **78**, 045426 (2008). doi:10.1103/PhysRevB.78.045426.

[5] M. Z. Hasan and C. L. Kane, *Colloquium: Topological insulators*, Rev. Mod. Phys. **82**, 3045 (2010). doi:10.1103/RevModPhys.82.3045.

[6] X.-L. L. Qi and S.-C. C. Zhang, *Topological insulators and superconductors*, Rev. Mod. Phys. **83**, 1057 (2011). doi:10.1103/RevModPhys.83.1057.

[7] D. Pesin and A. H. MacDonald, *Spintronics and pseudospintronics in graphene and topological insulators*, Nat. Mater. **11**, 409 (2012). doi:10.1038/nmat3305.

[8] B. Scharf, A. Matos-Abiague, J. E. Han, E. M. Hankiewicz, and I. Žutić, *Tunneling Planar Hall Effect in Topological Insulators: Spin Valves and Amplifiers*, Phys. Rev. Lett. **117**, 166806 (2016). doi:10.1103/PhysRevLett.117.166806.

[9] A. R. Mellnik, J. S. Lee, A. Richardella, J. L. Grab, P. J. Mintun, M. H. Fischer, A. Vaezi, A. Manchon, E.-A. Kim, N. Samarth, and D. C. Ralph, *Spin-transfer torque generated by a topological insulator*, Nature **511**, 449 (2013). doi:10.1038/nature13534.

[10] R. Yu, W. Zhang, H.-J. Zhang, S.-C. Zhang, X. Dai, and Z. Fang, *Quantized Anomalous Hall Effect in Magnetic Topological Insulators*, Science **329**, 61 (2010). doi:10.1126/science.1187485.

[11] C.-Z. Chang, J. Zhang, X. Feng, J. Shen, Z. Zhang, M. Guo, K. Li, Y. Ou, P. Wei, L.-L. Wang, Z.-Q. Ji, Y. Feng, S. Ji, X. Chen, J. Jia, X. Dai, Z. Fang, S.-C. Zhang, K. He, Y. Wang, L. Lu, X.-C. Ma, and Q.-K. Xue, *Experimental Observation of the Quantum Anomalous Hall Effect in a Magnetic Topological Insulator*, Science **340**, 167 (2013). doi:10.1126/science.1234414.

[12] X.-L. Qi, T. L. Hughes, and S.-C. Zhang, *Topological field theory of time-reversal invariant insulators*, Phys. Rev. B **78**, 195424 (2008). doi:10.1103/PhysRevB.78.195424.

[13] L. Fu and C. L. Kane, *Superconducting Proximity Effect and Majorana Fermions at the Surface of a Topological Insulator*, Phys. Rev. Lett. **100**, 096407 (2008). doi:10.1103/PhysRevLett.100.096407.

[14] P. W. Anderson, *Basic Notions of Condensed Matter Physics*, Westview Press (1997).

[15] K. von Klitzing, G. Dorda, and M. Pepper, *New Method for High-Accuracy Determination of the Fine-Structure Constant Based on Quantized Hall Resistance*, Phys. Rev. Lett. **45**, 494 (1980). doi:10.1103/PhysRevLett.45.494.

[16] B. A. Bernevig and T. L. Hughes, *Topological Insulators and Topological Superconductors*, Princeton University Press (2013).

[17] F. D. M. Haldane, *Model for a Quantum Hall Effect without Landau Levels: Condensed-Matter Realization of the "Parity Anomaly"*, Phys. Rev. Lett. **61**, 2015 (1988). doi:10.1103/PhysRevLett.61.2015.

[18] K. S. Novoselov, A. K. Geim, S. V. Morozov, D. Jiang, Y. Zhang, S. V. Dubonos, I. V. Grigorieva, and A. A. Firsov, *Electric Field Effect in Atomically Thin Carbon Films*, Science **306**, 666 (2004). doi:10.1126/science.1102896.

[19] C. L. Kane and E. J. Mele, $\mathbb{Z}_2$ *Topological Order and the Quantum Spin Hall Effect*, Phys. Rev. Lett. **95**, 146802 (2005). doi:10.1103/PhysRevLett.95.146802.

[20] C. L. Kane and E. J. Mele, *Quantum Spin Hall Effect in Graphene*, Phys. Rev. Lett. **95**, 226801 (2005). doi:10.1103/PhysRevLett.95.226801.

[21] C. Xu and J. E. Moore, *Stability of the quantum spin Hall effect: Effects of interactions, disorder, and* $\mathbb{Z}_2$ *topology*, Phys. Rev. B **73**, 045322 (2006). doi:10.1103/PhysRevB.73.045322.

[22] M. König, S. Wiedmann, C. Brüne, A. Roth, H. Buhmann, L. W. Molenkamp, X.-L. Qi, and S.-C. Zhang, *Quantum Spin Hall Insulator State in HgTe Quantum Wells*, Science **318**, 766 (2007). doi:10.1126/science.1148047.

[23] A. Roth, C. Brüne, H. Buhmann, L. W. Molenkamp, J. Maciejko, X.-L. Qi, and S.-C. Zhang, *Nonlocal Transport in the Quantum Spin Hall State*, Science **325**, 294 (2009). doi:10.1126/science.1174736.

[24] B. A. Bernevig, T. L. Hughes, and S.-C. Zhang, *Quantum Spin Hall Effect and Topological Phase Transition in HgTe Quantum Wells*, Science **314**, 1757 (2006). doi:10.1126/science.1133734.

[25] J. Moore and L. Balents, *Topological invariants of time-reversal-invariant band structures*, Phys. Rev. B **75**, 121306 (2007). doi:10.1103/PhysRevB.75.121306.

[26] D. Hsieh, D. Qian, L. Wray, Y. Xia, Y. S. Hor, R. J. Cava, and M. Z. Hasan, *A topological Dirac insulator in a quantum spin Hall phase*, Nature **452**, 970 (2008). doi:10.1038/nature06843.

[27] H. Zhang, C.-X. Liu, X.-L. Qi, X. Dai, Z. Fang, and S.-C. Zhang, *Topological insulators in Bi_2Se_3, Bi_2Te_3 and Sb_2Te_3 with a single Dirac cone on the surface*, Nat. Phys. **5**, 438 (2009). doi:10.1038/nphys1270.

[28] Y. Xia, D. Qian, D. Hsieh, L. Wray, A. Pal, H. Lin, A. Bansil, D. Grauer, Y. S. Hor, R. J. Cava, and M. Z. Hasan, *Observation of a large-gap topological-insulator class with a single Dirac cone on the surface*, Nat. Phys. **5**, 398 (2009). doi:10.1038/nphys1274.

[29] D. Hsieh, Y. Xia, D. Qian, L. Wray, J. H. Dil, F. Meier, J. Osterwalder, L. Patthey, J. G. Checkelsky, N. P. Ong, A. V. Fedorov, H. Lin, A. Bansil, D. Grauer, Y. S. Hor, R. J. Cava, and M. Z. Hasan, *A tunable topological insulator in the spin helical Dirac transport regime*, Nature **460**, 1101 (2009). doi:10.1038/nature08234.

[30] D. Hsieh, Y. Xia, D. Qian, L. Wray, F. Meier, J. Dil, J. Osterwalder, L. Patthey, a. Fedorov, H. Lin, a. Bansil, D. Grauer, Y. Hor, R. Cava, and M. Hasan, *Observation of Time-Reversal-Protected Single-Dirac-Cone Topological-Insulator States in Bi_2Te_3 and Sb_2Te_3*, Phys. Rev. Lett. **103**, 146401 (2009). doi:10.1103/PhysRevLett.103.146401.

[31] Y. Ando, *Topological Insulator Materials*, J. Phys. Soc. Japan **82**, 102001 (2013). doi:10.7566/JPSJ.82.102001.

[32] Y. Zhang, K. He, C.-Z. Chang, C.-L. Song, L.-L. Wang, X. Chen, J.-F. Jia, Z. Fang, X. Dai, W.-Y. Shan, S.-Q. Shen, Q. Niu, X.-L. Qi, S.-C. Zhang, X.-C. Ma, and Q.-K. Xue, *Crossover of the three-dimensional topological insulator Bi2Se3 to the two-dimensional limit*, Nat. Phys. **6**, 584 (2010). doi:10.1038/nphys1689.

[33] G. Landolt, S. Schreyeck, S. V. Eremeev, B. Slomski, S. Muff, J. Osterwalder, E. V. Chulkov, C. Gould, G. Karczewski, K. Brunner, H. Buhmann, L. W. Molenkamp,

and J. H. Dil, *Spin Texture of Bi_2Se_3 Thin Films in the Quantum Tunneling Limit*, Phys. Rev. Lett. **112**, 057601 (2014). doi:10.1103/PhysRevLett.112.057601.

[34] J. Linder, T. Yokoyama, and A. Sudbø, *Anomalous finite size effects on surface states in the topological insulator Bi_2Se_3*, Phys. Rev. B **80**, 205401 (2009). doi:10.1103/PhysRevB.80.205401.

[35] C.-X. Liu, H. Zhang, B. Yan, X.-L. Qi, T. Frauenheim, X. Dai, Z. Fang, and S.-C. Zhang, *Oscillatory crossover from two-dimensional to three-dimensional topological insulators*, Phys. Rev. B **81**, 041307 (2010). doi:10.1103/PhysRevB.81.041307.

[36] H.-Z. Lu, W.-Y. Shan, W. Yao, Q. Niu, and S.-Q. Shen, *Massive Dirac fermions and spin physics in an ultrathin film of topological insulator*, Phys. Rev. B **81**, 115407 (2010). doi:10.1103/PhysRevB.81.115407.

[37] L. Fu, *Topological Crystalline insulators*, Phys. Rev. Lett. **106**, 106802 (2011). doi:10.1103/PhysRevLett.106.106802.

[38] Y. Ando and L. Fu, *Topological Crystalline Insulators and Topological Superconductors: From Concepts to Materials*, Annu. Rev. Condens. Matter Phys. **6**, 361 (2015). doi:10.1146/annurev-conmatphys-031214-014501.

[39] T. H. Hsieh, H. Lin, J. Liu, W. Duan, A. Bansil, and L. Fu, *Topological crystalline insulators in the SnTe material class*, Nat. Commun. **3**, 982 (2012). doi:10.1038/ncomms1969.

[40] Y. Tanaka, Z. Ren, T. Sato, K. Nakayama, S. Souma, T. Takahashi, K. Segawa, and Y. Ando, *Experimental realization of a topological crystalline insulator in SnTe*, Nat. Phys. **8**, 800 (2012). doi:10.1038/nphys2442.

[41] M. Z. Hasan and J. E. Moore, *Three-Dimensional Topological Insulators*, Annu. Rev. Condens. Matter Phys. **2**, 55 (2011). doi:10.1146/annurev-conmatphys-062910-140432.

[42] X.-L. Qi and S.-C. Zhang, *The quantum spin Hall effect and topological insulators*, Physics Today **63**, 33 (2010). doi:10.1063/1.3293411.

[43] J. E. Moore, *The birth of topological insulators*, Nature **464**, 194 (2010). doi:10.1038/nature08916.

[44] J. Alicea, *New directions in the pursuit of Majorana fermions in solid state systems*, Rep. Prog. Phys. **75**, 076501 (2012). doi:10.1088/0034-4885/75/7/076501.

[45] C. Nayak, S. H. Simon, A. Stern, M. Freedman, and S. Das Sarma, *Non-Abelian anyons and topological quantum computation*, Rev. Mod. Phys. **80**, 1083 (2008). doi:10.1103/RevModPhys.80.1083.

[46] S. M. Girvin, *The Quantum Hall Effect: Novel Excitations and Broken Symmetries*, arXiv:cond-mat/9907002 (1999).

[47] R. Laughlin, *Quantized Hall conductivity in two dimensions*, Phys. Rev. B **23**, 5632 (1981). doi:10.1103/PhysRevB.23.5632.

[48] R. B. Laughlin, *Nobel Lecture: Fractional quantization*, Rev. Mod. Phys. **71**, 863 (1999). doi:10.1103/RevModPhys.71.863.

[49] D. R. Hofstadter, *Energy levels and wave functions of Bloch electrons in rational and irrational magnetic fields*, Phys. Rev. B **14**, 2239 (1976). doi:10.1103/PhysRevB.14.2239.

[50] J. Zak, *Magnetic Translation Group*, Phys. Rev. **134**, A1602 (1964). doi:10.1103/PhysRev.134.A1602.

[51] N. W. Ashcroft and N. D. Mermin, *Solid State Physics*, Brooks Cole (1976).

[52] D. J. Thouless, M. Kohmoto, M. P. Nightingale, and M. den Nijs, *Quantized Hall Conductance in a Two-Dimensional Periodic Potential*, Phys. Rev. Lett. **49**, 405 (1982). doi:10.1103/PhysRevLett.49.405.

[53] C. Nash and S. Siddhartha, *Topology and Geometry for Physicists*, Dover (2011).

[54] R. Jackiw and C. Rebbi, *Solitons with fermion number* $\frac{1}{2}$, Phys. Rev. D **13**, 3398 (1976). doi:10.1103/PhysRevD.13.3398.

[55] J. J. Sakurai, *Modern Quantum Mechanics*, Addison-Wesley (1994).

[56] S. Murakami, *Phase transition between the quantum spin Hall and insulator phases in 3D: emergence of a topological gapless phase*, New J. Phys. **9**, 356 (2007). doi:10.1088/1367-2630/9/9/356.

[57] S. Murakami, S. Iso, Y. Avishai, M. Onoda, and N. Nagaosa, *Tuning phase transition between quantum spin Hall and ordinary insulating phases*, Phys. Rev. B **76**, 205304 (2007). doi:10.1103/PhysRevB.76.205304.

[58] N. N. Berchenko and M. V. Pashkovskiĭ, *Mercury telluride–a zero-gap semiconductor*, Phys. Usp. **19**, 462 (1976). doi:10.1070/PU1976v019n06ABEH005265.

[59] L. Fu and C. L. Kane, *Time reversal polarization and a* $\mathbb{Z}_2$ *adiabatic spin pump*, Phys. Rev.B **74**, 195312 (2006). doi:10.1103/PhysRevB.74.195312.

[60] J. Zak, *Berry's phase for energy bands in solids*, Phys. Rev. Lett. **62**, 2747 (1989). doi:10.1103/PhysRevLett.62.2747.

[61] L. A. Wray, S.-Y. Xu, Y. Xia, D. Hsieh, A. V. Fedorov, Y. S. Hor, R. J. Cava, A. Bansil, H. Lin, and M. Z. Hasan, *A topological insulator surface under strong Coulomb, magnetic and disorder perturbations*, Nat. Phys. **7**, 32 (2011). doi:10.1038/nphys1838.

[62] M.-X. Wang, C. Liu, J.-P. Xu, F. Yang, L. Miao, M.-Y. Yao, C. L. Gao, C. Shen, X. Ma, X. Chen, Z.-A. Xu, Y. Liu, S.-C. Zhang, D. Qian, J.-F. Jia, and Q.-K. Xue, *The Coexistence of Superconductivity and Topological Order in the Bi_2Se_3 Thin Films*, Science **336**, 52 (2012). doi:10.1126/science.1216466.

[63] V. M. Apalkov and T. Chakraborty, *Superluminal tachyon-like excitations of Dirac fermions in a topological insulator junction*, EPL **100**, 17002 (2012). doi:10.1209/0295-5075/100/17002.

[64] C.-X. Liu, X.-L. Qi, H. Zhang, X. Dai, Z. Fang, and S.-C. Zhang, *Model Hamiltonian for topological insulators*, Phys. Rev. B **82**, 045122 (2010). doi:10.1103/PhysRevB.82.045122.

[65] P. G. Silvestrov, P. W. Brouwer, and E. G. Mishchenko, *Spin and charge structure of the surface states in topological insulators*, Phys. Rev. B **86**, 1 (2012). doi:10.1103/PhysRevB.86.075302.

[66] L. Fu, *Hexagonal Warping Effects in the Surface States of the Topological Insulator Bi_2Te_3*, Phys. Rev. Lett. **103**, 266801 (2009). doi:10.1103/PhysRevLett.103.266801.

[67] Y. L. Chen, J. G. Analytis, J.-H. Chu, Z. K. Liu, S.-K. Mo, X. L. Qi, H. J. Zhang, D. H. Lu, X. Dai, Z. Fang, S. C. Zhang, I. R. Fisher, Z. Hussain, and Z.-X. Shen, *Experimental Realization of a Three-Dimensional Topological Insulator, Bi_2Te_3*, Science **325**, 178 (2009). doi:10.1126/science.1173034.

[68] W.-Y. Shan, H.-Z. Lu, and S.-Q. Shen, *Effective continuous model for surface states and thin films of three-dimensional topological insulators*, New J. Phys. **12**, 043048 (2010). doi:10.1088/1367-2630/12/4/043048.

[69] R. Takahashi and S. Murakami, *Gapless Interface States between Topological Insulators with Opposite Dirac Velocities*, Phys. Rev. Lett. **107**, 166805 (2011). doi:10.1103/PhysRevLett.107.166805.

[70] C. De Beule and B. Partoens, *Gapless interface states at the junction between two topological insulators*, Phys. Rev. B **87** (2013). doi:10.1103/PhysRevB.87.115113.

[71] T. Habe and Y. Asano, *Robustness of gapless interface states in a junction of two topological insulators*, Phys. Rev. B **88**, 155442 (2013). doi:10.1103/PhysRevB.88.155442.

[72] T. Rauch, M. Flieger, J. Henk, I. Mertig, and A. Ernst, *Dual Topological Character of Chalcogenides: Theory for Bi_2Te_3*, Phys. Rev. Lett. **112**, 016802 (2014). doi:10.1103/PhysRevLett.112.016802.

[73] C. De Beule, R. Saniz, and B. Partoens, *Crystalline topological states at a topological insulator junction*, Invited paper submitted to J. Phys. Chem. Solids (2017).

[74] J. Vidal, X. Zhang, V. Stevanović, J.-W. Luo, and A. Zunger, *Large insulating gap in topological insulators induced by negative spin-orbit splitting*, Phys. Rev. B **86**, 075316 (2012). doi:10.1103/PhysRevB.86.075316.

[75] C. Brüne, C. X. Liu, E. G. Novik, E. M. Hankiewicz, H. Buhmann, Y. L. Chen, X. L. Qi, Z. X. Shen, S. C. Zhang, and L. W. Molenkamp, *Quantum Hall Effect from the Topological Surface States of Strained Bulk HgTe*, Phys. Rev. Lett. **106**, 126803 (2011). doi:10.1103/PhysRevLett.106.126803.

[76] T. Rauch, S. Achilles, J. Henk, and I. Mertig, *Spin Chirality Tuning and Topological Semimetals in Strained $HgTe_xS_{x-1}$*, Phys. Rev. Lett. **114**, 236805 (2015). doi:10.1103/PhysRevLett.114.236805.

[77] F. Virot, R. Hayn, M. Richter, and J. van den Brink, *Metacinnabar (β-HgS): A Strong 3D Topological Insulator with Highly Anisotropic Surface States*, Phys. Rev. Lett. **106**, 236806 (2011). doi:10.1103/PhysRevLett.106.236806.

[78] Y. Cao, J. a. Waugh, X.-W. Zhang, J.-W. Luo, Q. Wang, T. J. Reber, S. K. Mo, Z. Xu, A. Yang, J. Schneeloch, G. D. Gu, M. Brahlek, N. Bansal, S. Oh, A. Zunger, and D. S. Dessau, *Mapping the orbital wavefunction of the surface states in three-dimensional topological insulators*, Nat. Phys. **9**, 499 (2013). doi:10.1038/nphys2685.

[79] H. Zhang, C.-X. Liu, and S.-C. Zhang, *Spin-Orbital Texture in Topological Insulators*, Phys. Rev. Lett. **111**, 066801 (2013). doi:10.1103/PhysRevLett.111.066801.

[80] F. Zhang, C. L. Kane, and E. J. Mele, *Surface states of topological insulators*, Phys. Rev. B **86**, 081303 (2012). doi:10.1103/PhysRevB.86.081303.

[81] C. Timm, *Transport through a quantum spin Hall quantum dot*, Phys. Rev. B **86**, 155456 (2012). doi:10.1103/PhysRevB.86.155456.

[82] G. J. Ferreira and D. Loss, *Magnetically Defined Qubits on 3D Topological Insulators*, Phys. Rev. Lett. **111**, 106802 (2013). doi:10.1103/PhysRevLett.111.106802.

[83] M. V. Berry and R. J. Mondragon, *Neutrino Billiards: Time-Reversal Symmetry-Breaking Without Magnetic Fields*, Proc. R. Soc. A Math. Phys. Eng. Sci. **412**, 53 (1987). doi:10.1098/rspa.1987.0080.

[84] T. Paananen, R. Egger, and H. Siedentop, *Signatures of Wigner molecule formation in interacting Dirac fermion quantum dots*, Phys. Rev. B **83**, 1 (2011). doi:10.1103/PhysRevB.83.085409.

[85] H. S. Cohl, A. R. P. Rau, J. E. Tohline, D. A. Browne, J. E. Cazes, and E. I. Barnes, *Useful alternative to the multipole expansion of* $1/r$ *potentials*, Phys. Rev. A **64**, 052509 (2001). doi:10.1103/PhysRevA.64.052509.

[86] G. Giuliani and G. Vignale, *Quantum Theory of the Electron Liquid*, Cambridge University Press (2005).

[87] E. Wigner, *On the Interaction of Electrons in Metals*, Phys. Rev. **46**, 1002 (1934). doi:10.1103/PhysRev.46.1002.

[88] H. P. Dahal, Y. N. Joglekar, K. S. Bedell, and A. V. Balatsky, *Absence of Wigner crystallization in graphene*, Phys. Rev. B **74**, 233405 (2006). doi:10.1103/PhysRevB.74.233405.

[89] R. Egger, W. Häusler, C. H. Mak, and H. Grabert, *Crossover from Fermi Liquid to Wigner Molecule Behavior in Quantum Dots*, Phys. Rev. Lett. **82**, 3320 (1999). doi:10.1103/PhysRevLett.82.3320.

[90] S. M. Reimann and M. Manninen, *Electronic structure of quantum dots*, Rev. Mod. Phys. **74**, 1283 (2002). doi:10.1103/RevModPhys.74.1283.

[91] L. P. Kouwenhoven, D. G. Austing, and S. Tarucha, *Few-electron quantum dots*, Rep. Prog. Phys. **64**, 701 (2001). doi:10.1088/0034-4885/64/6/201.

[92] Y.-S. Fu, T. Hanaguri, K. Igarashi, M. Kawamura, M. S. Bahramy, and T. Sasagawa, *Observation of Zeeman effect in topological surface state with distinct material dependence*, Nat. Commun. **7**, 10829 (2016). doi:10.1038/ncomms10829.

[93] R. Wiesendanger, *Spin mapping at the nanoscale and atomic scale*, Rev. Mod. Phys. **81**, 1495 (2009). doi:10.1103/RevModPhys.81.1495.

[94] M. Bode, *Spin-polarized scanning tunnelling microscopy*, Rep. Prog. Phys. **66**, 523 (2003). doi:10.1088/0034-4885/66/4/203.

[95] P. Maletinsky, S. Hong, M. S. Grinolds, B. Hausmann, M. D. Lukin, R. L. Walsworth, M. Loncar, and A. Yacoby, *A robust scanning diamond sensor for nanoscale imaging with single nitrogen-vacancy centres*, Nat. Nanotechnol. **7**, 320 (2012). doi:10.1038/nnano.2012.50.

[96] M. S. Grinolds, S. Hong, P. Maletinsky, L. Luan, M. D. Lukin, R. L. Walsworth, and A. Yacoby, *Nanoscale magnetic imaging of a single electron spin under ambient conditions*, Nat. Phys. **9**, 215 (2013). doi:10.1038/nphys2543.

[97] D. Vasyukov, Y. Anahory, L. Embon, D. Halbertal, J. Cuppens, L. Neeman, A. Finkler, Y. Segev, Y. Myasoedov, M. L. Rappaport, M. E. Huber, and E. Zeldov, *A scanning superconducting quantum interference device with single electron spin sensitivity*, Nat. Nanotechnol. **8**, 639 (2013). doi:10.1038/nnano.2013.169.

[98] C. De Beule, N. T. Ziani, M. Zarenia, B. Partoens, and B. Trauzettel, *Correlation and current anomalies in helical quantum dots*, Phys. Rev. B **94**, 155111 (2016). doi:10.1103/PhysRevB.94.155111.

[99] N. Read and D. Green, *Paired states of fermions in two dimensions with breaking of parity and time-reversal symmetries and the fractional quantum Hall effect*, Phys. Rev. B **61**, 10267 (2000). doi:10.1103/PhysRevB.61.10267.

[100] A. F. Volkov, P. H. C. Magnée, B. J. van Wees, and T. M. Klapwijk, *Proximity and Josephson effects in superconductor-two-dimensional electron gas planar junctions*, Physica C **242**, 261 (1995). doi:10.1016/0921-4534(94)02429-4.

[101] J. H. Bardarson, P. W. Brouwer, and J. E. Moore, *Aharonov-Bohm Oscillations in Disordered Topological Insulator Nanowires*, Phys. Rev. Lett. **105**, 156803 (2010). doi:10.1103/PhysRevLett.105.156803.

[102] M. Zarenia, A. Perali, D. Neilson, and F. Peeters, *Enhancement of electron-hole superfluidity in double few-layer graphene*, Sci.Rep. **4**, 7319 (2014). doi:10.1038/srep07319.

[103] Y. Jang, E. H. Hwang, A. H. MacDonald, and H. Min, *Stacking dependence of carrier interactions in multilayer graphene systems*, Phys. Rev. B **92**, 041411 (2015). doi:10.1103/PhysRevB.92.041411.

[104] L. Miao, Z. F. Wang, W. Ming, M.-Y. Yao, M. Wang, F. Yang, Y. R. Song, F. Zhu, A. V. Fedorov, Z. Sun, C. L. Gao, C. Liu, Q.-K. Xue, C.-X. Liu, F. Liu, D. Qian, and J.-F. Jia, *Quasiparticle dynamics in reshaped helical dirac cone of topological insulators*, PNAS **110**, 2758 (2013). doi:10.1073/pnas.1218104110.

[105] K. Govaerts, K. Park, C. De Beule, B. Partoens, and D. Lamoen, *Effect of Bi bilayers on the topological states of Bi_2Se_3: A first-principles study*, Phys. Rev. B **90**, 155124 (2014). doi:10.1103/PhysRevB.90.155124.

[106] T. Shoman, A. Takayama, T. Sato, S. Souma, T. Takahashi, K. Oguchi, T. Segawa, and Y. Ando, *Topological proximity effect in a topological insulator hybrid*, Nat. Comm **6**, 6547 (2015). doi:10.1038/ncomms7547.

[107] A. H. Castro Neto, F. Guinea, N. M. R. Peres, K. S. Novoselov, and A. K. Geim, *The electronic properties of graphene*, Rev. Mod. Phys. **81**, 109 (2009). doi:10.1103/RevModPhys.81.109.

[108] J. Zhang, C. Triola, and E. Rossi, *Proximity Effect in Graphene–Topological-Insulator Heterostructures*, Phys. Rev. Lett. **112**, 096802 (2014). doi:10.1103/PhysRevLett.112.096802.

[109] W. Cao, R.-X. Zhang, P. Tang, G. Yang, J. Sofo, W. Duan, and C.-X. Liu, *Heavy Dirac fermions in a graphene/topological insulator hetero-junction*, 2D Materials **3**, 034006 (2016). doi:10.1088/2053-1583/3/3/034006.

[110] H. Steinberg, L. A. Orona, V. Fatemi, J. D. Sanchez-Yamagishi, K. Watanabe, T. Taniguchi, and P. Jarillo-Herrero, *Tunneling in graphene–topological insulator hybrid devices*, Phys. Rev. B **92**, 241409 (2015). doi:10.1103/PhysRevB.92.241409.

[111] L. Zhang, Y. Yan, H.-C. Wu, D. Yu, and Z.-M. Liao, *Gate-Tunable Tunneling Resistance in Graphene/Topological Insulator Vertical Junctions*, ACS Nano **10**, 3816 (2016). doi:10.1021/acsnano.6b00659.

[112] K. Vaklinova, A. Hoyer, M. Burghard, and K. Kern, *Current-Induced Spin Polarization in Topological Insulator–Graphene Heterostructures*, Nano Letters **16**, 2595 (2016). doi:10.1021/acs.nanolett.6b00167.

[113] G. Bian, T.-F. Chung, C. Chen, C. Liu, T.-R. Chang, T. Wu, I. Belopolski, H. Zheng, S.-Y. Xu, D. S. Sanchez, N. Alidoust, J. Pierce, B. Quilliams, P. P. Barletta, S. Lorcy, J. Avila, G. Chang, H. Lin, H.-T. Jeng, M.-C. Asensio, Y. P. Chen, and M. Z. Hasan, *Experimental observation of two massless Dirac-fermion gases in graphene-topological insulator heterostructure*, 2D Materials **3**, 021009 (2016). doi:10.1088/2053-1583/3/2/021009.

[114] S. Rajput, Y.-Y. Li, M. Weinert, and L. Li, *Indirect Interlayer Bonding in Graphene–Topological Insulator van der Waals Heterostructure: Giant Spin–Orbit Splitting of the Graphene Dirac States*, ACS Nano **10**, 8450 (2016). doi:10.1021/acsnano.6b03387.

[115] L. Zhang, B.-C. Lin, Y.-F. Wu, H.-C. Wu, T.-W. Huang, C.-R. Chang, X. Ke, M. Kurttepeli, G. V. Tendeloo, J. Xu, D. Yu, and Z.-M. Liao, *Electronic Coupling between Graphene and Topological Insulator Induced Anomalous Magnetotransport Properties*, ACS Nano **11**, 6277 (2017). doi:10.1021/acsnano.7b02494.

[116] T. Sato, K. Segawa, H. Guo, K. Sugawara, S. Souma, T. Takahashi, and Y. Ando, *Direct Evidence for the Dirac-Cone Topological Surface States in the Ternary Chalcogenide $TlBiSe_2$*, Phys. Rev. Lett. **105**, 136802 (2010). doi:10.1103/PhysRevLett.105.136802.

[117] K. Kuroda, M. Ye, A. Kimura, S. V. Eremeev, E. E. Krasovskii, E. V. Chulkov, Y. Ueda, K. Miyamoto, T. Okuda, K. Shimada, H. Namatame, and M. Taniguchi, *Experimental Realization of a Three-Dimensional Topological Insulator Phase in*

Ternary Chalcogenide $TlBiSe_2$, Phys. Rev. Lett. **105**, 146801 (2010). doi:10.1103/PhysRevLett.105.146801.

[118] Y. L. Chen, Z. K. Liu, J. G. Analytis, J.-H. Chu, H. J. Zhang, B. H. Yan, S.-K. Mo, R. G. Moore, D. H. Lu, I. R. Fisher, S. C. Zhang, Z. Hussain, and Z.-X. Shen, *Single Dirac Cone Topological Surface State and Unusual Thermoelectric Property of Compounds from a New Topological Insulator Family*, Phys. Rev. Lett. **105**, 266401 (2010). doi:10.1103/PhysRevLett.105.266401.

[119] S. N. Toubektsis and E. K. Polychroniadis, *Growth and structural considerations on single $TlBiSe_2$ crystals*, J. Cryst. Growth **84**, 316 (1987). doi:10.1016/0022-0248(87)90147-3.

[120] S. Nakajima, *The crystal structure of $Bi_2Te_{3-x}Se_x$*, J. Phys. Chem. Solids **24**, 479 (1963). doi:10.1016/0022-3697(63)90207-5.

[121] Y. Jiang, Y. Wang, M. Chen, Z. Li, C. Song, K. He, L. Wang, X. Chen, X. Ma, and Q.-K. Xue, *Landau Quantization and the Thickness Limit of Topological Insulator Thin Films of Sb_2Te_3*, Phys. Rev. Lett. **108**, 016401 (2012). doi:10.1103/PhysRevLett.108.016401.

[122] Z. Ren, A. A. Taskin, S. Sasaki, K. Segawa, and Y. Ando, *Large bulk resistivity and surface quantum oscillations in the topological insulator Bi_2Te_2Se*, Phys. Rev. B **82**, 241306 (2010). doi:10.1103/PhysRevB.82.241306.

[123] K.-H. Jin and S.-H. Jhi, *Proximity-induced giant spin-orbit interaction in epitaxial graphene on a topological insulator*, Phys. Rev. B **87**, 075442 (2013). doi:10.1103/PhysRevB.87.075442.

[124] F. Guinea, A. H. Castro Neto, and N. M. R. Peres, *Electronic states and Landau levels in graphene stacks*, Phys. Rev. B **73**, 245426 (2006). doi:10.1103/PhysRevB.73.245426.

[125] J. Nilsson, A. H. Castro Neto, F. Guinea, and N. M. R. Peres, *Transmission through a biased graphene bilayer barrier*, Phys. Rev. B **76**, 165416 (2007). doi:10.1103/PhysRevB.76.165416.

[126] T. Nakanishi, M. Koshino, and T. Ando, *Transmission through a boundary between monolayer and bilayer graphene*, Phys. Rev. B **82**, 125428 (2010). doi:10.1103/PhysRevB.82.125428.

[127] L. Brey and H. A. Fertig, *Electronic states of graphene nanoribbons studied with the Dirac equation*, Phys. Rev. B **73**, 235411 (2006). doi:10.1103/PhysRevB.73.235411.

[128] S.-Y. Xu, I. Belopolski, N. Alidoust, M. Neupane, G. Bian, C. Zhang, R. Sankar, G. Chang, Z. Yuan, C.-C. Lee, S.-M. Huang, H. Zheng, J. Ma, D. S. Sanchez, B. Wang, A. Bansil, F. Chou, P. P. Shibayev, H. Lin, S. Jia, and M. Z. Hasan, *Discovery of a Weyl Fermion semimetal and topological Fermi arcs*, Science (2015). doi:10.1126/science.aaa9297.

[129] C. Wang, A. C. Potter, and T. Senthil, *Classification of Interacting Electronic Topological Insulators in Three Dimensions*, Science **343**, 629 (2014). doi:10.1126/science.1243326.

[130] W. A. Benalcazar, B. A. Bernevig, and T. L. Hughes, *Quantized electric multipole insulators*, Science **357**, 61 (2017). doi:10.1126/science.aah6442.

List of publications

1. Christophe De Beule and Bart Partoens, *Gapless interface states at the junction between two topological insulators*, Phys. Rev. B **87**, 115113 (2013).

2. Kyungwha Park, Christophe De Beule, and Bart Partoens, *The ageing effect in topological insulators: evolution of the surface electronic structure of Bi_2Se_3 upon K adsorption*, New J. Phys. **15**, 113031 (2013).

3. Kirsten Govaerts, Kyungwha Park, Christophe De Beule, Bart Partoens, and Dirk Lamoen, *Effect of Bi bilayers on the topological states of Bi_2Se_3: A first-principles study*, Phys. Rev. B **90**, 155124 (2014).

4. Christophe De Beule, Niccolò T. Ziani, Mohammad Zarenia, Bart Partoens, and Björn Trauzettel, *Correlation and current anaomalies in helical quantum dots*, Phys. Rev. B **94**, 155111 (2016).

5. Matthias Van der Donck, Christophe De Beule, Bart Partoens, François Peeters, and Ben Van Duppen, *Piezoelectricity in asymmetrically strained bilayer graphene*, 2D Mater. **3**, 035015 (2016).

6. Christophe De Beule, Mohammad Zarenia, and Bart Partoens, *Transmission in graphene–topological insulator heterostructures*, Phys. Rev. B **95**, 115424 (2017).

7. Christophe De Beule, Rolando Saniz, and Bart Partoens, *Crystalline topological states at a topological insulator junction*, Invited paper submitted to J. Phys. Chem. Solids (2017).